



universität
wien

DISSERTATION / DOCTORAL THESIS

Titel der Dissertation /Title of the Doctoral Thesis

„Modelling of energetic processes in the circumstellar
environment of young solar-like stars“

verfasst von / submitted by

Christian Rab, Bakk. MSc

angestrebter akademischer Grad / in partial fulfilment of the requirements for the degree of
Doktor der Naturwissenschaften (Dr. rer. nat.)

Wien, 2017 / Vienna 2017

Studienkennzahl lt. Studienblatt /
degree programme code as it appears on the student
record sheet:

A 796 605 413

Dissertationsgebiet lt. Studienblatt /
field of study as it appears on the student record sheet:

Astronomie

Betreut von / Supervisor:

Univ. Prof. Dr. Manuel Güdel

Für Katrin, Anika und Franka

Abstract

How the Sun and the solar system were formed is a question of great interest not only for the astronomical community. By observing and studying solar-like but young stars, we can learn about the young Sun and how our solar system was formed. Those young stars, only about a million years old, are very active and are still surrounded by gas and dust. Out of this circumstellar material a rotating disk forms which eventually becomes the birthplace of a planetary system.

Compared to the contemporary Sun, young stars are in a rather active and rough phase of their evolution. They show up to 10 000 times stronger X-ray emission than the Sun, and possibly also an enhanced production of stellar energetic particles. Such high energy sources play an important role in disk evolution as they can ionize molecular hydrogen, the most abundant chemical species. Young stars still acquire mass via accretion of circumstellar material. In this process, they experience short periods (approx. 100 yr) of strongly enhanced mass accretion rates causing an increase of the object's luminosity by factors of several hundred. Such accretion bursts likely have a significant impact on the evolution of the star and its environment. In this work, we study the impact of such energetic processes on the chemistry of the circumstellar material and aim to identify observational tracers to constrain physical properties of young stars, such as their stellar energetic particle flux or their accretion history.

For our investigations, we used and further improved the 2D radiation thermo-chemical disk code PRODiMo (PROtoplanetary DIsk MOdel). We extended PRODiMo with a new X-ray radiative transfer module, including scattering, X-ray dust opacities and a treatment for X-ray background fields. We implemented a method for stellar particle ionization based on detailed particle transport models. Furthermore, we added a parameterized description for an envelope structure for our study on episodic accretion.

We modelled the impact of X-ray radiation and stellar energetic particles on the chemistry of a protoplanetary disk. We find that for a disk located in a typical star formation region, the presence of an X-ray background field has only little impact on its chemistry. However, under certain circumstances (e.g. low cosmic-ray flux) X-ray background fields can have a significant impact on the outer disk chemistry. Stellar energetic particles have an observable impact on disk ionization tracers, assuming flux levels expected for young solar-like stars and that the particles reach the disk. To constrain the particle flux, spatially resolved molecular ion observations and detailed modelling is required to disentangle the contribution of stellar particles from other competing high-energy ionization sources such as X-rays and cosmic rays. Our simulations of episodic accretion chemistry reveal observable features in spectral line images of the circumstellar environment, such as rings and X-shaped emission patterns. Those features are a consequence of the delayed inside-out freeze-out of molecules after the end of the luminosity burst. Based on our results, we propose a model-independent method to identify post-burst targets directly from observations.

For the future, we plan to apply our new models of high-energy disk ionization to spatially resolved molecular ion observations that become more and more common with modern (sub)mm interferometers. With the presented models, it is now also possible to study high-energy ionization in the early embedded phases of star formation. Our studies of episodic accretion chemistry will be continued in an ongoing project with the goal to identify permanent chemical signatures of episodic accretion events.

Contents

1	Introduction	1
1.1	Low-mass star formation and disk evolution	2
1.2	Accretion	5
1.3	T Tauri stars	6
1.3.1	Far-UV radiation	8
1.3.2	Extreme-UV radiation	8
1.3.3	X-ray radiation	9
1.3.4	Stellar energetic particles	11
1.3.5	Environment	12
1.4	Protoplanetary disks	12
1.4.1	Physical structure	13
1.4.2	Chemical structure	15
1.5	Radiation thermo-chemical disk model PRODIMO	16
1.5.1	Gas and dust density structure	17
1.5.2	Radiative transfer	21
1.5.3	Chemistry and thermal balance	23
1.5.4	Synthetic observables (Ray-tracing module)	27
1.6	The DIANA project	27
1.6.1	A fitting example: MWC 480 (HD 31648)	28
2	X-ray radiative transfer in protoplanetary disks	33
2.1	Introduction	35
2.2	Methods	36
2.2.1	Reference model	36
2.2.2	Model groups	38
2.2.3	X-ray radiative transfer	38
2.3	Results	41
2.3.1	X-ray disk ionization rates	41
2.3.2	Molecular ion column densities	44
2.4	Discussion	46

2.4.1	Observational implications of X-ray background fields	46
2.4.2	UV background fields and external photo-evaporation	47
2.5	Summary and conclusions	48
2.6	References	48
2.7	Appendix A: Comparison of X-ray photoelectric cross-sections	50
2.8	Appendix B: Comparison to the MC X-ray RT code MOCASSIN	50
2.9	Appendix C: HCO ⁺ formation pathway via excited molecular hydrogen	51
3	Stellar energetic particle ionization	53
3.1	Introduction	55
3.2	Method	56
3.2.1	Stellar energetic particle spectra	56
3.2.2	Stellar particle transport and ionization rate	57
3.2.3	Other ionization sources	57
3.2.4	Model series	58
3.2.5	Disk model	59
3.3	Results	60
3.3.1	Ionization rates as a function of column density	60
3.3.2	Disk ionization rates	60
3.3.3	Impact on HCO ⁺ and N ₂ H ⁺	61
3.4	Discussion	65
3.4.1	Constraining the stellar particle flux of T Tauri stars	65
3.4.2	Chemical implications	66
3.4.3	Future prospects	68
3.5	Summary and conclusions	69
3.6	References	69
3.7	Appendix A: X-ray radiative transfer	71
3.8	Appendix B: Chemistry	71
3.9	Appendix C: Steady-state versus time-dependent chemistry	73
3.10	Appendix D: The Turner model	74
3.11	Appendix E: Comparison to observations	74
4	The chemistry of episodic accretion	75
4.1	Introduction	77
4.2	Method	78
4.2.1	Physical model	78
4.2.2	Chemical model	80

4.2.3	Burst scenario	82
4.2.4	Synthetic observations	82
4.3	Results	82
4.3.1	Adsorption timescale	82
4.3.2	CO gas phase abundance	83
4.3.3	ALMA simulations	85
4.3.4	Impact of structure	87
4.4	Discussion	87
4.4.1	A model independent method to identify post-burst sources	87
4.4.2	CO extent versus bolometric luminosity	89
4.4.3	Further considerations	90
4.5	Summary and conclusions	91
4.6	References	92
4.7	Appendix A: Comparison to Visser et al. (2015)	94
4.8	Appendix B: ALMA/CASA simulations	96
4.9	Appendix C: ALMA simulations for inclined models	96
4.10	Appendix D: Radial intensity profiles for the structure models	98
4.11	Appendix E: Further fitting examples	99
5	Summary & Outlook	103
	References	107
	Appendix A	119
	List of Figures	121
	List of Tables	123
	Zusammenfassung	125
	Reprint Permission	127
	Acknowledgements	129
	Appendix B	131
	Publication List	133
	Successful observing proposals	135
	Curriculum Vitae	137

Chapter 1

Introduction

How the Sun and the solar system were formed is a question of great interest not only for the astronomical community. There are different ways to investigate those questions. One way is to look at solar system bodies, such as meteorites, which were formed early on in the evolution of the solar system (see e.g. [Dauphas and Chaussidon 2011](#); [Mumma and Charnley 2011](#)). Another one is to actually look at stars which are similar to our Sun but much younger. By observing and studying such young stars and their circumstellar environment we can learn about the young Sun and how our solar system was formed.

Young solar-like stars are called T Tauri stars, named after the prototype T Tau located in the Taurus molecular cloud ([Joy 1945](#)). T Tauri stars are not formed in isolation but are formed within clusters. The cluster environment influences the evolution of the star and its disk, a scenario which is also likely for our Sun (see e.g. [Adams 2010](#)). T Tauri stars are only a couple of million years old and are still surrounded by circumstellar material, in particular a disk in Keplerian rotation. Such disks are called protoplanetary disks as they are considered to be the birthplaces of planets. T Tauri stars have similar masses as our Sun and it is expected that they follow the same evolutionary pathway as our Sun did. Compared to the contemporary Sun, T Tauri stars are in a very active and violent phase in their evolution. This enhanced activity is likely driven by strong stellar magnetic fields and fast stellar rotation (see e.g. [Feigelson and Montmerle 1999](#); [Güdel 2007](#)).

As a consequence of their enhanced activity, T Tauri stars show strong X-ray emission with X-ray luminosities of about 10^4 times higher than the contemporary Sun ([Feigelson et al. 2002](#)). As young stars are formed within clusters, the high X-ray luminosity emitted by the individual cluster members might produce a X-ray background field strong enough to influence the circumstellar environment of cluster members ([Adams et al. 2012](#)). Similar to the Sun T Tauri stars likely also produce energetic particles (e.g. protons). Again due to the activity of the star, stellar energetic particle fluxes of T Tauri stars might be much stronger than what we know from our Sun. In contrast to the Sun, the particle fluxes of T Tauri stars cannot be directly measured. These particles are of special interest as their impact on the solid material in the early phases of the Solar System can still be measured in meteoritic material (see e.g. [Meyer and Clayton 2000](#)). X-rays and stellar energetic particles can ionize molecular hydrogen, the most abundant chemical species in disks. Ionization is not only an important driver for disk chemistry but is also

most relevant for the coupling of the gaseous material to magnetic fields. Studying high energy ionization processes is therefore crucial to understand the physical and chemical evolution of disks.

Young stars still accrete material from their surroundings. How this accretion process works in detail is still not well understood. However, there is evidence that accretion is not a continuous process but rather happens episodically (see e.g. [Audard et al. 2014](#)). Strong indications for episodic accretion events are the observed strong luminosity bursts (an increase of the luminosity by orders of magnitudes) of young stars which can last for decades or centuries. Stars showing such bursts are called FU Orionis objects, named after their prototype FU Ori. Episodic accretion likely has a significant impact on the evolution of the star and its circumstellar material.

In this work, we use radiation thermo-chemical models to study the circumstellar environment of T Tauri stars. We focus on the above mentioned high energy processes like X-ray emission, stellar energetic particles and episodic accretion events. With the models presented it is not only possible to study the impact of those high energy processes on the circumstellar environment of the star, but also to constrain properties of young stars, such as their stellar particle flux or their accretion history.

This thesis is organized in the following way. To put our work into context we start with an overview of low mass star formation (Sect. 1.1), the accretion process (Sect. 1.2), the properties of T Tauri stars (Sect. 1.3) and protoplanetary disks (Sect. 1.4). In Section 1.5 we describe the radiation thermo-chemical disk model PRODIMO (PROtoplanetary DISK MOdel), our main modelling tool. This thesis was done in the frame of the EU FP7 project DIANA (DISK ANALYSIS), which is briefly introduced in Section 1.6. The core of this PhD thesis is presented as one submitted and two published papers in Chapters two to four. In Chapter 2 we present our study about the impact of X-ray emission on disk chemistry. Chapter 3 is about the importance of stellar energetic particles for disk ionization. Our work on the chemistry of episodic accretion is presented in Chapter 4. We conclude the thesis with a summary of our results and an outlook about future applications of our new models in Chapter 5.

1.1 Low-mass star formation and disk evolution

Protoplanetary disks are a natural outcome of the low-mass star formation process. In the following, we provide a very brief introduction of low-mass star formation with a focus on the evolution of the disk component. The main stages of low-mass star formation, from the initial collapse of a dense core to the formation of a planetary system, are depicted in Fig. 1.1. This sketch also shows the typical time and spatial scale for each stage of the star formation process. Also indicated is the observational classification (Class 0 to III) according to [Lada \(1987\)](#) and [Andre et al. \(1993\)](#).

Stars are formed out of dark cores located in dense molecular clouds. Such dark cores collapse under their own gravity. This is the start of the star formation process. In the center of the collapsing cloud a protostar forms that continues to accrete material from the surrounding molecular cloud. Due to the rotation of the initial dense core and angular momentum conservation, a disk is formed around the protostar, which is called

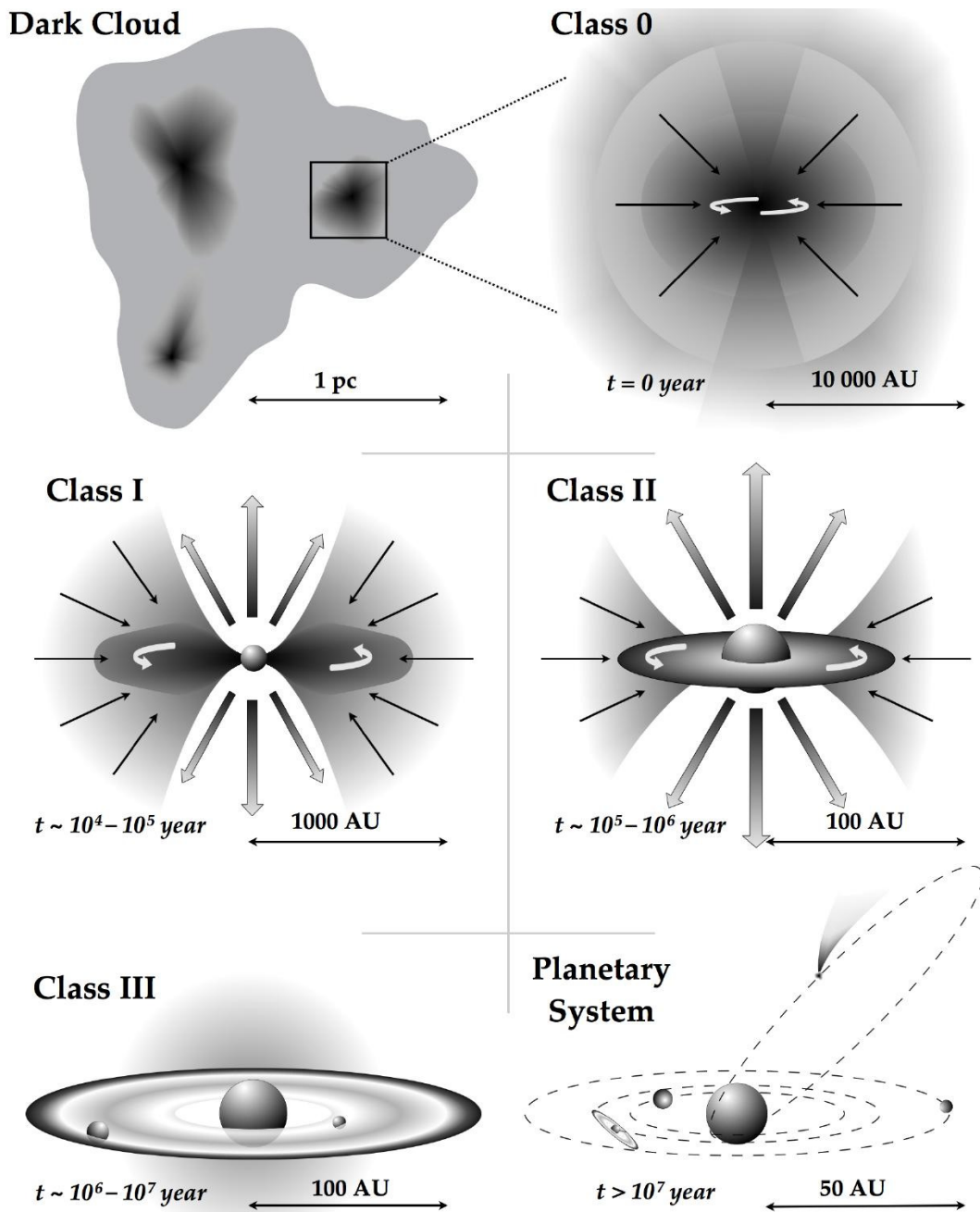


Figure 1.1 – Sketch of the main stages of low-mass star formation, from a molecular cloud to a planetary system. Credit: Wilfred Frieswijk, [Aresu \(2012\)](#)

a protostellar disk. Recent observations indicate that protostellar disks form early on, have sizes of a few 100au and some show clear Keplerian rotation curves (e.g. [Murillo et al. 2013](#); [Tobin et al. 2015](#)). However, the properties of protostellar disks are still not well known, mainly because they are still deeply embedded in the parent core and are therefore difficult to observe (see e.g. [Li et al. 2014](#)).

Observationally this first stage of low-mass star formation is classified as *Class 0*, showing still no (or undetectable) emission from the protostar itself and only emission in the far-infrared to mm wavelength range is detectable. Although theoretically expected, so far no clear detections of X-rays in the Class 0 stage are reported. However, that might simply be a consequence of the high extinction towards Class 0 sources ([Feigelson 2010](#)). Observations indicate an upper limit for the X-ray luminosity of $L_X \lesssim 10^{29} \text{ erg s}^{-1}$ (e.g. [Giardino et al. 2007](#); [Feigelson 2010](#)), which is significantly lower than typical X-ray luminosities of more evolved young stars (see also Section 1.3.3). On the other hand there is some evidence for energetic particle emission in the deeply embedded protostar OMC-2 FIR 4 indicating that high energy processes are already at work in those early stages of star formation ([Ceccarelli et al. 2014](#), see also Section 3.1).

Common phenomena around protostars are jets and outflows. Jets and outflows transport matter and angular momentum outwards and produce cavities orientated along the rotation axis of the system, partly revealing the protostar in the center. Observationally this stage is classified as *Class I*, where the emission of the system is still dominated by near and mid-infrared emission of the disk and envelope structure but a contribution of the protostar is already visible. Disks in the Class I stage are rather massive with masses in the range of approximately 0.01 to 0.1 M_\odot and already show evidence of dust grain growth (up to mm sizes), similar to protoplanetary disks ([Li et al. 2014](#)). X-rays from Class I sources are detected on a regular basis ([Feigelson 2010](#)). [Imanishi et al. \(2001\)](#) reported a X-ray detection rate of approximately 70% for Class I sources in the ρ Ophiuchi cloud. Their observed X-ray luminosities are in the range of $10^{29} - 3 \times 10^{30} \text{ erg s}^{-1}$, very similar to T Tauri stars (see Sect. 3.1).

When the envelope is depleted and outflows and jets have produced a large cavity the star becomes visible in the optical. Observationally this stage is classified as *Class II* and is also called the T Tauri phase (for solar-like stars). The star has now evolved to a T Tauri star and the disk is called a protoplanetary disk. We provide further details on T Tauri stars and their disks in Sections 1.3 and 1.4. Protoplanetary disks evolve on a timescale of several million years. Their main dispersal mechanisms are accretion onto the star, disk winds including photo-evaporation but also planet formation itself. The presence of disks with inner (dust) holes, so called transitional disks, indicate that the dispersal happens from inside out. One such example is LkCa 15, a large transitional disk, with three giant planets located in a large ($r \approx 50 \text{ au}$) inner dust hole ([Sallum et al. 2015](#)). The relatively low number of detected transitional disks points towards rapid disk dispersal on a time scale of $\gtrsim 10^5 \text{ yr}$ ([Alexander et al. 2014](#); [Espaillat et al. 2014](#)).

In the final stage of protoplanetary disk evolution, the *Class III* stage, the disk becomes optically thin and the spectral energy distribution in this phase is mostly dominated by the star. Such objects are also called “weak lined T Tauri stars” as their stellar spectrum does not show strong emission lines anymore; this is an indication that accretion of material onto the star has stopped. Further evolution leads to a debris disk that consists of material produced by the destructive interaction of planetesimals ([Matthews et al. 2014](#)).

The star itself further evolves towards the main sequence and can then be surrounded by a planetary system.

1.2 Accretion

One of the most important processes for the formation and evolution of the disk and the star itself is accretion. Although it is clear that accretion must be at work during the star formation process, it is still quite unclear what actually drives accretion in protostellar/protoplanetary disks and in what way a star accumulates its mass (Hartmann et al. 2016).

One of the most promising mechanisms to drive accretion in disks is (or was) the magneto-rotational instability (MRI) (Balbus and Hawley 1991). However, MRI requires an ionization fraction of about 10^{-12} of the for the disk material, which is not necessarily the case in all regions of a protoplanetary disk. Further, non-ideal MHD effects might also suppress the efficiency of MRI (Turner et al. 2014). Other proposed mechanisms for efficient angular-momentum transport are gravitational instabilities in the protostellar disk phase, hydrodynamic instabilities (Turner et al. 2014) or magnetically driven disk winds (e.g. Bai and Stone 2013). It is also a possibility that all these mechanisms are relevant but are at work at different stages of disk evolution and/or in different regions of the disk. Recent observations provide first constraints on the turbulence in protoplanetary disks and indicate that turbulence in the disk upper layers might be lower than predicted by models (e.g. Flaherty et al. 2017; Teague et al. 2016).

To model accretion processes in disks sophisticated and complex (magneto) hydrodynamical simulations are required, but such simulations usually cannot treat in detail the thermo-chemical processes. An important input for such simulations are for example the detailed thermal structure of the disk (as strong temperature gradients might produce instabilities) or the disk ionization fraction at every point in the disk relevant for the coupling of the magnetic field to the disk material (see Turner et al. 2014). Further, it is important to constrain the efficiency of disk ionization and heating agents such as cosmic rays, X-rays, UV-radiation or stellar energetic particles. For example, recent results indicate that cosmic rays might not reach the disks around T Tauri stars at all as the disk might be shielded by the analogue of the solar heliosphere, a so called “T Tauriosphere” (Cleeves et al. 2014, 2015). Models with a detailed and consistent treatment of radiation transport, chemistry and heating/cooling processes that can directly be compared to observations are required to provide stringent constraints on the thermal and chemical structure of protoplanetary disks. With such models, it is also possible to constrain stellar (e.g. emission of energetic particles) and environmental properties of young stellar objects (see Chapters 2 and 3).

When a star accretes material most of the energy of the infalling material is radiated away. It is, therefore, useful to define an accretion luminosity which can be written as (Hartmann et al. 2016)

$$L_{\text{acc}} = \eta GM_* \dot{M} / R_*, \quad (1.1)$$

where η is the fraction of accretion energy radiated away, G is the gravitational constant,

M_* and R_* are the stellar mass and radius, respectively and \dot{M} is the mass accretion rate onto the star. In the early phases of the star formation process (Class 0/I) the luminosity of the protostar is mostly dominated by the accretion luminosity. However, measurements of protostellar luminosities indicate that their luminosities are lower than predicted by models assuming a constant accretion rate (Kenyon et al. 1990). This discrepancy is called the “luminosity problem”.

One solution to the luminosity problem is that protostars accrete most of their mass during short periods of strongly enhanced accretion, hence showing a low accretion luminosity most of the time (e.g. Kenyon and Hartmann 1995). This paradigm is called the “Episodic Accretion scenario”. One indication for episodic accretion events are the observed strong luminosity bursts (an increase of the luminosity by orders of magnitudes) of young stellar objects (e.g. Herbig 1977; Audard et al. 2014). Stars showing such strong luminosity bursts belong to the class of FU Orionis objects, named after their prototype FU Orionis (Herbig 1966). Those accretion outbursts are likely triggered by instabilities in the disk and/or by external perturbation of the disk, but the details of the triggering process are still unclear (Audard et al. 2014). As shown by Dunham and Vorobyov (2012), low mass star formation models including episodic accretion events, in this particular case triggered by gravitation instabilities (Vorobyov and Basu 2010), are consistent with the observed distribution of protostellar luminosities. However, models assuming a constant accretion rate but inefficient accretion onto the star are also able to explain the observations but the process of making accretion inefficient remains unclear (Myers 2014).

As FU Ori like episodic accretion events last only for about 100 yr the number of detected FU Ori like objects remains low (≈ 30 , Audard et al. 2014). It is still unclear if all solar-like stars and in particular the young Sun had to experience such violent events during their early evolution. However, episodic accretion likely has a significant impact on the evolution of the star (see Hartmann et al. 2016) and its circumstellar material. In Chapter 4 we present a new two-dimensional model to study the impact of luminosity bursts on the chemistry in circumstellar environment of young stars. The impact of the burst on the chemistry lasts much longer than the burst itself. Observations of molecules in the circumstellar environments of young stars opens up the possibility to identify a larger number of young stars that experienced a recent accretion burst (e.g. Jørgensen et al. 2015).

1.3 T Tauri stars

T Tauri stars were initially characterized as a distinct class of variable stars of spectral type F5-G5 showing rapid irregular light variations, low luminosities and a likely association with nebulosity Joy (1945). Further studies revealed that they are indeed associated with molecular clouds and that they appear in groups (see reviews of Appenzeller and Mundt 1989 and Bertout 1989). Nowadays we know that T Tauri stars are young ($< 10^7$ yr) and low mass ($M_* < 2 - 3 M_\odot$) pre-main-sequence stars surrounded by circumstellar matter (Appenzeller and Mundt 1989). In the low-mass star formation scenario, they belong to the Class II objects representing the evolutionary stage between deeply embedded young stellar objects (Class 0/I) and main-sequence stars. The group

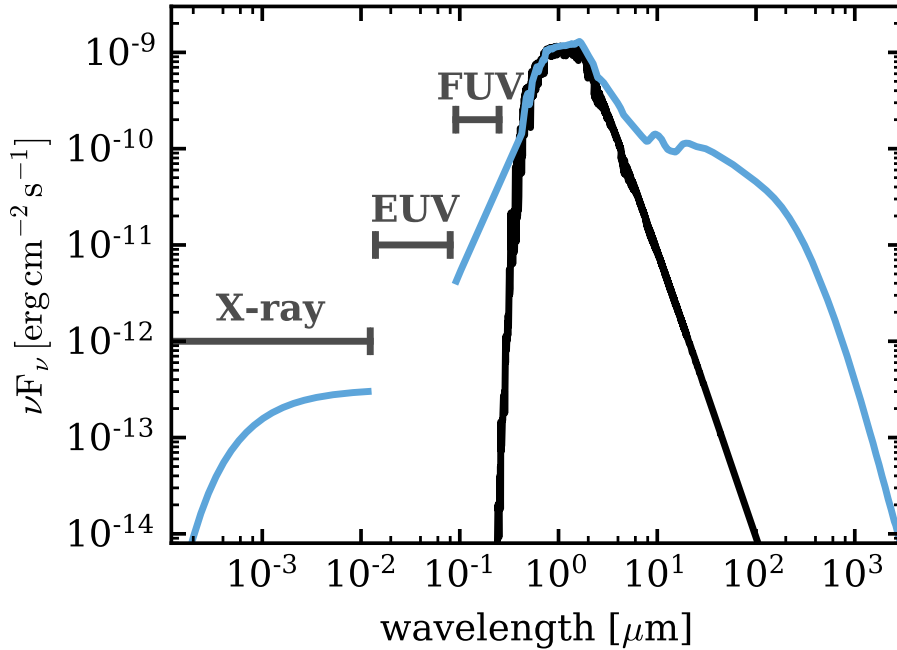


Figure 1.2 – Synthetic spectral energy distribution (SED) of a representative T Tauri star/disk model. The blue line shows the “observed” SED for a distance of 140 pc and a disk inclination of 45° . The black solid line shows the modelled photosphere for a star with a mass of $M_* = 0.7 M_\odot$, an effective temperature $T_* = 4000$ K and a luminosity of $L_* = 1 L_\odot$. Also indicated are the wavelength regimes for X-ray, extreme-UV (EUV) (not included in the model) and far-UV (FUV) radiation.

of T Tauri stars was separated into classical and weak-lined T Tauri stars (Class III, see also Sect. 1.1). Here the expression T Tauri star always refers to classical T Tauri stars.

Most relevant for this work is the energy output of T Tauri stars, in particular at high energies. In Fig. 1.2 we show a synthetic spectral energy distribution (SED) for a representative T Tauri star and disk model. This is the same model as is used in Chapters 2 and 3. Fig. 1.2 shows most parts of the wavelength range (X-ray to the mm regime) relevant for the study of T Tauri stars and their disks. Of particular importance for the disk chemistry is X-ray and far-ultraviolet (FUV) radiation. The optical part of the emission spectrum is well represented by a stellar atmosphere model (here we use PHOENIX stellar atmosphere models, [Brott and Hauschildt 2005](#)). For wavelengths larger than $\approx 0.1 - 1.0 \mu\text{m}$ the emission is dominated by thermal emission of the dust disk.

To study and understand T Tauri stars and their disks, observations covering the whole wavelength range shown in Fig. 1.2 are required. Observations of the stellar emission (or emission close to the star) are an essential ingredient for disk modelling as this radiation mostly determines the temperature structure of the disk and drives disk chemistry. Disk observations from the near-infrared to the radio regime are required to trace different disk regions (e.g. near-infrared for the inner disk, mm for the outer disk), various disk properties (e.g. mm observations for the disk dust mass) and of course to constrain theoretical models (see also Sect. 1.6).

In the following, we provide a brief overview of the X-ray, EUV and FUV radiation properties of T Tauri stars. Furthermore, we discuss stellar energetic particles, as their impact on disk ionization is the topic of Chapter 3.

1.3.1 Far-UV radiation

Compared to main-sequence stars, T Tauri stars show an excess of emission in the FUV wavelength regime (6 – 13.6 eV; 0.0912 – 0.205 μm) and near-UV regime. This excess emission is produced by accretion shocks close to the stellar surface, that additionally heat the stellar photosphere (e.g. Calvet and Gullbring 1998; Gullbring et al. 2000; Herczeg et al. 2004). Typical FUV luminosities of T Tauri stars are in the range of $\approx 10^{30} - 10^{32} \text{ erg s}^{-1}$ (Yang et al. 2012; Aresu et al. 2014).

Although the UV range can be observed with space telescopes like the Hubble Space Telescope (HST), IUE (International Ultraviolet Explorer) and FUSE (Far Ultraviolet Spectroscopic Explorer) an accurate estimate of the total flux is challenging. Most of the FUV emission arises from spectral lines, in particular, the Ly- α line ($\gtrsim 80\%$ of the total FUV flux, Schindhelm et al. 2012) and therefore high spectral resolution observations and careful reconstruction of the spectra (i.e. to compensate for extinction) are required (France et al. 2014). Such accurate data is still rare and it is therefore often necessary for disk modelling to use approximations for the stellar FUV field (as used in Fig. 1.2; see also Voitke et al. 2016).

The stellar FUV radiation field is up to 10^6 times stronger than the interstellar FUV radiation field and dominates the disk irradiation out to hundreds of au (measured from the star). This essentially makes disks 2D/3D photo-dissociation regions (see e.g. Voitke et al. 2009). Although FUV photons cannot ionize molecular hydrogen it is a very important ionization source in the upper layers of the disk, as it efficiently ionizes atomic species like carbon and sulphur (see e.g. Teague et al. 2015). Further FUV photons dissociate important molecules like H_2 , CO or N_2 and therefore determine the transition from the atomic to the molecular layer (see also Sect. 1.4). Besides being an important disk chemistry driver FUV radiation is also an important heating agent for both the dust, which is the main opacity source for FUV photons, and the gas. Gas heating by FUV photons drives spectral line emission (e.g. [O I] Aresu et al. 2014) and might contribute to disk photo-evaporation (e.g. Gorti et al. 2016; Ercolano and Pascucci 2017).

To study the impact of FUV radiation on disk chemistry and observables is not the main focus of this thesis. However, as it is an important chemistry driver a proper treatment of FUV radiation in the radiative transfer and the chemistry (see also Sect. 1.5) is included in all the models presented.

1.3.2 Extreme-UV radiation

Extreme ultraviolet radiation (EUV; 13.6 – 100 eV; 0.0124 – 0.0912 μm) of T Tauri stars cannot be directly measured as EUV photons are easily absorbed by neutral hydrogen. However, the EUV flux of T Tauri stars can be roughly estimated by indirect methods. Using FUV line emission measurements, Alexander et al. (2005) estimated EUV photon fluxes of the order of $10^{41} - 10^{44} \text{ photons s}^{-1}$ for five different T Tauri stars. For comparison, the contemporary Sun emits only $10^{38} \text{ photons s}^{-1}$ (Alexander et al. 2005) in the EUV range. There seems to be no correlation of the EUV luminosity with disk or stellar evolutionary stage (i.e. accretion rate) pointing towards a chromospheric origin of EUV photons (Alexander et al. 2005). The high EUV fluxes of T Tauri stars, compared to the

contemporary Sun, are therefore probably a result of the enhanced magnetic activity of T Tauri stars (see also Sect. 1.3.3).

Although the EUV flux of T Tauri stars can be high, it is unlikely that many EUV photons actually reach the disk as they are easily absorbed by accretion columns located between the star and the disk (Alexander et al. 2004). Pascucci et al. (2014) used free-free continuum observations of 14 T Tauri stars to estimate the EUV flux impinging on the disk surface. Assuming that this free-free emission is produced by the ionized disk surface and that the disk surface is mainly ionized by EUV photons they find an upper limit for the impinging EUV flux of $\lesssim 2 \times 10^{41}$ photons s^{-1} . This is at the lower end of the values found by Alexander et al. (2005) but consistent with efficient absorption of EUV photons by accretion columns. Such low EUV photon fluxes are not sufficient to efficiently drive photo-evaporative disk winds, indicating that EUV-radiation is of less relevance for disk evolution (Pascucci et al. 2014; Gorti and Hollenbach 2009).

Although the EUV radiation properties of T Tauri stars are not well known, it is likely that not many EUV photons actually reach the disk. In any case they can only penetrate disk hydrogen column densities of $N_H \lesssim 10^{20}$ cm^{-2} (see e.g. Ercolano et al. 2009) and are therefore of little relevance for the chemical evolution of the disk, in particular the molecular layer. In the disk models presented in this work EUV radiation is not considered (i.e. we assume that no EUV photons reach the disk, see also Voitke et al. 2016).

1.3.3 X-ray radiation

X-ray emission ($100 - 10^4$ eV; $1.24 \times 10^{-4} - 0.0124$ μm ; $0.124 - 12.4$ nm) is a well observed property of T Tauri stars. X-ray surveys of star forming regions such as COUP (Chandra Orion Ultradeep Project, Getman et al. 2005) and XEST (XMM-Newton Extended Survey of the Taurus Molecular Cloud, Güdel et al. 2007a) indicate that most, if not all, T Tauri stars show strong X-ray emission. The observed luminosities are in the range of $L_X \approx 10^{29} - 10^{31}$ erg s^{-1} with typical values of $L_X/L_* \approx 10^{-4} - 10^{-3}$ (e.g. Preibisch et al. 2005; Güdel et al. 2007a). Typical T Tauri X-ray luminosities are about a factor of $10^2 - 10^4$ higher than the X-ray luminosity of the contemporary Sun (Feigelson et al. 2002). T Tauri stars show also variable activity in X-rays which can be mainly attributed to flares. Single strong flares have median peak luminosities of $L_X \approx 10^{31}$ erg s^{-1} (but flares with $L_X \gtrsim 10^{32}$ erg s^{-1} are also reported) and can last for a couple of hours to several days with a frequency of about once per week (Wolk et al. 2005).

The spectral shape of the X-ray emission can be roughly separated into a soft and hard component. The soft component refers to X-ray photon energies of $E_X \approx 0.1 - 1$ keV whereas the hard component is attribute to energies $E_X \approx 1$ keV $- 10$ keV. To account for the soft and hard part, X-ray spectra are usually fitted with two component fits comprising two plasmas with different temperatures (see e.g. Güdel et al. 2007a). In Fig. 1.3 we show the unabsorbed X-ray spectrum of the T Tauri star DM Tau. The spectrum was produced by fitting the observations with XSPEC (Arnaud 1996) assuming two plasma components with temperatures of $T_{X,1} \approx 3.5 \times 10^6$ K for the soft component, and $T_{X,1} \approx 4.6 \times 10^7$ K for the hard component of the spectrum (Liebhart priv. comm., see also Voitke et al. 2016). For comparison also an isothermal bremsstrahlung spectrum with $T_X \approx 2 \times 10^7$ K is shown. Such a spectrum is commonly used for generic disk

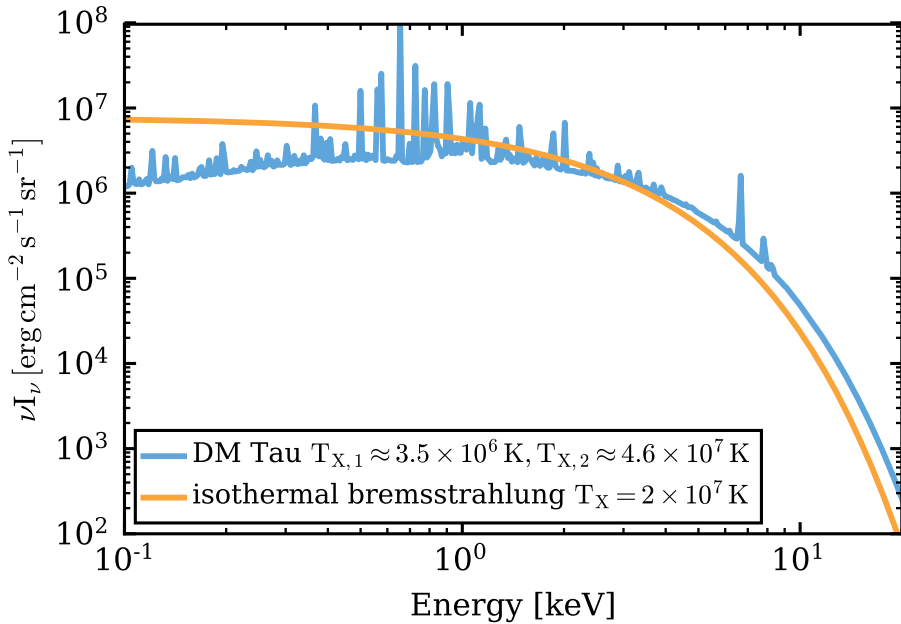


Figure 1.3 – Unabsorbed X-ray spectrum of the T Tauri star DM Tau. For comparison also a isothermal bremsstrahlung spectrum is shown (orange solid line). Both spectra are scaled to the same luminosity.

models (e.g. [Glassgold et al. 1997](#); [Aresu et al. 2011](#)) and, as can be seen from Fig. 1.3, is a reasonably accurate representation of real X-ray spectra.

The strong X-ray emission of T Tauri stars is most likely a consequence of the enhanced stellar and magnetic activity of young stars. Violent magnetic reconnection events are the cause of high coronal plasma temperatures ($T_X \approx 10^7 - 10^8$ K) and the rapid variability of the X-ray emission. However, also other processes can contribute to X-ray emission. Classical T Tauri stars show an excess in the soft X-ray emission compared to main-sequence or non-accreting stars ([Güdel and Telleschi 2007](#)). The exact origin of this soft excess is still unclear but is most likely connected to the accretion process. Material falling onto the stellar surface can cool the hot coronal gas but might also be responsible for additional absorption of X-rays very close to the star ([Güdel and Telleschi 2007](#); [Flaccomio et al. 2012](#)). In the x -wind model of [Shu et al. \(1997\)](#), X-rays are produced at the interaction point of the accreting material with the magnetosphere of the star, as a consequence X-rays would be emitted in rings located above and below the star at a distance of about $10 R_*$ ([Igea and Glassgold 1999](#)). However, recent observational studies indicate compact coronal structures (i.e. close to the stellar surface) as the main X-ray origin of T Tauri stars ([Flaccomio et al. 2005](#); [Gregory et al. 2006](#); [Ercolano et al. 2009](#)). Another alternative X-ray source might be jets. [Güdel et al. \(2005\)](#) found weak and soft X-ray emission displaced from the stellar center along the jet axis in DG Tau, indicating a shock origin of X-rays ([Güdel et al. 2007b](#)).

Stellar X-ray emission is most relevant for the evolution of the disk and its chemical structure (see e.g. [Güdel 2015](#)). Soft X-rays efficiently heat the gas to temperatures up to $\approx 5000 - 1000$ K and might be the main driver of photo-evaporative disk winds (see recent reviews of [Gorti et al. 2016](#) and [Ercolano and Pascucci 2017](#)). The hard X-ray photons can penetrate deeper into the disk and are therefore important for the ionization structure of the disk (i.e. ionization of molecular hydrogen). In this thesis we focus on

the ionization aspect of X-rays and their importance in the context of other high-energy ionization sources such as cosmic-rays and stellar energetic particles (see Chapters 2 and 3).

1.3.4 Stellar energetic particles

It is expected that T Tauri stars also show enhanced stellar energetic particle (SP) production. Those stellar particles, also often called “stellar cosmic rays”, have energies in the range of approximately 100 keV to 10 GeV. The production mechanism of those energetic particles is not well understood, even for the Sun, but they are most likely accelerated in flares and/or coronal mass ejections (Reames 2015). In contrast to X-rays, SPs cannot be directly observed in young stars but only for the Sun. However, it is possible to roughly estimate their flux by scaling the solar particle fluxes according to the enhanced X-ray luminosities of T Tauri stars. Feigelson et al. (2002) estimated that SP fluxes of T Tauri stars are about a factor of 10^5 higher than the particle flux of the contemporary Sun. However, it remains unclear if SP fluxes really scale with the X-ray luminosity.

The main interaction of SPs with the disk is twofold. Due to their high energies they efficiently ionize molecular hydrogen (just like cosmic rays) but they also interact with the solid component of the disk via spallation reactions. Measured anomalies in the decay products of short-lived radionuclides (SLR) such as ^{10}Be or ^{26}Al in meteoritic samples of the solar system (see e.g. Gounelle et al. 2013) indicate an over-abundance of SLR in the solar nebula (the circumstellar material surrounding the young Sun). One explanation for this is the irradiation of the solar nebula by energetic particles. However, much higher particle fluxes than observed in the contemporary Sun are required. The required fluxes are consistent with what is expected from scaling the SP flux with the X-ray luminosities of T Tauri stars. However, alternative causes of the observed anomalies, such as Galactic cosmic rays (Desch et al. 2004), are also possible (e.g. Feigelson et al. 2002; Gounelle et al. 2013).

Recently, Ceccarelli et al. (2014) claimed a first indirect detection of SPs in the young protostar OMC-2 FIR 4. Using *Herschel Space Observatory* observations of molecular ions they derived a H_2 ionization rate of $\gtrsim 10^{-14} \text{ s}^{-1}$ throughout the protostellar envelope, which is three orders of magnitude higher than what would be expected from typical galactic cosmic ray fluxes. Ceccarelli et al. (2014) argue that such a high ionization rate can neither be produced by Galactic cosmic-rays nor X-rays and interpreted their findings as a strong indication for high SP fluxes in young (proto)stars.

The impact of SP ionization on the chemistry of protoplanetary disks is still unexplored. In Chapter 3 we investigate the impact of SP ionization on disk chemistry and discuss possible ways to infer SP fluxes of T Tauri stars from molecular ion observations. The presented radiation thermo-chemical disk model includes detailed SP transport, X-ray radiative transfer and cosmic-ray ionization. With such a model it is possible to study the individual contributions of the high-energy ionization sources to disk ionization and to infer possible observational signatures.

1.3.5 Environment

Most stars are not born in isolation but rather form in groups or clusters. This scenario is also likely for our Sun. Such a cluster environment had likely a significant impact on the evolution of the early solar system (see the review of [Adams 2010](#)) and of course also on disks around T Tauri stars.

One rather extreme example for external irradiation of disks are nearby massive O-type stars that irradiate nearby disks with strong UV radiation, several orders of magnitude higher than the typical interstellar UV radiation field (e.g. [Walsh et al. 2013](#)). However, even a small enhancement of the interstellar radiation field might already contribute to the external photo-evaporation of disks (e.g. [Williams and Cieza 2011](#); [Haworth et al. 2017](#)) and does not necessarily require the presence of a nearby O star. Besides UV radiation, T Tauri disks are also irradiated by Galactic cosmic-rays. However, galactic cosmic-rays might not reach the disk due to shielding by the so-called T Tauriosphere (the analogue of the heliosphere, [Cleeves et al. 2013, 2015](#)); on the other hand, cosmic-ray fluxes could be enhanced by a nearby supernova.

As already mentioned, T Tauri stars show strong X-ray emission and therefore might also have an impact on the disks of other cluster members. [Adams et al. \(2012\)](#) estimated the strength of such a cluster X-ray background field and found that it can dominate the X-ray radiation field in the outer regions of disks. In [Chapter 2](#) we investigate the impact of cluster X-ray background fields on the disk chemistry and discuss possible observational implications.

1.4 Protoplanetary disks

The term protoplanetary disk is used for disks surrounding young stars that are currently in the Class II phase of the star formation process (see [Sect. 1.1](#)). Disks are the birth-places of planets and define the physical conditions of planet formation and the initial composition of planets and their atmospheres. An understanding of their physical (e.g. disk mass) and chemical properties (e.g. chemical abundances) is therefore crucial to understand planet formation and the formation of our solar system.

As already mentioned in [Sect. 1.1](#) rotationally supported disks form already early on in the star formation process (Class 0 phase). Such disks are called protostellar disks. The main difference to protoplanetary disks is that protostellar disks are still deeply embedded in an envelope, from which they still accrete material. In this work we mainly focus on protoplanetary disks ([Chapters 2 and 3](#)) but also present a new disk+envelope model representative of a late Class I object ([Chapter 4](#)), assuming properties of the embedded disk similar to protoplanetary disks. Therefore we focus here on the description of protoplanetary disks.

In this section, we do not describe the evolution of the disk but apply the steady-state picture of disks. Although disks are dynamical structures, such a simplified picture is applicable, as the main physical properties of protoplanetary disks do not significantly change over timescales of million years. Protoplanetary disks are accretion disks, however, their thermal structure is mainly determined by the stellar irradiation and accretion

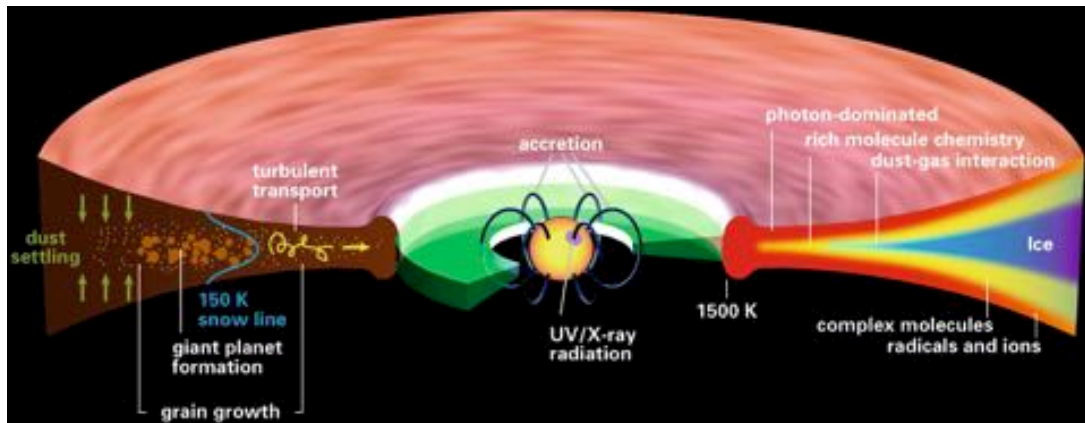


Figure 1.4 – Schematic view of a protoplanetary disk. In the left part of the figure, important physical processes are indicated, where the right part shows the chemical structure of the disk. The inner gas disk (in green) and the accretion funnels onto the star are also indicated. Adapted with permission from [Henning and Semenov \(2013\)](#), ©(2013) American Chemical Society.

heating is likely only relevant in the densest regions closest to the star. Although this is a simplified picture of protoplanetary disks, this kind of disk model is successful in explaining many observational properties of protoplanetary disks (e.g. [Kenyon and Hartmann 1987](#); [Chiang and Goldreich 1997](#); [D’Alessio et al. 1998](#); [Dullemond et al. 2007](#); [Woitke et al. 2016](#)). Furthermore, the approach of a fixed steady-state disk structure allows for putting the focus on disk microphysics such as detailed radiative transfer and chemistry.

In [Fig. 1.4](#) a schematic view of a protoplanetary disk is shown. This figure indicates several important physical processes, such as dust settling, and the global chemical structure of protoplanetary disks. In the following two sections we provide a brief overview of the main physical and chemical properties of disks. Further relevant details are discussed in the main chapters of this thesis.

1.4.1 Physical structure

Protoplanetary disks around low mass stars have masses of about $\lesssim 1\%$ of the mass of the stellar host (with a scatter of nearly an order of magnitude, [Andrews et al. 2013](#); [Ansdell et al. 2016](#)). Disks consist of gas and dust with a total gas to dust mass ratio of about 100.

Estimating disk masses from observations, in particular the gas mass, is challenging. The main reason is that the most abundant molecule H_2 is difficult to observe and one has to rely on tracer species such as carbon monoxide (CO) or hydrogen deuteride (HD). Such tracer species are affected by chemistry and the details of the physical disk structure, as a consequence disk gas mass estimates are still quite species and model dependent ([Kamp et al. 2011](#); [Williams and Best 2014](#); [Miotello et al. 2014, 2017](#); [Trapman et al. 2017](#); [Yu et al. 2017](#)). Although HD is a very promising gas mass tracer ([Bergin et al. 2013](#); [McClure et al. 2016](#)) it was so far only detected with the Herschel space telescope and only a handful of detections exist. However, current (sub)mm facilities (i.e. for CO) like ALMA (Atacama Large Millimetre Array), SMA (Submillimeter Array) and NOEMA (NOthern Extended Millimeter Array) and possible future far-infrared space

observatories (i.e. for HD) such as SPICA (Space Infrared Telescope for Cosmology and Astrophysics) will significantly improve this situation, and will provide more stringent constraints on disk dust and gas masses.

Typical radial disk extensions are of the order of a few hundreds of au (e.g. [Guilloteau et al. 2011](#)). However, the measured extent of disks depends on the observational tracer. Spatially resolved CO line measurements show disks sizes in the range of 100 – 1000 au (e.g. [Öberg et al. 2011](#); [Cleeves et al. 2016](#)), whereas the disk of mm-sized grains seems to be smaller (e.g. [de Gregorio-Monsalvo et al. 2013](#)). This difference might be caused by radial migration of dust grains (e.g. [Cleeves 2016](#)), but can to some extent also be explained by optical depths effects ([Woitke et al. 2016](#); [Facchini et al. 2017](#)).

The inner dust disk radius (inner rim) can be measured with near-infrared interferometers like the VLTI (Very Large Telescope Interferometer) and is roughly determined by the dust sublimation temperature (≈ 1500 K) and therefore depends on the stellar luminosity. Typical inner disk radii are in the range of 0.01 – 0.2 au for T Tauri disks ([Dullemond and Monnier 2010](#); [Anthonioz et al. 2015](#)). The inner radius of the inner gas disk (see Fig. 1.4) is closer to the star than the dust inner radius and is truncated by the stellar magnetic field. However, little is known about the inner gas disk and direct measurements are difficult ([Dullemond and Monnier 2010](#)).

With modern telescopes, it is now also possible to directly measure the vertical extent of disks. The mm-sized dust grain disk is nearly geometrically thin with vertical scale heights of about 1 au at a disk radius of $r = 100$ au ([Pinte et al. 2016](#)); this is a strong indication for efficient dust growth and settling. However, the small sub-micron sized dust grains and the gas are in vertical hydrostatic equilibrium and are therefore more extended, with typical scale-heights of about 10 au at $r = 100$ au. Many disks also show flared structures caused by direct stellar irradiation ([Dullemond et al. 2002](#)). Directly measuring the vertical extent of the (CO) gas becomes now also possible with ALMA, and first results seem to be consistent with disk structure models ([Dutrey et al. 2017](#); [Pinte et al. 2017](#)).

Recent observations show that protoplanetary disk structures can be quite complex. In some disks (especially in transitional disks) clear azimuthal asymmetries (e.g. horseshoes) were detected both in gas and dust (e.g. [van der Marel et al. 2013](#); [de Gregorio-Monsalvo et al. 2013](#); [van der Plas et al. 2014](#)). The origin of these asymmetries are likely vortices, possibly induced by planets and/or disk instabilities. Trapping of mm-sized dust particles in those vortices is the origin of the observed horseshoe like asymmetries. Such processes might play a significant role for planet formation (e.g. [Zhu et al. 2014](#); [Zhu and Stone 2014](#); [Owen and Kollmeier 2017](#)).

A further remarkable feature revealed by high spatial resolution observations (ALMA, VLT-SPHERE) are azimuthally symmetric rings and gaps in the radial intensity profiles of dust and gas emission ([ALMA Partnership et al. 2015](#); [Andrews et al. 2016](#); [Nomura et al. 2016](#); [Yen et al. 2016](#); [Teague et al. 2017](#); [van Boekel et al. 2017](#)). So far only two objects, namely HL Tau and TW Hya, were targeted with ALMA's highest spatial resolution ($\approx 0.01''$), and several gaps and rings were detected in both objects, indicating that such structures might be a common feature of protoplanetary disks. The measured width of these gaps are about 10 au and the surface density inside the gaps is lower than it the gap vicinity by approximately a factor of ten, for the mm-sized dust and a factor of

a few, for the gas (e.g. [Yen et al. 2016](#)). Those gaps are an intriguing indication for planet formation; however, their real origin remains unclear (see e.g. [Andrews et al. 2016](#) for a discussion). The models presented in this work do not include such gaps. However, their presence does not have a significant impact on our results as they are rather narrow and the overall radial density distribution remains intact (see e.g. [Pinte et al. 2016](#); [Teague et al. 2017](#)).

1.4.2 Chemical structure

Disk chemistry is quite diverse and many different chemical processes are important to study disk chemistry and to interpret observations. This diversity is a natural consequence of the physical disk structure with number densities in the range of $10^4 - 10^{16} \text{ cm}^{-3}$, temperatures in the range of ten to several thousand Kelvin and the accompanied steep gradients. It is therefore common and useful to divide the disk into distinct regions to discuss the main chemical processes. Here we follow [Henning and Semenov \(2013\)](#) and [Rab et al. \(2016\)](#) and separate the chemical structure of the disk in three radial zones and three vertical layers. In the following, we also provide typical numbers for the extent of these zones and their temperatures. Those numbers should only be seen as a rough guide as they depend on stellar properties (e.g. luminosity), disk properties (e.g. disk mass) and the considered molecule itself.

The radial chemical structure of the disk midplane can be separated into three different zones:

- *inner zone*: extends up to a distance of a few au from the star. Typical temperatures are $T > 100 \text{ K}$. This region is mostly shielded from radiation due to high optical depths. Important molecules like water and CO are in the gas phase. The chemistry can reach an equilibrium due to the high temperatures and densities ($\gtrsim 10^{12} \text{ cm}^{-3}$).
- *middle zone*: extends from a few au up to about 100 au. Temperatures are in the range of $100 \gtrsim T \gtrsim 20 \text{ K}$. Depending on their binding energy molecules start to freeze-out (e.g. water). This region is still well shielded from stellar and interstellar UV radiation and the main chemical drivers are cosmic rays, radionuclide ionization and potentially very hard X-rays.
- *outer zone*: temperatures drop below $T \lesssim 20 \text{ K}$. Most chemical species are frozen out on dust grains. Due to the low densities, this region is only partly shielded from radiation and non-thermal desorption processes can release molecules back into the gas phase (most efficient close to the outer radius of the disk).

In vertical direction it is common to define three distinct layers:

- *midplane*: see above for the three radial zones; for most of the disk midplane the chemistry is dominated by gas grain interaction (freeze-out of molecules, dust surface chemistry).
- *rich molecular layer*: this region is warm enough ($20 \lesssim T \lesssim 100 \text{ K}$) to keep important molecules, such as CO, in the gas phase. This layer is located deep enough in the disk so that photo-dissociation of molecules becomes inefficient. These conditions allow for rich molecular chemistry including molecular ion chemistry.

- *photon-dominated layer*: temperatures can be as high as $100 \gtrsim T \lesssim 5000$ K with the highest temperatures close to the star. The chemistry is mainly driven by stellar X-ray and UV radiation (ionization, photo-dissociation). Most species are in atomic form and often ionized. In this disk layer, chemical conditions are very similar to PDRs (photo-dissociation regions).

Those three vertical layers are also indicated in Fig. 1.4. The above-described chemical structure is also clearly visible in the two-dimensional CO abundance distribution shown in Fig. 1.6, for a representative T Tauri disk model.

For this work, the most relevant region is the rich molecular layer. This layer is also of particular interest as it can be well observed with modern (sub)mm telescopes (see Dutrey et al. 2014 for a review). The upper border of this layer is well defined by the transition of the atomic to the molecular layer where photo-dissociation becomes inefficient. The location of the upper border depends significantly on the dust properties as dust is the most important UV opacity source, but also on the self-shielding properties of the particular molecules (see e.g. Sect. 3.8 for N_2). The lower vertical border of the rich molecular layer is defined by the freeze-out of molecules and depends mainly on the dust temperature structure and the binding energy of the individual molecules (i.e. at which temperature a particular molecule freezes out).

In Chapters 2 and 3 we use the molecular ions HCO^+ and N_2H^+ to study the impact of X-ray radiation (stellar and background) and stellar energetic particles on the disk ion chemistry. In particular, we use those molecules to investigate possible observational signatures of X-ray background fields and stellar particles, as these two high-energy sources cannot be directly observed. In Chapters 2 and 3 we also discuss the chemistry of HCO^+ and N_2H^+ in more detail.

In Chapter 4 we use the chemical process of adsorption (freeze-out) of molecules onto dust grains and the desorption (sublimation) of molecules from the dust grains to study the impact of episodic accretion events (see Sect. 1.2) on the chemistry in the disk and envelope surrounding the star. A strong luminosity burst heats up the circumstellar environment and many molecules can sublime. After the burst, the material cools quickly and the molecules can freeze out again. Compared to cooling, the freeze out of molecules is a rather slow process and we investigate to what extent it is possible to trace an already past episodic accretion event using chemistry. In Chapter 4 we also provide more details on adsorption/desorption chemistry.

1.5 Radiation thermo-chemical disk model PRODIMO

For all models presented in this thesis we used and further developed the disk modelling code PRODIMO (PROtoplanetary DIsk MODEL, Woitke et al. 2009; Kamp et al. 2010; Thi et al. 2011; Woitke et al. 2016). PRODIMO is a so-called radiation thermo-chemical disk modelling code. It solves for the wavelength dependent disk radiation field, the gas and dust thermal balance and the chemical abundances. PRODIMO also includes a module to produce observables like SEDs (spectral energy distributions), visibilities, spectral lines and images. The main physical assumption of a PRODIMO model is the fixed steady-state disk structure; that means that any dynamical evolution of the disk structure is

neglected. Furthermore, it is assumed that the structure is azimuthally symmetric and the physical quantities considered can only vary as a function of radius r (distance from the star in the center) and height z of the disk (the disk midplane is a $z = 0$). The disk is exposed to stellar and interstellar radiation. This radiation mainly determines the disk gas and dust temperature structure. The gas temperature is solved consistently with the chemistry, including various heating and cooling processes; this allows for decoupled gas and dust temperatures.

In the following sections, we describe the physical processes considered in `PRODiMo` and briefly discuss the corresponding equations. The main code structure of `PRODiMo` and its main modules are shown in Fig. 1.5. We use a representative T Tauri disk model to illustrate the typical modelling results produced by `PRODiMo` (Fig. 1.6). This T Tauri disk model is the same as the models used in Chapters 2 and 3, where also all physical parameters of the model are listed. However, for what is discussed in the following sections the detailed properties of the disk structure and star are not important. Further explanations for Figs. 1.5 and 1.6 are provided throughout the following text. The aim of this section is to provide the reader with a general picture of `PRODiMo`, but we also provide relevant references for further details. The `PRODiMo` code developments done for this thesis are described in detail in the corresponding chapters.

1.5.1 Gas and dust density structure

The first main ingredient to model a disk is the density structure. `PRODiMo` includes different methods to construct a realistic disk density structure. It is possible to use a fully parameterized fixed disk structure or to let `PRODiMo` solve for the detailed vertical hydrostatic disk structure. In the latter case, the vertical disk structure is solved consistently with the gas or dust temperature structure of the disk applying an iterative scheme.

For the fully parameterized method, the main parameters required are the disk mass, the disk extensions, a reference scale height and a radial surface density profile. The density structure as a function of the cylindrical coordinates r (distance to the star) and z (height of the disk) is given by

$$\rho(r, z) = \frac{\Sigma(r)}{\sqrt{2\pi} \cdot h(r)} \exp\left(-\frac{z^2}{2h(r)^2}\right) \quad [\text{g cm}^{-3}], \quad (1.2)$$

where ρ is the gas density, $\Sigma(r)$ the radial surface density profile, and $h(r)$ the scale height of the disk at each radial point. For $\Sigma(r)$ either an input file providing the radial surface density profile or a parameterized equation of the form

$$\Sigma(r) = \Sigma_0 \left(\frac{r}{R_{\text{in}}}\right)^{-\epsilon} \exp\left(-\left(\frac{r}{R_{\text{tap}}}\right)^{2-\epsilon}\right) \quad [\text{g cm}^{-2}]. \quad (1.3)$$

can be used. With Eq. (1.3) the radial density profile is approximated by a power-law for $r < R_{\text{tap}}$ and an exponential profile, starting at the transition radius R_{tap} , for the outer disk (tapered outer edge). Such a radial surface density profile is a consequence of the viscous evolution of a vertically thin Keplerian disk (similarity solution; Lynden-Bell and

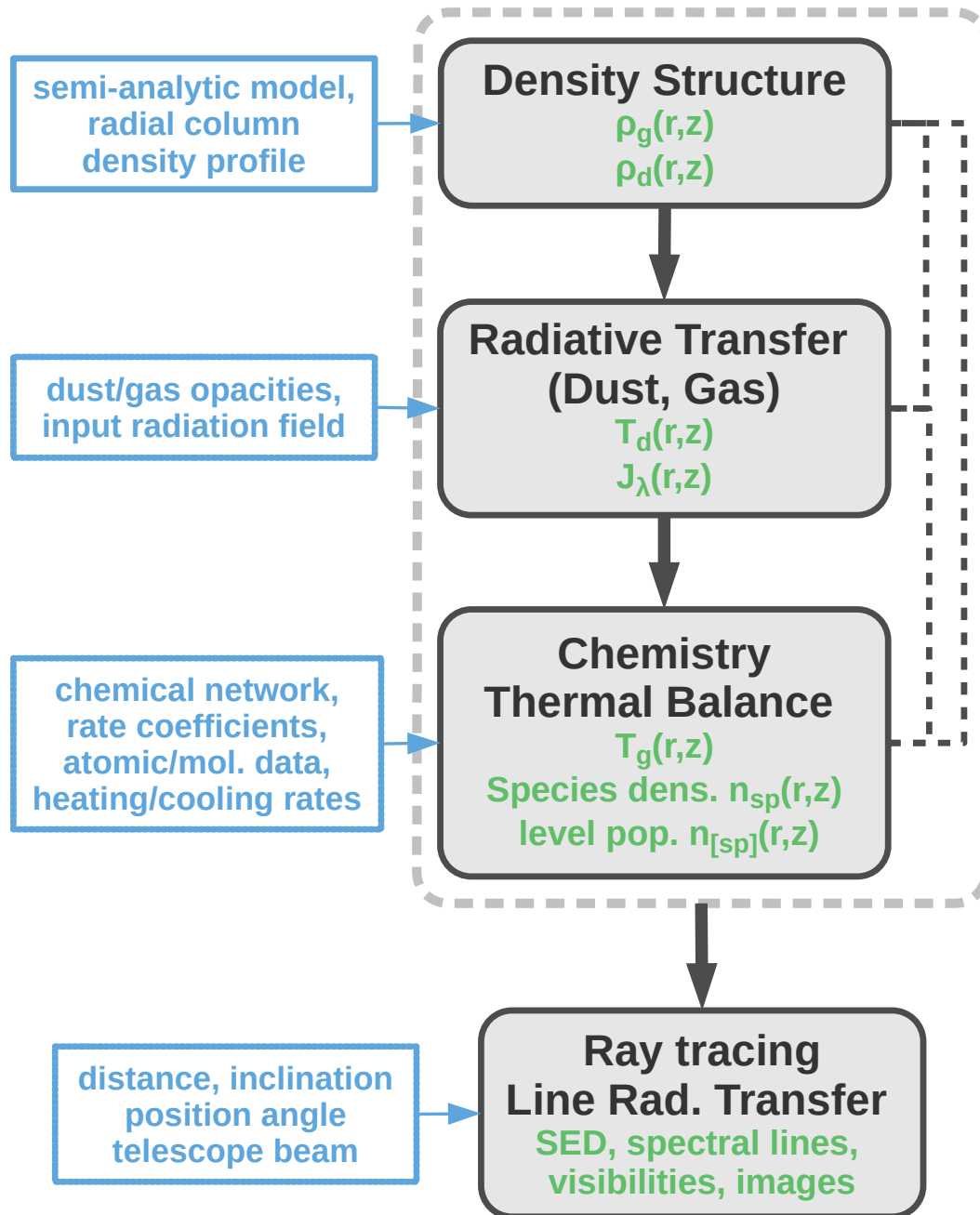


Figure 1.5 – General code structure of PRODIMO. The grey boxes indicate the main modules of PRODIMO. The main quantities calculated by each module are given in green. In the blue boxes the most important input data for each module is listed. The grey dashed box encloses the main physical modules; the black dashed lines indicate possible iterations between the individual modules. The ray tracing module for the calculation of synthetic observables is an integral but optional part of PRODIMO and is therefore depicted separately.

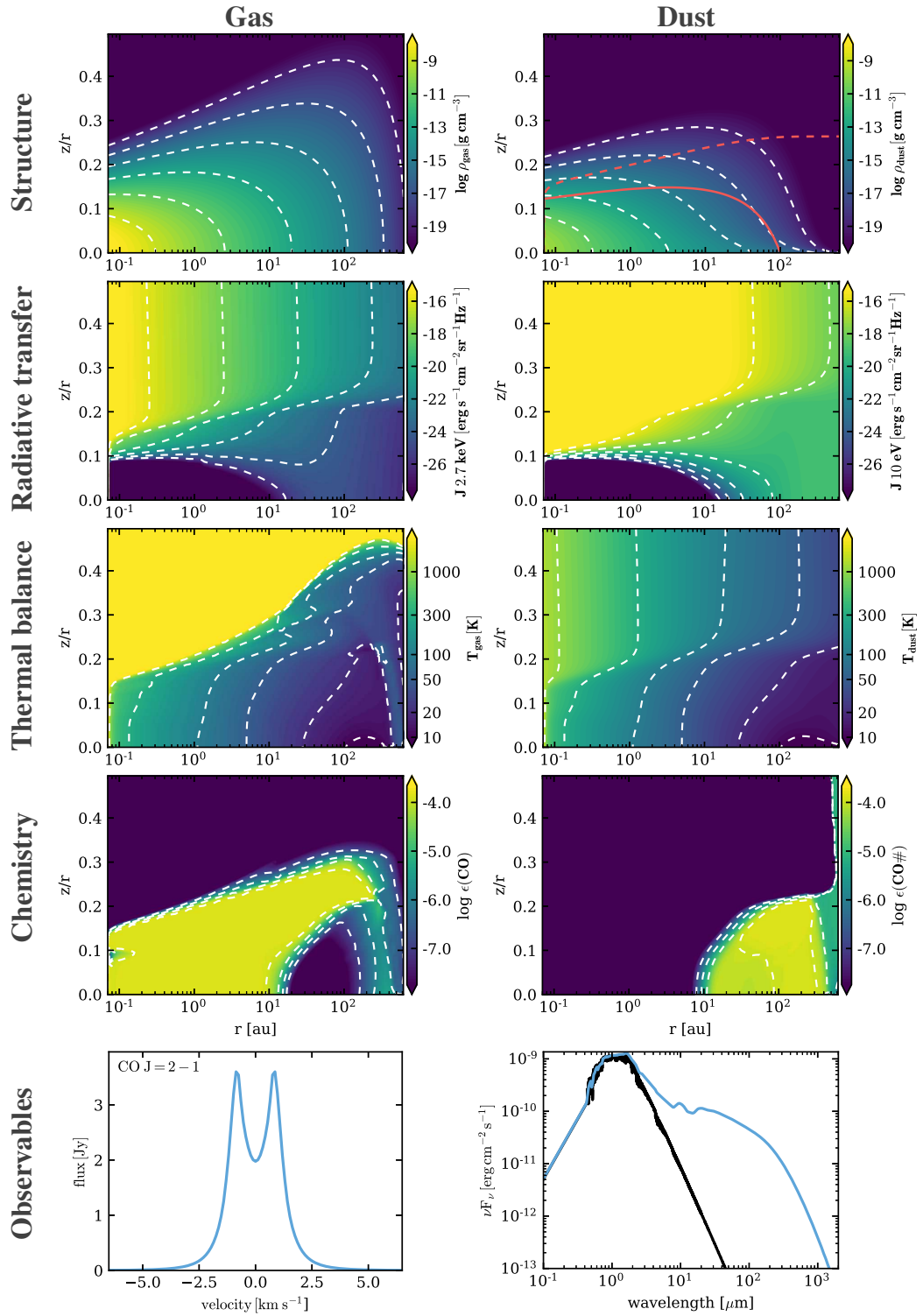


Figure 1.6 – Typical output of a PRODIMO for a T Tauri disk model. The left and right column shows quantities related to gas and dust, respectively. The individual rows show the output related to each main module of PRODIMO. The contour plots show (from top to bottom) the gas and dust structure, the radiation field (mean intensity J) at 2.7 keV (X-rays) and 10 eV (far-UV), the gas and dust temperature and the chemical abundances for CO gas ($\epsilon(\text{CO})$) and ice ($\epsilon(\text{CO}\#)$). The dashed white contours in each contour plot correspond to the levels shown in each colour bar. The red solid (dashed) contour line in the top right plot show where the vertical (radial) visual extinction is unity. In the bottom row, a spectral line profile for the CO $J=2-1$ line and the spectral energy distribution (the black solid line is the stellar spectrum) are shown.

Pringle 1974; Hartmann et al. 1998) assuming that the disk viscosity can be described by a radial power-law. The scaling factor Σ_0 in Eq. (1.3) can be determined via the given disk mass using

$$M_{\text{disk}} = 2\pi \int_{R_{\text{in}}}^{R_{\text{out}}} \Sigma(r)rdr \text{ [g]}. \quad (1.4)$$

In the fully parameterized approach a simple power-law for the vertical disk scale height of the form

$$h(r) = H(100 \text{ au}) \left(\frac{r}{100 \text{ au}} \right)^\beta \text{ [au]}, \quad (1.5)$$

is applied. $H(100 \text{ au})$ is the reference scale height of the disk at $r = 100 \text{ au}$. The flaring power-index β accounts for a possible flaring of the outer disk (i.e. $\beta > 1$).

The fully parameterized approach described above does not directly depend on the stellar properties nor the physical conditions in the disk such as the temperature. However, such an approach has its advantages in particular for fitting and the interpretation of observations.

A more physical approach is to actually solve for the vertical hydrostatic disk structure given by

$$\frac{1}{\rho} \frac{dp}{dz} = \frac{zGM_\star}{(r^2 + z^2)^{3/2}}, \quad (1.6)$$

where p is the gas pressure and M_\star is the stellar mass. Here, the self-gravity of the disk is neglected and it is assumed that the radial and vertical components of the equation of motions decouple (i.e. the radial pressure gradient is small compared to the vertical one, see eg. D'Alessio et al. 1998; Woitke et al. 2009). This equation can then be solved at each radial point of the disk (1+1D approach, e.g. D'Alessio et al. 1998) if the temperature structure of the disk is known. As the disk temperature structure is mainly determined by stellar irradiation an iterative approach is required to consistently solve for the vertical disk and temperature structure (see Woitke et al. 2009 for details).

The structure of the dust disk is in principle given by the gas density structure, where the dust density is simply given by the gas to dust mass ratio (free parameter). However, due to dust evolution processes such as grain growth, settling and radial migration the gas and dust density structure can decouple (see e.g. Birnstiel et al. 2016 for a review). This is in particular true for large grains with a grain radius $a \gtrsim 1 \mu\text{m}$. To account for dust growth, PRODIMO uses a dust size distribution instead of a single grain size (see also Sect. 1.5.2). To account for vertical settling of the dust particles the method of Dubrulle et al. (1995) is used. In this approach, the scale height of the dust for a particular size is given by the equilibrium of turbulent mixing and gravitation. Therefore the scale height of the dust depends on the gas density and the sizes of the dust grains (assuming they all have the same composition). It is assumed that settling happens early on in the disk evolution and reaches a steady-state. For more details on the treatment of dust in PRODIMO see Woitke et al. (2016). The resulting gas and dust density structure for a fully parameterized structure model, including dust settling, is shown in the top row of Fig. 1.6.

The radial column density profile of the disk does not necessarily have to be continuous for the whole radial extent of the disk. It is also possible to use different radial zones with different parameters for the radial and vertical profile but also for parameters such as the dust to gas mass ratio. In this way it is possible to also simulate gaps in disks or transitional disks where the inner disk is gas/dust depleted.

For this thesis also a parameterized prescription for a Class I structure was implemented in PRODiMo. This allows for modelling of embedded sources where the disk component is still surrounded by an envelope. The new disk plus envelope mode of PRODiMo is described in detail in Chapter 4.

1.5.2 Radiative transfer

The stellar and interstellar radiation field heats the disk gas (e.g. photo-electric effect) and dust (absorption) and therefore has a significant impact on the temperature structure of the disk. For the chemistry, the radiation field at each point of the disk needs to be known, as it drives important chemical processes such as photo-ionization, photo-dissociation and photo-desorption.

The radiative transfer module of PRODiMo solves the radiative transfer equation including scattering and thermal emission. The change in the intensity of radiation due to interaction with matter along a straight path is given by

$$\frac{1}{\rho(\vec{r})} \frac{\partial I_\nu(\vec{r}, \hat{k})}{\partial s} = -\kappa_\nu^{\text{ext}} I_\nu(\vec{r}, \hat{k}) + \kappa_\nu^{\text{abs}} B_\nu(T(\vec{r})) + \kappa_\nu^{\text{sca}} J_\nu(\vec{r}). \quad (1.7)$$

$I_\nu(\vec{r}, \hat{k})$ is the specific intensity at position \vec{r} into a solid angle $d\Omega$ towards the direction \hat{k} at frequency ν . κ^{ext} is the extinction coefficient in units of $[\text{cm}^2 \text{g}^{-1}]$ and is given by the sum of the absorption (κ_ν^{abs}) and scattering (κ_ν^{sca}) coefficients. $B_\nu(T(\vec{r}))$ is the value of the Planck function at temperature T and describes the thermal emission of dust at a point \vec{r} . The mean intensity $J_\nu(\vec{r})$ is given by

$$J_\nu = \frac{1}{4\pi} \oint_{4\pi} I_\nu(\hat{k}') d\Omega' \quad (1.8)$$

and accounts for the radiation scattered into the beam of light under consideration. $\partial/\partial s$ is the derivative along the light propagation path, assuming that light travels along straight lines. To solve Eq. (1.7) a ray-based iterative method (discrete ordinates) combined with a Λ -iteration scheme (to solve the scattering problem) is applied (see [Woitke et al. 2009](#) for details).

The star is the main irradiation source of the disk. The emission of the star is simulated by using PHOENIX stellar atmosphere models ([Brott and Hauschildt 2005](#)) for a given stellar radius, effective temperature and luminosity. Additionally to the stellar atmosphere spectrum, UV excess emission accounting for the accretion luminosity of young stars and coronal X-ray emission can also be included. The input spectrum for the radiative transfer can be either determined in a fully parameterized way (e.g. stellar properties, far-UV and X-ray luminosity) or by directly providing an input stellar spectrum (see [Woitke et al. 2016](#) for examples). Isotropic irradiation by interstellar background fields

is taken into account, where X-ray (Adams et al. 2012; see also Chapter 2), UV (Draine and Bertoldi 1996) and infrared background (Mathis et al. 1983) fields can be considered for the radiative transfer.

PRODiMO solves the radiative transfer equation (Eq. 1.7) for typically 20 – 40 (given by a parameter) frequency/wavelength bands from the far-UV (0.1 μm) to the mm-range. For those bands, all quantities (e.g. stellar intensity) are averaged over the bandwidth. As the radiation field is also used as input for the chemistry there are dedicated bands which cover particular wavelength ranges most relevant for chemistry (i.e. far-UV 0.091 – 0.111 μm and 0.111 – 0.2050 μm). The band averaged method allows for an efficient but still accurate solution of the radiative transfer problem (see Woitke et al. 2009 for details).

For this thesis, the radiative transfer module of PRODiMO was extended towards the X-ray regime to calculate accurately the X-ray radiation field in the disk. The details of this new X-ray radiative transfer module and an application to X-ray background fields are presented in Chapter 2.

As can be seen from Eq. (1.7) the local radiation field depends on the thermal emission of matter, which itself depends on the temperature. The temperature can be estimated by assuming local radiative equilibrium (i.e. all energy absorbed is re-emitted by matter). The radiative equilibrium equation is given by

$$\int_0^\infty \kappa_\nu^{\text{abs}}(\vec{r}) B_\nu(T(\vec{r})) d\nu = \int_0^\infty \kappa_\nu^{\text{abs}}(\vec{r}) J_\nu(\vec{r}) d\nu, \quad (1.9)$$

where all quantities have the same meaning as above. Equations 1.7 and 1.9 are solved by an iterative scheme that provides both the temperature and the radiation field at each point in the disk.

We want to emphasize that PRODiMO does not assume that the dust and gas temperatures are in equilibrium. The radiative transfer module therefore provides the dust temperature and an initial temperature structure for the more detailed heating/cooling balance calculations for the gas temperature (see Sect. 1.5.3). It is also possible to add additional heating/cooling terms in Eq. (1.9) (modified radiative equilibrium Woitke et al. 2009). With this approach it is possible to model feedback from the gas temperature to the dust temperature (e.g. viscous heating).

A crucial input for dust radiative transfer are the optical properties of the dust (opacities) which are represented as κ_ν^{abs} and κ_ν^{sca} in equations 1.7 and 1.9. PRODiMO also includes an integrated module to calculate dust opacities. This module considers different dust mixtures (compositions) and different dust size distributions. Based on the given parameters PRODiMO calculates the required dust opacities to solve the radiative transfer problem. More details can be found in Woitke et al. (2016). One simplifying assumption usually made is that dust particles are perfect spheres (e.g. Mie-theory). In Min et al. (2016) we also investigated the impact of shape defects of dust particles (i.e. they are likely non-spherical) on the opacities. For this, we applied the discrete dipole approximation code ADDA (Yurkin and Hoekstra 2011) for irregularly shaped particles. Such kind of calculations are computationally expensive and can only be done for certain types of dust and dust sizes. However, to approximate the impact of shape defects, distributed hollow spheres (Min et al. 2005) can be used in PRODiMO with parameter settings guided by the

results of [Min et al. \(2016\)](#).

As already mentioned, for this thesis also X-ray radiative transfer was implemented into PRODiMo. The opacity in the X-ray regime is mostly dominated by the gas component where the photoelectric cross-section of atoms and molecules is the most relevant quantity. However, under certain circumstances, dust can also become an important X-ray opacity source. Optical properties for the dust in the X-ray regime are still rare (e.g. [Draine 2003](#)), we therefore developed a code to calculate X-ray optical constants based on the method of [Draine \(2003\)](#). With this module, it is possible to calculate X-ray optical constants for various dust compositions. Those optical constants are then used for the opacity calculations. The new tool is not part of PRODiMo but X-ray optical constants, which are the input for the opacity calculations, for various dust types are included in PRODiMo.

Besides the internal radiative transfer module, PRODiMo also provides interfaces to the Monte Carlo dust radiative transfer codes MCFOST ([Pinte et al. 2006](#)) and MCMAX ([Min et al. 2009](#)). Such Monte Carlo radiative transfer codes are better suited for the interpretation of scattered light images (e.g. [Pinte et al. 2008](#); [Mulders et al. 2013](#)) as they also consider anisotropic scattering (see [Pinte et al. 2009](#) for a discussion). Models of these Monte Carlo RT codes can directly be used as input for PRODiMo. The chemical abundances and gas thermal balance are then calculated on top of the provided density and temperature structure and the disk radiation field. Those interfaces can also be used together with the new X-ray radiative transfer module. In that case, only the radiative transfer in the X-ray wavelength regime is done in PRODiMo.

It is also possible to model the emission of polycyclic aromatic hydrocarbon molecules (PAHs) with PRODiMo; PAHs can be an important opacity source in the far-UV. This can be either done by using the internal PAH radiative transfer module of PRODiMo ([Woitke et al. 2016](#)) or by making use of the interface to the Monte Carlo radiative transfer codes. In PRODiMo the PAH temperatures are determined assuming radiative equilibrium, whereas the Monte Carlo codes use a more sophisticated method considering quantum heating of PAHs and a stochastic temperature distribution. Anyway, the method used in PRODiMo provides a simple and robust but also accurate way to model PAH radiative transfer (see [Woitke et al. 2016](#) for details and a comparison to the Monte Carlo codes).

To summarize, the radiative transfer module of PRODiMo provides the dust/PAH temperature structure, the wavelength dependent (X-ray to mm) disk radiation field (see [Fig. 1.6](#)) and the dust properties for the chemistry and thermal balance module. The radiation field is used to calculate the chemical rates for the photo-chemistry and the dust size distribution is in particular important for freeze-out chemistry (see [Chapter 4](#) for details).

1.5.3 Chemistry and thermal balance

Besides studying disk chemistry itself, including chemistry in a protoplanetary disk model is important for two reasons. Firstly, the chemical composition of protoplanetary disks provides the initial conditions for planet formation and consequently also for the composition of planets. Secondly, observations of molecules and atoms are crucial to constrain

physical disk properties such as disk mass or temperatures. Those quantities are most relevant for understanding star and planet formation. However, interpretation of such observations requires knowledge about the chemical processes happening under certain physical conditions and therefore detailed physical and chemical models. In this section, we describe the chemical model of PRODIMO and the heating/cooling module as those are strongly coupled.

The number density n_i as a function of time, for a certain species i is given by a so called rate equation

$$\begin{aligned} \frac{dn_i}{dt} = & \sum_{j \in F_j} k_j(T_g) n_l n_m + \sum_{j \in F_j^{\text{phot}}} k_j^{\text{phot}} n_l + \dots \\ & - \sum_{j \in D_j} k_j(T_g) n_i n_m - \sum_{j \in D_j^{\text{phot}}} k_j^{\text{phot}} n_i - \dots \end{aligned} \quad (1.10)$$

The first row of Eq. (1.10) corresponds to the sum of all formation reactions F_j producing species i ; the second row to all destruction reactions D_j destroying species i . k_j are the corresponding rate coefficients which are given by the chemical network describing all chemical reactions considered for a particular model. In Eq. (1.10) only two kinds of reactions are shown, namely two-body gas phase reactions and photo reactions (e.g. photo-ionization). The dots indicate that there are typically also other kinds of reactions (e.g. X-ray chemistry, freeze-out).

As indicated in Eq. (1.10) the rate coefficients k can depend on the gas temperature. The gas temperature would be only known if one assumes that the dust and gas temperature are coupled. However, this assumption does not hold everywhere in the disk. Therefore PRODIMO also solves for the thermal gas balance considering various gas heating and cooling processes. The thermal balance can be written as

$$0 = \sum_k \Gamma_k(T_g, n_{\text{sp}}) - \sum_k \Lambda_k(T_g, n_{\text{sp}}), \quad (1.11)$$

where Γ_k and Λ_k are the various heating and cooling rates in units of $\text{erg s}^{-1} \text{cm}^{-3}$, T_g is the gas temperature and n_{sp} is the species number density. With Eq. (1.11) the gas temperature at every point in the disk can be determined. However, as the chemical rates depend on the gas temperature (see Eq. 1.10) and T_g depends on the species densities an iterative scheme is required to solve consistently for the species densities (or chemical abundances) and the gas temperature (see [Woitke et al. 2009](#) for details).

With equations 1.10 and 1.11 the gas temperature and species abundances at every point in the disk can be determined. PRODIMO can solve Eq. (1.10) time-dependently or assuming that the abundances reach a steady-state (i.e. setting $\frac{dn_i}{dt}$ to zero). The latter approach has the advantage that it is computationally less expensive. However, it is not guaranteed that a chemical steady-state is reached everywhere in the disk within typical disk lifetimes. In the upper disk layers, chemical steady-state is usually reached within 10^4 yr, whereas in the disk midplane the chemical timescale can be larger than 10^7 yrs (see e.g. [Woitke et al. 2009](#); [Helling et al. 2014](#)). However, depending on the problem, the steady-state approach is very efficient as it is typically a factor of ten to 100 faster than the time-dependent approach. For this work, we used both approaches.

For our investigation of X-ray and stellar particle ionization (Chapters 2 and 3) we used the steady-state approach for most models, but verified our results by comparing with time-dependent models. For the episodic accretion chemistry (Chapter 4) we used the time-dependent approach because in that case we are actually interested in the evolution of the freeze-out chemistry with time.

Chemical network

The chemistry and heating/cooling module of PRODiMo is very flexible. One needs to provide a list of chemical species and a chemical network containing all relevant reactions. PRODiMo includes a set of chemical reactions relevant for disks and additionally uses the gas-phase chemical database UMIST (Woodall et al. 2007; McElroy et al. 2013) or alternatively KIDA (KInetic Database for Astrochemistry, Wakelam et al. 2012, 2015). Such chemical databases include a large number of gas-phase chemical reactions (typically 5 000 to 10 000 reactions) and their corresponding rate coefficients, which are either estimated theoretically or via experiments. For a given set of chemical species all reactions involving those species are automatically selected from the chemical databases and the PRODiMo specific reactions. This defines the final chemical network used for a PRODiMo model. To some extent, it is also possible to adapt the network manually (e.g. adding/removing reactions) without changing the code.

Besides the gas-phase chemical reactions provided by the chemical databases mentioned above, PRODiMo additionally includes X-ray chemistry (Meijerink et al. 2012), PAH charge-exchange chemistry (Thi et al. 2014; Thi et al. 2017b), adsorption and desorption (thermal, cosmic-ray and photo desorption) for ice species, H₂ formation on dust grains (Cazaux and Tielens 2002, 2004) and excited H₂ chemistry. For photon-induced reactions such as photo-ionization and photo-dissociation, the frequency dependent radiation field (i.e. the mean intensity J) from the radiative transfer module is used. However, also self-shielding for H₂, CO, and N₂ photo-dissociation and neutral carbon photo-ionization is considered. The chemical network used for this work is described in detail in Kamp et al. (2017). The most recent version of PRODiMo also includes dust surface chemistry including H₂/HD formation (Thi et al. 2017b) and the formation of phyllosilicates (Thi et al. 2017a). Not included in the chemical model of PRODiMo are mixing processes (see e.g. Semenov and Wiebe 2011; Furuya and Aikawa 2014).

In this work, the focus is on high-energy ionization and adsorption/desorption chemistry. We extended the chemical model of PRODiMo with ionization due to stellar energetic particles, a more detailed treatment of cosmic-ray ionization (see Chapter 3) and a simple treatment of radionuclide ionization following Umebayashi and Nakano (2009). Furthermore, an alternative treatment for ice desorption (first order desorption) was implemented (see Sect. 4.7).

Heating and cooling processes

The current version of PRODiMo includes up to 90 heating and up to 81 cooling processes for the thermal balance (Eq. 1.11). In Fig. 1.7 we show the most important heating and cooling processes as a function of position in the disk for the same disk model as is shown in Fig. 1.6. Most of these heating and cooling processes are due to the interaction

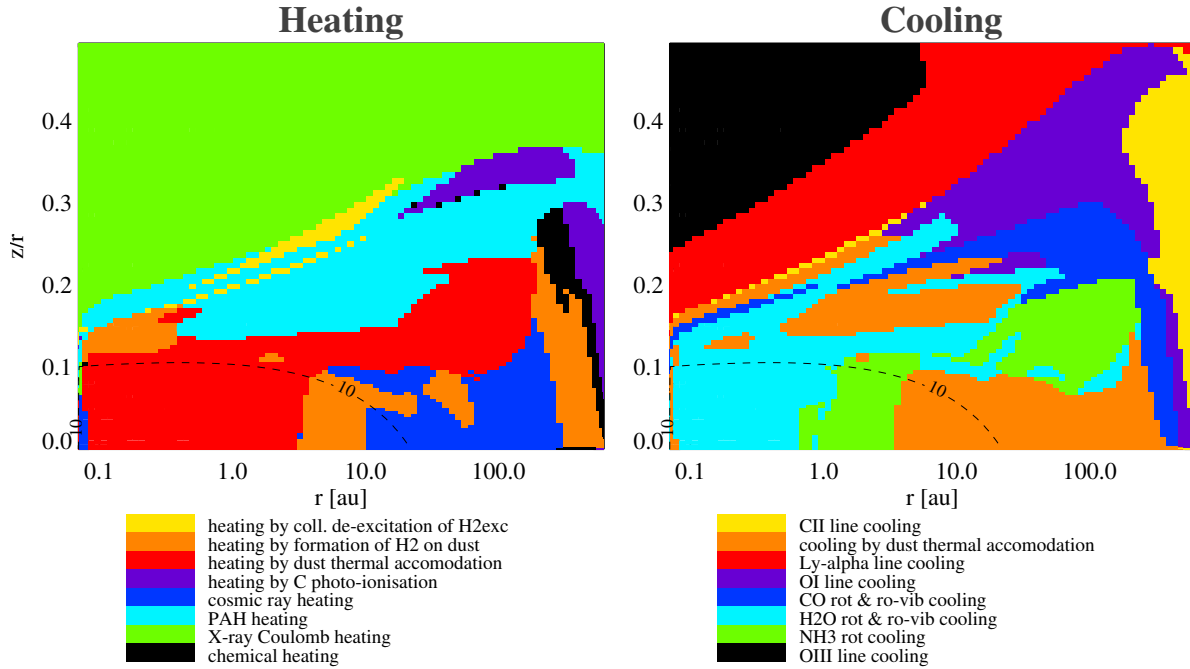


Figure 1.7 – Most efficient heating (left panel) and cooling (right panel) processes at each position in the disk for the PRODIMO model shown in Fig.1.6. The individual heating/cooling processes are identified by different colors and listed below each panel. The dashed contour line indicates a visual extinction of $A_V = 10$.

of matter with radiation such as absorption and emission of line photons by and from molecules and atoms. These line heating/cooling processes are treated with a non-LTE approach. Several other processes are treated in a (semi-)analytical way.

In layers where radiation cannot penetrate (i.e. the disk midplane), the most relevant heating and cooling process is thermal accommodation on grains. Due to inelastic collisions between dust grains and gas particles in these high-density regions, the gas temperature becomes equal to the dust temperature. Cosmic rays also contribute to heating in dense regions due to ionization of atomic and molecular hydrogen. Also included in PRODIMO is viscous heating which, depending on the accretion rate, can be an important heating process in the midplane of the disk (not included in the model shown in Fig. 1.7). In higher disk layers mostly stellar radiation is responsible for the gas heating. Important radiative processes are photoelectric heating, that is the ejection of electrons from dust and PAHs (named PAH heating in Fig. 1.6), carbon photo-ionization and X-ray Coulomb heating. Also, the energy released by chemical processes (chemical heating) can become important (e.g. H_2 formation on grains). Due to such heating processes and the inefficiency of thermal accommodation at low densities, the gas temperature decouples from the dust temperature in certain regions of the disk (see Fig. 1.6). More details on the heating and cooling processes can be found in [Woitke et al. \(2009, 2011\)](#) and [Aresu et al. \(2011\)](#).

For an accurate calculation of line cooling and heating rates, the level populations of the single atoms and molecules need to be known. PRODIMO calculates the non-LTE level populations via the 1+1D escape probability formalism (e.g. [Avrett and Hummer 1965](#); [Mihalas 1978](#)). It is assumed that the stellar radiation (radial direction) is responsible for radiative pumping of the molecules and that the line photons can mainly escape in

the vertical direction of the disk (Woitke et al. 2009). Such an approach is quite efficient (e.g. Woitke et al. 2009; Bruderer 2013) and, at the same time, provides an accurate description of line heating and cooling in disks (Kamp et al. 2010). A crucial input for the non-LTE calculations are the collisional and radiative data for the various molecules and atoms. Most of this data is taken from the Leiden Atomic and Molecular Database (low temperatures; Schöier et al. 2005), CHIANTI database (high-temperatures; Dere et al. 1997) and the HITRAN database for molecular spectroscopy (Rothman et al. 2013). The level populations calculated via the escape-probability method are also used as input for the line radiative transfer to produce synthetic observables (see Sect. 1.5.4).

1.5.4 Synthetic observables (Ray-tracing module)

PRODiMo also includes a module to produce synthetic observables. This is required to compare model results to real observations. Observables that can be produced by PRODiMo are spectral energy distributions (SEDs) and visibilities for the continuum emission (dust), spectral line emission from the gaseous component (see Fig. 1.6) and images for both the dust and gas emission.

This is done by performing radiative transfer (ray-tracing) on top of the physical and chemical model. The line radiative transfer in PRODiMo is done for single lines only. However, in the infrared wavelength regime line blends are common and require a more thorough treatment of the line transfer problem. For this the new FLiTs (Fast Line Ray Tracer, Woitke et al. 2017) line ray-tracing code can be used, which was developed for the DIANA project (see Sect. 1.6).

Relevant input parameters to produce synthetic observables that can be compared to observations are the inclination, position angle and the distance of the target. However, it is also often required to actually simulate the telescope and instrument itself. Although this can be done to some extent by PRODiMo (e.g. convolution with a given telescope beam) often additional post-processing tools such as the CASA/ALMA simulator are required (see Chapter 4).

As the ray tracing module is an integral part of PRODiMo it is relatively straightforward to make theoretical predictions which can be verified by future observations, but it is also possible to fit existing observations of a particular target. An example for the first case are our results shown in Chapter 4 (ALMA simulations), for the second case we briefly discuss an example in Sect. 1.6.

1.6 The DIANA project

Large parts of this thesis were done in the context of the EU-FP7 project DIANA (Disk ANALysis). The main goal of DIANA was the systematic collection of multi-wavelength observational data and coherent modelling of those data. The modelling was conducted with the Monte Carlo Dust radiative transfer codes MCFOST and MCMAX for the continuum observations (e.g. SED), and PRODiMo for the gas observations. New tools and new physics were implemented in the modelling codes such as the X-ray radiative transfer module and stellar particle ionization for PRODiMo. The modelling

results and the collected observational data are publicly available in online databases (see www.diana-project.com). Two model reconstructions of protoplanetary disks were also done by myself, one for the Herbig Ae/Be disk MWC 480 and one for the T Tauri disk DM Tau. In the following section, we present the results for MWC 480 to show exemplary how PRODiMo is used to model real observations. Further examples can be found in e.g. [Woitke et al. \(2011\)](#) and [Tilling et al. \(2012\)](#).

1.6.1 A fitting example: MWC 480 (HD 31648)

To fit disk observations of a particular target, the first crucial step is to determine the stellar properties as good as possible. We used available observational data in the UV and optical wavelength regime to constrain the stellar spectrum. The data was fitted with a PHOENIX stellar atmosphere model ([Brott and Hauschildt 2005](#)). To derive the X-ray input spectrum the X-ray emission model XSPEC ([Arnaud 1996](#)) was used to fit the available observational X-ray data (Liebhart, priv. comm.). For more details on this procedure see [Woitke et al. \(2016\)](#).

One crucial part of every fitting attempt is the collection of the observational data for the disk. This was a DIANA team effort and much of the data used for fitting MWC 480 was provided by other team members. For the continuum we used photometric observations and the *Spitzer* and ISO (Infrared Space Observatory) infrared spectra. To constrain the gas disk properties we used 32 line observations, three spectral line profiles and two line intensity maps.

The fitting procedure follows the usual χ^2 minimization procedure where all the above data was considered but with different weights for the calculation of the total χ^2 (see [Woitke et al. 2011](#) for a discussion). At first, the SED was fitted to constrain the structure of the disk and the dust properties. This was initially done by hand but the fit was subsequently improved by using automatic fitting routines (e.g. genetic algorithms). In the next step, the line data was included in the χ^2 fitting. The line data provides additional constraints on the structure, disk gas mass and the gas to dust mass ratio. To fit the lines, it was required to adapt parameters which affect also the SED fit (e.g. disk radius, flaring power index). We iterated between the SED fitting and line fitting until a best-fit model was found.

In [Fig. 1.8](#) we show the modelled SED including the stellar spectrum, [Fig. 1.9](#) shows the fitted line fluxes and in [Fig. 1.10](#) we show the fitted line profiles for the CO $J=2-1$ and the HCO⁺ $J=3-2$ spectral lines. In [Table 1.1](#) we list the main properties of the star and the disk for the best-fit model. The values for the distance, disk inclination and position angle are from the literature ([Meeus et al. 2012](#); [Grady et al. 2010](#); [Öberg et al. 2010](#)) and were kept fixed during the fitting. In the following, we discuss certain interesting aspects of the model but also its shortcomings.

Despite its rather advanced age ($\gtrsim 7$ Myr, [Simon et al. 2000](#)) the photometry and high-resolution imaging data of the disk of MWC 480 does not show any indication of structural features like gaps, holes or spiral arms (e.g. [Grady et al. 2010](#); [Kusakabe et al. 2012](#); [Honda et al. 2015](#)). Therefore we used a simple single-zone structure for our disk model. The SED ([Fig. 1.8](#)) can be conveniently fitted with a mildly flared, strongly settled disk, where the near-IR excess of about $3 L_{\odot}$ is a natural by-product. Such a flat disk structure is

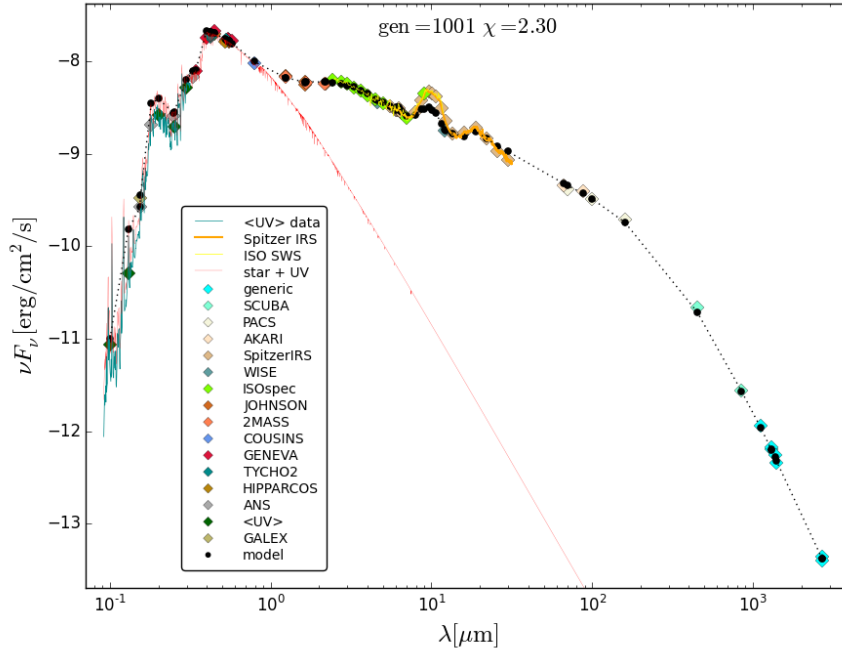


Figure 1.8 – Spectral energy distribution fit for MWC 480. The black large dots are the modelling results, the coloured symbols are the photometric observations. The orange and yellow solid lines are the *Spitzer* and ISO spectra, respectively. The red solid line shows the modelled stellar spectrum.

typical for a Meeus Group II disk and is in agreement with other studies (e.g. Piétu et al. 2007; Grady et al. 2010; Kusakabe et al. 2012).

A remarkable feature of the MWC 480 disk is its observed variability in the infrared including the silicate feature (see e.g. Kusakabe et al. 2012). We did not consider this variability for our best-fit model, but only modelled data from one epoch. However, it is possible to simulate the variability in the disk emission by changing the scale height of the disk (i.e. increased scale height in the inner disk results in a higher near-infrared flux). We found that this possible cause of the variability has no significant impact on the line observations. In contrast to the continuum, there is no multi-epoch data for the spectral lines to proof this. The continuum data collection also includes two continuum images. One (sub)mm image at 850 μm (Guzmán et al. 2015) and a NICMOS scattered light image at 1.6 μm (marginal detection, Grady et al. 2010). We fit the (sub)mm radial intensity profile reasonably well but cannot reproduce the NICMOS data. The 1.6 μm image used represents an epoch with a strong near-IR excess, where the inner disk scale height is supposed to be larger. In that case the inner disk casts a stronger shadow and extended scattered light emission is more difficult to detect (Kusakabe et al. 2012). That is likely the reason why we fail to fit the NICMOS data.

MWC 480 is particularly well-observed in (sub)mm lines including CO, ^{13}CO , HCO^+ , CN and HCN, and the model manages to reproduce all these observations, though less convincing for CN and HCN. In particular, we do not reproduce the slope of the CN and HCN radial intensity profiles (not shown). Similar to other chemical models (e.g. Walsh et al. 2012; Chapillon et al. 2012) our model predicts rather flat or even increasing intensity profiles whereas the ALMA data (Guzmán et al. 2015) shows a decreasing intensity profile for both molecules. This might indicate a general problem in disk chemistry mod-

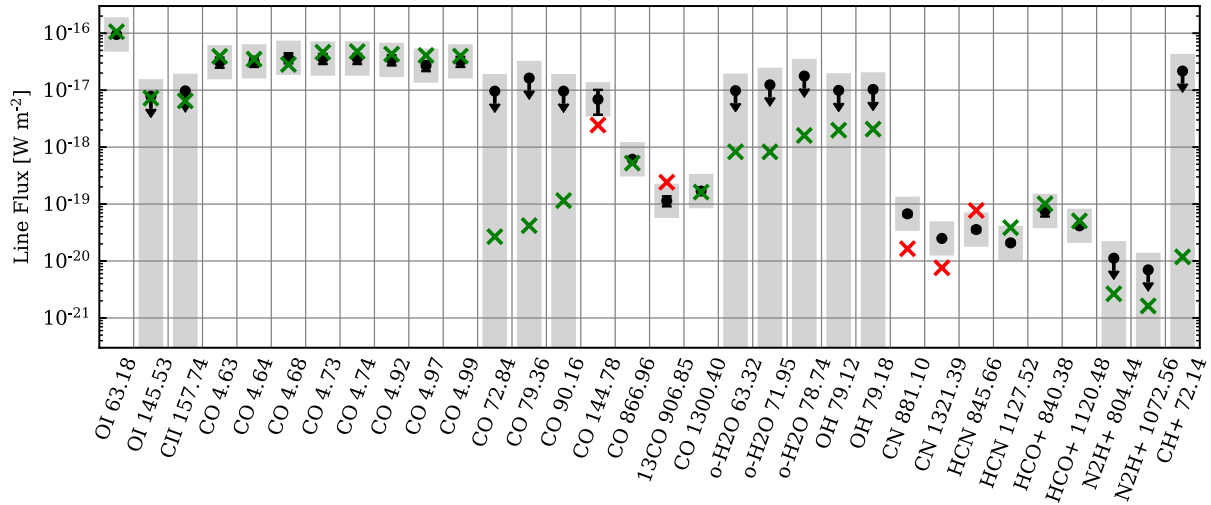


Figure 1.9 – Fitted line fluxes for MWC 480. The black symbols are the observations where the arrows indicate upper limits. The coloured crosses are the modelling results. The symbols are green if the modelled line flux agrees within a factor of two with the observations, otherwise they are red (the symbols are also green if the modelled flux is below an upper limit). The grey boxes mark a factor of three deviation compared to the observed value. The individual lines are identified by the species name and the wavelength of the line (in units of μm). References for the observational data: [Meeus et al. \(2012\)](#); [Blake and Boogert \(2004\)](#); [Dent et al. \(2005\)](#); [Thi et al. \(2004\)](#); [Öberg et al. \(2010\)](#); [Guzmán et al. \(2015\)](#).

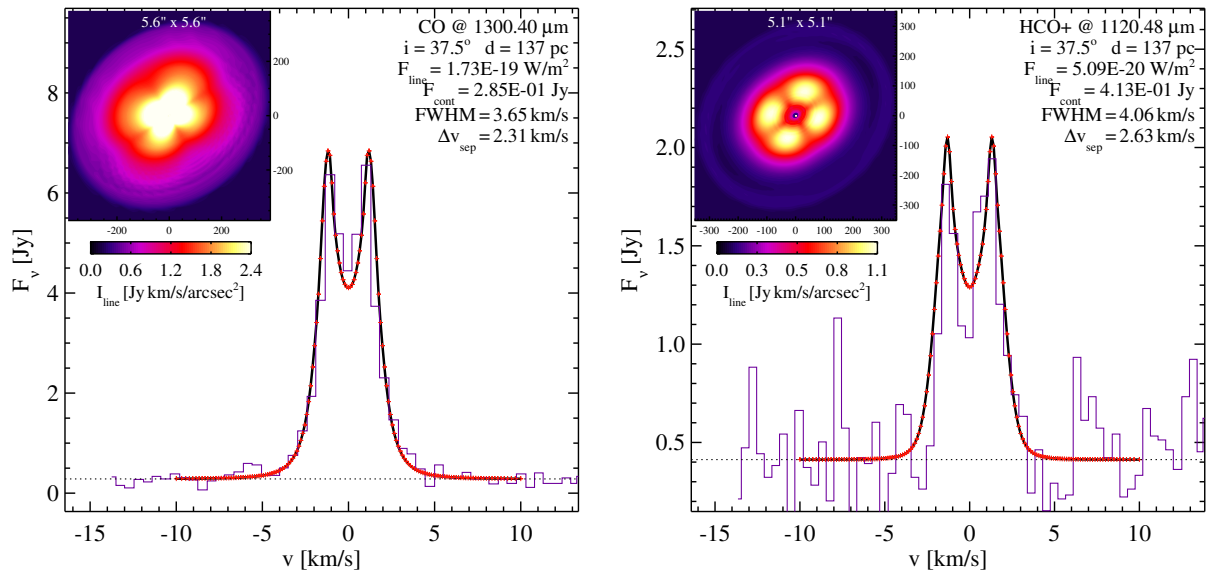


Figure 1.10 – Fitted line profiles for the CO $J=2-1$ (left panel) and HCO⁺ $J=3-2$ spectral lines for the MWC 480 model. The magenta solid lines show the observations the black solid line and the red symbols indicate the modelled line profile.

Table 1.1 – Star and disk properties of the MWC 480 model.

Quantity	Symbol	Value
stellar mass	M_*	$1.97 M_\odot$
stellar effective temperature	T_*	8250 K
stellar luminosity	L_*	$13.7 L_\odot$
X-ray luminosity	L_X	$6.4 \times 10^{29} \text{ erg s}^{-1}$
disk gas mass	M_{disk}	$0.022 M_\odot$
dust/gas mass ratio	d/g	0.01
inner disk radius	R_{in}	0.28 au
tapering-off radius	R_{tap}	100 au
outer disk radius	R_{out}	475 au
column density power index	ϵ	0.66
reference scale height	$H(100 \text{ au})$	12.25 au
flaring power index	β	1.095
minimum dust particle radius	a_{min}	$0.02 \mu\text{m}$
maximum dust particle radius	a_{max}	4.3 mm
dust size distribution power index	a_{pow}	3.62
turbulent mixing parameter	α_{settle}	7.3×10^{-5}
PAH abundance relative to ISM	f_{PAH}	0.1
distance	d	137 pc
inclination	i	37.5°
position angle	PA	-35.0°

els, in particular for nitrogen chemistry. We find a similar issue for the DM Tau model where comparable ALMA observations for CN and HCN exist.

The infrared CO ro-vibrational line fluxes also fit astonishingly well. However, the full-width half maximum of the modelled line profiles are too broad compared to the observed values. The *Herschel* high- J CO lines (e.g. CO $J=33-32$ at $79.63 \mu\text{m}$) seem to be too weak. Those lines trace the inner disk and indicate that a model with higher temperatures in the inner disk might be required. This could be achieved by a vertically more extended and less dense inner disk but might require a more complex structure (e.g. two zone model).

Previous disk mass estimates from the literature span two orders of magnitude ($0.0065 - 0.8 M_\odot$, Meeus et al. 2012; Hamidouche et al. 2006; Mannings and Sargent 1997; Piétu et al. 2007; Guilloteau et al. 2011; Sitko et al. 2008). This large scatter is not surprising as very different approaches were used to derive the mass (e.g. only the continuum or only some gas lines were considered). Our result of $0.022 M_\odot$ for the disk gas mass is well within this range. The mass estimate in our model is mainly driven by the continuum modelling but is also consistent with the line observations.

The model presented here fits the available continuum data and most of the spectral lines reasonably well. The biggest problem of our model are the ALMA observations of CN and HCN that seem to contradict current chemical disk models. This certainly requires further more detailed investigations. However, the rather simple structure and the presumably advanced age makes MWC 480 a very interesting object for future chemical studies. Recently complex organic molecules (e.g. CH_3CN , methyl cyanide) were detected in

MWC 480 (Öberg et al. 2015). A detailed model for MWC 480 as presented here is an ideal starting point to attempt the certainly challenging task to model the chemistry of those complex organic molecules. Furthermore, we plan to use the model of MWC 480 to study disk ionization processes in Herbig Ae/Be disk in comparison to T Tauri disks. Such investigations will provide further insight into molecular ion chemistry and disk ionization processes but spatially resolved observations of molecular ions is required to achieve this (see Chapters 2 and 3). The importance of studying molecular ion chemistry in Herbig Ae/Be stars is briefly discussed in Chapter 5.

Chapter 2

X-ray radiative transfer in protoplanetary disks

The aim of this project was the development of a wavelength dependent X-ray radiative transfer module for the protoplanetary disk code PRODiMO to study the impact of X-ray radiation on disk chemistry. The new module includes a proper treatment of X-ray scattering, X-ray dust opacities and a treatment for X-ray background fields. This project was carried out in the context of the EU-FP7 project DIANA (Subproject: Impact of X-ray and Particle Irradiation, PI M. Güdel) in close collaboration with the main PRODiMO developers. The new X-ray radiative transfer module is fully integrated into the PRODiMO code and is available on a collaborative basis. With the new X-ray radiative transfer, we investigated the importance of dust as an X-ray opacity source in protoplanetary disks and discussed the impact of X-ray background fields on the disk ion chemistry.

The results of this project will be published in a paper called *X-ray radiative transfer in protoplanetary disks - The role of dust and X-ray background fields*, which was submitted to the journal *Astronomy & Astrophysics* and was still under peer-review at the time of submission of this thesis. In this thesis, the submitted version is included.

Individual contributions to the paper

Own contribution: writing of the paper, code development for the X-ray radiative transfer module and model runs.

M. Güdel: PI of the DIANA subproject leading to this publication; provided valuable scientific input on X-ray emission and X-ray physics of young stars.

P. Woitke: support for the implementation of the X-ray RT module in PRODiMO.

I. Kamp, W.-F. Thi: PRODiMO modelling support.

M. Min: provided important input for the treatment of anisotropic scattering.

G. Aresu, R. Meijerink: main developers of the X-ray chemistry module of PRODiMO which was used together with the newly developed X-ray radiative transfer module.

All authors read the manuscript before publication and provided valuable scientific input and very useful suggestions concerning the presentation and writing of the paper.

X-ray radiative transfer in protoplanetary disks

The role of dust and X-ray background fields

Ch. Rab^{1,3}, M. Güdel¹, P. Woitke², I. Kamp³, W.-F. Thi⁴, M. Min^{5,6}, G. Aresu⁷, and R. Meijerink⁸

¹ University of Vienna, Dept. of Astrophysics, Türkenschanzstr. 17, 1180 Wien, Austria e-mail: christian.rab@univie.ac.at

² SUPA, School of Physics & Astronomy, University of St. Andrews, North Haugh, St. Andrews KY16 9SS, UK

³ Kapteyn Astronomical Institute, University of Groningen, P.O. Box 800, 9700 AV Groningen, The Netherlands

⁴ Max-Planck-Institut für extraterrestrische Physik, Giessenbachstrasse 1, 85748 Garching, Germany

⁵ SRON Netherlands Institute for Space Research, Sorbonnelaan 2, 3584 CA Utrecht, The Netherlands

⁶ Astronomical institute Anton Pannekoek, University of Amsterdam, Science Park 904, 1098 XH, Amsterdam, The Netherlands

⁷ INAF, Osservatorio Astronomico di Cagliari, via della Scienza 5, 09047 Selargius, Italy

⁸ Leiden Observatory, Leiden University, PO Box 9513, 2300 RA Leiden, The Netherlands

Received xx xx 2017 / Accepted xx xx 2017

ABSTRACT

Context. The X-ray luminosities of T Tauri stars are about two to four orders of magnitude higher than the luminosity of the contemporary Sun. As these stars are born in clusters, their disks are not only irradiated by their parent star but also by an X-ray background field produced by the cluster members.

Aims. We aim to quantify the impact of X-ray background fields produced by young embedded clusters on the chemical structure of disks. Further we want to investigate the importance of the dust for X-ray radiative transfer in disks.

Methods. We present a new X-ray radiative transfer module for the radiation thermo-chemical disk code PRODIMO (PROtoplanetary Disk MOdel), which includes X-ray scattering and absorption by both the gas and dust component. The X-ray dust opacities can be calculated for various dust compositions and dust size distributions. For the X-ray radiative transfer we consider irradiation by the star and by X-ray background fields. To study the impact of X-rays on the chemical structure of disks we use the well established disk ionization tracers N_2H^+ and HCO^+ .

Results. For evolved dust populations (e.g. grain growth), X-ray opacities are mostly dominated by the gas; only for photon energies $E \gtrsim 5 - 10$ keV, dust opacities become relevant. Consequently the local disk X-ray radiation field is only affected in dense regions close to the disk midplane. X-ray background fields can dominate the local X-ray disk ionization rate for disk radii $r \gtrsim 20$ au. However, the N_2H^+ and HCO^+ column densities are only significantly affected in case of low cosmic-ray ionization rates ($\lesssim 10^{-19} s^{-1}$), or if the background flux is at least a factor of ten higher than the flux level of $\approx 10^{-5} erg cm^{-2} s^{-1}$ expected for clusters typical for the solar vicinity.

Conclusions. Observable signatures of X-ray background fields in low-mass star-formation regions, like Taurus, are only expected for cluster members experiencing a strong X-ray background field (e.g. due to their location within the cluster). For the majority of the cluster members, the X-ray background field has only little impact on the disk chemical structure.

Key words. Stars: formation - Stars: circumstellar matter - Radiative transfer - Astrochemistry - Methods: numerical

1. Introduction

Strong X-ray emission is a common property of pre-main sequence stars. T Tauri stars, often considered as young solar analogs, show strong X-ray emission with luminosities in the range of approximately $10^{29} - 10^{31} erg s^{-1}$ (e.g. Preibisch et al. 2005; Güdel et al. 2007a), which is about $10^2 - 10^4$ times higher than the X-ray luminosity of the contemporary Sun (Feigelson et al. 2002). The origin of such high X-ray luminosities is likely the enhanced stellar and magnetic activity of the young stars (e.g. Feigelson et al. 2002), but also jets close to the star and the protoplanetary disk (Güdel et al. 2007c) caused by interaction of the stellar and disk magnetic fields (e.g. X-wind Shu et al. 1997) might contribute. Accretion shocks probably do not contribute significantly to the X-ray emission of T Tauri stars (Güdel et al. 2007b), but accreting material absorbs soft X-rays and might cool the hot coronal gas (Güdel & Telleschi 2007).

X-ray irradiation plays an important role for the thermal and chemical structure of protoplanetary disks. Soft X-rays heat the

upper disk layers to temperatures larger than 5000 K (Glassgold et al. 2004; Nomura et al. 2007; Aresu et al. 2011) and possibly drive, together with far and extreme ultraviolet radiation, disk photo-evaporation (e.g. Ercolano et al. 2008a; Gorti & Hollenbach 2009). Diagnostics of the interaction of X-rays with the disk atmosphere are mainly atomic lines (e.g. Gorti & Hollenbach 2004; Meijerink et al. 2008; Ercolano et al. 2008a; Ádámkóvics et al. 2011; Aresu et al. 2012). These lines trace the hot upper layers (vertical column densities of $10^{19} - 10^{20} cm^{-2}$) in the inner $\approx 10 - 50$ au of protoplanetary disks (Glassgold et al. 2007; Aresu et al. 2012). X-rays can influence atomic line emission via heating (e.g. [OI], Aresu et al. 2014) and/or direct ionization (e.g. the neon ion fine-structure lines Glassgold et al. 2007). Güdel et al. (2010) found a correlation between the [NeII] 12.81 μm line, observed with the *Spitzer* Space telescope, and stellar X-ray luminosity in a sample of 92 pre-main sequence stars. Such a correlation is consistent with predictions of sev-

eral thermo-chemical disk models (Meijerink et al. 2008; Gorti & Hollenbach 2008; Schisano et al. 2010; Aresu et al. 2012).

Hard X-ray emission with energies larger than 1 keV can also penetrate deeper disk layers where they become an important ionization source of molecular hydrogen (e.g. Igea & Glassgold 1999; Ercolano & Glassgold 2013) and therefore drive molecular-ion chemistry. However, in those deep layers X-rays compete with other high energy ionization sources like cosmic rays, decay of short-lived radionuclides (e.g. Umebayashi & Nakano 2009; Cleeves et al. 2013b) and stellar energetic particles (Rab et al. 2017). Observationally those ionization processes can be traced by molecular ions, where HCO^+ and N_2H^+ are the most frequently observed ones (e.g. Thi et al. 2004; Dutrey et al. 2007, 2014; Öberg et al. 2011b; Cleeves et al. 2015; Guilloteau et al. 2016). In contrast to the atomic lines, X-ray heating does not play a prominent role for molecular ion line emission. Consequently molecular ions are good tracers of chemical processes such as ionization. Nevertheless, there is no clear picture yet, both observationally and theoretically, about the main ionization process determining the abundances of those molecules. For example, Salter et al. (2011) found no correlation of HCO^+ millimetre line fluxes with stellar properties like mass, bolometric luminosity or X-ray luminosity.

Predictions from models concerning the impact of X-ray emission on HCO^+ and N_2H^+ are quite different. The models of Teague et al. (2015) indicate a strong sensitivity of the HCO^+ column density to the X-ray luminosity at all disk radii assuming an ISM like cosmic-ray ionization rate. However, in the models of Cleeves et al. (2014) HCO^+ and N_2H^+ column densities become sensitive to stellar X-rays only if the cosmic-ray ionization rate is as low as $\zeta_{\text{CR}} \approx 10^{-19} \text{ s}^{-1}$. Walsh et al. (2012) concluded that far-UV photochemistry plays a more dominant role for molecular ions than X-rays (using $\zeta_{\text{CR}} \approx 10^{-17} \text{ s}^{-1}$). Rab et al. (2017) included energetic stellar particles as additional high-energy ionization source. In their models N_2H^+ is sensitive to X-rays but only for low cosmic-ray ionization rates, where HCO^+ might be dominated by stellar particle ionization, assuming that the paths of the particles are not strongly affected by magnetic fields that may guide them away from the disk.

An aspect not yet considered in radiation thermo-chemical disk models are X-ray background fields of embedded clusters. Adams et al. (2012) estimated the X-ray background flux distribution for typical clusters in the solar vicinity. They find that the background flux impinging on the disk surface can be higher than the stellar X-ray flux in the outer disk regions ($r \gtrsim 10 \text{ au}$).

In this work we introduce a new X-ray radiative transfer module for the radiation thermo-chemical disk code PRODiMO. This module includes X-ray scattering and a detailed treatment of X-ray dust opacities, considering different dust compositions and grain size distributions. In addition, we also include an X-ray background field, as proposed by Adams et al. (2012), as additional disk irradiation source. We investigate the impact of X-ray background fields on the disk chemistry in particular on the common disk ionization tracers HCO^+ and N_2H^+ .

In Sect. 2, we describe the X-ray radiative transfer module and our disk model used to investigate the impact of stellar and interstellar X-ray radiation. Our results are presented in Sect. 3. At first we show the resulting X-ray disk ionization rates for models including scattering, X-ray dust opacities and X-ray background fields. The impact on the disk ion chemistry is studied via comparison of HCO^+ and N_2H^+ column densities. In Sect. 4, we discuss observational implications of X-ray background fields also in context of enhanced UV background fields. A summary and our main conclusions are presented in Sect. 5.

2. Methods

We use the radiation thermo-chemical disk code PRODiMO (PROtoplanetary DIsk MOdel) to model the thermal and chemical structure of a passive disk irradiated by the stellar and interstellar radiation fields. PRODiMO solves consistently for the dust temperature, gas temperature and chemical abundances in the disk (Woitke et al. 2009) and includes modules producing observables like spectral energy distributions (Thi et al. 2011) and line emission (Kamp et al. 2010; Woitke et al. 2011).

The disk model we use here is based on the so-called reference model developed for the DIANA¹ (DiscAnalysis) project. This model is consistent with typical dust and gas observational properties of T Tauri disks, and is described in detail in Woitke et al. (2016) and Kamp et al. (2017). We therefore provide here only a brief overview of this reference model (Sect. 2.1). For this work we also use different dust size distributions to study the impact of dust on the X-ray RT; those models are described in Sect. 2.2. The new X-ray radiative transfer module of PRODiMO is described in Sect. 2.3.

2.1. Reference model

In the following we describe the gas and dust disk structure of the reference model and the chemical network we used. In Table 1 we provide an overview of all model parameters including the properties of the central star. The stellar and interstellar X-ray properties are described in Sect. 2.3.

2.1.1. Gas disk structure

We use a fixed parameterized density structure for the disk. The axisymmetric flared 2D gas density structure as a function of the cylindrical coordinates r and z (height of the disk) is given by (e.g. Lynden-Bell & Pringle 1974; Andrews et al. 2009; Woitke et al. 2016)

$$\rho(r, z) = \frac{\Sigma(r)}{\sqrt{2\pi} \cdot h(r)} \exp\left(-\frac{z^2}{2h(r)^2}\right) \quad [\text{g cm}^{-3}], \quad (1)$$

For the vertical disk scale height $h(r)$ we use a radial power-law

$$h(r) = H(100 \text{ au}) \left(\frac{r}{100 \text{ au}}\right)^\beta \quad (2)$$

where $H(100 \text{ au})$ gives the disk scale height at $r = 100 \text{ au}$ (here 10 au) and $\beta = 1.15$ is the flaring power index. For the radial surface density we use again a power-law with a tapered outer edge

$$\Sigma(r) = \Sigma_0 \left(\frac{r}{R_{\text{in}}}\right)^{-\epsilon} \exp\left(-\left(\frac{r}{R_{\text{tap}}}\right)^{2-\epsilon}\right) \quad [\text{g cm}^{-2}]. \quad (3)$$

The inner disk radius is $R_{\text{in}} = 0.07 \text{ au}$ (the dust condensation radius), the characteristic radius is $R_{\text{tap}} = 100 \text{ au}$ and the outer radius is $R_{\text{out}} = 620 \text{ au}$ where the total vertical hydrogen column density is as low as $N_{(\text{H}),\text{ver}} \approx 10^{20} \text{ cm}^{-2}$. The constant Σ_0 is given by the disk mass $M_{\text{disk}} = 0.01 M_\odot$ and determined via the relation $M_{\text{disk}} = 2\pi \int \Sigma(r)r dr$ to be $1011 \text{ [g cm}^{-2}]$. The 2D gas density structure and the radial column density profile of the disk are shown in Fig. 1. The gas density structure is the same for all models presented in this paper.

¹ DIANA website: <http://diana-project.com/>

Table 1. Main parameters for the reference disk model.

Quantity	Symbol	Value
stellar mass	M_*	$0.7 M_\odot$
stellar effective temp.	T_*	4000 K
stellar luminosity	L_*	$1.0 L_\odot$
FUV excess	L_{FUV}/L_*	0.01
FUV power law index	p_{UV}	1.3
X-ray luminosity	L_X	$10^{30} \text{ erg s}^{-1}$
X-ray emission temp.	T_X	$2 \times 10^7 \text{ K}$
strength of interst. FUV	χ^{ISM}	1^a
disk gas mass	M_{disk}	$0.01 M_\odot$
dust/gas mass ratio	d/g	0.01
inner disk radius	R_{in}	0.07 au
tapering-off radius	R_{tap}	100 au
column density power ind.	ϵ	1.0
reference scale height	$H(100 \text{ au})$	10 au
flaring power index	β	1.15
min. dust particle radius	a_{min}	$0.05 \mu\text{m}$
max. dust particle radius	a_{max}	3 mm
dust size dist. power index	a_{pow}	3.5
turbulent mixing param.	α_{settle}	10^{-2}
max. hollow volume ratio ^b	$V_{\text{hollow,max}}$	0.8
dust composition	$\text{Mg}_{0.7}\text{Fe}_{0.3}\text{SiO}_3$	60%
(volume fractions)	amorph. carbon	15%
	porosity	25%
PAH abun. rel. to ISM	f_{PAH}	0.01
chem. heating efficiency	γ^{chem}	0.2

Notes. If not noted otherwise, these parameters are kept fixed for all our models presented in this work. For more details on the parameter definitions see [Woitke et al. \(2009, 2011, 2016\)](#). ^(a) χ^{ISM} is given in units of the Draine field ([Draine & Bertoldi 1996](#); [Woitke et al. 2009](#)). ^(b) We use distributed hollow spheres for the dust opacity calculations ([Min et al. 2005, 2016](#)).

2.1.2. Dust disk structure

We assume a dust to gas mass ratio of $\delta = 0.01$, which also determines the total dust mass. However, due to dust evolution processes like dust growth, dust settling and drift (see e.g. [Birnstiel et al. 2012](#)), the dust density structure in a protoplanetary disk does not necessarily follow the gas density structure.

We account for this by including a dust size distribution with a minimum dust grain size of $a_{\text{min}} = 0.05 \mu\text{m}$ and a maximum grain size of $a_{\text{max}} = 3000 \mu\text{m}$. The size distribution itself is given by a simple power-law $f(a) \propto a^{-a_{\text{pow}}}$ with $a_{\text{pow}} = 3.5$ ([Mathis et al. 1977](#)). Dust settling is incorporated by applying the method of [Dubrulle et al. \(1995\)](#), using a turbulent mixing parameter of $\alpha_{\text{settle}} = 10^{-2}$. This results in a size and density dependent dust scale height and the dust to gas mass ratio varies within the disk, however the total gas to dust mass ratio stays the same ([Woitke et al. 2016](#)). We use porous grains composed of a mixture of amorphous carbon and silicate (see Table 1). The resulting dust grain density is $\rho_{\text{gr}} = 2.1 \text{ g cm}^{-3}$. Our model does not account for possible radial drift of large dust particles.

In PRODiMO the same dust model is consistently used for the radiative transfer, including X-rays and the chemistry. For more details on the dust model and opacity calculations see [Woitke et al. \(2016\)](#); [Min et al. \(2016\)](#).

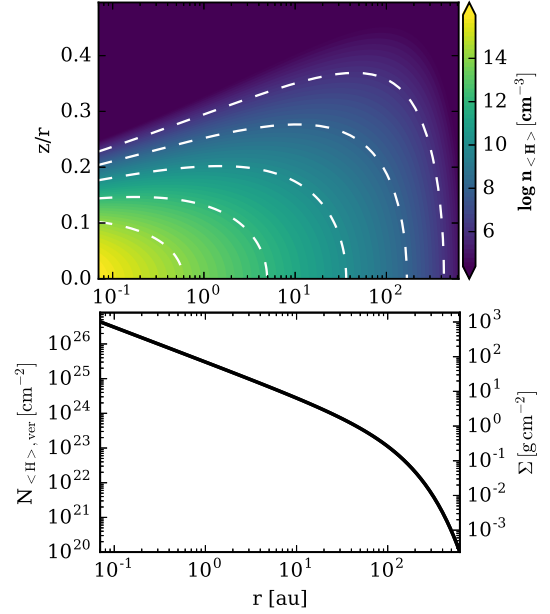


Fig. 1. Gas disk structure. The top panel shows the total hydrogen number density n_{H} . The height of the disk z is scaled by the radius r . The white dashed contours correspond to the density levels shown in the colourbar. The bottom panel shows the total vertical hydrogen column number density $N_{\text{H,ver}}$ as a function of radius where on the right hand side also the scale for the surface density Σ in g cm^{-2} is given.

2.1.3. Chemical network

Our chemical network is based on the gas-phase chemical database UMIST 2012 ([McElroy et al. 2013](#)) where we only use a subset of reactions according to our selection of species. Additionally to the gas phase reactions from the UMIST database we include detailed X-ray chemistry ([Meijerink et al. 2012](#)), charge exchange chemistry of PAHs ([Thi et al. 2014](#), [Thi et al. in prep.](#)), excited H_2 chemistry, H_2 formation using the analytical function of [Cazaux & Tielens \(2002, 2004\)](#) and adsorption and thermal, photo and cosmic-ray desorption of ices. Dust surface chemistry is not included in our model.

The chemical network used here is described in detail in [Kamp et al. \(2017\)](#). We used their so called large chemical network which consists of 235 chemical species (64 of them are ices) and 3143 chemical reactions. The element abundances are listed in [Kamp et al. \(2017\)](#). The element abundances correspond to the group of low metal abundances (e.g. [Graedel et al. 1982](#); [Lee et al. 1998](#)). Further details concerning the chemistry of HCO^+ and N_2H^+ and the used binding energies are given in [Rab et al. \(2017\)](#).

To solve for the chemical abundances we used the steady-state approach. In [Woitke et al. \(2016\)](#) and [Rab et al. \(2017\)](#) comparisons of time-dependent and steady-state chemistry models are presented, which show that in our models steady-state is reached within typical lifetimes of disks in most regions of the disk. In [Rab et al. \(2017\)](#) it is shown that the assumption of steady-state is well justified for HCO^+ and N_2H^+ (see also [Aikawa et al. 2015](#)). The resulting differences between the steady-state and time-dependent models in the radial column density profiles of the molecular ions are not significant for our study.

Table 2. Dust models.

Name	Parameters	$A_V = 1^a$ (cm^{-2})	Surface ^b (cm^2)
small grains SG	single size $a = 0.1 \mu\text{m}$ no settling	1.4(21) ^c	2.8(-21)
medium grains MG	$a_{\min} = 0.005 \mu\text{m}$ $a_{\max} = 1000 \mu\text{m}$ $a_{\text{pow}} = 3.7$	1.9(22)	7.6(-22)
large grains LG, reference	$a_{\min} = 0.05 \mu\text{m}$ $a_{\max} = 3000 \mu\text{m}$ $a_{\text{pow}} = 3.5$	1.2(23)	2.7(-23)

Notes. ^(a) hydrogen column density $N_{\text{(H)}}$ where the visual extinction A_V is unity. ^(b) total dust surface per hydrogen nucleus (unsettled value) ^(c) $a(b)$ means $a \times 10^b$.

2.2. Model groups

2.2.1. Dust models

For our investigations of the impact of the dust on the X-ray radiative transfer and on the molecular column densities we use three different dust size distributions. All three distributions have the same dust composition as listed in Table 1. The parameters varied are a_{\min} , a_{\max} and a_{pow} . In all three dust models the gas density structure is the same as described in Sect. 2.1.1 and the dust to gas mass ratio is $\delta = 0.01$. The details of the dust models are provided in Table 2.

The small grains model (SG) includes only a single dust size with $a = 0.1 \mu\text{m}$ and no dust settling. Although such a dust model is likely not a good representation for the conditions in protoplanetary disks, it is useful as a reference and to show the impact of the dust on the X-ray radiative transfer and chemical disk structure.

The medium grain and large grain models are more appropriate in the context of grain growth and dust settling. (see Sect. 2.1.2). Although, such dust models are a simplified representation of dust evolution in disks (Birnstiel et al. 2012; Vasyunin et al. 2011; Akimkin et al. 2013; Facchini et al. 2017), they still provide insight on the role of dust for the chemistry and X-ray radiative transfer. The main difference of the medium and large grain model is the amount of small particles. In the medium grain model about 10% of the total dust mass is in grains with $a \leq 1 \mu\text{m}$ whereas in the large grain models it is only about 1.5%. Both models include dust settling as described in Sect. 2.1.2.

Most relevant for the chemistry is the total dust surface area per hydrogen nucleus (i.e. for the freeze-out of molecules). The dust surface area varies by about two orders of magnitude in our models (Table 2, see also Voitke et al. 2016; Rab et al. 2017 for details).

In Fig. 2 we show the dust density structure, the dust and gas temperature and the local UV radiation field in the disk, for the small grains and large grains model. The main difference in the dust models is the visual extinction A_V , which significantly affects the dust temperature structure and the local disk radiation field.

2.2.2. Cosmic rays

There is some uncertainty about how many of the cosmic rays actually reach the disk of T Tauri stars. Similar to the Sun, the stellar wind of young stars, which might be significantly stronger

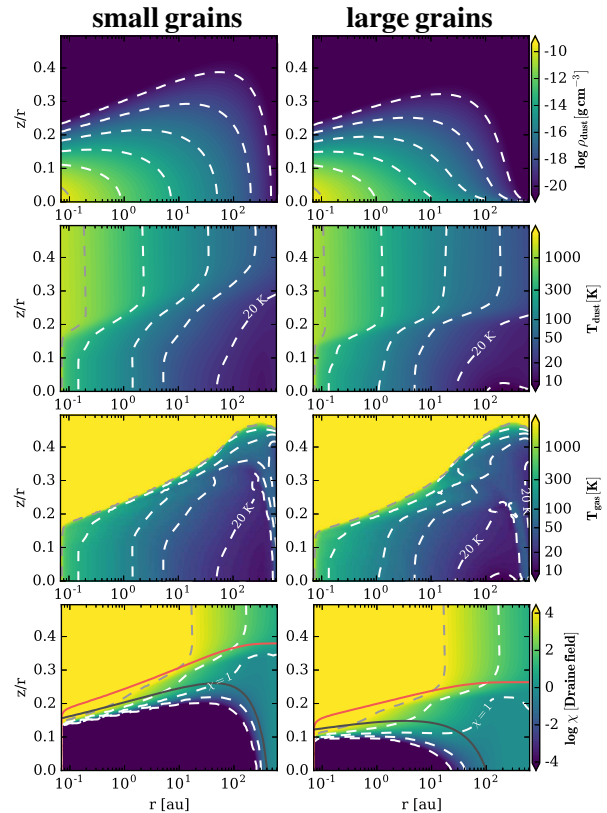


Fig. 2. Large grains (left column) and small grains (right column) disk model. From top to bottom the dust density, dust temperature, gas temperature and the disk UV radiation field χ in units of the Draine field is shown. The dashed contours in each plot correspond to the levels shown in the respective colourbar. The additional contours in the UV plots (bottom row) indicate where the radial (red solid line) and vertical (black solid line) visual extinction are equal to unity. For both models the same gas density structure as shown in Fig. 1 is used.

compared to the Sun, can power a heliosphere-like analog which is called a “T Tauriosphere”. The existence of such a T Tauriosphere might reduce the cosmic-ray ionization rate in the disk by several orders of magnitude (Cleeves et al. 2013a).

To account for this, we use two different cosmic-ray input spectra, one is the canonical local ISM cosmic-ray spectrum (Webber 1998) and the second is a modulated spectrum which accounts for the suppression of cosmic-rays by a heliosphere. For the latter we use the “Solar Max” spectrum of Cleeves et al. 2013a. To calculate the cosmic-ray ionization rate we use the fitting formula of Padovani et al. (2013) and Cleeves et al. (2013a). The ISM cosmic-ray spectrum gives a cosmic-ray ionization rate per hydrogen nucleus of $\zeta_{\text{CR}} \approx 10^{-17}$ and the Solar Max spectrum gives $\zeta_{\text{CR}} \approx 10^{-19}$, which is consistent with the upper limit of the total H_2 ionization rate in TW Hya derived by Cleeves et al. (2015). We call these two model groups “ISM cosmic rays” and “low cosmic rays”, respectively.

2.3. X-ray radiative transfer

For the X-ray radiative transfer (RT) we extended the already available radiative transfer module of PRODIMO to the X-ray

wavelength regime. The 2D radiative transfer problem including scattering is solved with a ray-based method and a simple iterative scheme (Λ -iteration). The radiative transfer equation is solved for a coarse grid of wavelengths bands. For each band the relevant quantities (e.g. incident intensities, opacities) are averaged over the wavelength range covered by each band. The details of this method are described in [Woitke et al. \(2009\)](#). For the X-ray regime we find that about 20 wavelength bands are sufficient to represent the energy range of 0.1 – 20 keV used in our models. Besides the stellar radiation also interstellar radiation fields (UV and X-rays) are considered. For the interstellar radiation fields we assume that the disk is irradiated isotropically.

The X-ray RT module provides the X-ray radiation field for each point in the disk as a function of wavelength. Those values are used in the already available X-ray chemistry module of PRODIMO to calculate the X-ray ionization rate for the various chemical species. The X-ray chemistry used in this paper is the same as presented in [Aresu et al. \(2011\)](#) and [Meijerink et al. \(2012\)](#). As the chemistry influences the gas composition which in turn determines the gas opacities, we iterate between the X-ray RT and the chemistry. For each X-ray radiative transfer step the chemical abundances are kept fixed where for each chemistry step the X-ray ionization rates are fixed. We find that typically three to five iterations are required until convergence is reached.

2.3.1. X-ray scattering

Compton scattering, which reduces to Thomson scattering at low energies, is the dominant scattering process in the X-ray regime. The anisotropic behaviour of Compton scattering is treated via an approximation by reducing the isotropic scattering cross-section by a factor $(1 - g)$, where $g = \langle \cos \theta \rangle$ is the asymmetry parameter and θ is the scattering angle (see also [Laor & Draine 1993](#)). We use this approach for both the gas and the dust scattering cross-sections. We call this reduced cross-section the pseudo anisotropic (pa) scattering cross-section. g is zero for isotropic scattering and approaches unity in case of strong forward scattering. We apply this approach because the treatment of anisotropic scattering in a ray-based radiative transfer code is expensive, in contrast to Monte Carlo radiative transfer codes. Although this method is a simple approximation it is very efficient and we find that our results concerning X-ray gas radiative transfer and the X-ray ionization rate are in reasonably good agreement with the Monte Carlo X-ray radiative transfer code MOCASSIN (see Appendix. B).

2.3.2. X-ray gas opacities

For the X-ray gas opacities we used the open source library `xraylib`² ([Brunetti et al. 2004](#); [Schoonjans et al. 2011](#)). This library provides the X-ray absorption and scattering cross-sections (Rayleigh and Compton scattering) for atomic and molecular species. Concerning the X-ray gas absorption cross-section we find that the cross-section provided by `xraylib` are similar to the commonly used X-ray absorption cross-section of [Verner & Yakovlev \(1995\)](#); [Verner et al. \(1996\)](#).

2.3.3. X-ray dust opacities

In the literature, only X-ray optical constants for Astronomical Silicates and carbon are available ([Draine 2003](#)). However, for

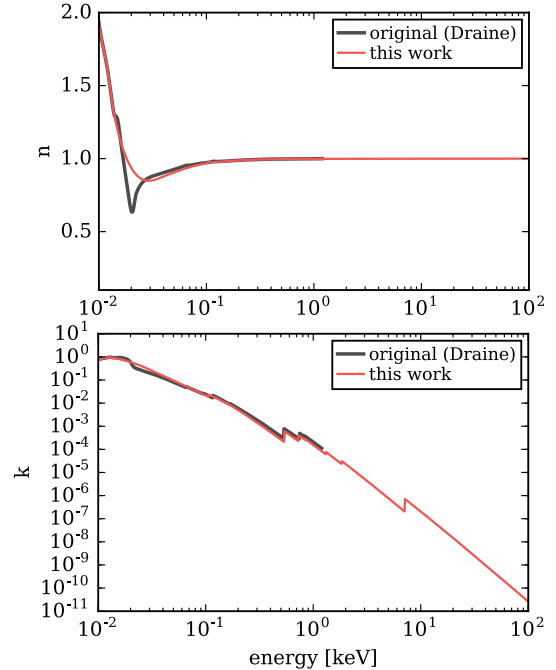


Fig. 3. Optical constants (n, k) for Astronomical Silicates in the X-ray regime. n (top panel) is the real and k (bottom panel) the imaginary part of the complex refractive index. The red solid lines show the results from this work, the black solid lines show the results from [Draine \(2003\)](#).

protoplanetary disks often a mixture of different dust species is used.

We implemented the method of [Draine \(2003\)](#) to calculate X-ray optical constants for various dust compositions. This method uses the available optical constants, or more precisely the dielectric function, for the ultraviolet to the millimetre wavelength range and additionally the atomic gas phase photo-electric cross-sections for the X-ray regime. With this, the imaginary part of the complex dielectric function can be constructed from the X-ray to the millimetre regime. Via the Kramers-Kronig relation the real part of the dielectric function can be calculated knowing the imaginary part.

To be consistent with [Draine \(2003\)](#) we use the photo-electric cross-sections from [Verner et al. \(1996\)](#) to construct the imaginary part of the dielectric function. However, in contrast to [Draine \(2003\)](#) we do not include any additional measured data for the K edge absorption profiles (e.g. for graphite). The details of the absorption edges are less important here, as we are mainly interested in the resulting X-ray ionization rate which is an energy-integrated quantity.

In [Fig. 3](#) we compare the optical constants for Astronomical Silicates (MgFeSiO_4 composition) calculated via the above described method to the original optical constants provided by [Draine \(2003\)](#). The deviations of our results from the [Draine \(2003\)](#) data are likely a consequence of our simplified treatment of absorption edges. However, our approach is sufficient for deriving X-ray ionization rates.

By using these newly available optical constants we calculated the X-ray dust opacities with a combination of the Mie-theory, the Rayleigh-Gans approximation ([Krügel 2002](#)) and ge-

² `xraylib` source code <https://github.com/tschoonj/xraylib>

A&A proofs: manuscript no. xrt

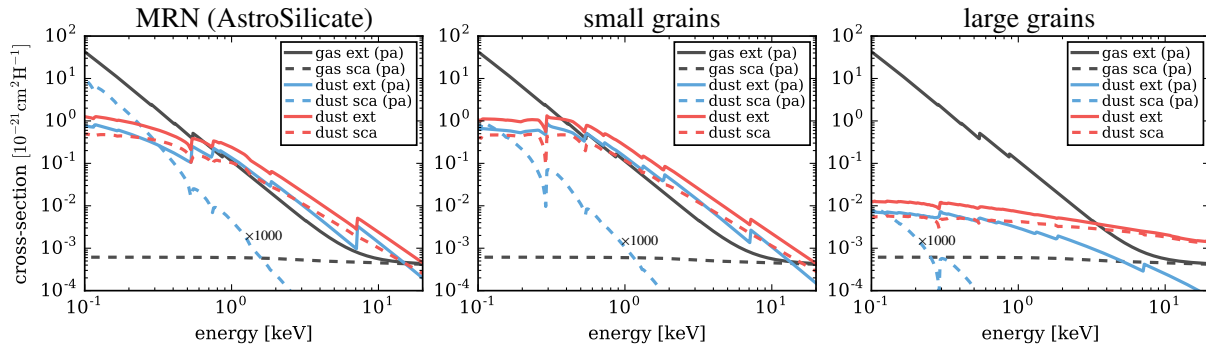


Fig. 4. X-ray cross-sections for the gas (black lines) and dust (blue and red lines) per hydrogen nucleus for three different dust size distributions. The solid lines show the extinction (absorption+scattering) cross section, the dashed lines are the scattering cross sections. The left panel is for the MRN size distribution (Mathis et al. 1977) using pure Astronomical Silicates (Draine 2003). The two other panels are for the small and large grains dust models (see Sect. 2.2.1). For the dust, the red lines are for isotropic and the blue lines for pseudo anisotropic (pa) scattering (see Sect. 2.3.2). The pseudo anisotropic scattering values (blue dashed lines) are multiplied by a factor of 1000. The shown gas cross-sections are the same in all three panels.

ometrical optics (Zhou et al. 2003) similar to Draine (2003) and Ercolano et al. (2008a). Also here we use the pseudo anisotropic scattering cross-sections in our calculations (see Sect. 2.3.1).

In Fig. 4 we show the dust extinction (sum of absorption and scattering cross-sections) and the scattering cross-sections per hydrogen nucleus for three examples of dust size distributions and compositions, in a similar way as presented in Draine (2003). For comparison we also show the gas cross-section for the initial elemental abundances used in our models (low metal abundances, see Kamp et al. 2017), assuming that all hydrogen is molecular and all other elements are present as neutral atoms. For all cases shown in Fig. 4 we assumed a gas to dust mass ratio of 0.01.

The first panel in Fig. 4 shows the results for an MRN (Mathis, Rumpl, Nordsieck; Mathis et al. 1977) size distribution ($a_{\min} = 0.005 \mu\text{m}$, $a_{\max} = 0.25 \mu\text{m}$ and $a_{\text{pow}} = 3.5$) for pure Astronomical Silicates (Draine 2003). Although we do not use such a dust size distribution in our disk model the results are shown for reference. A comparison with Fig. 6 of Draine (2003) shows that our results are in good qualitative agreement with their results. However, Draine (2003) considered two individual dust populations with different dust compositions and size distribution: Astronomical Silicates and very small carbonaceous grains, the latter are not considered here. As a consequence the carbon absorption edge at around 0.3 eV is missing in our MRN dust model.

Fig. 4 clearly shows that for energies below 1 keV the gas is the main opacity source even for the case of small grains. For higher energies dust becomes the dominant opacity source in the X-ray regime. However, considering a dust size distribution more typical for protoplanetary disks ($a_{\min} = 0.05 \mu\text{m}$, $a_{\max} = 3000 \mu\text{m}$ and $a_{\text{pow}} = 3.5$), the dust extinction becomes only important for energies $\geq 4 \text{keV}$. However, Fig. 4 also shows that the dust scattering cross-section is significantly reduced if the g factor approximation is applied. The scattering phase function for dust is strongly forward peaked resulting in a g factor very close to unity (i.e. small scattering angle Draine 2003). The main consequence is that dust scattering is insignificant for disks as it does not produce a diffuse radiation field as most photons are simply forward scattered (Bethell & Bergin 2011).

The gas scattering cross-section is nearly independent of energy and becomes the dominant opacity source for energies $E_X \geq 5 \text{keV}$. The scattering phase function of the gas is not

strongly forward peaked as X-ray photons are mainly scattered by the electrons bound to hydrogen or helium. However, there is a slight decrease in the scattering cross-section with energy as Compton scattering becomes more anisotropic for higher energies, and in our simplified model this results in a reduced scattering cross-section.

We note that in our model the dust is simply an additional opacity source and we neglect actually any real interaction of X-rays with the dust, such like ionization or heating. The interaction of X-rays with solids is a very complex process (see e.g. Dwek & Smith 1996). Besides heating (e.g. Laor & Draine 1993) and ionization (Weingartner & Draine 2001), recent experiments indicate also possible dust amorphization by soft and hard X-rays (Ciaravella et al. 2016; Gavilan et al. 2016). However, we focus here on the X-ray ionization of the gas component and a detailed investigation of the impact of X-rays on the dust component is out of the scope of this paper.

2.3.4. Stellar X-rays

To model the X-ray emission of T Tauri stars we assume that the origin of the emission is close to the stellar surface (see e.g. Ercolano et al. 2009) and place the source of the emission on the star. The spectral shape of the emission is modeled with an isothermal bremsstrahlung spectrum (Glassgold et al. 2009; Aresu et al. 2011) of the form

$$I(E) \propto \frac{1}{E} \cdot \exp\left(-\frac{E}{kT_X}\right). \quad (4)$$

Where E is the energy in keV, I is the intensity, k is the Boltzmann constant and $T_X = 2 \times 10^7 \text{K}$ is the plasma temperature. We considered a X-ray energy range of 0.1 – 20 keV for the stellar spectrum. The spectrum is normalized to a given total X-ray luminosity L_X in the range of 0.3 – 10 keV as such an energy range is typical for reported observed X-ray luminosities (e.g. Güdel et al. 2007a).

We note that it is also possible to use a more realistic thermal line plus continuum X-ray spectrum as input in PRODIMO (see Woitke et al. 2016). However, as we do not model here a particular source we use Eq. 4, which is a reasonable approximation for the general shape of observed X-ray spectra (Glassgold et al. 2009; Woitke et al. 2016).

Ch. Rab et al.: X-ray radiative transfer in protoplanetary disks

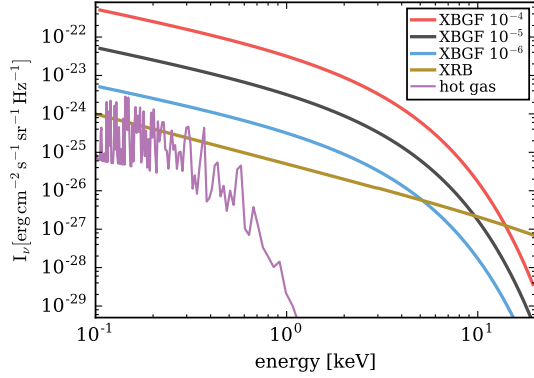


Fig. 5. X-ray background field spectra. The black solid line shows a cluster X-ray background field as proposed by Adams et al. (2012) with a flux of $2 \times 10^{-5} \text{ erg cm}^{-2} \text{ s}^{-1}$ modelled with a bremsstrahlung spectrum with $T_X = 2 \times 10^7 \text{ K}$. The red and blue solid lines are for fluxes ten times higher and lower, respectively. For comparison we also show the diffuse extragalactic X-ray background field (XRB, brown solid line) using the fits described in Fabian & Barcons (1992) and a hot gas spectrum (magenta line) from e.g. Supernova remnants (see Tielens 2005 chap. 1, Slavin & Frisch 2008).

2.3.5. X-ray background field

A star embedded in a young cluster likely receives X-ray radiation from the other cluster members. In Adams et al. (2012) typical flux values for such a cluster X-ray background field (XBGf) are derived, where the values depend on the cluster properties (e.g. number of cluster members) and the position of the considered target within the cluster. Such a cluster background field is probably one to two orders of magnitude stronger than the diffuse extragalactic background field (Adams et al. 2012).

In Adams et al. (2012) only the total flux or energy averaged values of the XBGf are considered and now detailed X-ray radiative transfer method is applied. Here we included the XBGf in the energy dependent X-ray radiative transfer module. To do this we modelled the spectrum of the background field in the same way as the stellar X-ray spectrum. We used an isothermal bremsstrahlung spectrum (Eq. (4)) with $T_X = 2 \times 10^7 \text{ K}$ ($kT_X \approx 1.7 \text{ keV}$) and normalized the spectrum to the given total flux in the energy range of $0.1 - 20 \text{ keV}$. We assumed that the disk is irradiated isotropically by the XBGf.

Adams et al. (2012) estimated a characteristic flux level for a cluster X-ray background field (XBGf) of $F_{\text{XBGf}} = 1 - 6 \times 10^{-5} \text{ erg cm}^{-2} \text{ s}^{-1}$. As discussed by Adams et al. (2012) variations from cluster to cluster and also between single cluster members (i.e. location within the cluster) can be significant. Therefore we consider here flux levels for the XBGf in the range of $F_X = 2 \times 10^{-6} - 2 \times 10^{-4} \text{ erg cm}^{-2} \text{ s}^{-1}$, including the benchmark value of 2×10^{-5} from Adams et al. (2012). These values roughly cover the width of the X-ray background flux distributions derived by Adams et al. (2012). We note that we considered here a slightly wider X-ray energy range as Adams et al. (2012), who used $0.2 - 15 \text{ keV}$. Therefore the given total flux levels differ slightly, for example $F_X(0.1 - 20 \text{ keV}) = 2 \times 10^{-5} \text{ erg cm}^{-2} \text{ s}^{-1}$ corresponds to $F_X(0.2 - 15 \text{ keV}) \approx 1.4 \times 10^{-5} \text{ erg cm}^{-2} \text{ s}^{-1}$.

Adams et al. (2012) assumes that there is no absorption of X-rays within the cluster. However, absorption of soft X-rays ($E \lesssim 1 \text{ keV}$) is possible, either by material between the star and the disk (see Ercolano et al. 2009) or the interstellar medium itself. To account for such a scenario in a simple way we also

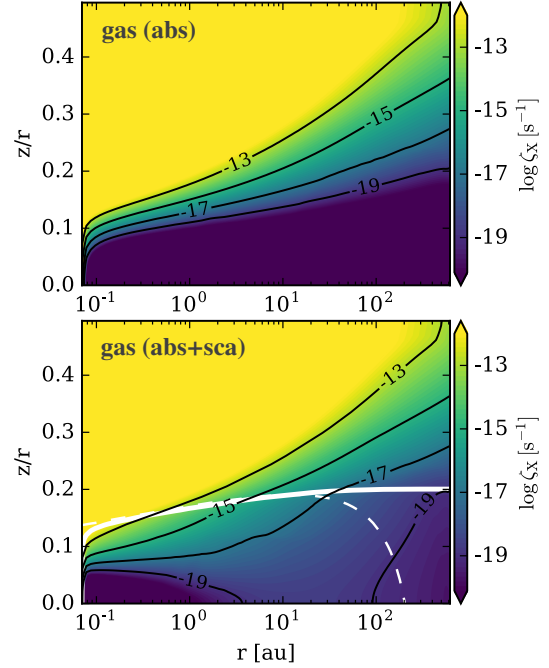


Fig. 6. X-ray ionization rate ζ_X for the 2D disk structure. The top panel shows a model with only gas absorption the bottom panel a model with gas absorption and scattering. The white solid contour line shows $N_{\text{(H),rad}} = 2 \times 10^{24} \text{ cm}^{-2}$, which corresponds roughly to the X-ray scattering surface. Below this surface ζ_X starts to be dominated by scattered X-ray photons. The white dashed line shows $N_{\text{(H),ver}} = 2 \times 10^{22} \text{ cm}^{-2}$.

used input spectra with low-energy cut-offs of 0.3 and 1 keV , respectively (see Sect. 3.2.2).

In Fig. 5 we show our XBGf spectra and additionally the spectrum measured for the diffuse extragalactic background field (Fabian & Barcons 1992) and a “hot gas” spectrum (e.g. produced by supernova remnants Tielens 2005). This figure shows that typically the cluster XBGf will dominate the X-ray background flux impinging on the disk.

3. Results

Our results are presented in the following way. In Sect. 3.1 we show the impact of scattering, dust opacities and X-ray background fields on the X-ray disk ionization rate ζ_X . In Sect. 3.2 we present the molecular column densities of HCO^+ and N_2H^+ for our three different dust models and for models with and without X-ray background fields.

3.1. X-ray disk ionization rates

In PRODIMO the X-ray ionization rate is calculated individually for the single atoms and molecules (see Meijerink et al. 2012 for details). ζ_X used in the following is simply the sum of the ionization rates of atomic and molecular hydrogen (we use a similar definition as Ádámkóvics et al. 2011). We note that we define ζ_X per hydrogen nucleus, which is a factor of two lower compared to the ionization rate per molecular hydrogen. For all models discussed in this section $L_X = 10^{30} \text{ erg s}^{-1}$, if not noted otherwise.

A&A proofs: manuscript no. xrt

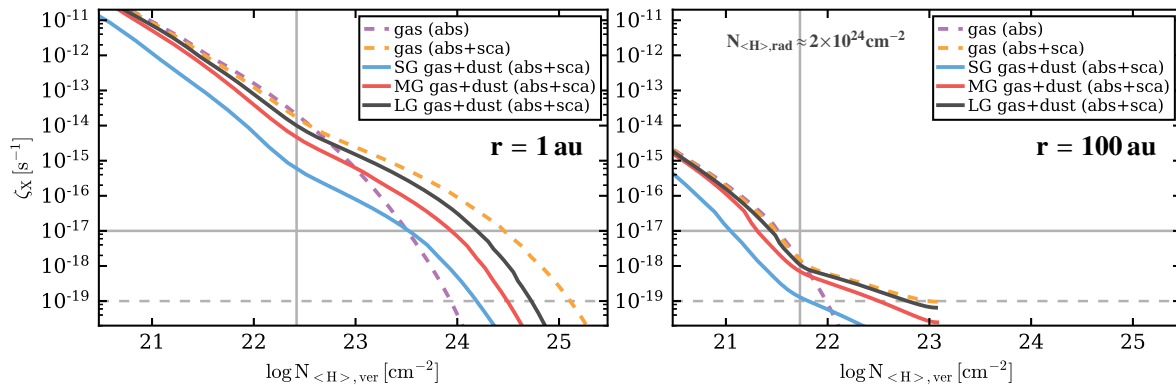


Fig. 7. X-ray ionization rate ζ_X versus vertical column density $N_{(H),ver}$ at disk radii of 1 au (left panel) and 100 au (right panel), respectively. The dashed lines show models with X-ray gas opacities only, where the purple line is for pure absorption and the orange line for absorption plus scattering. The solid lines are for models including X-ray dust opacities (absorption+scattering), where results for the small grains (SG, blue), medium grains (MG, red) and large grains (LG, black) dust models are shown. The vertical grey line in both plots indicates the scattering surface at $N_{(H),rad} = 2 \times 10^{24} \text{ cm}^{-2}$ (see also Fig. 6); at the right hand side of this line ζ_X is dominated by scattered high energy photons. The horizontal lines mark the cosmic-ray ionization rates for the ISM ($\zeta_{CR} \approx 10^{-17}$), and low cosmic-ray case ($\zeta_{CR} \approx 10^{-19} \text{ s}^{-1}$).

3.1.1. Scattering of stellar X-rays

X-ray scattering is already a quite common ingredient in protoplanetary disk modelling codes (e.g. Igea & Glassgold 1999; Nomura et al. 2007; Cleeves et al. 2013a; Ercolano et al. 2008a). However, it was not yet shown in detail in which regions of the disk X-ray scattering is actually relevant for ζ_X and disk chemistry.

In Fig. 6 we show ζ_X for the whole 2D disk structure for a model with X-ray gas absorption only and a model including scattering. In these models dust is not considered as a X-ray opacity source. The same models are also included in Fig. 7 where ζ_X is plotted as a function of vertical hydrogen column density $N_{(H),ver}$ at radii of 1 and 100 au distance from the central star.

Due to the nearly energy independent scattering cross-section of the gas component it is possible to define a single scattering surface in the disk for the whole X-ray energy range. A scattering optical depth of unity is reached at a hydrogen column density of $N_{(H)} \approx 2 \times 10^{24} \text{ cm}^{-2}$ (see Fig. 4 and Igea & Glassgold 1999). For stellar X-rays the radial column density defines the location of the scattering surface in the disk (see Fig. 6). Below the scattering surface the X-ray ionization rate is dominated by scattered X-rays. We want to note that the location of the scattering surface depends on the location of the X-ray source. For example in the model of Igea & Glassgold (1999) the central X-ray source is located $12 R_\odot$ above and below the star. Compared to our model where the X-ray source is the star itself, the scattering surface moves to deeper layers in the disk as the radial column density seen by stellar X-rays is reduced (see also Appendix B). This can cause differences in ζ_X by about an order of magnitude in vertical layers close to the scattering surface (Igea & Glassgold 1999). In terms of vertical column density the scattering surface is located at $N_{(H),ver} \approx 2 \times 10^{22} \text{ cm}^{-2}$ for $r \lesssim 50 \text{ au}$, but drops rapidly to lower vertical column densities due to the disk structure (see Fig. 6).

In Fig. 7, ζ_X is also shown for models with and without scattering. This figure shows that at high column densities, ζ_X is dominated by X-ray scattering, whereas at low column densities, ζ_X is not significantly affected by scattering and is dominated by direct stellar X-rays. The reason is that the scattering

cross-section becomes only comparable to the absorption cross-section for X-ray energies $E \gtrsim 5 \text{ keV}$ (see Fig. 4). This means that mainly the energetic X-ray photons are scattered towards the midplane of the disk, where above the scattering surface ζ_X is dominated by the softer X-rays which are not efficiently scattered.

3.1.2. Impact of dust opacities

In Fig. 8 we show the X-ray ionization rate for models with three different dust size distributions: small grains, medium grains and large grains (see Sect. 2.2.1). In these models both the gas and dust opacities are considered in the X-ray RT, but the X-ray gas opacities are the same in all three dust models. To compare ζ_X to models without X-ray dust opacities they are also included in Fig. 7.

As already mentioned, scattering of X-rays by dust can be neglected due to the strongly forward peaked scattering phase function (see Sect. 2.3.3). As the dust acts only as an additional absorption agent, ζ_X is reduced wherever the dust opacity becomes similar or larger than the gas opacity. This is in particular the case for high X-ray energies (see Fig. 4) but depends on the chosen dust properties. In the case of the small grains, dust absorption dominates the X-ray opacity for X-ray energies $E_X \gtrsim 1 \text{ keV}$. As a consequence ζ_X drops by about an order of magnitude and more, compared to the model with gas opacities only (see Fig. 7). For the medium and large grain models the impact of dust is much less severe. For the medium grains dust extinction becomes relevant for $E_X \gtrsim 3 \text{ keV}$ and for the large grains only for $E_X \gtrsim 10 \text{ keV}$, but in the large grains model, gas extinction remains always higher than dust absorption (see Fig. 4).

Our results imply that dust extinction plays an important role for young disks, whereas for evolved disks with large grains, X-rays can penetrate deeper. In evolved disks only the most energetic X-rays are affected as the gas opacity drops rapidly with energy. Therefore the impact on ζ_X is the largest in the deep, high density, layers of the disk where ζ_X is dominated by high energy X-rays. In young objects, where the disk is still embedded in an envelope, small grains can be important and should be included in X-ray radiative transfer models. We will investigate

Ch. Rab et al.: X-ray radiative transfer in protoplanetary disks

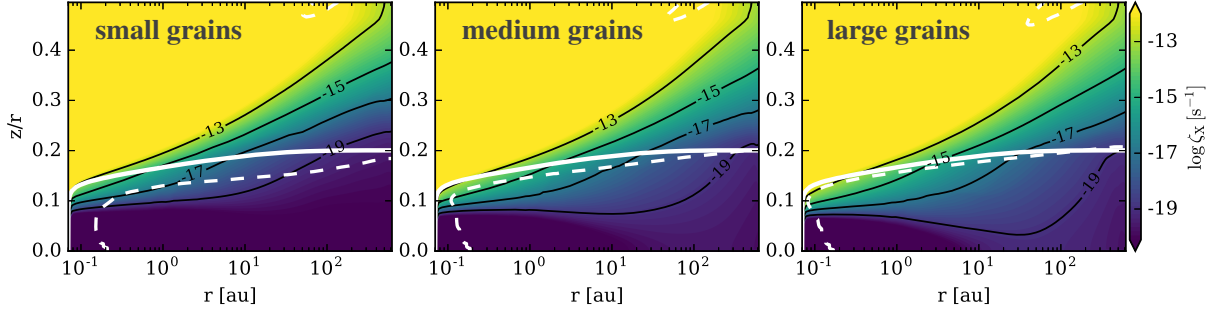


Fig. 8. X-ray ionization rate ζ_X for the three different dust models including X-ray gas and dust opacities and scattering. The white solid contour shows $N_{(\text{H}),\text{rad}} = 2 \times 10^{24} \text{ cm}^{-2}$, which corresponds to the scattering surface. The dashed white contour shows where ζ_X is equal to $\zeta_{X,\text{abs}}$ of the gas absorption only model. Above this line $\zeta_X \leq \zeta_{X,\text{abs}}$ (additional absorption by the dust) below $\zeta_X > \zeta_{X,\text{abs}}$ (scattering).

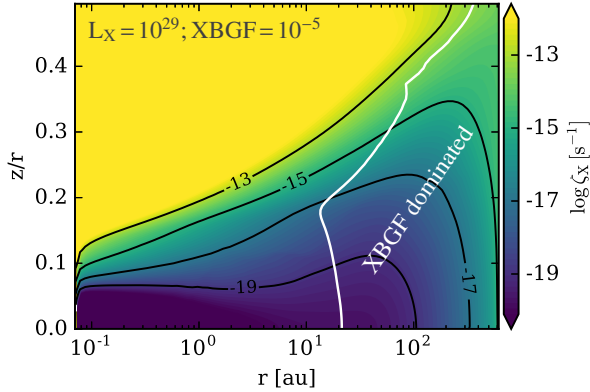


Fig. 9. X-ray ionization rate ζ_X for a model with $L_X = 10^{29} \text{ erg s}^{-1}$ and $F_{\text{XBGF}} = 2 \times 10^{-5} \text{ erg cm}^{-2} \text{ s}^{-1}$ (i.e. the benchmark values of Adams et al. 2012). The white solid contour line encloses the region where the XBGF dominates ζ_X (i.e. $\zeta_{X,\text{XBGF}} \geq \zeta_{X,*}$).

such a scenario based on the Class I PRODiMO model presented in Rab et al. (2017) in a future study.

3.1.3. Impact of X-ray background fields

The importance of X-ray background fields for disks was estimated analytically by Adams et al. (2012). They find that the X-ray background flux can be larger than the stellar X-ray flux for disk radii $r \gtrsim 14 \text{ au}$, assuming a geometrically flat disk and a typical disk impact angle for the stellar radiation. Their estimated radius corresponds to the radius where the stellar and interstellar X-ray flux becomes equal. However, attenuation by the disk itself was not taken into account (i.e. they compared the stellar and background X-ray fluxes at the disk surface).

In Fig. 9 we show ζ_X for our full 2D disk model using $L_X = 10^{29} \text{ erg s}^{-1}$ and an X-ray background flux of $F_{\text{XBGF}} = 2 \times 10^{-5} \text{ erg cm}^{-2} \text{ s}^{-1}$ (these are the values used by Adams et al. 2012 for their benchmark case). We mark the region where the X-ray background field dominates ζ_X (i.e. $\zeta_{X,\text{XBGF}} \geq \zeta_{X,*}$). In the midplane of the disk ($z = 0$) the XBGF dominates for $r \gtrsim 20 \text{ au}$. Assuming a geometrically flat disk, the XBGF dominates in our model for $r \gtrsim 15 \text{ au}$ (we simply projected the smallest radius at the maximum height, where the XBGF dominates, to the midplane). For the same XBGF but $L_X = 10^{30} \text{ erg s}^{-1}$ we find that the XBGF dominates for $r \gtrsim 30 \text{ au}$ for a geometrically

flat disk and $r \gtrsim 45 \text{ au}$ for the midplane of our 2D model. Those radii are consistent with the analytical estimates of Adams et al. (2012).

In Fig. 10 we show ζ_X in the midplane and for a vertical cut at $r = 150 \text{ au}$ for models with different XBGF fluxes and a fixed stellar X-ray luminosity of $L_X = 10^{30} \text{ erg s}^{-1}$. Additionally we show models with a low energy cut-off for the stellar and XBGF spectrum at 0.3 and 1 keV, respectively. With this low energy cut-off we simulate (in a simple way) a possible absorption of the X-rays before they actually impinge on disk. Such an absorption can happen by material close to the star (e.g. accretion columns Grady et al. 2010) for the stellar X-rays and in case of the X-ray background field additional extinction due to the interstellar medium is also possible. The corresponding absorption columns required for those cut-offs are $N_{(\text{H})} \approx 10^{21} \text{ cm}^{-2}$ for 0.3 keV and $N_{(\text{H})} \approx 10^{22} \text{ cm}^{-2}$ for 1 keV (see Fig. 4 and Ercolano et al. 2009).

As seen from the left panel of Fig. 10, ζ_X at the outer radius of the disk can be as high as 10^{-14} s^{-1} but strongly depends on the assumed low energy cut-off. Adams et al. (2012) also estimated ζ_X for their benchmark X-ray background field ($F_{\text{XBGF}} = 2 \times 10^{-5} \text{ erg cm}^{-2} \text{ s}^{-1}$) assuming an average X-ray photon energy of $E_X = 1 \text{ keV}$, they find $\zeta_X = 8 \times 10^{-17} \text{ s}^{-1}$. This is similar to our model with the 0.3 keV low energy cut-off.

The low energy cut-off has no significant impact on the radius down to which the XBGF dominates ζ_X . For this high density regions only the most energetic X-rays, which are not affected by the low energy cut-off, are of relevance. However, as seen from Fig. 10 a possible absorption of the XBGF photons before they reach the disk has a significant impact for radii $r \gtrsim 200 \text{ au}$ and at higher layers of the disk. For the 1 keV-cut-off ζ_X can be lower by more than an order of magnitude compared to the reference model with a minimum X-ray energy of 0.1 keV.

More important than the value of ζ_X at the outer disk radius is the value at higher densities where the actual emission from molecular ions originates. From Fig. 10 we can see that ζ_X drops already below the ISM cosmic-ray ionization rate at $r \approx 200 \text{ au}$ even for the strongest XBGF considered. However, for the low cosmic-ray case the XBGF can be the dominant high energy ionization source in the midplane for radii as small as $r \approx 50 \text{ au}$. This is also seen in the right panel of Fig. 10, depending on the XBGF flux ζ_X can reach values around $5 \times 10^{-18} \text{ s}^{-1}$ close to the midplane of the disk at $r = 150 \text{ au}$.

A&A proofs: manuscript no. xrt

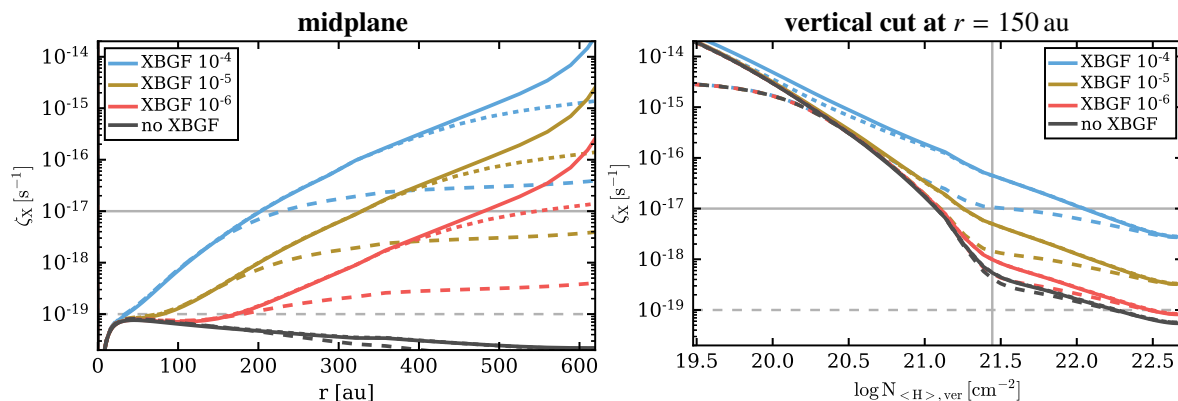


Fig. 10. X-ray ionization rate in the midplane (left panel) and for a vertical cut at $r = 150$ au (right panel) for models with fixed stellar X-ray luminosity ($L_X = 10^{30}$ erg s^{-1}) but varying X-ray background fields with fluxes of 2×10^{-4} (blue), 2×10^{-5} (brown) and 2×10^{-6} erg $cm^{-2} s^{-1}$ (red); the black lines are for the model without an XBGf. The solid lines are for the full X-ray spectra (0.1 – 20 keV); the dotted and dashed lines correspond to models with a low-energy cut-off of at 0.3 keV and 1 keV, respectively. The horizontal lines mark the cosmic-ray ionization rates for the ISM ($\zeta_{CR} \approx 10^{-17}$), and low cosmic-ray case ($\zeta_{CR} \approx 10^{-19}$ s $^{-1}$). In the right panel the vertical grey solid line indicates the scattering surface at $N_{(H),rad} = 2 \times 10^{24}$ cm $^{-2}$ (see also Fig. 7).

3.2. Molecular ion column densities

In this Section we show results for the radial column density profiles of the disk ionization tracers HCO^+ and N_2H^+ . We use these two molecules because they are the most commonly detected molecular ions in disks (e.g. Thi et al. 2004; Dutrey et al. 2007; Öberg et al. 2011a; Guilloteau et al. 2016) and because they trace different regions in the disk.

HCO^+ and N_2H^+ are mainly formed via proton exchange of H_3^+ with CO and N_2 , respectively. The main destruction pathway is dissociative recombination with free electrons, where the metals (e.g. sulphur) play a significant role as additional electron donors (e.g. Graedel et al. 1982; Teague et al. 2015; Kamp et al. 2013; Rab et al. 2017). HCO^+ and N_2H^+ are sensitive to high energy ionization sources such as X-rays and cosmic-rays, because the formation of H_3^+ involves the ionization of H_2 (15.4 eV ionization potential).

Besides free electrons another efficient destruction pathway for N_2H^+ and HCO^+ are ion-neutral reactions. N_2H^+ is efficiently destroyed by CO and therefore resides mainly in regions where gas phase CO is depleted (e.g. frozen-out). This makes it a good observational tracer of the CO ice line in disks (e.g. Qi et al. 2013; Aikawa et al. 2015; van't Hoff et al. 2017). In case of HCO^+ , gas phase water is the destructive reaction partner. Observations of protostellar envelopes indicate that HCO^+ is indeed sensitive to the water gas phase abundances (e.g. Jørgensen et al. 2013; Bjerkeli et al. 2016; van Dishoeck et al. 2014). In disks this is more difficult to observe, due to the more complex structure and because the water snow line in disks is located at much smaller radii ($r \approx 1$ au for a T Tauri star) compared to CO ($r \approx 20$ au). However, HCO^+ follows mainly the distribution of gas phase CO in the disks, whereas N_2H^+ traces regions where CO is frozen-out (i.e. where the temperature is $\lesssim 25$ K).

For the abundance of the molecular ions also the so called sink-effect for CO and N_2 is of relevance. The main mechanism of the sink-effect is the conversion of CO and N_2 to less volatile species which freeze-out at higher temperatures or remain on the dust grains. This can happen via surface chemistry and/or via dissociation of neutral molecules by He^+ (e.g. Aikawa et al. 1996; Bergin et al. 2014; Cleaves et al. 2015; Helling et al. 2014; Furuya & Aikawa 2014; Reboussin et al. 2015; Aikawa et al.

2015). The main consequence of the sink-effect is the depletion of gas phase CO and N_2 in regions with temperatures above their respective sublimation temperatures. However, the efficiency of the sink-effect is not very well understood as it depends on various chemical parameters (see Aikawa et al. 2015 for more details). In our model only the He^+ sink-effect is considered.

Our model also includes excited H_2 chemistry that opens up another formation pathway for HCO^+ . This formation pathway can be important close to the $C^+/C/CO$ transition (see Greenwood et al. 2017 and Appendix C). The relevance of this pathway will be discussed later on.

The typical abundance structure for HCO^+ and N_2H^+ in our reference model is presented in Rab et al. (2017). Here we focus on the radial column densities because they can be more easily compared to observations and other thermo-chemical disk models.

3.2.1. Impact of dust grain size distributions on chemistry

In Fig. 11 we show the molecular ion column densities N_{HCO^+} and $N_{N_2H^+}$ for the three different dust models, small grains (SG), medium grains (MG) and large grains (LG) described in Sect. 2.2.1. For each dust model also both cases of cosmic-ray ionization rates, low and ISM cosmic rays are shown (Sect. 2.2.2). Further we show models with and without X-ray dust opacities. All models shown in Fig. 11 have $L_X = 10^{30}$ erg s^{-1} and no X-ray background field.

It is clearly seen in Fig. 11 that neither for the medium grains nor for large grains the inclusion of X-ray dust opacities has a significant impact on the molecular ion column densities. Only for N_2H^+ a slight decrease on the column density can be seen in the models with low cosmic rays (e.g. compare model MG gas with MG gas+dust). The column densities are not significantly affected by including X-ray dust opacities as the strongest impact of the dust on ζ_X is limited to regions close to the midplane (see Fig. 7). There CRs mostly dominate the molecular ion abundances as the X-ray ionization is typically $\zeta_X \lesssim 10^{-19}$ s $^{-1}$, even if dust opacities are not included. Further the contribution to the molecular ion column densities from regions close to the midplane is limited as the parent molecules of the ions are frozen

Ch. Rab et al.: X-ray radiative transfer in protoplanetary disks

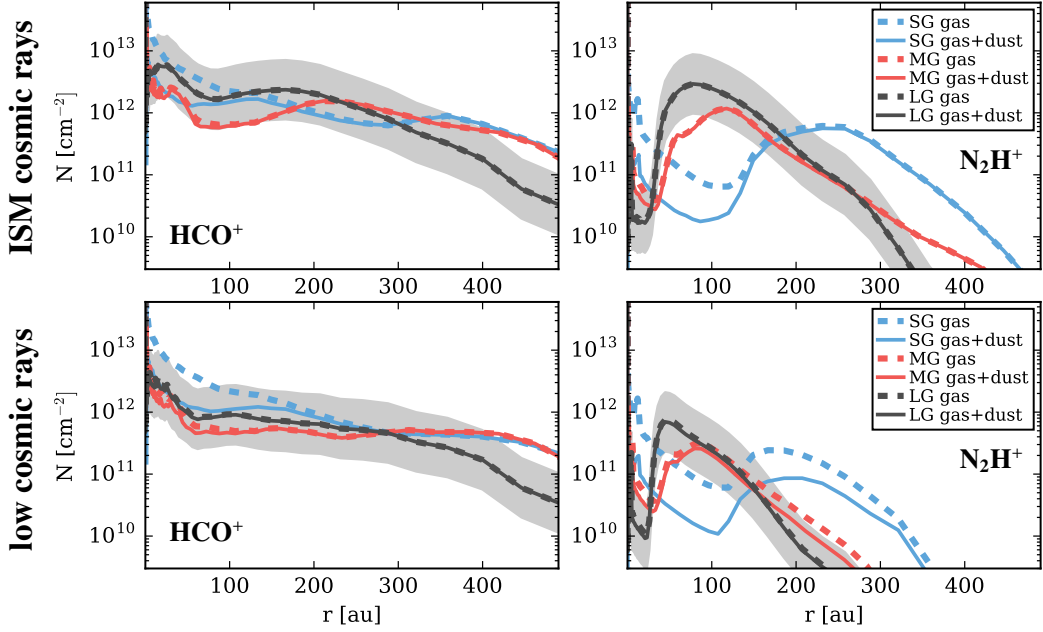


Fig. 11. HCO^+ (left column) and N_2H^+ (right column) radial column density profiles for models with different dust size distributions: small grains (SG, blue), medium grains (MG, red) and large grains (LG, black). The dashed lines are for models where only the gas component is considered in the X-ray RT, where the solid lines show models where both X-ray gas and dust opacities are included. The ISM cosmic-ray models are shown in the top row, the low cosmic-ray models in the bottom row. The grey shaded area marks a difference of a factor three in N with respect to the reference model (LG gas+dust).

out anyway. The situation is different for the SG model, where ζ_X is affected by the dust at all disk layers (see Fig. 7) and N_{HCO^+} and $N_{\text{N}_2\text{H}^+}$ can drop by factors of three to ten. This shows that it is justified, in case of HCO^+ and N_2H^+ , to neglect X-ray dust opacities for evolved disk dust populations but not necessarily for ISM like dust.

Fig. 11 also shows that, independent of the X-ray dust opacities, the dust grain size distributions themselves have a significant impact on the molecular column densities. In the SG model the gas disk is more efficiently shielded from the stellar and interstellar UV radiation field but also the total dust surface per hydrogen nucleus increases significantly (see Table 2). This has mainly two consequences:

Firstly, the ionization of metals such as carbon and sulphur is significantly reduced. This causes a decrease in the number of free electrons available for the dissociative recombination with molecular ions. On the other hand the impact of the dust opacities on the X-ray disk radiation field (and on ζ_X) is less significant (SG model), or not significant at all (MG and LG model) compared to the impact of the dust on the UV radiation field. Consequently the abundance of the molecular ions increases in regions which are efficiently shielded from the UV radiation fields by the presence of small grains.

Secondly, the freeze-out and the sink-effect become more important if the total dust surface increases. This reduces the abundance of molecular ions in high density regions that are efficiently shielded from UV radiation (i.e. no photo-desorption).

These effects are best seen for $N_{\text{N}_2\text{H}^+}$. Compared to the LG model, in the SG model the abundance of N_2H^+ is reduced close to the midplane of the disk due to the sink-effect and freeze-out (i.e. lower gas phase abundance of the parent molecule N_2) but increases in the outer and upper layers of the disk due to the

shielding of the UV radiation by small grains (i.e. lower abundance of metal ions). This results in a shift of the $N_{\text{N}_2\text{H}^+}$ peak to larger radii ($r \approx 150 - 200$ au), and the peak is not tracing the radial CO ice line anymore (which is at $r \approx 45$ au in the SG model). For radii $r \lesssim 150$ au, $N_{\text{N}_2\text{H}^+}$ is now dominated by the N_2H^+ layer just below the $\text{C}^+/\text{C}/\text{CO}$ transition where the X-ray ionization rate is high enough so that N_2H^+ survives also in layers with gas phase CO (see Aikawa et al. 2015; van't Hoff et al. 2017; Rab et al. 2017). In contrast to the LG grain model, $N_{\text{N}_2\text{H}^+}$ in the SG model can reach comparable or even higher values in the inner disk ($r \lesssim 100$ au) compared to the peak value around $r \approx 150 - 200$ au.

Aikawa et al. (2015) also used two different dust size distributions (ISM like and large grains) for their detailed study on N_2H^+ in protoplanetary disks. Their resulting column density profiles are very similar to what is shown in Fig. 11. In the chemical models of Dutrey et al. (2007) for DM Tau and LkCa 15 the peak in their $N_{\text{N}_2\text{H}^+}$ profiles are at very large radii ($r \gtrsim 400$ au), which is likely due to their assumed single grain size of $0.1 \mu\text{m}$. Cleevess et al. (2015) used a reduced dust surface area, compared to $0.1 \mu\text{m}$ grains, to model $N_{\text{N}_2\text{H}^+}$ for TW Hya, however they also required a lower cosmic-ray ionization rate ($\zeta_{\text{CR}} \approx 10^{-19} \text{s}^{-1}$) to match the observed sharp peak in $N_{\text{N}_2\text{H}^+}$, located close to the CO ice line. A lower cosmic-ray ionization rate decreases the efficiency of the He^+ sink-effect. A strong impact of the low-cosmic ray ionization rate on the $N_{\text{N}_2\text{H}^+}$ peak is not really seen in our models or in the models of Aikawa et al. (2015). This might be caused by differences in the time-scales for the sink-effect (Bergin et al. 2014). In our LG model, steady-state for $N_{\text{N}_2\text{H}^+}$ is already reached at a chemical age of approximately 1 Myr (see Rab et al. 2017). For the SG models a time-dependent test run with ISM cosmic rays showed that steady-state is only

reached after 2 – 3 Myr in regions around the radial CO ice line, whereas at ≈ 1 Myr the $N_{\text{N}_2\text{H}^+}$ peak is still tracing the radial CO ice line.

Despite the differences in the various chemical models, they all indicate that the sink-effect plays a crucial role for the shape of the N_2H^+ radial column density profile. Further, only models accounting for dust growth are able to reproduce a sharp peak in the $N_{\text{N}_2\text{H}^+}$ profile near the radial CO ice line as is observed for TW Hya (Qi et al. 2013, but see also Aikawa et al. 2015; van't Hoff et al. 2017 for a discussion on the robustness of $N_{\text{N}_2\text{H}^+}$ as a CO ice line tracer). This is consistent with dust observations clearly indicating grain growth and dust settling in disks (e.g. Andrews & Williams 2005; Pinte et al. 2016). In any case the chemical modelling results for $N_{\text{N}_2\text{H}^+}$ indicate that N_2H^+ is not only a tracer of the radial CO ice line but also for dust evolution in disks.

3.2.2. Impact of X-ray background fields on chemistry

To show the impact of X-ray background fields (XBGF) on the molecular column densities we compare in Fig. 12 models with $L_X = 10^{30} \text{ erg s}^{-1}$ but varying XBGF fluxes, including models with a low-energy cut-off for the X-rays of 0.1 and 1 keV, respectively. For each of these models the results for low and ISM cosmic-rays are shown. For all models the large grains dust model is used.

For the case of the ISM cosmic-ray ionization rate the impact of the XBGF on the column densities is limited. Only for models with the highest XBGF flux of $2 \times 10^{-4} \text{ erg cm}^{-2} \text{ s}^{-1}$ the column densities increase by more than a factor of three for radii $r \gtrsim 250$ au. Although the XBGF dominates the X-ray ionization rate down to $r \approx 20$ au, $\zeta_X > \zeta_{\text{CR}}$ is true only for $r \gtrsim 200$ au, and only for the case of the strongest XBGF (see Fig. 10).

The impact of the XBGF is much larger in the case of a low CR ionization rate. In that case the molecular ion column densities are generally lower compared to ISM CRs and the relative impact of the XBGF increases. However, the impact on N_{HCO^+} remains limited; only for the strongest XBGF, N_{HCO^+} increases by about a factor of five at most. For $N_{\text{N}_2\text{H}^+}$ the picture is quite different. Due to the low CRs the column densities for $r \gtrsim 200$ au are reduced by more than an order of magnitude compared to the ISM CRs models. In these regions the XBGF is now most effective and consequently $N_{\text{N}_2\text{H}^+}$ increases significantly. For the strongest XBGF $N_{\text{N}_2\text{H}^+}$ increases by up to two orders of magnitude for $r \gtrsim 200$ au and reaches levels similar to the ISM CR models. The reason why N_2H^+ is more sensitive to the high-energy ionization sources is its location in the disk. Compared to HCO^+ , N_2H^+ is mainly located in deeper layers of the disk; below the CO ice line. In those layers, the ionization balance is mostly dominated by molecular ions, as the ionization of atomic metals by UV becomes less important.

In the models with a low-energy cut-off at 1 keV for the X-ray spectra, HCO^+ is not affected by the XBGF even in the low CR model. Also the impact on $N_{\text{N}_2\text{H}^+}$ is now weaker. $N_{\text{N}_2\text{H}^+}$ is typically a factor of a few up to an order of magnitude lower compared to the models with a cut-off at 0.1 keV. Although we use the low-energy cut-off also for the stellar X-rays, such a drop in the column densities is not seen in the models without XBGFs. The reasons are the geometrical dilution of the stellar X-ray radiation and that the stellar X-rays have to penetrate the high radial and vertical column densities in the inner disk. The XBGF irradiates the disk isotropically and only has to penetrate the low column densities of the outer disk. Therefore also the low-energy

X-rays can penetrate larger areas of the disk and have more impact on ζ_X in disk regions relevant for the molecular ions.

For HCO^+ we actually also see a drop in the column density for $r \gtrsim 400$ au for the strongest XBGF. The reason for this is a lower CO abundance caused by X-ray photo-dissociation which is also included in our chemistry model. The CO abundance at $r \gtrsim 450$ au drops by factors of approximately three to five down to heights of $z \approx 20$ au, which results in a drop of the HCO^+ abundance by nearly an order of magnitude. The situation is similar for N_2 and N_2H^+ , however the abundance of N_2H^+ is already below 10^{-12} .

As noted (Sect. 3.2) our model includes also chemistry of excited molecular hydrogen H_2^* . This opens up a formation channel for HCO^+ via the ion-neutral reaction of H_2^* with C^+ (see Appendix C for details). In the inner disk this reaction is only effective in a very thin layer at the $\text{C}^+/\text{C}/\text{CO}$ transition. However, in the outer disk for $r \gtrsim 300$ au this reaction becomes significant, as the $\text{C}^+/\text{C}/\text{CO}$ transition is not as sharp as in the inner disk. If this reaction is deactivated, we find that for such a model the slope of N_{HCO^+} for $r > 300$ au becomes steeper. However, our findings concerning the impact of XBGFs are not significantly affected, N_{HCO^+} becomes slightly more sensitive to XBGFs for $r \gtrsim 300$ au and X-ray photo-dissociation becomes less significant for N_{HCO^+} at large radii where N_{HCO^+} drops below 10^{10} cm^{-2} ($r \approx 400$ au). The results for N_2H^+ are not affected by H_2^* chemistry.

4. Discussion

4.1. Observational implications of X-ray background fields

Our results indicate that the molecular ion column densities in the outer disk are sensitive to X-ray background fields. At least for N_2H^+ the effect on the column density can be strong enough to be observable with modern (sub)millimetre telescopes like ALMA (Atacama Large Millimeter Array), NOEMA (NOthern Extended Millimeter Array) and SMA (Submillimeter Array). However, our results also show that certain conditions such as a strong XBGF and low CR ionization rates are required.

The typical value for the X-ray background flux in young embedded clusters of $2 \times 10^{-5} \text{ erg cm}^{-2} \text{ s}^{-1}$ corresponds to cluster member sizes with $N < 3000$, typical for clusters in the solar vicinity (Adams et al. 2012). However, this value drops to $\lesssim 10^{-5} \text{ erg cm}^{-2} \text{ s}^{-1}$ for smaller clusters with $N \approx 100$, which is more typical for the Taurus star formation region; the X-ray XEST survey detected 136 X-ray sources (Güdel et al. 2007a). A typical disk in Taurus would only be affected by an XBGF if it is shielded efficiently from cosmic-rays (see Fig. 12). However, even in a small cluster some of the sources might experience a higher X-ray background flux depending on their location within the cluster (e.g. closer to the cluster center, see Adams et al. 2012). To identify such sources a large sample of spatially resolved N_2H^+ observations (see below) would be required. The current number of N_2H^+ detections in protoplanetary disk is less than ten (Dutrey et al. 2014) and it is therefore not surprising that signatures of XBGF have not been found yet.

Due to the rather poor knowledge concerning the impact of individual high-energy ionization sources on disk chemistry (see e.g. Rab et al. 2017) and as can only the stellar X-ray luminosity can be measured, it will be certainly challenging to discriminate the influence of XBGFs from the stellar high-energy ionization sources (X-rays and stellar energetic particles), cosmic-rays and radionuclide ionization. However, all these ionization sources are different in the way they irradiate the disk.

Ch. Rab et al.: X-ray radiative transfer in protoplanetary disks

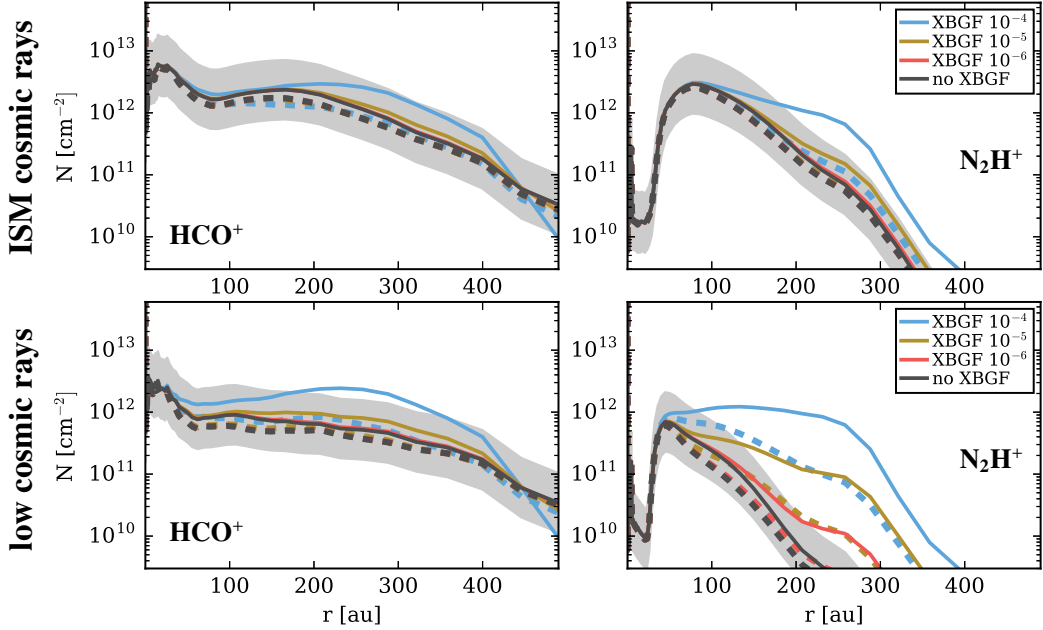


Fig. 12. Radial column density profiles for HCO^+ and N_2H^+ with (coloured lines) and without (black lines) XBGF for the ISM (top row) and low (bottom row) cosmic-ray case. The dashed lines are for models with a low-energy cut-off of the X-ray spectra (stellar and XBGF) of 1 keV, for the solid lines the lowest X-ray energy is 0.1 keV. The grey shaded area marks a factor of three difference in N with respect to the models without XBGF (the solid black line).

The stellar high energy ionization sources have less impact on the outer disk; they need to penetrate the high densities in the inner disk and also experience geometric dilution as they irradiate the disk as a point source (see also Rab et al. 2017). Cosmic rays irradiate the disk isotropically and therefore have an impact on the whole disk. Due to their high energies, CRs are only significantly absorbed in the inner disk ($r \lesssim 10$ au) and provide therefore a nearly constant H_2 ionization rate for the bulk of the disk material (this is similar for radionuclide ionization). In contrast to CRs, the XBGF experiences significant absorption by the disk material even in the outer disk. Those differences result in different shapes of the N_2H^+ radial column density profiles as is seen in Fig. 12. XBGFs make the profile shallower as the impact on the molecular column densities decreases for smaller disk radii (measured from the star). In contrast, a change in the CR ionization rate affects the radial column density profile at all radii.

In any case modelling of spatially resolved N_2H^+ observations of disks are required to discriminate the contribution of XBGF to disk ionization. Such observations for T Tauri disks are still rare (Dutrey et al. 2007; Qi et al. 2013) but certainly will become more common in the near future due to the significant advances, in particular in terms of spatial resolution, of modern (sub)mm interferometers.

4.2. UV background fields and external photo-evaporation

For all models presented here we assumed the canonical value for the interstellar UV radiation of $\chi^{\text{ISM}} = 1$ (in units of the Draine field). This is a reasonable assumption for low-mass star formation regions as an enhanced UV background field would be mostly produced by massive stars with spectral type O, B and A. In contrast to the UV field, the X-ray background field

is mainly produced by X-ray emission of solar-like low mass stars (see Adams et al. 2012). However, a presence of an enhanced UV background field certainly has an impact on the outer disk due to photo-dissociation of molecules, photo-desorption of ices and photo-ionization of metals (see e.g. Teague et al. 2015). These processes will reduce the abundances of molecular ions in the outer disk as their parent molecules are dissociated and metals like carbon and sulphur are ionized and will therefore dominate the ionization balance. Consequently, the presence of an enhanced UV background field will lower the impact of the XBGF on the outer disk molecular abundances. In high-mass star formation regions like Orion with UV background fields up to $\chi^{\text{ISM}} \approx 10^4$, most likely the UV field will completely dominate the chemistry in the outer disk (Walsh et al. 2013; Antonellini et al. 2015).

There is evidence that already weak UV background fields $\chi^{\text{ISM}} \gtrsim 4$ can drive photo-evaporation of the outer disk (Haworth et al. 2017, but see also Adams 2010; Williams & Cieza 2011). Such a process is not included in our model. However, we do not expect a huge impact of photo-evaporation on our results. For the X-ray RT mainly the column density matters that photons have to penetrate until they reach the regions of the disk where the molecular ions become abundant. These column densities are not significantly affected if parts of the outer disk material would slowly drift radially outwards.

On the other hand XBGFs can act as an additional heating source for the outer disk and therefore could contribute to external disk photo-evaporation. We find that only the strongest X-ray background field with $F_{\text{XBGF}} = 2 \times 10^{-4} \text{ erg cm}^{-2} \text{ s}^{-1}$ has a significant impact on the gas temperature in our models. In the midplane of the disk at $r \approx 500$ au ($n_{\text{H}} \approx 4 \times 10^5 \text{ cm}^{-3}$), the gas temperature increases from about $T_{\text{g}} \approx 24$ K to $T_{\text{g}} \approx 36$ K, where for the canonical XBGF we find only an increase of about 2 K

A&A proofs: manuscript no. xrt

(always $\chi^{\text{ISM}} = 1$ is used). Those gas temperatures are lower than the typical temperatures reported by [Facchini et al. \(2016\)](#) derived from hydrodynamical disk photo-evaporation models with $\chi^{\text{ISM}} \geq 30$. This indicates that in the presence of a modestly enhanced UV background field, XBGFs would play a rather minor role for external disk photo-evaporation. However, a more detailed investigation of the possible importance of XBGFs for external disk photo-evaporation is required to be more quantitative.

5. Summary and conclusions

We introduced a new X-ray radiative transfer module for the radiation thermo-chemical disk code PRODiMO. This new module includes X-ray scattering and a detailed treatment of X-ray dust opacities, which can be applied to different dust compositions and dust size distributions. We investigated the importance of X-ray scattering, X-ray dust opacities and X-ray background fields of embedded young clusters for the X-ray ionization rates by means of a representative T Tauri protoplanetary disk model. Further, we studied the impact of X-ray background fields on the disk chemistry, where we used the observed disk ionization tracers HCO^+ and N_2H^+ . Our main conclusions are:

- Inclusion of Compton scattering in X-ray disk radiative transfer increases the X-ray ionization rate by several orders of magnitude in the midplane of the disk. However, in layers above the scattering surface ($N_{(\text{H}),\text{rad}} \approx 2 \times 10^{24} \text{ cm}^{-2}$ and $N_{(\text{H}),\text{ver}} \approx 2 \times 10^{22} \text{ cm}^{-2}$ for $r \lesssim 100 \text{ au}$) the X-ray ionization rate is not significantly affected by scattering as only high energy X-ray photons ($E_X \gtrsim 5 \text{ keV}$) are scattered efficiently towards the midplane (see Fig. 6). Therefore in the upper layers of the disk the X-ray ionization rate is dominated by direct stellar X-ray radiation. Consequently atomic X-ray tracers like neon are not sensitive to X-ray scattering as they typically reside in layers with $N_{(\text{H}),\text{ver}} \lesssim 10^{20} \text{ cm}^{-2}$, well above the scattering surface.
- For evolved dust size distributions (e.g. including grain growth) X-ray opacities are mostly dominated by the gas, only for energies $E_X \gtrsim 5 - 10 \text{ keV}$ dust opacities become relevant. Consequently the disk X-ray ionization rates are only reduced in high density regions close to the midplane if dust opacities are included in the X-ray RT. For ISM like dust size distributions (i.e. maximum grain size $\lesssim 0.1 \mu\text{m}$) the X-ray ionization rate is affected throughout the disk and is reduced by more than an order of magnitude due to efficient absorption of X-rays by the dust.
- For a typical X-ray background flux, as expected for embedded young clusters in the solar vicinity, the XBGF dominates the X-ray ionization rate in the disk down to $r \approx 20 \text{ au}$. This is consistent with the analytical estimates of [Adams et al. \(2012\)](#). However, due to absorption by the disk material, the XBGF ionization rate drops already below the ISM cosmic-ray ionization rate ($\zeta_{\text{CR}} \approx 10^{-17} \text{ s}^{-1}$) at $r \approx 200 - 300 \text{ au}$.
- XBGFs can have a significant impact on the vertical column densities of HCO^+ and N_2H^+ , where N_2H^+ is most sensitive. However, this is only the case for a low cosmic-ray ionization rate $\zeta_{\text{CR}} \approx 10^{-19} \text{ s}^{-1}$, or for XBGF fluxes at least ten times stronger than the typical value. In case of an enhanced UV background field, the outer disk molecular chemistry would be strongly affected due to photo-dissociation and photo-ionization and the impact of XBGFs might become insignificant.
- Our results indicate that for an ordinary disk in a typical low-mass star formation region like Taurus the expected X-ray background flux has likely only little impact on the disk chemistry. However, it is possible that a fraction of the cluster members experience stronger fluxes depending on their location within the cluster.
- The various high energy ionization sources relevant for disk ionization are different in their energetic properties (e.g. X-rays versus cosmic-rays) and in the way they irradiate the disk (e.g. point source versus isotropic irradiation). This makes it possible to discriminate the individual contributions of the various sources, including X-ray background fields, to disk ionization from observations. However, modelling of spatially resolved molecular ion emission is required to achieve this.

With PRODiMO it is now possible to model several high-energy disk ionization processes including cosmic-rays, radionuclide ionization (not presented in this study), stellar energetic particles ([Rab et al. 2017](#)) and X-rays (stellar and interstellar). However, further observational constraints are required to constrain the disk ionization fractions, and to better understand ion chemistry. Besides, a good knowledge of the stellar properties, in particular UV and X-ray radiation, spatially resolved observations of molecular ions such as N_2H^+ and HCO^+ are most crucial. Such observations are still rare but will likely be quite common in the near future due to the modern (sub)millimetre interferometers like ALMA, NOEMA and SMA.

Acknowledgements. We want to thank A. Tielens and J. Slavin for providing the hot gas spectrum shown in Fig. 5. The research leading to these results has received funding from the European Union Seventh Framework Programme FP7-2011 under grant agreement no 284405. CHR and MG acknowledge funding by the Austrian Science Fund (FWF): project number P24790. The computational results presented have been achieved using the Vienna Scientific Cluster (VSC). This publication was supported by the Austrian Science Fund (FWF). This research has made use of NASA's Astrophysics Data System. All figures were made with the free Python module Matplotlib ([Hunter 2007](#)).

References

- Ádámkócs, M., Glassgold, A. E., & Meijerink, R. 2011, *ApJ*, 736, 143
 Adams, F. C. 2010, *ARA&A*, 48, 47
 Adams, F. C., Fatuzzo, M., & Holden, L. 2012, *PASP*, 124, 913
 Aikawa, Y., Furuya, K., Nomura, H., & Qi, C. 2015, *ApJ*, 807, 120
 Aikawa, Y., Miyama, S. M., Nakano, T., & Umembayashi, T. 1996, *ApJ*, 467, 684
 Akimkin, V., Zhukovska, S., Wiebe, D., et al. 2013, *ApJ*, 766, 8
 Andrews, S. M. & Williams, J. P. 2005, *ApJ*, 631, 1134
 Andrews, S. M., Wilner, D. J., Hughes, A. M., Qi, C., & Dullemond, C. P. 2009, *ApJ*, 700, 1502
 Antonellini, S., Kamp, I., Riviere-Marichalar, P., et al. 2015, *A&A*, 582, A105
 Aresu, G., Kamp, I., Meijerink, R., et al. 2014, *A&A*, 566, A14
 Aresu, G., Kamp, I., Meijerink, R., et al. 2011, *A&A*, 526, A163
 Aresu, G., Meijerink, R., Kamp, I., et al. 2012, *A&A*, 547, A69
 Bergin, E. A., Cleeves, L. I., Crockett, N., & Blake, G. A. 2014, *Faraday Discussions*, 168, 61
 Bethell, T. J. & Bergin, E. A. 2011, *ApJ*, 740, 7
 Birmstiel, T., Klahr, H., & Ercolano, B. 2012, *A&A*, 539, A148
 Bjerkeli, P., Jørgensen, J. K., Bergin, E. A., et al. 2016, *A&A*, 595, A39
 Brunetti, A., Sanchez Del Rio, M., Golosio, B., Simionovici, A., & Somogyi, A. 2004, *Spectrochimica Acta*, 59, 1725
 Cazaux, S. & Tielens, A. G. G. M. 2002, *ApJ*, 575, L29
 Cazaux, S. & Tielens, A. G. G. M. 2004, *ApJ*, 604, 222
 Ciaravella, A., Cecchi-Pestellini, C., Chen, Y.-J., et al. 2016, *ApJ*, 828, 29
 Cleeves, L. I., Adams, F. C., & Bergin, E. A. 2013a, *ApJ*, 772, 5
 Cleeves, L. I., Adams, F. C., Bergin, E. A., & Visser, R. 2013b, *ApJ*, 777, 28
 Cleeves, L. I., Bergin, E. A., & Adams, F. C. 2014, *ApJ*, 794, 123
 Cleeves, L. I., Bergin, E. A., Qi, C., Adams, F. C., & Öberg, K. I. 2015, *ApJ*, 799, 204
 Draine, B. T. 2003, *ApJ*, 598, 1026
 Draine, B. T. & Bertoldi, F. 1996, *ApJ*, 468, 269
 Dubrulle, B., Morfill, G., & Sterzik, M. 1995, *Icarus*, 114, 237

Ch. Rab et al.: X-ray radiative transfer in protoplanetary disks

- Dutrey, A., Henning, T., Guilloteau, S., et al. 2007, *A&A*, 464, 615
- Dutrey, A., Semenov, D., Chapillon, E., et al. 2014, in *Protostars and Planets VI*, ed. H. Beuther, R. Klessen, C. Dullemond, & T. Henning (University of Arizona Press), 317–338
- Dwek, E. & Smith, R. K. 1996, *ApJ*, 459, 686
- Ercolano, B., Clarke, C. J., & Drake, J. J. 2009, *ApJ*, 699, 1639
- Ercolano, B., Drake, J. J., Raymond, J. C., & Clarke, C. C. 2008a, *ApJ*, 688, 398
- Ercolano, B. & Glassgold, A. E. 2013, *MNRAS*, 436, 3446
- Ercolano, B., Young, P. R., Drake, J. J., & Raymond, J. C. 2008b, *ApJS*, 175, 534
- Fabian, A. C. & Barcons, X. 1992, *ARA&A*, 30, 429
- Facchini, S., Birnstiel, T., Bruderer, S., & van Dishoeck, E. F. 2017, *ArXiv e-prints* [[arXiv:1705.06235](https://arxiv.org/abs/1705.06235)]
- Facchini, S., Clarke, C. J., & Bisbas, T. G. 2016, *MNRAS*, 457, 3593
- Feigelson, E. D., Garmire, G. P., & Pravdo, S. H. 2002, *ApJ*, 572, 335
- Furuya, K. & Aikawa, Y. 2014, *ApJ*, 790, 97
- Gavilan, L., Jäger, C., Simionovici, A., et al. 2016, *A&A*, 587, A144
- Glassgold, A. E., Meijerink, R., & Najita, J. R. 2009, *ApJ*, 701, 142
- Glassgold, A. E., Najita, J., & Igea, J. 2004, *ApJ*, 615, 972
- Glassgold, A. E., Najita, J. R., & Igea, J. 2007, *ApJ*, 656, 515
- Gorti, U. & Hollenbach, D. 2004, *ApJ*, 613, 424
- Gorti, U. & Hollenbach, D. 2008, *ApJ*, 683, 287
- Gorti, U. & Hollenbach, D. 2009, *ApJ*, 690, 1539
- Grady, C. A., Hamaguchi, K., Schneider, G., et al. 2010, *ApJ*, 719, 1565
- Graedel, T. E., Langer, W. D., & Frerking, M. A. 1982, *ApJS*, 48, 321
- Greenwood, A. J., Kamp, I., Waters, L. B. F. M., et al. 2017, *A&A*, 601, 11
- Güdel, M., Briggs, K. R., Arzner, K., et al. 2007a, *A&A*, 468, 353
- Güdel, M., Lahuis, F., Briggs, K. R., et al. 2010, *A&A*, 519, A113
- Güdel, M., Skinner, S. L., Mel'Nikov, S. Y., et al. 2007b, *A&A*, 468, 529
- Güdel, M. & Telleschi, A. 2007, *A&A*, 474, L25
- Güdel, M., Telleschi, A., Audard, M., et al. 2007c, *A&A*, 468, 515
- Guilloteau, S., Reboussin, L., Dutrey, A., et al. 2016, *A&A*, 592, A124
- Haworth, T. J., Facchini, S., Clarke, C. J., & Cleaves, L. I. 2017, *MNRAS*, 468, L108
- Helling, C., Woitke, P., Rimmer, P. B., et al. 2014, *Life*, volume 4, issue 2, pages 142–173, 4, 142
- Hierl, P. M., Morris, R. A., & Viggiano, A. A. 1997, *J. Chem. Phys.*, 106, 10145
- Hunter, J. D. 2007, *Computing In Science & Engineering*, 9, 90
- Igea, J. & Glassgold, A. E. 1999, *ApJ*, 518, 848
- Jørgensen, J. K., Visser, R., Sakai, N., et al. 2013, *ApJ*, 779, L22
- Kamp, I., Thi, W.-F., Meeus, G., et al. 2013, *A&A*, 559, A24
- Kamp, I., Thi, W.-F., Woitke, P., et al. 2017, *A&A*, in press [[arXiv:1707.07281](https://arxiv.org/abs/1707.07281)]
- Kamp, I., Tilling, I., Woitke, P., Thi, W.-F., & Hogerheijde, M. 2010, *A&A*, 510, A18
- Krügel, E., ed. 2002, *Wiley Praxis Series in Astronomy and Astrophysics*, Vol. 10, *The Physics of Interstellar Dust*
- Laor, A. & Draine, B. T. 1993, *ApJ*, 402, 441
- Lee, H.-H., Roueff, E., Pineau des Forets, G., et al. 1998, *A&A*, 334, 1047
- Lynden-Bell, D. & Pringle, J. E. 1974, *MNRAS*, 168, 603
- Mathis, J. S., Rumpl, W., & Nordsieck, K. H. 1977, *ApJ*, 217, 425
- McElroy, D., Walsh, C., Markwick, A. J., et al. 2013, *A&A*, 550, A36
- Meijerink, R., Aresu, G., Kamp, I., et al. 2012, *A&A*, 547, A68
- Meijerink, R., Glassgold, A. E., & Najita, J. R. 2008, *ApJ*, 676, 518
- Min, M., Hovenier, J. W., & de Koter, A. 2005, *A&A*, 432, 909
- Min, M., Rab, C., Woitke, P., Dominik, C., & Ménard, F. 2016, *A&A*, 585, A13
- Nomura, H., Aikawa, Y., Tsujimoto, M., Nakagawa, Y., & Millar, T. J. 2007, *ApJ*, 661, 334
- Öberg, K. I., Qi, C., Fogel, J. K. J., et al. 2011a, *ApJ*, 734, 98
- Öberg, K. I., Qi, C., Wilner, D. J., & Andrews, S. M. 2011b, *ApJ*, 743, 152
- Padovani, M., Galli, D., & Glassgold, A. E. 2013, *A&A*, 549, C3
- Pinte, C., Dent, W. R. F., Ménard, F., et al. 2016, *ApJ*, 816, 25
- Preibisch, T., Kim, Y.-C., Favata, F., et al. 2005, *ApJS*, 160, 401
- Qi, C., Öberg, K. I., Wilner, D. J., et al. 2013, *Science*, 341, 630
- Rab, C., Elbakyan, V., Vorobyov, E., et al. 2017, *A&A*, in press
- Rab, C., Güdel, M., Padovani, M., et al. 2017, *A&A*, in press
- Reboussin, L., Wakelam, V., Guilloteau, S., Hersant, F., & Dutrey, A. 2015, *A&A*, 579, A82
- Salter, D. M., Hogerheijde, M. R., van der Burg, R. F. J., Kristensen, L. E., & Brinch, C. 2011, *A&A*, 536, A80
- Schisano, E., Ercolano, B., & Güdel, M. 2010, *MNRAS*, 401, 1636
- Schoonjans, T., Brunetti, A., Golosio, B., et al. 2011, *Spectrochimica Acta*, 66, 776
- Shu, F. H., Shang, H., Glassgold, A. E., & Lee, T. 1997, *Science*, 277, 1475
- Slavin, J. D. & Frisch, P. C. 2008, *A&A*, 491, 53
- Teague, R., Semenov, D., Guilloteau, S., et al. 2015, *A&A*, 574, A137
- Thi, W.-F., Pinte, C., Pantin, E., et al. 2014, *A&A*, 561, A50
- Thi, W.-F., van Zadelhoff, G.-J., & van Dishoeck, E. F. 2004, *A&A*, 425, 955
- Thi, W.-F., Woitke, P., & Kamp, I. 2011, *MNRAS*, 412, 711
- Tielens, A. G. G. M. 2005, *The Physics and Chemistry of the Interstellar Medium* (Cambridge University Press)
- Umeyayashi, T. & Nakano, T. 2009, *ApJ*, 690, 69
- van Dishoeck, E. F., Bergin, E. A., Lis, D. C., & Lunine, J. I. 2014, *Protostars and Planets VI*, 835
- van't Hoff, M. L. R., Walsh, C., Kama, M., Facchini, S., & van Dishoeck, E. F. 2017, *A&A*, 599, A101
- Vasyunin, A. I., Wiebe, D. S., Birnstiel, T., et al. 2011, *ApJ*, 727, 76
- Verner, D. A., Ferland, G. J., Korista, K. T., & Yakovlev, D. G. 1996, *ApJ*, 465, 487, <http://www.pa.uky.edu/~verner/atom.html>
- Verner, D. A. & Yakovlev, D. G. 1995, *A&AS*, 109, 125
- Walsh, C., Millar, T. J., & Nomura, H. 2013, *ApJ*, 766, L23
- Walsh, C., Nomura, H., Millar, T. J., & Aikawa, Y. 2012, *ApJ*, 747, 114
- Webber, W. R. 1998, *ApJ*, 506, 329
- Weingartner, J. C. & Draine, B. T. 2001, *ApJS*, 134, 263
- Williams, J. P. & Cieza, L. A. 2011, *ARA&A*, 49, 67
- Woitke, P., Kamp, I., & Thi, W.-F. 2009, *A&A*, 501, 383
- Woitke, P., Min, M., Pinte, C., et al. 2016, *A&A*, 586, A103
- Woitke, P., Riaz, B., Duchêne, G., et al. 2011, *A&A*, 534, A44
- Zanchet, A., Godard, B., Bulut, N., et al. 2013, *ApJ*, 766, 80
- Zhou, X., Li, S., & Stannnes, K. 2003, *Appl. Opt.*, 42, 4295

A&A proofs: manuscript no. xrt

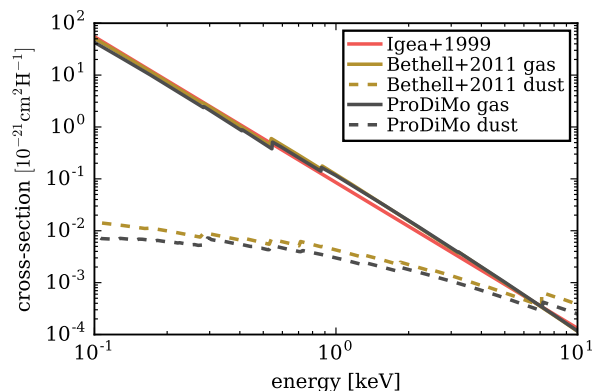


Fig. A.1. Comparison of X-ray photoelectric (absorption) cross-sections per hydrogen nucleus as a function of photon energy. The red line shows the gas absorption cross-section from *Igea & Glassgold (1999)*. The brown lines show the cross-sections derived by *Bethell & Bergin (2011)*. The black lines show the PRODiMO results for the large grains dust model.

Appendix A: Comparison of X-ray photoelectric cross-sections

In Fig. A.1, we compare the X-ray photoelectric cross-sections as used in PRODiMO to the cross-sections derived by *Igea & Glassgold (1999)* and *Bethell & Bergin (2011)*. For the PRODiMO case we used the depleted element abundances (*Kamp et al. 2017*) assuming all hydrogen is in H_2 and all other elements are present as neutral atoms. For the dust, we use the large grains dust model (see Table 1) and the opacity calculations as described in Sect. 2.3.3.

For the *Igea & Glassgold (1999)* cross-sections, we used their Eq. 10 for the case of heavy element depletion. *Igea & Glassgold (1999)* did not include a treatment of the absorption edges and also neglected the dust component. For the *Bethell & Bergin (2011)* cross-sections we used their Eq. 1 with the corresponding fitting coefficients for their “Gas” case (their Table 2); for the dust we used the coefficients for their dust size distribution with $a_{\min} = 0.01 \mu\text{m}$, $a_{\max} = 1000 \mu\text{m}$ and $a_{\text{pow}} = 3.5$ (their Table 3). We note that *Bethell & Bergin (2011)* did not use Mie-theory for the opacity calculations but rather used directly the photo-electric cross-sections for the atoms and assumed that all heavy metals (except noble gases) and a certain fraction of C and O are in solid form. To account for different dust sizes they used self-blanketing factors.

The deviations between the *Igea & Glassgold (1999)* and PRODiMO cross-sections are on average $\approx 20\%$ with a maximum of $\approx 30\%$. For the *Bethell & Bergin (2011)* cross-sections we find deviations of $\approx 10\%$ with a maximum of $\approx 50\%$, relative to PRODiMO. The agreement for the gas cross-section is remarkably good considering that we did not adapt the exact same element abundances (although in all three cases some form of depleted abundances are used).

The *Bethell & Bergin (2011)* dust cross-sections are about a factor of 1.2 – 2 higher than the PRODiMO cross-sections. The differences are probably caused by the different dust properties (e.g. in the PRODiMO case $a_{\max} = 3000 \mu\text{m}$). However, considering the general uncertainties connected to X-ray dust opacities the agreement is quite good.

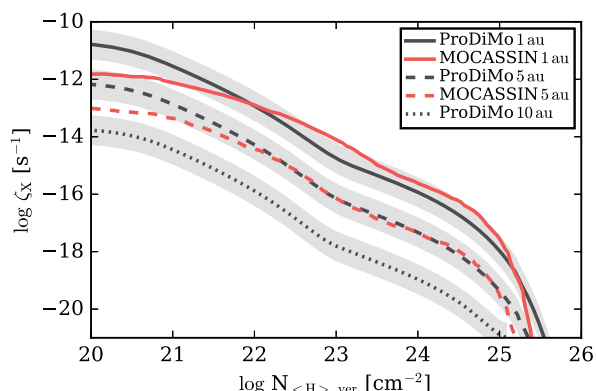


Fig. B.1. Comparison of the X-ray ionization rate ζ_X as a function of vertical hydrogen column density $N_{\text{H,ver}}$ at radii of 1 au (solid lines), 5 au (dashed lines) and 10 au (dotted line). The red lines are the results from MOCASSIN the black lines are the results from PRODiMO. The 10 au result from MOCASSIN were not available for this test case. The 10 au results have been scaled down by a factor of 10 for better visibility. The gray shaded area indicates a factor of three deviation relative to the PRODiMO results. An isothermal X-ray spectrum with $kT_X = 5 \text{ keV}$ and $L_X = 10^{29} \text{ erg s}^{-1}$ is used.

Appendix B: Comparison to the Monte Carlo X-ray radiative transfer code MOCASSIN

Ercolano & Glassgold (2013) presented a comparison of the 3D Monte Carlo radiative transfer and photoionization code MOCASSIN (*Ercolano et al. 2008b*) to the Monte Carlo X-ray radiative transfer model of *Igea & Glassgold (1999)*. For the comparison a minimum mass solar nebula disk model is used (see *Igea & Glassgold 1999* for details). The X-ray emitting source is modelled via two rings with radius $5 R_\odot$ located at a height of $5 R_\odot$ above and below the star. Dust absorption and scattering is not considered in those models. *Ercolano & Glassgold (2013)* found a good agreement for the resulting X-ray ionization rates per hydrogen nucleus between the two codes.

In Fig. B.1 we show a comparison of our X-ray radiative transfer model to the results from MOCASSIN. For this comparison we used the same physical disk parameters and the same initial element abundances (the “IG99 depleted”) as given in *Ercolano & Glassgold (2013)*. The X-ray luminosity is $L_X(1 - 20 \text{ keV}) = 10^{29} \text{ erg s}^{-1}$ and the spectrum has a single temperature of $kT_X = 5 \text{ keV}$. In contrast to the models presented in *Ercolano & Glassgold (2013)* we assume that the X-rays are emitted at the stellar surface. The X-ray ionization rate ζ_X is simply calculated for the given initial abundances (i.e. all species are neutral and all hydrogen is in molecular form) without solving for the chemistry.

As seen from Fig. B.1, the agreement of the two codes is quite good but there are also some significant differences. We want to emphasize that the radiative transfer methods used are very different. MOCASSIN uses the Monte Carlo approach with a proper treatment of anisotropic scattering. In PRODiMO, we apply a ray-base method (discrete-ordinates) with a simple approximation for the anisotropic scattering. Scattering dominates ζ_X for $N_{\text{H,ver}} \gtrsim 10^{23} \text{ cm}^{-2}$ (scattering shoulder *Igea & Glassgold 1999*). In this region the results of both codes are within a factor of three, indicating that our simplified treatment of anisotropic scattering is a reasonable approximation.

Ch. Rab et al.: X-ray radiative transfer in protoplanetary disks

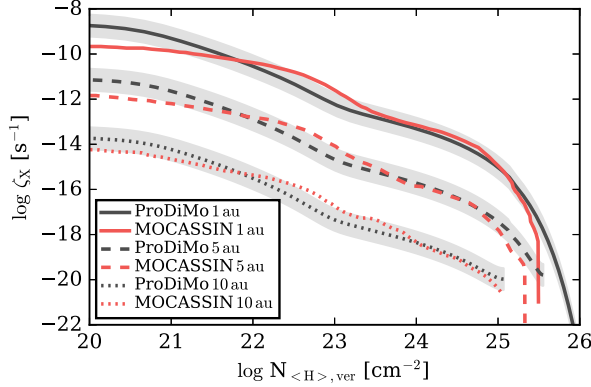


Fig. B.2. Same as Fig. B.1 but for a flared X-ray spectrum and low metal abundances. The 5 and 10 au results have been scaled down by factor of 10 and 1000, respectively. The X-ray luminosity is $L_X = 2 \times 10^{31}$ erg s^{-1} and the plasma temperature is $kT_X = 12$ keV (the COUP flared spectrum in Ercolano & Glassgold 2013).

The largest differences are actually at low column densities of $N_{(H),ver} \lesssim 10^{21}$ cm^{-2} where ζ_X is solely dominated by absorption of low energy X-ray photons (here $E_X \approx 1$ keV). Those deviations might be caused by the exact treatment of the low energy-cut off for the X-ray spectrum. We did run a test with a cut-off at 1.1 keV in that case ζ_X drops by a factor of a few at low column densities but is not affected at high column densities. However, we also performed a test with twice as much energy bands in our X-ray RT to more accurately treat the low energy cut-off, but we did not find significant differences. So, the origin of these deviations remains rather unclear. Although ζ_X at low columns is relevant for photo-evaporative winds (e.g. Ercolano et al. 2008a) it is of less relevance for our here presented models as we are mainly interested in the impact of X-ray ionization on the chemistry.

The deviations around $N_{(H),ver} = 10^{23}$ cm^{-2} are likely caused by the different locations of the X-ray emitting source. Compared to a pure stellar X-ray source, the X-ray photons emitted by an elevated ring source have encountered a lower column of material when they reach a certain height of the disk (see also Igea & Glassgold 1999). At larger distances the geometrical effects (e.g. incident angle on the disk surface) are less severe. The actual location of the X-ray source in T Tauri stars is not well known which is a general uncertainty in the models. However, as discussed by Ercolano et al. (2009) there are observational indications for a location of the X-ray source at or very close ($\lesssim 1 R_\odot$) to the stellar surface.

In Fig. B.2, we present a similar comparison as in Fig. B.1 but for a flared X-ray spectrum with $L_X(1 - 20$ keV) = 2×10^{31} erg s^{-1} and $kT_X = 12$ keV and different element abundances (“ISM depleted” from Table 1 of Ercolano & Glassgold 2013). The deviations between the models are similar to the first test case. However, now the impact of the X-ray source location is better visible. In the MOCASSIN models the scattering shoulder is located at slightly deeper layers than in the PRODiMO models. Due to the elevated location of the X-ray source the photons experience a lower radial column of material and can penetrate to deeper layers of the disk. The differences for $N_{(H),ver} > 10^{25}$ cm^{-2} are likely of technical nature. As noted by Ercolano & Glassgold (2013) the sudden drop in ζ_X is caused by the low number of photons reaching those layers. In the PRODiMO model

convergence of the iterative scheme might not be reached in the high energy range where scattering is most important. This results in an overestimate of ζ_X in deep and dense regions of the disk. However, in such regions, $\zeta_X \lesssim 10^{-19}$ s^{-1} , which is below the ionization rates expected from cosmic rays and the decay of short-lived radionuclides (e.g. Umebayashi & Nakano 2009; Cleeves et al. 2015).

Although there are differences concerning the X-ray ionization rate between PRODiMO and MOCASSIN, the overall agreement is quite good. In particular, it shows that our ray-based radiative transfer method gives similar results as the Monte Carlo radiative transfer method. However, as the calculation of the X-ray ionization rate is a rather complex topic, a proper and more detailed benchmarking of different X-ray radiative transfer codes is desirable for a better understanding of the remaining model differences.

Appendix C: HCO⁺ formation pathway via excited molecular hydrogen

The formation pathway for HCO⁺ via excited molecular hydrogen H₂^{*} works in the following



Key here is the reaction $H_2^* + C^+ \rightarrow CH^+ + H_2$, where we use the measured rate of Hierl et al. (1997) with an extrapolation to lower temperatures. However, in particular the rate at low temperatures ($T < 100$ K) is uncertain, and theoretical models indicate significantly lower rates (by orders of magnitude, Zanchet et al. 2013). A more detailed discussion and a comparison of different rates for $H_2^* + C^+$ is presented in Kamp et al. (2017).

Chapter 3

Stellar energetic particle ionization in protoplanetary disks around T Tauri stars

The aim of this project was to investigate, for the first time, the impact of stellar energetic particle irradiation on disk chemistry. This project was carried out in the context of the EU-FP7 project DIANA (Subproject: Impact of X-ray and Particle Irradiation, PI M. Güdel) and made use of the newly developed X-ray radiative transfer module (Chapter 2). In collaboration with M. Padovani a simple to use method to calculate the stellar energetic particle ionization rate throughout the two-dimensional disk structure was developed. This allowed us to study in detail the impact of this additional high-energy ionization source on the disk chemistry and its impact on the disk ionization tracers HCO^+ and N_2H^+ . With this work, it is now possible to study in detail the impact of several high-energy ionization sources, namely cosmic-rays, X-rays, stellar energetic particles and radionuclides, on the disk thermal and chemical structure. The results of this project were published in the paper *Stellar energetic particle ionization in protoplanetary disks around T Tauri stars*. In this thesis, the original published version is included.

Bibliography reference

Astronomy & Astrophysics, Volume 603, id.A96 (2017),
DOI: [10.1051/0004-6361/201630241](https://doi.org/10.1051/0004-6361/201630241).

Individual contributions to the paper

Own contribution: writing of the paper, required code development in PRODiMo and model runs.

M. Güdel: PI of the DIANA sub-project leading to this publication; provided valuable scientific input on high-energy physics of young stars.

M. Padovani: 1D modelling of stellar energetic particle transport in molecular gas using the input particle spectra provided by Ch. Rab.

I. Kamp, W.-F. Thi, P. Woitke: main developers of PRODiMo, disk modelling support.

G. Aresu: main developer of the X-ray chemistry module of PRODiMo.

All authors read the manuscript before publication and provided valuable scientific input and very useful suggestions concerning the presentation and writing of the paper.

A&A 603, A96 (2017)
 DOI: 10.1051/0004-6361/201630241
 © ESO 2017

**Astronomy
&
Astrophysics**

Stellar energetic particle ionization in protoplanetary disks around T Tauri stars

Ch. Rab¹, M. Güdel¹, M. Padovani², I. Kamp³, W.-F. Thi⁴, P. Woitke⁵, and G. Aresu⁶

¹ University of Vienna, Dept. of Astrophysics, Türkenschanzstr. 17, 1180 Wien, Austria
 e-mail: christian.rab@univie.ac.at

² INAF-Osservatorio Astrofisico di Arcetri, Largo E. Fermi, 5, 50125 Firenze, Italy

³ Kapteyn Astronomical Institute, University of Groningen, PO Box 800, 9700 AV Groningen, The Netherlands

⁴ Max-Planck-Institut für extraterrestrische Physik, Giessenbachstrasse 1, 85748 Garching, Germany

⁵ SUPA, School of Physics & Astronomy, University of St. Andrews, North Haugh, St. Andrews KY16 9SS, UK

⁶ INAF, Osservatorio Astronomico di Cagliari, via della Scienza 5, 09047 Selargius, Italy

Received 13 December 2016 / Accepted 23 February 2017

ABSTRACT

Context. Anomalies in the abundance measurements of short lived radionuclides in meteorites indicate that the protosolar nebulae was irradiated by a large number of energetic particles ($E \geq 10$ MeV). The particle flux of the contemporary Sun cannot explain these anomalies. However, similar to T Tauri stars the young Sun was more active and probably produced enough high energy particles to explain those anomalies.

Aims. We aim to study the interaction of stellar energetic particles with the gas component of the disk (i.e. ionization of molecular hydrogen) and identify possible observational tracers of this interaction.

Methods. We used a 2D radiation thermo-chemical protoplanetary disk code to model a disk representative for T Tauri stars. We used a particle energy distribution derived from solar flare observations and an enhanced stellar particle flux proposed for T Tauri stars. For this particle spectrum we calculated the stellar particle ionization rate throughout the disk with an accurate particle transport model. We studied the impact of stellar particles for models with varying X-ray and cosmic-ray ionization rates.

Results. We find that stellar particle ionization has a significant impact on the abundances of the common disk ionization tracers HCO^+ and N_2H^+ , especially in models with low cosmic-ray ionization rates (e.g. 10^{-19} s^{-1} for molecular hydrogen). In contrast to cosmic rays and X-rays, stellar particles cannot reach the midplane of the disk. Therefore molecular ions residing in the disk surface layers are more affected by stellar particle ionization than molecular ions tracing the cold layers and midplane of the disk.

Conclusions. Spatially resolved observations of molecular ions tracing different vertical layers of the disk allow to disentangle the contribution of stellar particle ionization from other competing ionization sources. Modelling such observations with a model like the one presented here allows to constrain the stellar particle flux in disks around T Tauri stars.

Key words. stars: formation – circumstellar matter – stars: activity – radiative transfer – astrochemistry – methods: numerical

1. Introduction

Our Sun acts as a particle accelerator and produces energetic particles with energies ≥ 10 MeV (e.g. Mewaldt et al. 2007). Such particles are also called solar cosmic rays as their energies are comparable to Galactic cosmic rays. They are accelerated in highly violent events like flares and/or close to the solar surface due to shocks produced by coronal mass ejections (Reames 2015). Therefore the energetic particle flux is strongly correlated with the activity of the Sun (e.g. Mewaldt et al. 2005; Reedy 2012).

From X-ray observations of T Tauri stars we know that their X-ray luminosities can be up to 10^4 times higher than the X-ray luminosity of the contemporary Sun (e.g. Feigelson & Montmerle 1999; Güdel et al. 2007). Such high X-ray luminosities are rather a result of enhanced flare activity of young stars than coronal effects (e.g. Feigelson et al. 2002). Enhanced activity of T Tauri stars implies an increase of their stellar energetic particle (SP) flux. From simple scaling with the X-ray luminosity and considering that young stars produce more powerful flares, Feigelson et al. (2002) derived a typical SP flux for T Tauri stars $\approx 10^5$ times higher than for the contemporary Sun. Under these

assumptions T Tauri stars might show on average a continuous proton flux of $f_p(E_p \geq 10 \text{ MeV}) \approx 10^7 \text{ protons cm}^{-2} \text{ s}^{-1}$ at a distance of 1 au from the star.

Such a scenario is also likely for the young Sun. Measurements of decay products of short-lived radionuclides (SLR) like ^{10}Be or ^{26}Al in meteorites indicate an overabundance of SLRs in the early phases of our solar system (e.g. Meyer & Clayton 2000). One likely explanation for these abundance anomalies are spallation reactions of SPs with the dust in the protosolar nebula (e.g. Lee et al. 1998b; McKeegan et al. 2000; Gounelle et al. 2001, 2006). However, this would require a strongly enhanced SP flux of the young Sun by a factor $\geq 3 \times 10^5$ compared to the contemporary Sun (McKeegan et al. 2000), consistent with the estimated SP flux of T Tauri stars derived by Feigelson et al. (2002).

More recently Ceccarelli et al. (2014) reported a first indirect measurement of SPs in the protostar OMC-2 FIR 4. They observed a low $\text{HCO}^+/\text{N}_2\text{H}^+$ abundance ratio between three and four that requires high H_2 ionization rates $> 10^{-14} \text{ s}^{-1}$ throughout the protostellar envelope. They explain this high ionization rate by the presence of SPs. From this ionization rate they derived a particle flux of $f_p(E_p \geq 10 \text{ MeV}) \geq 3-9 \times 10^{11} \text{ protons cm}^{-2} \text{ s}^{-1}$

at 1 au distance from the star. Such a high flux would be more than sufficient to explain the over-abundance of SLRs in the solar nebula.

A further indication of SPs in young stars is the anti-correlation of X-ray fluxes with the crystalline mass fraction of the circumstellar dust found by [Glauser et al. \(2009\)](#). They argue that SPs are responsible for the amorphization of dust particles and that the correlation can be explained if the SP flux scales with the stellar X-ray luminosity. [Trappitsch & Ciesla \(2015\)](#) tested such a scenario by using detailed models of SP transport for a protoplanetary disk (i.e. SP flux as a function of height of the disk). They also considered the vertical “mixing” of dust particles. According to their models SP irradiation of the disk cannot explain the total SLR abundances in the solar nebula but might play a role for dust amorphization.

Like Galactic cosmic rays SPs not only interact with the solid component but also with the gas component of the disk. However, little is known about the impact of SPs on the chemical structure of disks. [Turner & Drake \(2009\)](#) investigated the relevance of SPs on the size of dead-zones in disks. Assuming similar enhancement factors as mentioned above they find that SPs can decrease the size of the dead zone depending on the disk model and other ionization sources.

We present a first approach to study the impact of SP ionization on the chemical structure of the disk. We assume a typical SP flux as proposed for T Tauri stars to study the impact of SP ionization on the common disk ionization tracers HCO^+ and N_2H^+ . We use the radiation thermo-chemical disk model PRODiMO (PROtoplanetary Disk MOdel, [Woitke et al. 2009, 2016; Kamp et al. 2010; Thi et al. 2011](#)) to model the thermal and chemical structure of the disk. We argue that spatially resolved radial intensity profiles of molecular ion emission of the disk allow to constrain the SP flux of T Tauri stars.

In Sect. 2 we describe our method to derive the ionization rate due to SPs and the disk model. Our results are presented in Sect. 3 where we show the impact of SPs on the common disk ionization tracers HCO^+ and N_2H^+ . In Sect. 4 we discuss possibilities to constrain the SP flux via observations of molecular ion emission and future prospects for modelling of SP ionization in protoplanetary disks. We present a summary and our main conclusions in Sect. 5.

2. Method

To investigate the impact of SPs on the disk chemical structure we first needed to determine the SP flux and the particle energy distribution. With these particle spectra we were able to calculate the ionization rate throughout the disk. We applied this to a disk structure representative for disks around T Tauri stars. With the radiation thermo-chemical disk code PRODiMO we calculated the chemical abundances. We did this for a series of models in which we also considered other important high energy ionization sources like Galactic cosmic rays (CR) and X-rays.

2.1. Stellar energetic particle spectra

As the actual particle spectra and fluxes of young stars are unknown, we derived the spectra from the knowledge available from our Sun. The origin of solar energetic particles are most likely flares and/or shock waves driven by coronal-mass ejections (CME; [Reames 2013, 2015](#)). Flares act like point sources on the solar surface whereas the shock waves can fill half of the heliosphere at around 2 Solar radii ([Reames 2015](#)). Particle

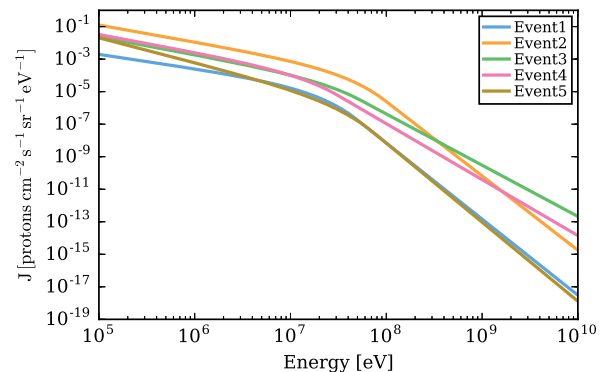


Fig. 1. Stellar particle (proton) spectra for five different solar particle events. Shown are fits to the measurements presented in [Mewaldt et al. \(2005\)](#).

fluxes are not continuous but rather produced in events lasting from several hours to days ([Feigelson et al. 2002; Mewaldt et al. 2005](#)).

Based on observed X-ray luminosities of solar analogs in the Orion nebula [Feigelson et al. \(2002\)](#) estimated that SP fluxes in young stars are likely $\approx 10^5$ times higher than in the contemporary Sun (see also [Glassgold et al. 2005](#)). As T Tauri stars are very active [Feigelson et al. \(2002\)](#) argue that it is likely that X-ray flares with luminosities below the detection limit occur several times a day (the same argument holds for CMEs). In that case the X-ray flares and consequently also SP events overlap, resulting in an enhanced continuous SP flux.

Based on these arguments we have assumed here a continuous and enhanced SP flux for young T Tauri stars. This approximation is consistent with the assumption of powerful and overlapping flare and CME events of T Tauri stars.

In [Mewaldt et al. \(2005\)](#) measurements of five different solar particle events are reported. We used their fitting formulae (see their Eq. (2) and Table 5) and derive SP spectra (protons in this case) averaged over the duration of the observed events. These measurements are for particles with energies up to several 100 MeV. We extrapolated their results up to energies typical for Galactic cosmic rays of ≈ 10 GeV. This is consistent with the maximum energy $E_{\text{max}} \approx 30$ GeV derived by [Padovani et al. \(2015, 2016\)](#) for particles accelerated on protostellar surfaces. The resulting spectra are shown in Fig. 1. The flux levels for the different events can vary by up to two orders of magnitude and there is also some variation in the shape of the spectra.

[Reedy \(2012\)](#) reported proton fluxes of the contemporary Sun for five solar cycles. Typical values for the cycle averaged fluxes at a distance of 1 au are $f_p(E_p > 10 \text{ MeV}) = 59\text{--}213 \text{ protons cm}^{-2} \text{ s}^{-1}$. For the *Event1* spectrum in Fig. 1 we get $f_p(E_p > 10 \text{ MeV}) = 151 \text{ protons cm}^{-2} \text{ s}^{-1}$ at 1 au, very similar to the reported values of [Reedy \(2012\)](#).

Here we used only the *Event1* spectrum, which we call the “active Sun” spectrum. We simply scaled the active Sun spectrum by a factor of $\approx 10^5$, as proposed by [Feigelson et al. \(2002\)](#), to get a typical “active T Tauri” spectrum. The resulting SP flux of $f_p(E_p > 10 \text{ MeV}) = 1.51 \times 10^7 \text{ protons cm}^{-2} \text{ s}^{-1}$ is consistent with the value of $\approx 10^7 \text{ protons cm}^{-2} \text{ s}^{-1}$ derived by [Feigelson et al. \(2002\)](#) for young solar analogs in the Orion Nebula cluster. The two SP spectra are shown in Fig. 2, where we also show two cases of Galactic cosmic-ray spectra for comparison (see Sect. 2.3.2).

Ch. Rab et al.: Stellar energetic particle ionization

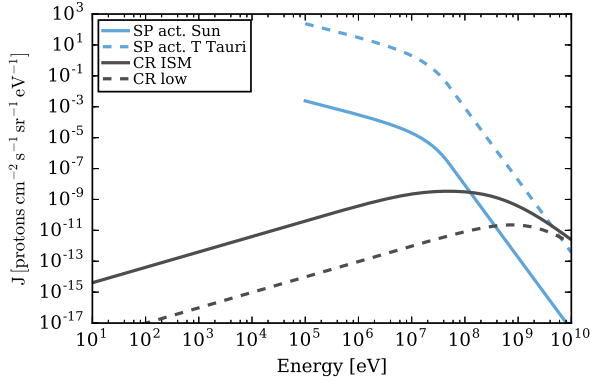


Fig. 2. Stellar energetic proton (SP) and cosmic-ray (CR) input spectra. The blue solid and dashed lines show the active Sun and active T Tauri SP spectrum, respectively. The black solid line shows the “LIS W98” CR spectrum from Webber (1998) and the dashed black line the attenuated “Solar Max” CR spectrum from Cleeves et al. (2013).

For comparison we also present models applying the same approach for the treatment of SPs as Turner & Drake (2009). For their model they assumed that SPs behave very similar to Galactic CRs (e.g. particle energies). The details of the Turner model are discussed in Appendix D.

It is not clear if SPs actually reach the disk (see Feigelson et al. 2002, for a discussion). However, as we are interested in the possible impact of SPs on the chemistry, we simply assumed that all SPs reach the disk. We further discuss this assumption in Sect. 4.3.

2.2. Stellar particle transport and ionization rate

Energetic particles hitting the disk interact with its gas and dust contents. Although the interaction with the solids is relevant for the production of SLR, here we are only interested in the interaction with the gas. Dust only plays a minor role in the actual attenuation of particles as only $\approx 1\%$ of the mass in protoplanetary disk is in solids (see also Trappitsch & Ciesla 2015). Very similar to Galactic cosmic rays, SPs mainly ionize the gaseous medium (i.e. molecular hydrogen). Energetic particles interact multiple times and ionize many atoms and molecules on their way until they eventually have lost their energy completely. This complex process requires detailed particle transport models.

To model the transport of energetic particles through the disk gas, we used the continuous slowing down approximation, which assumes that particles lose an infinitesimal fraction of their energy during propagation (Takayanagi 1973). We used the results obtained by Padovani et al. (2009, 2013a) who compute the propagation of CRs in a 1D slab, taking all the relevant energy loss processes into account. They give a useful fitting formula for the ionization rate as a function of the column density of molecular hydrogen.

In order to apply the results of this 1D transport model, we assumed that SPs travel along straight lines (i.e. no scattering due to their high energies) and that they originate from a point source (the star). We also disregarded the effect of magnetic fields that could increase or decrease the ionization rate depending on their configuration (Padovani & Galli 2011; Padovani et al. 2013b, see also Sect. 4.3.2).

From the detailed 1D particle transport model we derived a simple fitting formulae for the two SP spectra considered here.

Table 1. Fitting parameters for the stellar particle ionization rate for the two different input spectra.

Name	ζ_L (s^{-1})	a	ζ_H (s^{-1})	b
SP active Sun	$1.06(-12)^a$	-0.61	$8.34(-7)$	-2.61
SP active T Tauri	$1.06(-7)$	-0.61	$8.34(-2)$	-2.61

Notes. The values provided are for an unattenuated SP ionization rate at 1 au distance from the star (Eqs. (1) and (2)). $x(y)$ means $x \times 10^y$.

The SP ionization rate ζ_{SP} for molecular hydrogen as a function of the total hydrogen column density $N_{(H)} = N_H + 2 \times N_{H_2}$ is given by

$$\zeta_{SP}(N_{(H)}) = \left[\frac{1}{\zeta_L \left(\frac{N_{(H)}}{10^{20} \text{ cm}^{-2}} \right)^a} + \frac{1}{\zeta_H \left(\frac{N_{(H)}}{10^{20} \text{ cm}^{-2}} \right)^b} \right]^{-1} \text{ [s}^{-1}\text{]}, \quad (1)$$

and for $N_{(H)} > N_E$ by

$$\zeta_{SP,E}(N_{(H)}) = \zeta_{SP}(N_{(H)}) \times \exp \left[- \left(\frac{N_{(H)}}{N_E} - 1.0 \right) \right] \text{ [s}^{-1}\text{]}. \quad (2)$$

The two power laws in Eq. (1) are a consequence of the shape of the SP input spectra (see Fig. 2). The two parts of Eq. (1) account for the ionization rate at low (ζ_L) and high (ζ_H) column densities. Equation (2) accounts for the exponential drop of the SP ionization rate starting at a certain column density given by N_E (i.e. similar to CRs). For the two SP spectra considered here $N_E = 2.5 \times 10^{25} \text{ cm}^{-2}$. The other fitting parameters ζ_L , ζ_H , a and b are given in Table 1.

Equations (1) and (2) provide the unattenuated SP ionization rate at 1 au distance from the star (i.e. for a SP flux at 1 au). To account for geometric dilution we scaled $\zeta_{SP}(N_{(H)})$ by $1/r^2$ at every point in the disk (r is the distance to the star in au). For the chemistry we simply added ζ_{SP} to the ionization rate for Galactic cosmic rays ζ_{CR} (see Sect. 2.3.2).

2.3. Other ionization sources

To investigate the impact of SPs on the disk ionization structure also other ionization sources common to T Tauri stars must be considered. Besides SPs our model includes stellar UV and X-ray radiation, interstellar UV radiation and Galactic cosmic rays (CRs). However, most relevant for our study are the high energy ionization sources capable of ionizing molecular hydrogen: SPs, X-rays and CRs.

2.3.1. X-rays

To model the stellar X-ray spectrum we used an approximation for an isothermal bremsstrahlung spectrum (Glassgold et al. 1997; Aresu et al. 2011)

$$F(E) \propto \frac{1}{E} \exp(-E/kT_X), \quad (3)$$

where E is the photon energy (here in the range of 0.1 to 20 keV), k the Boltzmann constant and T_X is the plasma temperature. This spectrum is scaled to a given total X-ray luminosity L_X ($0.3 \leq E \leq 10 \text{ keV}$, e.g. Güdel et al. 2010).

As a result of the activity of the stars (e.g. flares) X-ray radiation of young stars is variable. We account for this in a simple way by including a spectrum with a X-ray luminosity and

A&A 603, A96 (2017)

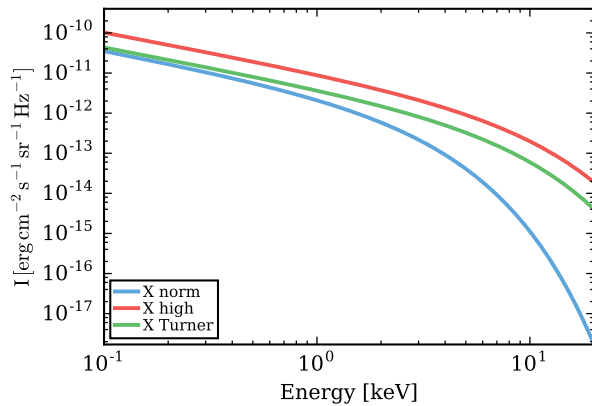


Fig. 3. Stellar X-ray input spectra (see Table 2).

Table 2. Parameters for the stellar X-ray input spectra (see Fig. 3).

Name	Spectrum	L_X (erg s $^{-1}$)	T_X (K)
X norm	typical T Tauri	1(30)	2(7)
X high	flared T Tauri	5(30)	7(7)
X Turner	Turner & Drake (2009)	2(30)	5.8(7)

temperature representative for a typical T Tauri star, and a spectrum which represents a flaring spectrum (more activity) with higher luminosity and a harder (hotter) radiation. However, we actually ignored the variability and assume time averaged X-ray fluxes. According to Ilgner & Nelson (2006) this is a reasonable assumption as typically the recombination timescales in the disk are longer than the flaring period and large parts of the disk ($r \gtrsim 2$ au in their model) respond to an enhanced average X-ray luminosity.

We also included the stellar X-ray properties used in Turner & Drake (2009) for the Turner models (Appendix D). The parameters for the various X-ray input spectra are given in Table 2 and the spectra are shown in Fig. 3.

To derive the X-ray ionization rate ζ_X we used X-ray radiative transfer including scattering and a detailed treatment of X-ray chemistry (Aresu et al. 2011; Meijerink et al. 2012). For more details on the new X-ray radiative transfer module in PRODiMO see Appendix A.

2.3.2. Galactic cosmic rays

Protoplanetary disks are exposed to Galactic cosmic rays (CR). Differently to SPs and X-rays, CRs are not of stellar origin and hit the disk isotropically. Cleeves et al. (2013) proposed that for T Tauri disks the actual CR ionization rate might be much lower compared to the interstellar medium (ISM) due to modulation of the impinging CRs by the heliosphere (“T-Tauriosphere”).

From modelling molecular ion observations of the TW Hya disk, Cleeves et al. (2015) derived an upper limit for the total H₂ ionization rate of $\zeta \lesssim 10^{-19}$ s $^{-1}$. This upper limit applies for all ionization sources including SLRs (e.g. Umebayashi & Nakano 2009). SLR ionization is a potentially important ionization source in the midplane of disks. However, similar to Cleeves et al. (2015) we modelled the low ionization rate scenario by reducing the CR ionization rate and did not explicitly treat SLR ionization in the models presented here.

Table 3. Fitting parameters for the cosmic-ray ionization rate.

Name	ζ_1 (s $^{-1}$)	ζ_h (s $^{-1}$)	Σ_0 (g cm $^{-2}$)	a
ISM CR ^a	2(-17)	2.6(-18)	244	0.021
low CR ^b	2(-19)	8.0(-19)	230	-0.01

Notes. ^(a) ISM W98 spectrum (Padovani et al. 2009, 2013a); ^(b) modulated “Solar Max” spectrum (Cleeves et al. 2013)

We considered two different CR input spectra, the canonical local ISM CR spectrum (Webber 1998) and a modulated CR spectrum which accounts for the exclusion of CRs by the “T-Tauriosphere” (Cleeves et al. 2013, 2015). For simplicity we call these two spectra “ISM CR” and “low CR”, respectively. To calculate the CR ionization rate ζ_{CR} in the disk we applied the fitting formulae provided by Padovani et al. (2013a) and Cleeves et al. (2013):

$$\zeta_{CR}(N_{(H)}) = \frac{\zeta_1 \zeta_h}{\zeta_h [N_{(H)}/10^{20} \text{ cm}^{-2}]^a + \zeta_1 [\exp(\Sigma/\Sigma_0) - 1]} \quad (4)$$

For simplicity we have assumed that CRs enter the disk perpendicular to the disk surface. Therefore we used the disk vertical hydrogen column density $N_{(H),\text{ver}}$ and surface density Σ_{ver} for Eq. (4) to calculate ζ_{CR} at every point in the disk. The fitting parameters ζ_1 , ζ_h , Σ_0 and a for the two CR input spectra are given in Table 3 (see Padovani et al. 2009, 2013a, for details). The typical resulting H₂ ionization rates in the disk are $\zeta_{CR} \approx 2 \times 10^{-17}$ s $^{-1}$ for the ISM CR spectrum and $\zeta_{CR} \approx 2 \times 10^{-19}$ s $^{-1}$ for the low CR spectrum (see Sects. 3.1 and 3.2).

2.4. Disk model

To model the disk we used the radiation thermo-chemical disk code PRODiMO (Woitke et al. 2009, 2016; Kamp et al. 2010; Thi et al. 2011). PRODiMO solves the wavelength dependent continuum radiative transfer which provides the disk dust temperature and the local radiation field. The gas temperature (the balance between heating and cooling) was determined consistently with the chemical abundances. The chemical network included 235 different species and 3143 chemical reactions (see Appendix B for more details).

We used a disk model representing the main properties of a disk around a typical T Tauri star. The stellar properties and the disk structure of this model are identical to the so-called reference model presented in Woitke et al. (2016). Here we only provide a brief overview of the disk model and refer the reader to Woitke et al. (2016) for details.

In Fig. 4 we show the gas number density, dust density, the local far-UV (FUV) radiation field, gas temperature, dust temperature and the vertical hydrogen column density for the reference model (model CI_XN, see Sect. 2.5 and Table 5). All relevant disk model parameters are given in Table 4.

Based on the similarity solution for viscous accretion disks, we used an axisymmetric flared gas density structure with a Gaussian vertical profile and a powerlaw with a tapered outer edge for the radial column density profile (e.g. Lynden-Bell & Pringle 1974; Andrews et al. 2009). The vertical scale height as a function of radius is expressed by a simple powerlaw. The disk has a total mass of $0.01 M_\odot$ and extends from 0.07 au (the dust sublimation radius) to 620 au where the total vertical hydrogen column density reaches $N_{(H),\text{ver}} \approx 10^{20}$ cm $^{-2}$ (panel (f) in Fig. 4).

Ch. Rab et al.: Stellar energetic particle ionization

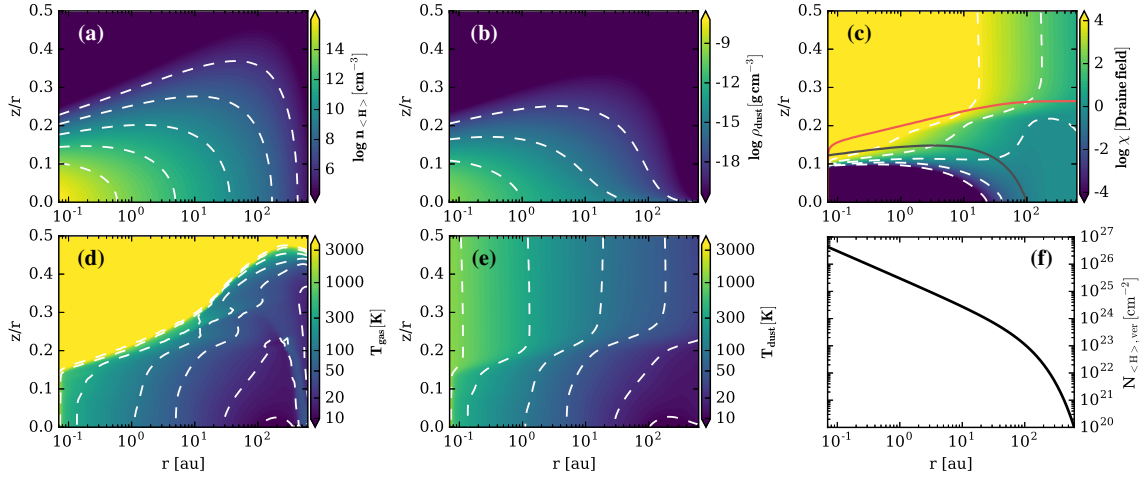


Fig. 4. Two dimensional structure of the reference disk model CI_XN. The height of the disk z is scaled by the radius (z/r). *From top left to the bottom right:* **a)** gas number density n_{H} ; **b)** dust density ρ_{dust} (note the dust settling); **c)** FUV radiation field χ in units of the ISM Draine field; **d)** gas temperature T_{gas} ; **e)** dust temperature T_{dust} and **f)** the vertical hydrogen column density $N_{\text{H},\text{ver}}$ versus radius. The white dashed contour lines in each contour plot correspond to the levels shown in the respective colorbar. The black (red) solid contour in panel **c)** indicate a vertical (radial) visual extinction equal to unity.

Table 4. Main fixed parameters of the disk model.

Quantity	Symbol	Value
stellar mass	M_*	$0.7 M_{\odot}$
stellar effective temp.	T_*	4000 K
stellar luminosity	L_*	$1.0 L_{\odot}$
FUV excess	L_{FUV}/L_*	0.01
FUV power law index	p_{UV}	1.3
strength of interst. FUV ^a	χ^{ISM}	1
disk gas mass	M_{disk}	$0.01 M_{\odot}$
dust/gas mass ratio	d/g	0.01
inner disk radius	R_{in}	0.07 au
tapering-off radius	R_{tap}	100 au
column density power ind.	γ	1.0
reference scale height	$H(100 \text{ au})$	10 au
flaring power index	β	1.15
min. dust particle radius	a_{min}	$0.05 \mu\text{m}$
max. dust particle radius	a_{max}	3 mm
dust size dist. power index	a_{pow}	3.5
turbulent mixing param.	α_{settle}	10^{-2}
max. hollow volume ratio ^b	$V_{\text{hollow,max}}$	0.8
dust composition	$\text{Mg}_{0.7}\text{Fe}_{0.3}\text{SiO}_3$	60%
(volume fractions)	amorph. carbon	15%
	porosity	25%

Notes. If not noted otherwise, these parameters are kept fixed for all our models presented in this work. For more details on the parameter definitions see [Woitke et al. \(2009, 2011, 2016\)](#). ^(a) χ^{ISM} is given in units of the Draine field ([Draine & Bertoldi 1996](#); [Woitke et al. 2009](#)). ^(b) We use distributed hollow spheres for the dust opacity calculations ([Min et al. 2005, 2016](#)).

For the dust density distribution we assumed a dust to gas mass ratio of $d/g = 0.01$. There is observational evidence for dust growth and settling in protoplanetary disks (e.g. [Williams & Cieza 2011](#); [Dullemond & Dominik 2004](#)). To account for

dust growth we assumed a power law dust size distribution $f(a) = a^{-3.5}$ with a minimum and maximum grain radius of $a_{\text{min}} = 0.05 \mu\text{m}$ and $a_{\text{max}} = 3000 \mu\text{m}$. For dust settling we applied the method of [Dubrulle et al. \(1995\)](#) with a turbulent mixing parameter of 10^{-2} .

The irradiation of the disk by the star is important for the temperature and the chemical composition of the disk. For the photospheric emission of the star we use PHOENIX stellar atmosphere models ([Brott & Hauschildt 2005](#)). We considered a $0.7 M_{\odot}$ star with an effective temperature of 4000 K and a luminosity of $1 L_{\odot}$. In addition to the photospheric emission, T Tauri stars commonly show far ultra-violet (FUV) excess (e.g. [France et al. 2014](#)) due to accretion shocks and strong X-ray emission (e.g. [Güdel & Nazé 2009](#)). For the excess FUV emission, we used a simple power law spectrum with a total integrated FUV luminosity of $L_{\text{FUV}} = 0.01 L_*$ in the wavelength interval [91.2 nm, 250 nm]. The details for the stellar X-ray properties are discussed in Sect. 2.3.1 above.

We use the molecules HCO^+ and N_2H^+ primarily to study the impact of SP ionization. To verify if our model gives reasonable results concerning HCO^+ and N_2H^+ abundances, we compared the modelled fluxes for the $J = 3-2$ transition of HCO^+ and N_2H^+ with the observational sample of [Öberg et al. \(2010, 2011a\)](#) finding a good agreement (for details see Appendix E).

2.5. Model series

It is likely that the different ionization sources are correlated. As already discussed the SP flux of young stars is actually derived from their stellar X-ray properties ([Lee et al. 1998b](#); [Feigelson et al. 2002](#)). Also the CR ionization rate might be anti-correlated with the activity of the star ([Cleeves et al. 2013](#)). However, these possible correlations are not well understood. We therefore ran a series of full disk models using the X-ray, SP and CR spectra (described above) as inputs and also included the Turner SP model (Appendix D). We do not discuss any model with the active Sun SP spectrum as in this case SPs do not have a significant impact on the disk chemical structure

Table 5. Model series.

Name	X-rays	Stellar particles	Cosmic rays
CI_XN	normal ^a	–	ISM ^d
CI_XH	high ^b	–	ISM
CL_XN_SP	normal	active T Tauri	ISM
CI_XH_SP	high	active T Tauri	ISM
CL_T	Turner ^c	Turner	ISM
CL_XN	normal	–	low ^e
CL_XH	high	–	low
CL_XN_SP	normal	active T Tauri	low
CL_XH_SP	high	active T Tauri	low
CL_T	Turner	Turner	low

Notes. In the model names CI (CL) stands for ISM (low) CR ionization rates, XN (XH) for normal (high) X-ray luminosities, SP for stellar particles and T for Turner model. ^(a) X-ray luminosity $L_X = 10^{30}$ erg s⁻¹. ^(b) $L_X = 5 \times 10^{30}$ erg s⁻¹. ^(c) $L_X = 2 \times 10^{30}$ erg s⁻¹. ^(d) CR ionization rate $\zeta_{CR} \approx 2 \times 10^{-17}$ s⁻¹. ^(e) $\zeta_{CR} \approx 2 \times 10^{-19}$ s⁻¹.

(see Sect. 3.1). An overview of all presented models is given in Table 5.

3. Results

3.1. Ionization rates as a function of column density

Before we discuss our results for the full disk model, we compare the SP, X-ray and CR ionization rates as a function of the total hydrogen column density $N_{(H)}$ ($N_{(H)} = N_H + 2N_{H_2}$). Figure 5 shows such a comparison for our different input spectra discussed in Sects. 2.2 and 2.3.

From visual inspection of Fig. 5 it becomes clear that for a SP flux comparable to our Sun (active Sun spectrum) SP ionization cannot compete with X-ray ionization assuming typical T Tauri X-ray luminosities. However, for the active T Tauri SP spectrum SP ionization becomes comparable to X-ray ionization or even dominates for $N_{(H)} \lesssim 10^{24} - 10^{25}$ cm⁻². For $N_H \lesssim 10^{23}$ cm⁻² ζ_{SP} is determined by the particles with $E_p \lesssim 5 \times 10^7$ eV whereas higher energy particles dominate for $N_{(H)} \gtrsim 10^{23}$ cm⁻². The kink at $N_{(H)} \approx 2 \times 10^{25}$ cm⁻² is caused by the rapid attenuation of the SPs at high column densities. At such high column densities even the most energetic particles have lost most of their energy and the ionization rate drops exponentially.

For X-rays, Fig. 5 shows the differences between the normal and high X-ray spectrum. The X-ray ionization rates are higher for the high X-ray spectrum due to the higher X-ray luminosity. Additionally, the harder X-ray photons can penetrate to deeper layers but are also more efficiently scattered than lower energy X-ray photons. Compared to the normal X-ray case, the X-ray ionization rate increases by several orders of magnitude for $N_{(H)} \gtrsim 10^{24}$ cm⁻² for the high X-ray case.

Galactic cosmic rays are the most energetic ionization source. The peak in the particle energy distribution is around $10^8 - 10^9$ eV (see Fig. 2). As a consequence the CR ionization rate ζ_{CR} stays mostly constant and only decrease for $N_{(H)} \gtrsim 10^{25}$ cm⁻². Only for such high column densities CR particle absorption becomes efficient.

In the Turner model it is implicitly assumed that SPs have the same energy distribution than Galactic CRs (see Appendix D). As a consequence the SP ionization rate in the Turner model is simply a scaled up version of the CR ionization rate. The slight differences to our model in CR attenuation is caused by the

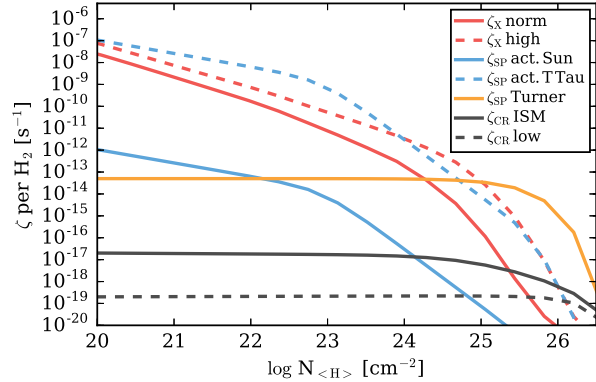


Fig. 5. SP, CR and X-ray ionization rates ζ as a function of hydrogen column density $N_{(H)}$.

different methods used to calculate the SP/CR ionization rates; Turner & Drake (2009) use the fitting formulae of Umebayashi & Nakano (2009). Compared to our active T Tauri SP spectrum ζ_{SP} in the Turner model is larger for $N_{(H)} > 10^{25}$ cm⁻² but significantly lower at low column densities.

3.2. Disk ionization rates

In Fig. 6 we show the ionization rates as a function of the vertical hydrogen column density $N_{(H),ver}$ at two different radii of the disk. Shown on the figure are the models CI_XN_SP (ISM CR, normal X-rays; left panel) and CL_XH_SP (low CR, high X-rays; right panel).

CRs are only significantly attenuated for $N_{(H),ver} > 10^{25}$ cm⁻² and $r \lesssim 1$ au. For most of the disk, CRs provide a nearly constant ionization rate of $\zeta_{CR} \approx 2 \times 10^{-17}$ s⁻¹ for the ISM like and $\zeta_{CR} \approx 2 \times 10^{-19}$ s⁻¹ for the low CR spectrum.

X-rays are strongly attenuated as a function of height and radius (i.e. geometric dilution). However, due to scattering X-rays can become the dominant midplane ionization source for large regions of the disk. For ISM-like CRs, CR ionization is the dominant midplane ionization source even in the high X-ray models. In the low CRs models X-rays are the dominant midplane ionization source for $r \lesssim 100$ au in the normal X-ray model and for all radii in the high X-ray model.

Differently to X-rays, SPs are not scattered towards the midplane. Due to their high energies they propagate along straight lines (provided that the SPs are not shielded by magnetic fields, see Sect. 4.3.2). As SPs are of stellar origin they penetrate the disk only along radial rays. The radial column densities close to the midplane of the disk are $N_{(H),rad} \gg 10^{25}$ cm⁻² and therefore SPs are already strongly attenuated at the inner rim of the disk. From Fig. 6 we see that the SP ionization rate ζ_{SP} drops below 10^{-19} s⁻¹ for $N_{(H),ver} \gtrsim 10^{24}$ cm⁻² at $r = 1$ au and for $N_{(H),ver} \gtrsim 10^{22}$ cm⁻² at $r = 100$ au. However, at higher layers ($N_{(H),ver} \lesssim 10^{22} - 10^{23}$ cm⁻²) SPs are the dominant ionization source even in the high X-ray models. Expressed in radial column densities: SPs are the dominant ionization source in disk regions with $N_{(H),rad} \lesssim 10^{24} - 10^{25}$ cm⁻².

In Fig. 7 we show the dominant ionization source at every point in the disk for all SP models. An ionization source is dominant at a certain point in the disk if its value is higher than the sum of the two other ionization sources. The first two columns in Fig. 7 show our models, the last column shows the Turner models. In our models, SPs are the dominant ionization source in the

Ch. Rab et al.: Stellar energetic particle ionization

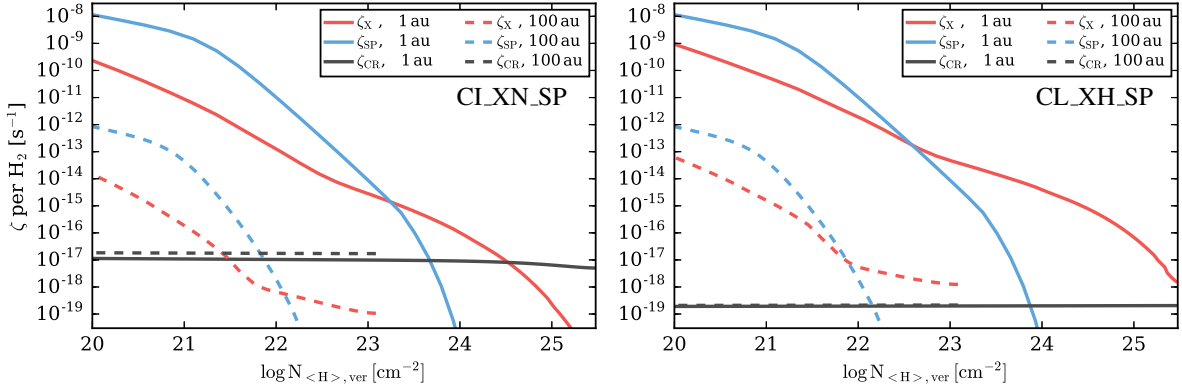


Fig. 6. Ionization rates ζ as a function of vertical column density $N_{(\text{H}),\text{ver}}$ at radii of 1 and 100 au (solid and dashed lines respectively). The maximum values for $N_{(\text{H}),\text{ver}}$ at the midplane of the disk, are $N_{(\text{H}),\text{ver}} \approx 4 \times 10^{25} \text{ cm}^{-2}$ and $N_{(\text{H}),\text{ver}} \approx 2 \times 10^{23} \text{ cm}^{-2}$ at 1 au and 100 au, respectively. Red lines are for X-rays, blue lines are for SPs and the black lines are for CRs. *Left panel:* model CL_XN_SP with ISM CRs and normal X-rays; *right panel:* model CL_XH_SP with low CRs and high X-rays.

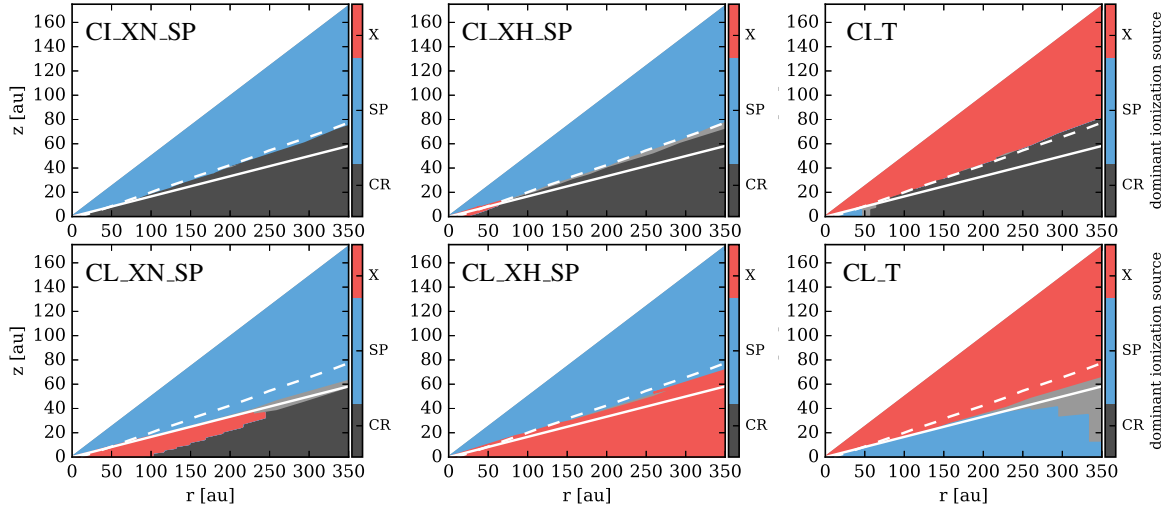


Fig. 7. Dominant disk ionization source throughout the disk. A light grey area indicates a region without a dominant ionization source. The different possible ionization sources, X-rays, SPs and CRs are identified by the different colors (color bar). The white solid contour line shows $N_{(\text{H}),\text{rad}} = 10^{25} \text{ cm}^{-2}$ the white dashed line shows the CO ice line. The model names are given in the top left of each panel. *Top row:* models with ISM CR ionization rate (CI); *bottom row:* models with low CR ionization rate (CL). *First column:* normal X-ray models (XN); *second column:* high X-ray models (XH); *third column:* turner models (T).

upper layers of the disk (above the white solid contour line for $N_{(\text{H}),\text{rad}} = 10^{25} \text{ cm}^{-2}$), whereas in the midplane always CRs or X-rays dominate.

For the Turner model the picture is quite different. In their model SPs can also penetrate the disk vertically (Appendix D) and reach higher vertical column densities before they are completely attenuated (Fig. 5). As a consequence SPs can become the dominant ionization source in the midplane of the disk (e.g. for the low CR case). In the upper layers always X-rays dominate as $\zeta_{\text{SP}} < \zeta_{\text{X}}$ for low column densities. In the Turner model $\zeta_{\text{SP}} \lesssim 10^{-13} \text{ s}^{-1}$ for $N_{(\text{H}),\text{rad}} < 10^{25} \text{ cm}^{-2}$ which is several orders of magnitudes lower than in our models. The reason for this is that in the Turner model SPs are simply a scaled version of ISM like CRs. The high ζ_{SP} values in our model in the upper layers of the disk are caused by the high number of particles with energies $E_p \lesssim 10^8 \text{ eV}$, which are missing in the Turner model.

3.3. Impact on HCO^+ and N_2H^+

The molecules HCO^+ and N_2H^+ are the two most observed molecular ions in disks (e.g. Dutrey et al. 2014) and are commonly used to trace the ionization structure of disks (e.g. Dutrey et al. 2007; Öberg et al. 2011b; Cleeves et al. 2015). Also Ceccarelli et al. (2014) used these two molecules to trace SPs in a protostellar envelope.

The main formation path of HCO^+ and N_2H^+ is the ion-neutral reaction of H_3^+ with their parent molecules CO and N_2 , respectively. H_3^+ is created by ionization of H_2 by CRs, X-rays and in our model additionally by SPs. The main destruction pathway for HCO^+ and N_2H^+ is via dissociative recombination with free electrons.

The chemistry of HCO^+ and N_2H^+ is linked to the CO freeze-out. To form HCO^+ , gas phase CO is required, whereas

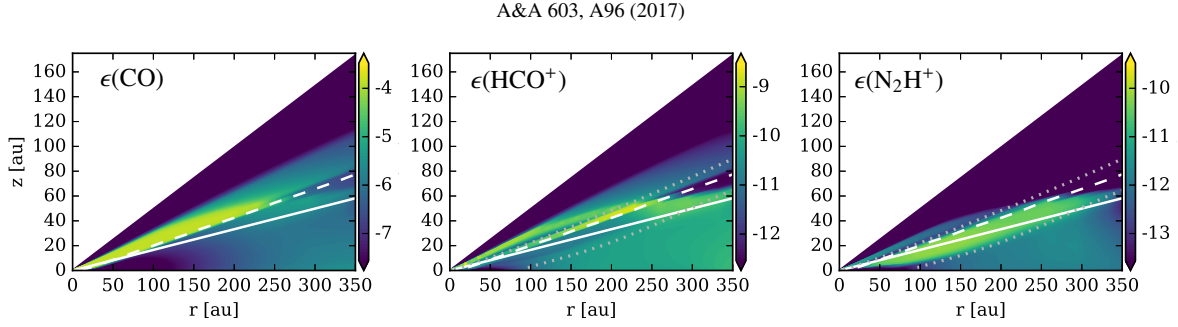


Fig. 8. Abundances $\epsilon(X)$ relative to hydrogen for CO, HCO⁺ and N₂H⁺ for the reference model CI_XN. The white solid contour line shows $N_{(\text{H}),\text{rad}} = 10^{25} \text{ cm}^{-2}$, the white dashed line shows the CO ice line. We call the regions above and below the CO ice line the warm and cold molecular layer, respectively. The dotted iso-contours show where the X-ray ionization rate is equal to the ISM CR ($\zeta_{\text{CR}} = 2 \times 10^{-17} \text{ s}^{-1}$) and equal to the low CR ($\zeta_{\text{CR}} = 2 \times 10^{-19} \text{ s}^{-1}$) ionization rate, respectively.

N₂H⁺ is efficiently destroyed by CO (e.g. Aikawa et al. 2015). Consequently the N₂H⁺ abundance peaks in regions where CO is depleted and N₂, the precursor of N₂H⁺, is still in the gas phase. The result of this chemical interaction is a vertically layered chemical structure for HCO⁺ and N₂H⁺ (see Fig. 8). For further details on the HCO⁺ and N₂H⁺ chemistry see Appendix B, where we also list the main formation and destruction pathways for HCO⁺ and N₂H⁺ (Table B.1).

3.3.1. Abundance structure

In the following we describe details of the molecular abundance structure that are relevant for the presentation of our results for our reference model CI_XN. The abundance ϵ of a molecule X is given by $\epsilon(X) = n_X/n_{(\text{H})}$, where n_X is the number density of the respective molecule and $n_{(\text{H})} = n_{\text{H}} + 2n_{\text{H}_2}$ is the total hydrogen number density. Figure 8 shows the resulting abundance structure for CO, HCO⁺ and N₂H⁺ for the CI_XN model.

We define the location of the CO ice line where the CO gas phase abundance is equal to the CO ice-phase abundance (white dashed line in Fig. 8). The CO ice line is located at dust temperatures in the range $T_{\text{d}} \approx 23\text{--}32 \text{ K}$ (density dependence of the adsorption/desorption equilibrium; e.g. Furuya & Aikawa 2014). The radial CO ice line in the midplane ($z = 0 \text{ au}$) is at $r \approx 12 \text{ au}$ and $T_{\text{d}} \approx 32 \text{ K}$. At $r \approx 50 \text{ au}$ the vertical CO ice line is at $z \approx 8.5 \text{ au}$ ($z/r \approx 0.17$) and $T_{\text{d}} \approx 26 \text{ K}$. Inside/above the CO ice line $\epsilon(\text{CO}) \approx 10^{-4}$. Outside/below the CO ice line $\epsilon(\text{CO})$ rapidly drops to values $\lesssim 10^{-6}$. In regions where non-thermal desorption processes are efficient ($r \gtrsim 150 \text{ au}$) $\epsilon(\text{CO}) \approx 10^{-6}$ down to the midplane. For the regions inside/above and outside/below the CO ice line we use the terms warm and cold molecular layer, respectively.

There are two main reservoirs for HCO⁺, one in the warm molecular layer above the CO ice line and one in the outer disk ($r \gtrsim 150 \text{ au}$) below the CO ice line where non-thermal desorption becomes efficient. In the warm molecular layer, the ionization fraction $\epsilon(e^-) \approx 10^{-7}$ is dominated by sulphur as it is ionized by UV radiation (e.g. Teague et al. 2015, see also Sect. 4.2.3). Those free electrons efficiently destroy molecular ions via dissociative recombination. This causes a dip in the vertical HCO⁺ abundance structure within the warm molecular layer with $\epsilon(\text{HCO}^+) \approx 10^{-12}\text{--}10^{-11}$, whereas at the top and the bottom of the warm molecular layer $\epsilon(\text{HCO}^+)$ reaches values of $\approx 10^{-10}\text{--}10^{-9}$. The peak in the top layer is mainly caused by the high X-ray ionization rate for H₂ ($\zeta_{\text{X}} \gtrsim 10^{-12} \text{ s}^{-1}$). At the bottom of the warm molecular layer more HCO⁺ survives. This region is already sufficiently shielded from UV radiation and the free

electron abundance drops rapidly. In the second reservoir, below the CO ice line where non-thermal desorption is efficient $\epsilon(\text{HCO}^+) \approx 10^{-11}\text{--}10^{-10}$.

The main N₂H⁺ reservoir resides in the cold molecular layer just below the CO ice line with $\epsilon(\text{N}_2\text{H}^+) \gtrsim 10^{-11}$. The lower boundary of this layer with $\epsilon(\text{N}_2\text{H}^+) < 10^{-11}$ is reached at $T_{\text{d}} \approx 16 \text{ K}$ where $\epsilon(\text{N}_2) \lesssim 10^{-6}$ due to freeze-out. Radially this layer extends from the inner midplane CO ice line out to $r \approx 250\text{--}300 \text{ au}$. Close to the midplane $\epsilon(\text{N}_2\text{H}^+) \lesssim 10^{-12}$ for $r \gtrsim 150 \text{ au}$ due to non-thermal desorption of ices. There is also a thin N₂H⁺ layer at the top of the warm molecular layer with $\epsilon(\text{N}_2\text{H}^+) \approx 10^{-12}$ extending from the inner radius of the disk out to $r \approx 100 \text{ au}$. In this layer the X-ray ionization rate is high enough to compensate for the destruction of N₂H⁺ by CO.

The detailed appearance of this layered structure is especially sensitive to the dust temperature and therefore also to dust properties (e.g. dust size distribution). The above described abundance structure for CO, HCO⁺ and N₂H⁺ is consistent with the model of Aikawa et al. (2015) that includes millimetre sized dust particles with a dust size distribution similar to what is used here (for details see Appendix B).

3.3.2. Vertical column densities

To study the impact of SP ionization quantitatively we compare vertical column densities of HCO⁺ and N₂H⁺ for models with and without SPs. In Fig. 9 we show the vertical column densities N_{HCO^+} and $N_{\text{N}_2\text{H}^+}$ as a function of the disk radius r for all models listed in Table 5. The left column in Fig. 9 shows the models with ISM CRs, the right column the models with low CRs. At first we discuss the models without SPs and compare them to other theoretical models.

The N_{HCO^+} profile shows a dip around $r \approx 50\text{--}100 \text{ au}$ in the ISM CR models CI_XN and CI_XH (high X-rays). This dip is also seen in the models of Cleeves et al. (2014). Unlike Cleeves et al. (2014), in our model this dip is not predominantly due to the erosion of CO by reactions with He⁺ (“sink effect” e.g. Aikawa et al. 1997, 2015; Bergin et al. 2014; Furuya & Aikawa 2014), but mainly due to the interplay of CO freeze-out and non-thermal desorption in the outer disk. The CO sink effect is also active in our model but less efficient (see Appendix B.2.2).

The lack of HCO⁺ in the disk midplane at $r \approx 50\text{--}100 \text{ au}$ due to CO freeze-out is also visible in the HCO⁺ abundance structure shown in Fig. 8. Non-thermal desorption in the midplane produces CO abundances $\gtrsim 10^{-7}$ for $r \gtrsim 150 \text{ au}$ and consequently also a slight increase in N_{HCO^+} . In the low CR models the ionization rate is too low to produce a significant amount

Ch. Rab et al.: Stellar energetic particle ionization

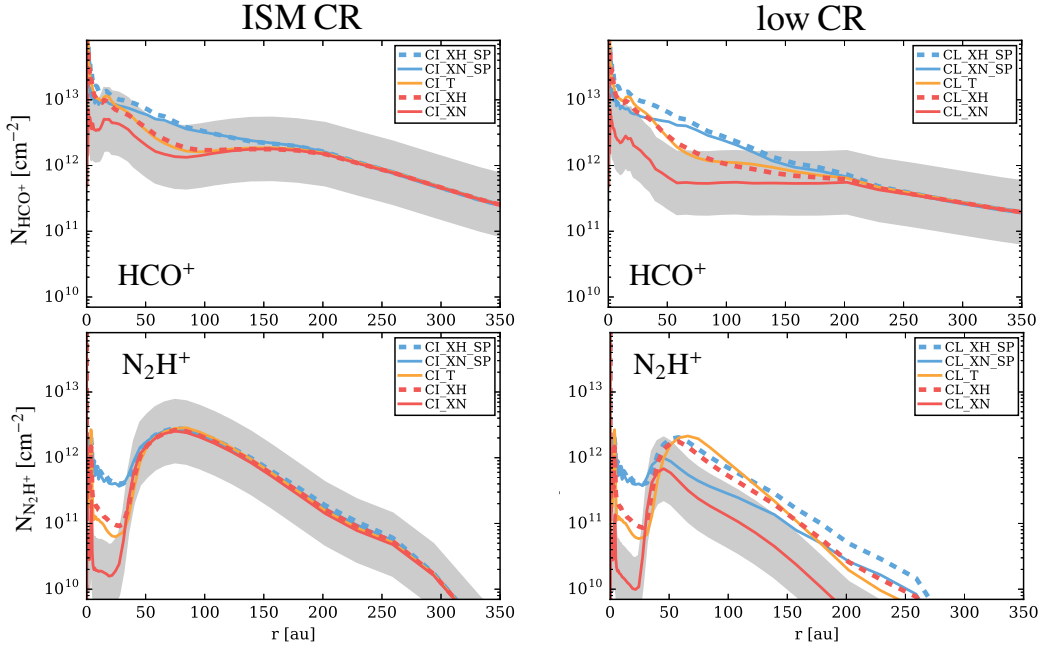


Fig. 9. Vertical column density profiles for HCO^+ and N_2H^+ for our model series (Table 5). The left column shows the models with the ISM like CRs ($\zeta_{\text{CR}} \approx 2 \times 10^{-17} \text{ s}^{-1}$), the right column with low CRs ($\zeta_{\text{CR}} \approx 2 \times 10^{-19} \text{ s}^{-1}$). The top row shows HCO^+ , the bottom row N_2H^+ . The blue lines are for models with, the red lines are for models without SPs. Dashed (solid) lines are for models with high (normal) X-rays. The orange solid line shows the Turner model. The grey shaded area marks a difference of a factor 3 in the column densities relative to the CI_XN (ISM CR, normal X-rays) and CL_XN model (low CR, normal X-rays), respectively.

of HCO^+ in the cold molecular layer and the dip in the profile vanishes.

N_2H^+ traces the distribution of gas phase CO as it is efficiently destroyed by CO (Qi et al. 2013a,b, 2015). This is also seen in our model. The sharp transition in the N_2H^+ column density at $r \approx 30$ au traces the onset of CO freeze-out (Fig. 9). We note, however, that the actual midplane CO ice-line is at ≈ 12 au (see Appendix C for details). In the ISM CR models $N_{\text{N}_2\text{H}^+}$ is dominated by CR ionization as N_2H^+ mainly resides in the cold molecular layer. In the warm N_2H^+ layer X-ray ionization dominates. However, due to the lower densities in the warm molecular layer, this layer only contributes significantly to the column density within the radial CO ice line, and the impact of X-rays is only visible there (compare models CI_XH and CI_XN in Fig. 9). The high X-ray luminosity decreases the contrast between the peak of $N_{\text{N}_2\text{H}^+}$ close to the radial CO ice line and $N_{\text{N}_2\text{H}^+}$ inside the CO ice line by about a factor of five.

For the low CR case $N_{\text{N}_2\text{H}^+}$ drops by more than an order of magnitude compared to the ISM CR case. Such a strong impact of CR ionization on $N_{\text{N}_2\text{H}^+}$ is also reported by Aikawa et al. (2015) and Cleaves et al. (2014). Higher X-ray luminosities can compensate for low CR ionization only to some extent. In the high X-ray model CL_XH , $N_{\text{N}_2\text{H}^+}$ is lower by a factor of five compared to the ISM CR models.

3.3.3. Impact of SPs

The column densities N_{HCO^+} and $N_{\text{N}_2\text{H}^+}$ for models with SPs are shown in Fig. 9 (blue solid and dashed lines). The solid orange line in Fig. 9 shows the results for the Turner model. We discuss the Turner model separately in Sect. 3.3.4. We define a change in the column densities by at least a factor of three compared to

the reference model as significant. This is indicated by the grey area around the column density profiles of the reference models CI_XN and CL_XN .

To better quantify the impact of SPs compared to the competing H_2 ionization sources, X-rays and CRs, we introduce the weighted column density

$$N_{\zeta}(r) = \int_0^{\infty} n(r, z) \times f_{\zeta}(r, z) dz \text{ [cm}^{-2}\text{]}. \quad (5)$$

N_{ζ} is the weighted column density for a particular H_2 ionization source ζ , n is the number density of a particular molecule in units of cm^{-3} and

$$f_{\zeta} = \frac{\zeta}{\zeta_{\text{X}} + \zeta_{\text{SP}} + \zeta_{\text{CR}}}. \quad (6)$$

N_{ζ} represents the fraction of the column density dominated by a particular ionization source ζ .

In Fig. 10 we show N_{ζ} for HCO^+ and N_2H^+ normalized to the total column density of the respective molecule as a function of radius. The region where more than 50% of the total column density of the molecules arise from disk regions above the CO ice line (i.e. from the warm molecular layer) is roughly indicated on each plot.

SP ionization has a significant impact on the N_{HCO^+} profile in all our models. In the ISM CR model (CI_XN_SP) N_{HCO^+} increases by a factor ≈ 3 for $50 \lesssim r \lesssim 100$ au and the dip in the profile seen in the models without SPs (CI_XN) vanishes (top left panel in Fig. 9). In the low CR models this region increases to $25 \lesssim r \lesssim 150$ au and N_{HCO^+} reaches values up to an order of magnitude higher compared to the CL_XN model (top right panel in Fig. 9). In the models with high X-rays, SP ionization

A&A 603, A96 (2017)

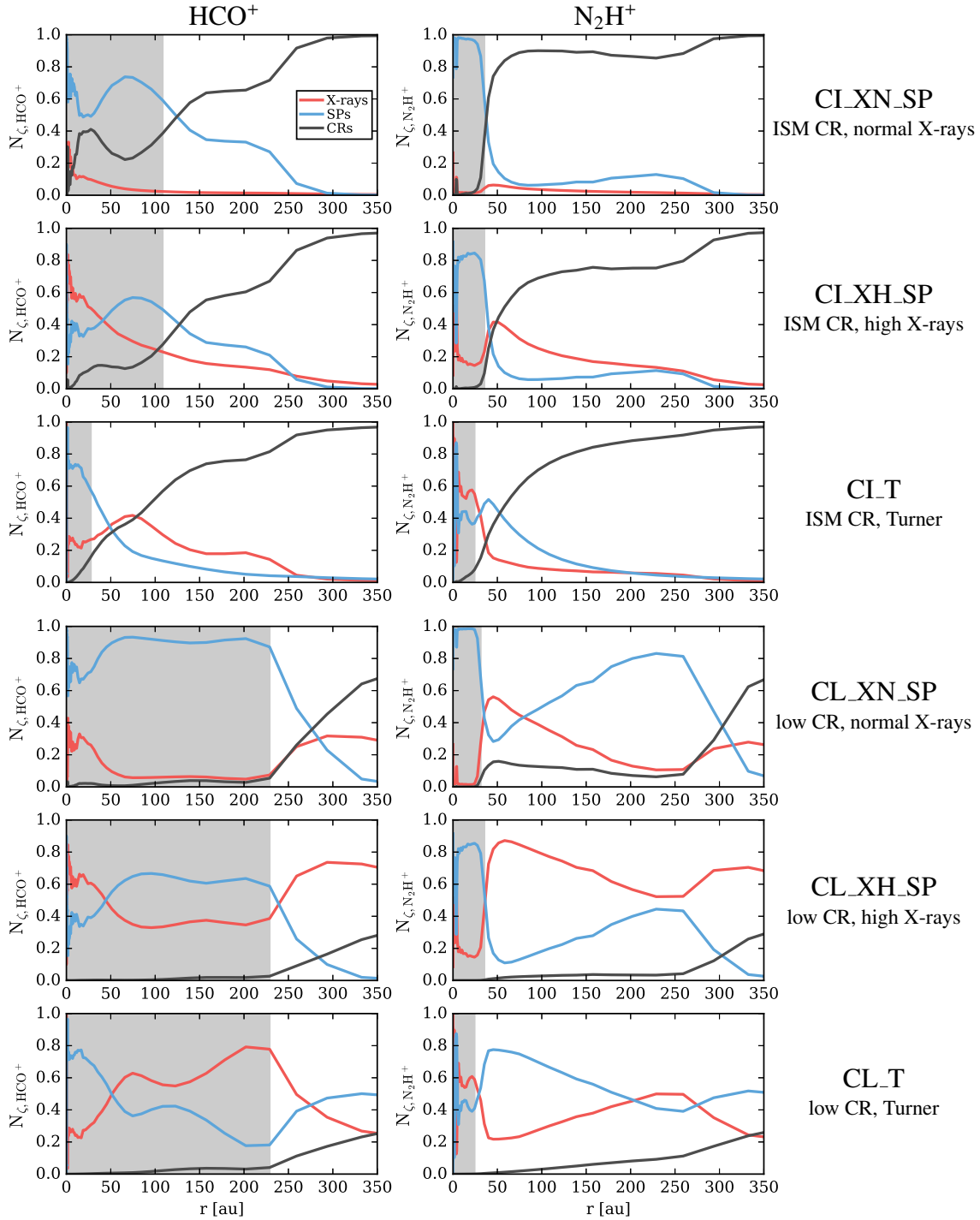


Fig. 10. Ionization rate weighted column densities N_c (Eq. (5)) as a function of radius for HCO^+ (left column) and N_2H^+ (right column). N_c is normalized to the total column density of the respective molecule. The individual colored solid lines show the fraction of the total column density dominated by a certain ionization source. Red is for X-rays ($N_{c,X}$), blue for SPs ($N_{c,SP}$) and black for CRs ($N_{c,CR}$). Each row corresponds to one model. On the right hand side the model descriptions are provided (see Table 5). The grey shaded area marks the region where more than 50% of the column density arise from regions above the CO ice line (i.e. the warm molecular layer).

still has a significant impact and N_{HCO^+} increases by up to a factor of three (dashed lines in Fig. 9).

This situation is also clearly visible in Fig. 10 where we show N_{ζ} as a function of radius (Eq. (5)). Although X-rays are the dominant ionization source close to the star, in all models N_{HCO^+} is dominated by SP ionization for $50 \lesssim r \lesssim 100\text{--}200$ au. Figure 10 also shows that in the low CR models N_{HCO^+} is mainly built up in the warm molecular layer for $r \lesssim 200$ au. In this region (indicated in Fig. 10) the warm molecular layer contributes more to the total column density than the cold molecular layer.

For N_2H^+ the picture is more complex. In the ISM CR models SPs have only very little impact on $N_{\text{N}_2\text{H}^+}$. Only in the inner 30 au, within the radial CO ice line, the N_2H^+ profile is significantly affected. The reason for this is the high SP ionization rate $\zeta_{\text{SP}} \gtrsim 10^{-12} \text{ s}^{-1}$ in the warm molecular layer of the disk close to the star. In this region the abundance ratio of $\text{HCO}^+/\text{N}_2\text{H}^+$ drops from $>10^3$, in the models without SPs, to around 10 to 100 in models with SPs. These high ratios can be explained by the efficient destruction of N_2H^+ by CO. However, due to the high ζ_{SP} this destruction path becomes less important, and the molecular ion abundance are mainly determined by the balance between ionization and recombination.

Ceccarelli et al. (2014) reported a very low measured $\text{HCO}^+/\text{N}_2\text{H}^+$ ratio between three and four in the Class 0 source OMC-2 FIR 4. They explain this low ratio by the high ionization rates due to SPs ($\zeta_{\text{SP}} > 10^{-14}$). In our disk model ζ_{SP} in the warm molecular layer is comparable, but the $\text{HCO}^+/\text{N}_2\text{H}^+$ ratio is much larger than four. This higher ratio is due to the higher densities of $10^8\text{--}10^{10} \text{ cm}^{-3}$ and the stronger UV field in the warm molecular layer, compared to the physical conditions in OMC-2 FIR 4. This is in agreement with the chemical models presented in Ceccarelli et al. (2014).

The impact of SPs on the N_2H^+ abundance in the warm layer can extend out to $r \approx 200$ au (similar to HCO^+). However, for $r > 30$ au this layer does not significantly contribute to the total N_2H^+ column density as $N_{\text{N}_2\text{H}^+}$ is dominated by the high density layer below the vertical CO ice line.

Beyond the radial CO ice line $N_{\text{N}_2\text{H}^+}$ is dominated by CRs in the ISM CR models and is not affected by X-rays nor SPs (bottom left panel in Fig. 9). Compared to the ISM CR models, $N_{\text{N}_2\text{H}^+}$ is reduced by a factor of a few around the peak and by more than an order of magnitude at larger radii in the low CR models. As a consequence the profile is also steeper. Although higher X-rays (CL_XH model) and also SPs can to some extent compensate low CR ionization rates, the $N_{\text{N}_2\text{H}^+}$ profile is still steeper and $N_{\text{N}_2\text{H}^+}$ is lower by a factor of between approximately two and six than in the ISM CR models for $r \gtrsim 30$ au.

From Fig. 10 we see that only in the CL_XN_SP model SPs dominate $N_{\text{N}_2\text{H}^+}$ for $r \gtrsim 70$ au. Actually the importance of SPs increases with r in this model. In the CL_XN_SP model SPs are the dominant ionization source in regions with $N_{(\text{H}),\text{rad}} \lesssim 10^{25} \text{ cm}^{-2}$. The $N_{(\text{H}),\text{rad}} = 10^{25} \text{ cm}^{-2}$ iso-contour is below the vertical CO ice line for $r > 70$ au and the layer between the CO ice line and $N_{(\text{H}),\text{rad}} = 10^{25} \text{ cm}^{-2}$ becomes thicker with radius (see Figs. 7 and 8). This also explains the change in the slope of $N_{\text{N}_2\text{H}^+}$ compared to models without SPs.

In the high X-ray model, CL_XH_SP, the picture is quite different. $N_{\text{N}_2\text{H}^+}$ is now dominated by X-rays for $r \gtrsim 30$ au. X-rays are efficiently scattered towards the midplane and therefore $\zeta_{\text{X}} > \zeta_{\text{SP}}$ in the cold N_2H^+ layer (see also Fig. 7). X-rays affect the cold N_2H^+ layer at all radii therefore the slope of $N_{\text{N}_2\text{H}^+}$ is steeper than in the model where SP dominate (compare the blue solid line with the red dashed line in Fig. 9).

Our results show that HCO^+ is always significantly affected by SP ionization but N_2H^+ only in models with low CRs and normal X-rays (for $r > 30$ au). As SPs can only reach the upper layers of the cold molecular layer, N_2H^+ is less sensitive to SP ionization than HCO^+ .

3.3.4. Impact of SPs in the Turner model

In the Turner model SP ionization is just a scaled up version of CR ionization where SPs can also penetrate the disk vertically (see Appendix D). The results of the Turner models are also shown in Figs. 9 and 10.

In the ISM CR models there is no significant impact on HCO^+ and N_2H^+ by SP ionization. ζ_{SP} is significantly lower at low column densities compared to our models (see Sect. 3.1). Therefore X-rays are the dominant ionization source in the warm molecular layer and HCO^+ is not significantly affected by SP ionization. The slight increase in the HCO^+ column density is mainly due to the higher X-ray luminosity in the Turner model compared to our reference model with normal X-rays. Similar to our models CRs dominate in the cold molecular layer.

In the Turner model with low CRs, SPs become the dominant ionization source in the cold molecular layer as they also penetrate the disk vertically. In this layer ζ_{SP} reaches values of $\approx 10^{-17} \text{ s}^{-1}$ at $r \approx 100$ au. However, in the Turner model SPs also cannot compensate for a low CR ionization rate as $\zeta_{\text{SP}} \propto 1/r^2$ (geometric dilution).

The impact of SPs in the Turner model is rather limited and restricted to the cold molecular layer, in strong contrast to our models. The differences are mainly due to the assumptions concerning the SP transport. In the Turner model SPs hit the surface of the disk and penetrate the disk vertically, whereas we assume that SPs travel only along radial rays. However, both approaches are an approximation of a likely more complex picture of SP transport in disks. We discuss this in more detail in Sect. 4.3.

4. Discussion

4.1. Constraining the SP flux of T Tauri stars

SP ionization has a significant impact on the column densities of HCO^+ and N_2H^+ in all our models. To actually constrain the SP flux from observations it is necessary to disentangle the contribution of SP ionization from the competing ionization sources CRs and X-rays.

From a chemical point of view all three ionization sources act the same way, they ionize molecular hydrogen and drive the molecular ion chemistry. However, they also show distinct differences in how they irradiate and penetrate the disk. CRs act like a background source and irradiate the disk isotropically, whereas X-rays and SPs originate from the star and act like a point source. A further difference is their energy distribution. Because of their high energies, CRs and SPs tend to move on straight lines whereas (hard) X-rays also experience scattering during their interaction with the disk.

Those differences in their irradiation properties and their energy distribution allow to disentangle their impact on the ion chemistry at different locations in the disk. Our models show that the stellar ionization sources are more effective closer to the star and at the surface layers of the disk (Fig. 10). X-rays can also become an important ionization source in the midplane of the disk but not for the whole disk as, roughly speaking, the ionization rate of stellar ionization sources is $\propto 1/r^2$. CR ionization affects the whole disk, but is, in contrast to the stellar ionization

A&A 603, A96 (2017)

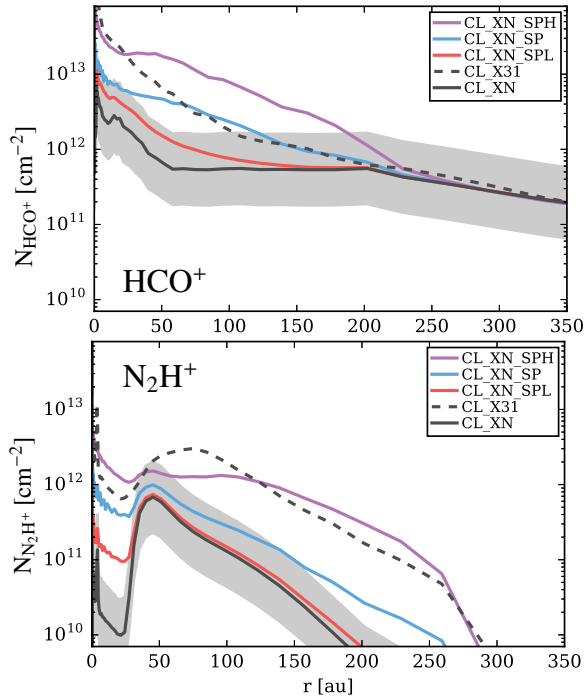


Fig. 11. Comparison of column densities for HCO^+ (top) and N_2H^+ (bottom) for models with varying SP flux and very strong X-ray emission. For all models the low CR ionization rates are used. Shown are the reference model with normal X-rays (black, CL_XN), the model with the typical SP flux (blue, CL_XN_SP) and models with a factor of ten higher (purple, CL_XN_SPH) and factor of ten lower (red, CL_XN_SPL) SP flux. The dashed black line shows the model with $L_X = 3 \times 10^{31} \text{ erg s}^{-1}$ and no SPs. The grey shaded area marks a difference of a factor of three in the column densities relative to the reference model CL_XN.

sources, more important for the outer disk and the cold layers and the midplane of the disk (this argument also holds for SLR ionization).

So far we have only shown models using the commonly proposed SP flux of $f_p(E_p \geq 10 \text{ MeV}) \approx 10^7 \text{ protons cm}^{-2} \text{ s}^{-1}$ (e.g. Feigelson et al. 2002). However, this value should be only seen as an order of magnitude estimate (see Sect. 2.2).

In Fig. 11 we show the column densities for HCO^+ and N_2H^+ for models with a SP flux a factor of ten higher and lower with respect to the reference value. Also shown are the reference model for the low CR case CL_XN and the model with the reference SP flux CL_XN_SP. For these models we use the low CR ionization rate ($\zeta_{\text{CR}} \approx 2 \times 10^{-19} \text{ s}^{-1}$) and the normal X-ray luminosity ($L_X = 10^{30} \text{ erg s}^{-1}$). Further we show a model with $L_X = 3 \times 10^{31} \text{ erg s}^{-1}$, to illustrate the impact of (very) strong X-ray emission (e.g. $\zeta_X \geq 10^{-17} \text{ s}^{-1}$ in the disk midplane).

In the low SP flux model (CL_XN_SPL) the impact on HCO^+ and N_2H^+ is quite limited. For such a case it is still possible to define upper limits for the SP flux in disks.

In the high SP flux model (CL_XN_SPH) the SP ionization rate reaches values of $\zeta_{\text{SP}} \geq 10^{-13} \text{ s}^{-1}$ and $\zeta_{\text{SP}} \approx 10^{-17} \text{ s}^{-1}$ in the warm and cold molecular layer respectively. The N_2H^+ column density profile beyond the radial CO ice line is comparable to the profile for models with ISM CRs (compare with Fig. 9). Also the model with very high X-rays (CL_X31) and no SPs shows

a similar profile for N_2H^+ . However, as seen from Fig. 11 the corresponding HCO^+ profiles differ significantly.

Comparing the very high X-ray model (CL_X31) to the reference model with SPs (CL_XN_SP) shows that the corresponding HCO^+ profiles are similar but the N_2H^+ profiles differ by an order of magnitude. This shows again that it is indeed possible to distinguish between the different ionization sources by simultaneous modelling of HCO^+ and N_2H^+ column density profiles.

To trace this interplay of ionization sources, spatially resolved observations of molecular ion lines tracing different vertical layers of the disk are required. With modern (sub)millimetre interferometers like the Atacama Large Millimeter Array (ALMA), the NOthern Extended Millimeter Array (NOEMA) and the Submillimeter Array (SMA) such observations with a spatial resolution of tens of au are already possible (e.g. Qi et al. 2013b; Cleeves et al. 2015; ALMA Partnership et al. 2015; Yen et al. 2016) and will become available on a regular basis in the near future. Here, we use HCO^+ and N_2H^+ as the tracers of the warm and cold molecular layer respectively, but also other molecules like DCO^+ , which traces similar regions as N_2H^+ (Teague et al. 2015; Mathews et al. 2013) can be used.

Complementary, far-infrared lines of HCO^+ and N_2H^+ , as used by Ceccarelli et al. (2014) to trace SP ionization in a protostellar envelope, are good tracers of molecular ion emission in the warm inner region of the disk. However, a more detailed analysis with proper modelling of line emission is required to identify the best observational tracers of SP ionization. We will present such an analysis in a follow-up paper.

4.2. Chemical implications

Besides the H_2 ionization rates there are other “chemical parameters”, which have an impact on the molecular ion abundance in disks. In the following we discuss the dependence of our results on the location of the CO ice line, depletion of CO and the assumed initial metal abundances. Those chemical properties of disks are not well constrained from observations and/or can vary between different targets.

4.2.1. Location of the CO ice line

Recent ALMA observations provide direct constraints on the location of the CO ice line. However, these results depend on the method or more precisely the molecule used to trace the CO ice line (see Qi et al. 2013b; Schwarz et al. 2016; Nomura et al. 2016, for TW Hya). Further, due to complex chemical processes like the CO sink effect it is possible that the actual location of the CO ice line does not only depend on the CO freeze-out temperature (Aikawa et al. 2015, Sect. 3.3.2).

To investigate the dependence of our results on the location of the CO ice line we artificially moved the CO ice line in our model by adapting the binding energy for CO. We consider two cases: $E_B(\text{CO}) = 950 \text{ K}$ and $E_B(\text{CO}) = 1350 \text{ K}$ (i.e. 200 K lower and higher compared to our reference model). In both cases we kept the ratio of $E_B(\text{N}_2)/E_B(\text{CO}) = 0.67$ constant (see Appendix B.2.2). As a consequence also the N_2H^+ layer moves accordingly to the CO ice line (see Sect. 3.3.1). For $E_B(\text{CO}) = 950 \text{ K}$ the CO ice line moves to $T_d \approx 20\text{--}24 \text{ K}$, (i.e. deeper into the disk) and for $E_B(\text{CO}) = 1350 \text{ K}$ to $T_d \approx 25\text{--}36 \text{ K}$ (i.e. higher up in the disk).

For a CO ice line deeper in the disk the contribution of CR ionization to the total column of HCO^+ and N_2H^+ increases in the ISM CR models. In the ISM CR models SP ionization is not

significant anymore (i.e. N_{HCO^+} increases by less than a factor two). However, in the low CR models the impact of SPs remains significant.

A CO ice line higher up in the disk has the opposite effect. The total column densities of the molecular ions are now dominated by layers higher up in the disk which can efficiently be ionized by SPs. As a consequence the relative contribution of SP ionization to N_{HCO^+} and $N_{\text{N}_2\text{H}^+}$ increases.

In summary for a CO ice line location deeper in the disk SP ionization becomes less important, for a CO ice line higher up in the disk SP ionization becomes more important. However, in both cases the interplay of the different ionization sources is qualitatively speaking similar to what is shown in Fig. 10.

4.2.2. CO depletion

There is observational evidence for CO depletion in protoplanetary disks (Dutrey et al. 1997; Bruderer et al. 2012; Favre et al. 2013; Kama et al. 2016a; Schwarz et al. 2016; McClure et al. 2016). The best constraint case is TW Hya. Using spatially resolved ALMA spectral line observations of several CO isotopologues Schwarz et al. (2016) derived a uniform CO abundance of $\approx 10^{-6}$ in the warm molecular layer, two orders of magnitude lower than the canonical value of $\approx 10^{-4}$. However, the degree of CO depletion seems to vary from source to source. Using *Herschel* HD J = 1–0 line observations McClure et al. (2016) derived CO depletions of a factor of approximately five and up to ≈ 100 for DM Tau and GM Aur, respectively.

The cause of CO depletion in disks is not yet clear. Although freeze-out of CO certainly contributes to depletion it is unlikely that it is the only process acting. Several other mechanisms that can at least partly explain CO depletion are proposed:

- the destruction of CO by He^+ and the subsequent conversion of atomic carbon to more complex carbon bearing molecules with higher freeze-out temperatures (Aikawa et al. 1996; Bergin et al. 2014; Helling et al. 2014; Furuya & Aikawa 2014);
- depletion of CO in layers above the CO ice line (up to $T \approx 30$ K) due to conversion of CO to CO_2 on the surfaces of dust grains (Reboussin et al. 2015);
- CO isotopologue selective photodissociation, which affects CO isotopologue line emission and therefore the derived CO depletion factors;
- carbon and/or oxygen depletion in the warm disk atmosphere due to settling and mixing of ice coated dust grains (Du et al. 2015; Kama et al. 2016b).

It is as yet unclear which of the proposed mechanisms is the most efficient one; none of them can be excluded with certainty. It is also possible that all of these processes are at work. So far the impact of CO (carbon and/or oxygen depletion) on molecular ion emission was not studied in detail. For the modelling of HCO^+ and N_2H^+ line emission of TW Hya, Cleaves et al. (2015) reduced the initial atomic carbon abundance by two orders of magnitude to match C^{18}O line observation. However, the impact of C and CO depletion on HCO^+ and N_2H^+ was not discussed in detail.

To simulate CO depletion we simply reduce the total carbon and oxygen element abundances by one order of magnitude throughout the disk. This results in a CO abundance of $\approx 10^{-5}$ in the warm molecular layer. We applied this “artificial” CO depletion to all models listed in Table 5; all other parameters of the models are fixed.

The CO depletion models show a factor of ≈ 5 –10 lower N_{HCO^+} for $r \gtrsim 50$ au compared to the non depleted models. For $r < 30$ au $N_{\text{N}_2\text{H}^+}$ increases by more than an order of magnitude. $N_{\text{N}_2\text{H}^+}$ beyond the CO ice line is not affected as $N_{\text{N}_2\text{H}^+}$ resides within the CO freeze-out zone where gas phase CO is anyway depleted.

In the CO depletion models SP ionization is slightly more efficient for $N_{\text{N}_2\text{H}^+}$ as the contribution of the warm N_2H^+ layer to $N_{\text{N}_2\text{H}^+}$ increases. Due to the lower CO abundance in the warm molecular layer the N_2H^+ abundance increases as the destruction pathway via CO is less efficient. For HCO^+ the opposite is true. The HCO^+ abundance decreases by roughly an order of magnitude in the warm molecular layer, whereas in the CO freeze-out zone the impact is smaller (i.e. CO is frozen-out anyway). Relatively speaking the contribution of the cold HCO^+ to N_{HCO^+} increases in the CO depletion models. Therefore the impact of SPs on N_{HCO^+} is less significant whereas X-rays and CRs become more important. Although there are some differences, the impact of SPs on $N_{\text{N}_2\text{H}^+}$ and N_{HCO^+} is qualitatively very similar to the non-depleted models. In particular the main trends derived from Fig. 10 are also seen in the CO depletion models.

CO depletion is certainly more complex than modelled here. A more thorough study of the impact of CO depletion on molecular ion abundances is certainly desirable and possibly provides new constraints on CO gas phase depletion in disks. However, this is beyond the scope of this paper.

4.2.3. Metal abundances

Heavy metals such as sulphur play an important role in the molecular ion disk chemistry (Teague et al. 2015, Rab et al., in prep.). Here we refer with the term metals to the elements Na, Mg, Si, S and Fe. Metal ionization due to UV radiation can produce a large number of free electrons. Those free electrons destroy molecular ions like HCO^+ and N_2H^+ via dissociative recombination. Dissociative recombination is more efficient than radiative recombination of metals. As a consequence a high abundance of metals significantly reduces the abundance of molecular ions (e.g. Mitchell et al. 1978; Graedel et al. 1982).

In the ISM and in disks most of the metals are likely locked up in refractory grains and are therefore depleted compared to Solar abundances. We use metal abundances similar to the commonly used “low metal” abundances (Graedel et al. 1982; Lee et al. 1998a). These low metal abundances are depleted by a factor of ≈ 100 –1000 compared to Solar abundances (i.e. low metal sulphur abundance $\epsilon(\text{S}) \approx 10^{-7}$). However, the actual gas phase abundance of metals is difficult to constrain from observations and a stronger degree of depletion already prior to disk formation is possible (e.g. Maret & Bergin 2007; Maret et al. 2013).

To investigate the dependence of our results on the metal abundances we deplete the initial gas phase metal abundance by an additional factor of ten compared to the low metal abundances (i.e. $\epsilon(\text{S}) \approx 10^{-8}$). This means that a larger fraction of metals is locked-up in refractory dust grains and cannot be released back into the gas phase.

Decreasing the metal abundances increases $\epsilon(\text{HCO}^+)$ in the warm molecular layer by up to an order of magnitude (i.e. the gap in the vertical $\epsilon(\text{HCO}^+)$ profile nearly vanishes; Sect. 3.3.1). In the cold molecular layer the metal abundances are not as important since the metals are frozen-out on dust grains anyway. However, in regions where non-thermal desorption processes are efficient (i.e. metal ices are released back into the gas-phase), $\epsilon(\text{HCO}^+)$ but also $\epsilon(\text{N}_2\text{H}^+)$ are higher by a factor of a few in the lower metal abundance models. The HCO^+ column density

is higher by a factor of between approximately two and three at all radii in the strong metal depletion models compared to the models with the reference abundances. The N_2H^+ column density is only affected for $r \gtrsim 150$ au (higher by a factor of between approximately two and three), where non-thermal desorption of metals is efficient.

Lower gas phase metal abundances lead to an increase of the molecular ion abundances in the warm molecular layer and the contribution of this layer to the total column densities increases. However, in the strong metal depletion models the interplay and the relative contributions to the column densities of the different ionization sources is nearly identical to the reference model grid (i.e. Fig. 10 does not change significantly). Our arguments concerning the impact of SPs on HCO^+ and N_2H^+ are therefore also valid for the case of strong metal depletion.

4.3. Future prospects

Our model results show that SPs can indeed become an important ionization source in T Tauri disks. However, our model should be seen as a first attempt at a comprehensive modelling of SP ionization in protoplanetary disks. In the following we discuss further important aspects like variability, non-stellar origin of SPs, the importance of magnetic fields and future prospects for SP modelling in protoplanetary disks.

4.3.1. Flares and variability

In our models we assumed continuous (i.e. time-averaged) particle fluxes and X-ray luminosities. Although this is a reasonable assumption (see Sect. 2.2) it is likely that the disk is also hit by singular powerful X-ray and/or SP flares.

From the X-ray COUP survey of the ONC cloud, Feigelson et al. (2002) and Wolk et al. (2005) derived a median X-ray flare luminosity of $\approx 6 \times 10^{30}$ erg s^{-1} , comparable to the X-ray luminosity in our high X-ray models, and peak flare luminosities up to 10^{31} erg s^{-1} . The duration of such flares can last from hours up to three days with a typical frequency of roughly one powerful flare per week.

Ilgner & Nelson (2006) argue that for such flare properties the disk ion chemistry responds to time-averaged ionization rates. However, in case the duration between two flares is longer than the recombination time scale in the disk, such singular and strong flares would produce asymmetric features in molecular ion emission (i.e. a singular flare only affects a certain fraction of the disk). The spatially resolved HCO^+ $J = 3-2$ SMA observations of TW Hya show indeed such an asymmetric structure (Cleeves et al. 2015). However, as discussed by Cleeves et al. (2015) these features could also have a different origin like spiral arms or an hidden planet locally heating the disk.

If such asymmetric structures are caused by stellar flares they would provide complementary constraints on the X-ray/SP activity of the star. Multi-epoch data of spatially resolved molecular ion emission is required to prove the flare scenario (i.e. the features should disappear quickly). The current (sub)mm interferometers like ALMA, NOEMA and SMA provide the required spatial resolution and might even allow for monitoring of disks in molecular ion lines on a daily/weekly basis in the future.

Modelling of such observations does not necessarily require 3D chemical models. Assuming that the disk physical structure is not affected by flares, radial cuts through the disk can be modelled with 2D (time-dependent) thermo-chemical models as presented here.

4.3.2. Magnetic fields

In our model we neglect the impact of magnetic fields on the SP transport. Stellar and disk magnetic fields are in particular relevant for the question if particles actually hit the disk (see Feigelson et al. 2002, for a discussion).

Magnetic fields can either drag the particles away from the disk (e.g. like in a wind) but could also funnel the particles and concentrate the ionizing flux in particular regions of the disk. In the first scenario SPs can still have an impact on the upper layers of the disk but certainly not on the disk midplane. In the second scenario particles are likely focused on regions close to the inner radius of the disk and their impact on the outer disk will become less significant. Also the trajectory of the particles will be affected, and they might penetrate the disk also vertically. Our models, where particles are transported only radially, are closer to the wind scenario whereas the Turner model would represent an extreme case for magnetically focused particles. However, to qualitatively estimate the impact of magnetic fields more complex SP transport models are required.

It is possible to consider magnetic field effects in high energy particle transport models (Desch et al. 2004; Padovani & Galli 2011; Padovani et al. 2013b). In principle such methods can also be applied to disk models. The main challenge though is to determine the structure of the star and disk magnetic fields. However, as argued by Ceccarelli et al. (2014) identifying distinct observational signatures of SP ionization in disks and/or envelopes would allow to derive constraints for the magnetic field structure. This is certainly challenging, but with the availability of spatially resolved observational data and interpretation of such data with (improved) thermo-chemical disk models this might be feasible in the near future.

4.3.3. Non-stellar origin of high energy particles

Besides the stellar surface the close environment of young stars offers also alternative particle acceleration sites. X-ray flares and particles can be produced close to the inner disk in the so called reconnection ring where the stellar and disk magnetic field interact (X-wind model Shu et al. 1994, 1997). More recently Padovani et al. (2015, 2016) proposed jet shocks as alternative acceleration sites for high energy particles.

In the X-wind model the particle source and also the X-ray emitting source is located closer to the disk and slightly above the disk midplane. The typically assumed source location in this “lamppost” scenario is $r_L \approx 0.05$ au and $z_L \approx 0.05$ au ($\approx 10 R_\odot$) (Lee et al. 1998b; Igea & Glassgold 1999). For X-rays Ercolano et al. (2009) found that the height of the emitting source has relatively little impact concerning X-ray radiative transfer in disks. Moving the emitting source closer to the disk certainly has an impact on the very inner disk but for e.g. 10 au distance from the star the stellar particle flux increases only by about 1% compared to the stellar origin. The height of the SP emitting source has some impact on where in the disk SPs see a column density $N_{(\text{H})} \gtrsim 10^{25}$ cm^{-2} . For particles accelerated at a height $z_L \approx 0.05$ au and moving along a ray parallel to the midplane this happens at $r \approx 0.5$ au. The consequences are that SPs can penetrate into slightly deeper layers of the disks but they still cannot penetrate to the disk midplane. Therefore our conclusions on the impact of SPs on HCO^+ and N_2H^+ remain valid for the X-wind scenario.

In the jet shock scenario, the emitting source would be located far above the disk. Padovani et al. (2016) considered a particle emitting source located at 1.8×10^3 au above the star and

calculated the resulting ionization rates for a 2D disk structure. Depending on their particle acceleration model they found ionization rates up to $\zeta \approx 10^{-14} \text{ s}^{-1}$ at the surface layers of the disk. Although X-ray ionization rates in the upper layer of the disk are typically higher such an irradiation scenario could have a significant impact on the ionization of the outer disk ($r \gtrsim 50 \text{ au}$). In the outer disk, the jet accelerated particles can penetrate the disk vertically and therefore can also reach the disk midplane (similar to the Turner model, Sect. 3.3.4). This might become important if Galactic CRs are efficiently attenuated (i.e. in the low CR case).

The scenarios described above for non-stellar particle sources are certainly worth being investigated in detail. For the future we plan to extend our model to a proper treatment of such non-stellar emitting sources.

5. Summary and conclusions

In this work we investigated the impact of stellar energetic particle (SP) ionization on disk chemistry with a focus on the common disk ionization tracers HCO^+ and N_2H^+ . We assumed a typical SP flux of $f_p(E_p \approx 10 \text{ MeV}) \approx 10^7 \text{ protons cm}^{-2} \text{ s}^{-1}$ (at 1 au) as commonly proposed for T Tauri stars and a particle energy distribution derived from measurements of solar particle events. Based on a detailed particle transport model we derived an easy to use formula (see Sect. 2.2) to calculate the SP ionization rate in the disk as a function of hydrogen column density and radius, assuming that the particles can penetrate the disk only radially. With a small grid of models considering varying properties of the competing high energy disk ionization sources, X-rays and Galactic cosmic rays, we studied the interplay of the different ionization sources and identified possible observational tracers of SP ionization. Our main conclusions are the following:

- SPs cannot penetrate the disk midplane. At hydrogen column densities $N_{(\text{H})} \gtrsim 10^{25} \text{ cm}^{-2}$ even the most energetic particles are attenuated (stopped) and the SP ionization rate drops rapidly. As the radial hydrogen column densities for full T Tauri disks are typically $N_{(\text{H})} \gg 10^{25} \text{ cm}^{-2}$ the midplane SP ionization rate is $\zeta_{\text{SP}} \ll 10^{-20} \text{ s}^{-1}$ already at a distance of 1 au from the star.
- For the assumed SP flux (see above), SPs become the dominant H_2 ionization source in the warm molecular layer of the disk above the CO ice line, provided that SPs are not shielded by magnetic fields. This is even true for enhanced X-ray luminosities (i.e. $L_X = 5 \times 10^{30} \text{ erg s}^{-1}$).
- SP ionization can increase the HCO^+ and N_2H^+ column densities by factors of between approximately three and ten for disk radii $r \lesssim 200 \text{ au}$. The impact is more significant in models with low CR ionization rates (i.e. $\zeta_{\text{CR}} \approx 10^{-19} \text{ s}^{-1}$).
- SP ionization becomes insignificant for an SP flux one order of magnitude lower than the proposed value for T Tauri stars. In such a case H_2 ionization is solely dominated by X-rays and CRs.
- As SPs cannot penetrate the deep layers of the disk, X-rays and/or CRs usually remain the dominant H_2 ionization source in the cold disk layers (i.e. below the CO ice line). Therefore HCO^+ , which traces the warm molecular layer, is more sensitive to SP ionization than N_2H^+ that resides in the cold molecular layer.
- Simultaneous modelling of spatially resolved radial intensity profiles of molecular ions tracing different vertical layers of the disk allows to disentangle the contributions of the competing high energy ionization sources to the total H_2 ionization rate. Consequently such observations allow to constrain

the SP flux in disks. Such a method is likely to be model dependent and ancillary observations constraining the vertical chemical structure of disks are required.

We have shown that stellar energetic particles can be an important ionization agent for disk chemistry. Modelling of spatially resolved observations of molecular ions with a model such as presented here allows to put first constraints on the stellar particle flux in disks around T Tauri stars.

Further model improvements concerning the stellar energetic particle transport (i.e. magnetic fields) are required to answer the question to what extent stellar particles reach the disk. Additionally non-stellar origins (i.e. jets) of high energy particles should be considered. With such models and spatially resolved molecular ion observations it will be possible to put stringent constraints on stellar energetic particle fluxes of T Tauri stars and to infer properties of the stellar and disk magnetic fields.

Acknowledgements. The authors thank the anonymous referee for useful suggestions and comments. We want to thank C. Dominik for very helpful discussions on stellar particle transport in disks. The research leading to these results has received funding from the European Union Seventh Framework Programme FP7-2011 under grant agreement No. 284405. R.CH. acknowledges funding by the Austrian Science Fund (FWF): project number P24790. M.P. acknowledges funding from the European Unions Horizon 2020 research and innovation programme under the Marie Skłodowska-Curie grant agreement No. 664931. The computational results presented have been achieved using the Vienna Scientific Cluster (VSC). This publication was supported by the Austrian Science Fund (FWF). This research has made use of NASA's Astrophysics Data System. All figures were made with the free Python module Matplotlib (Hunter 2007).

References

- Adams, N., Smith, D., & Grief, D. 1978, *International Journal of Mass Spectrometry and Ion Physics*, 26, 405
- Aikawa, Y., Miyama, S. M., Nakano, T., & Umebayashi, T. 1996, *ApJ*, 467, 684
- Aikawa, Y., Umebayashi, T., Nakano, T., & Miyama, S. M. 1997, *ApJ*, 486, L51
- Aikawa, Y., Furuya, K., Nomura, H., & Qi, C. 2015, *ApJ*, 807, 120
- ALMA Partnership, Brogan, C. L., Pérez, L. M., et al. 2015, *ApJ*, 808, L3
- Andrews, S. M., Wilner, D. J., Hughes, A. M., Qi, C., & Dullemond, C. P. 2009, *ApJ*, 700, 1502
- Aresu, G., Kamp, I., Meijerink, R., et al. 2011, *A&A*, 526, A163
- Bergeron, H., Rougeau, N., Sidis, V., et al. 2008, *J. Phys. Chem. A*, 112, 11921
- Bergin, E. A., & Langer, W. D. 1997, *ApJ*, 486, 316
- Bergin, E. A., Ciardi, D. R., Lada, C. J., Alves, J., & Lada, E. A. 2001, *ApJ*, 557, 209
- Bergin, E. A., Cleeves, L. I., Crockett, N., & Blake, G. A. 2014, *Faraday Discussions*, 168, 61
- Bethell, T. J., & Bergin, E. A. 2011, *ApJ*, 740, 7
- Bisschop, S. E., Fraser, H. J., Öberg, K. I., van Dishoeck, E. F., & Schlemmer, S. 2006, *A&A*, 449, 1297
- Bohme, D. K., Mackay, G. I., & Schiff, H. I. 1980, *J. Chem. Phys.*, 73, 4976
- Borget, F., Chiavassa, T., Allouche, A., & Aycard, J. P. 2001, *J. Phys. Chem. B*, 105, 449
- Botschwina, P., Horn, M., Flugge, J., & Seeger, S. 1993, *J. Chem. Soc., Faraday Trans.*, 89, 2219
- Brott, I., & Hauschildt, P. H. 2005, in *The Three-Dimensional Universe with Gaia*, eds. C. Turon, K. S. O'Flaherty, & M. A. C. Perryman, *ESA SP*, 576, 565
- Bruderer, S., van Dishoeck, E. F., Doty, S. D., & Herczeg, G. J. 2012, *A&A*, 541, A91
- Ceccarelli, C., & Dominik, C. 2005, *A&A*, 440, 583
- Ceccarelli, C., Dominik, C., López-Sepulcre, A., et al. 2014, *ApJ*, 790, L1
- Cleeves, L. I., Adams, F. C., & Bergin, E. A. 2013, *ApJ*, 772, 5
- Cleeves, L. I., Bergin, E. A., & Adams, F. C. 2014, *ApJ*, 794, 123
- Cleeves, L. I., Bergin, E. A., Qi, C., Adams, F. C., & Öberg, K. I. 2015, *ApJ*, 799, 204
- Cleeves, L. I., Bergin, E. A., O'D. Alexander, C. M., et al. 2016, *ApJ*, 819, 13
- Collings, M. P., Anderson, M. A., Chen, R., et al. 2004, *MNRAS*, 354, 1133
- Desch, S. J., Connolly, Jr., H. C., & Srinivasan, G. 2004, *ApJ*, 602, 528
- Draine, B. T., & Bertoldi, F. 1996, *ApJ*, 468, 269
- Du, F., Bergin, E. A., & Hogerheijde, M. R. 2015, *ApJ*, 807, L32
- Dubrulle, B., Morfill, G., & Sterzik, M. 1995, *Icarus*, 114, 237

A&A 603, A96 (2017)

- Dulieu, F., Congiu, E., Noble, J., et al. 2013, *Sci. Rep.*, **3**, 1338
- Dullemond, C. P., & Dominik, C. 2004, *A&A*, **421**, 1075
- Dutrey, A., Guilloteau, S., & Guelin, M. 1997, *A&A*, **317**, L55
- Dutrey, A., Henning, T., Guilloteau, S., et al. 2007, *A&A*, **464**, 615
- Dutrey, A., Semenov, D., Chapillon, E., et al. 2014, *Protostars and Planets VI*, 317
- Ercolano, B., & Glassgold, A. E. 2013, *MNRAS*, **436**, 3446
- Ercolano, B., Clarke, C. J., & Drake, J. J. 2009, *ApJ*, **699**, 1639
- Favre, C., Cleeves, L. I., Bergin, E. A., Qi, C., & Blake, G. A. 2013, *ApJ*, **776**, L38
- Fayolle, E. C., Balfé, J., Loomis, R., et al. 2016, *ApJ*, **816**, L28
- Feigelson, E. D., & Montmerle, T. 1999, *ARA&A*, **37**, 363
- Feigelson, E. D., Garmire, G. P., & Pravdo, S. H. 2002, *ApJ*, **572**, 335
- Flower, D. R. 1999, *MNRAS*, **305**, 651
- France, K., Schindhelm, E., Bergin, E. A., Roueff, E., & Abgrall, H. 2014, *ApJ*, **784**, 127
- Furuya, K., & Aikawa, Y. 2014, *ApJ*, **790**, 97
- Garrod, R. T., & Herbst, E. 2006, *A&A*, **457**, 927
- Glassgold, A. E., Najita, J., & Igea, J. 1997, *ApJ*, **480**, 344
- Glassgold, A. E., Feigelson, E. D., Montmerle, T., & Wolk, S. 2005, in *Chondrites and the Protoplanetary Disk*, eds. A. N. Krot, E. R. D. Scott, & B. Reipurth, *ASP Conf. Ser.*, **341**, 165
- Glassgold, A. E., Galli, D., & Padovani, M. 2012, *ApJ*, **756**, 157
- Glauser, A. M., Güdel, M., Watson, D. M., et al. 2009, *A&A*, **508**, 247
- Gounelle, M., Shu, F. H., Shang, H., et al. 2001, *ApJ*, **548**, 1051
- Gounelle, M., Shu, F. H., Shang, H., et al. 2006, *ApJ*, **640**, 1163
- Graedel, T. E., Langer, W. D., & Frerking, M. A. 1982, *ApJS*, **48**, 321
- Güdel, M., & Nazé, Y. 2009, *A&ARv*, **17**, 309
- Güdel, M., Briggs, K. R., Arzner, K., et al. 2007, *A&A*, **468**, 353
- Güdel, M., Lahuis, F., Briggs, K. R., et al. 2010, *A&A*, **519**, A113
- He, J., Jing, D., & Vidali, G. 2014, *Phys. Chem. Chem. Phys. (Incorporating Faraday Transactions)*, **16**, 3493
- Helling, C., Woitke, P., Rimmer, P. B., et al. 2014, *Life*, **4**, 142
- Herbst, E., Payzant, J. D., Schiff, H. I., & Bohme, D. K. 1975, *ApJ*, **201**, 603
- Hily-Blant, P., Walmsley, M., Pineau Des Forêts, G., & Flower, D. 2010, *A&A*, **513**, A41
- Hunter, J. D. 2007, *Comput. Sci. Eng.*, **9**, 90
- Igea, J., & Glassgold, A. E. 1999, *ApJ*, **518**, 848
- Ilgner, M., & Nelson, R. P. 2006, *A&A*, **455**, 731
- Kama, M., Bruderer, S., Carney, M., et al. 2016a, *A&A*, **588**, A108
- Kama, M., Bruderer, S., van Dishoeck, E. F., et al. 2016b, *A&A*, **592**, A83
- Kamp, I., Tilling, I., Woitke, P., Thi, W.-F., & Hogerheijde, M. 2010, *A&A*, **510**, A18
- Kamp, I., Thi, W.-F., Woitke, P., et al. 2017, *A&A*, submitted
- Klippenstein, S. J., Georgievskii, Y., & McCall, B. J. 2010, *J. Phys. Chem. A*, **114**, 278
- Lawson, P. A., Osborne, D., Jr., & Adams, N. G. 2011, *Int. J. Mass Spectr.*, **304**, 41
- Le Gal, R., Hily-Blant, P., Faure, A., et al. 2014, *A&A*, **562**, A83
- Lee, H.-H., Roueff, E., Pineau des Forets, G., et al. 1998a, *A&A*, **334**, 1047
- Lee, T., Shu, F. H., Shang, H., Glassgold, A. E., & Rehm, K. E. 1998b, *ApJ*, **506**, 898
- Li, X., Heays, A. N., Visser, R., et al. 2013, *A&A*, **555**, A14
- Lynden-Bell, D., & Pringle, J. E. 1974, *MNRAS*, **168**, 603
- Maret, S., & Bergin, E. A. 2007, *ApJ*, **664**, 956
- Maret, S., Bergin, E. A., & Tafalla, M. 2013, *A&A*, **559**, A53
- Mathews, G. S., Klaassen, P. D., Juhász, A., et al. 2013, *A&A*, **557**, A132
- McClure, M. K., Bergin, E. A., Cleeves, L. I., et al. 2016, *ApJ*, **831**, 167
- McElroy, D., Walsh, C., Markwick, A. J., et al. 2013, *A&A*, **550**, A36
- McKeegan, K. D., Chaussidon, M., & Robert, F. 2000, *Science*, **289**, 1334
- Meijerink, R., Aresu, G., Kamp, I., et al. 2012, *A&A*, **547**, A68
- Mewaldt, R. A., Cohen, C. M. S., Labrador, A. W., et al. 2005, *J. Geophys. Res. (Space Phys.)*, **110**, 9
- Mewaldt, R. A., Cohen, C. M. S., Mason, G. M., Haggerty, D. K., & Desai, M. I. 2007, *Space Sci. Rev.*, **130**, 323
- Meyer, B. S., & Clayton, D. D. 2000, *Space Sci. Rev.*, **92**, 133
- Min, M., Hovenier, J. W., & de Koter, A. 2005, *A&A*, **432**, 909
- Min, M., Rab, C., Woitke, P., Dominik, C., & Ménard, F. 2016, *A&A*, **585**, A13
- Minissale, M., Congiu, E., & Dulieu, F. 2014, *J. Chem. Phys.*, **140**, 074705
- Minissale, M., Congiu, E., & Dulieu, F. 2016a, *A&A*, **585**, A146
- Minissale, M., Dulieu, F., Cazaux, S., & Hocuk, S. 2016b, *A&A*, **585**, A24
- Mitchell, J. B. A. 1990, *Phys. Rep.*, **186**, 215
- Mitchell, G. F., Kuntz, P. J., & Ginsburg, J. L. 1978, *ApJS*, **38**, 39
- Noble, J. A., Congiu, E., Dulieu, F., & Fraser, H. J. 2012, *MNRAS*, **421**, 768
- Nomura, H., Tsukagoshi, T., Kawabe, R., et al. 2016, *ApJ*, **819**, L7
- Öberg, K. I., van Broekhuizen, F., Fraser, H. J., et al. 2005, *ApJ*, **621**, L33
- Öberg, K. I., Qi, C., Fogel, J. K. J., et al. 2010, *ApJ*, **720**, 480
- Öberg, K. I., Qi, C., Fogel, J. K. J., et al. 2011a, *ApJ*, **734**, 98
- Öberg, K. I., Qi, C., Wilner, D. J., & Andrews, S. M. 2011b, *ApJ*, **743**, 152
- Padovani, M., & Galli, D. 2011, *A&A*, **530**, A109
- Padovani, M., Galli, D., & Glassgold, A. E. 2009, *A&A*, **501**, 619
- Padovani, M., Galli, D., & Glassgold, A. E. 2013a, *A&A*, **549**, C3
- Padovani, M., Hennebelle, P., & Galli, D. 2013b, *A&A*, **560**, A114
- Padovani, M., Hennebelle, P., Marcowith, A., & Ferrière, K. 2015, *A&A*, **582**, L13
- Padovani, M., Marcowith, A., Hennebelle, P., & Ferrière, K. 2016, *A&A*, **590**, A8
- Payzant, J. D. 1975, *J. Chem. Phys.*, **63**, 149
- Qi, C., Kessler, J. E., Koerner, D. W., Sargent, A. I., & Blake, G. A. 2003, *ApJ*, **597**, 986
- Qi, C., Öberg, K. I., & Wilner, D. J. 2013a, *ApJ*, **765**, 34
- Qi, C., Öberg, K. I., Wilner, D. J., et al. 2013b, *Science*, **341**, 630
- Qi, C., Öberg, K. I., Andrews, S. M., et al. 2015, *ApJ*, **813**, 128
- Rakshit, A. 1982, *International Journal of Mass Spectrometry and Ion Physics*, **41**, 185
- Reames, D. V. 2013, *Space Sci. Rev.*, **175**, 53
- Reames, D. V. 2015, *Space Sci. Rev.*, **194**, 303
- Reboussin, L., Wakelam, V., Guilloteau, S., Hersant, F., & Dutrey, A. 2015, *A&A*, **579**, A82
- Reedy, R. C. 2012, *Lun. Planet. Sci. Conf.*, **43**, 1285
- Schöier, F. L., van der Tak, F. F. S., van Dishoeck, E. F., & Black, J. H. 2005, *A&A*, **432**, 369
- Schoonjans, T., Brunetti, A., Golosio, B., et al. 2011, *Spectrochim. Acta*, **66**, 776
- Schwarz, K. R., Bergin, E. A., Cleeves, L. I., et al. 2016, *ApJ*, **823**, 91
- Shu, F., Najita, J., Ostriker, E., et al. 1994, *ApJ*, **429**, 781
- Shu, F. H., Shang, H., Glassgold, A. E., & Lee, T. 1997, *Science*, **277**, 1475
- Takayanagi, K. 1973, *PASJ*, **25**, 327
- Teague, R., Semenov, D., Guilloteau, S., et al. 2015, *A&A*, **574**, A137
- Thi, W.-F., Woitke, P., & Kamp, I. 2011, *MNRAS*, **412**, 711
- Thi, W.-F., Pinte, C., Pantin, E., et al. 2014, *A&A*, **561**, A50
- Tielens, A. G. G. M., & Allamandola, L. J. 1987, in *Interstellar Processes*, eds. D. J. Hollenbach, & H. A. Thronson, Jr., *ASSL*, **134**, 397
- Trappitsch, R., & Ciesla, F. J. 2015, *ApJ*, **805**, 5
- Turner, N. J., & Drake, J. F. 2009, *ApJ*, **703**, 2152
- Umebayashi, T., & Nakano, T. 2009, *ApJ*, **690**, 69
- Wakelam, V., Herbst, E., Loison, J.-C., et al. 2012, *ApJS*, **199**, 21
- Wakelam, V., Loison, J.-C., Herbst, E., et al. 2015, *ApJS*, **217**, 20
- Wakelam, V., Smith, I. W. M., Loison, J.-C., et al. 2013, *ArXiv e-prints* [[arXiv:1310.4350](https://arxiv.org/abs/1310.4350)]
- Ward, M. D., Hogg, I. A., & Price, S. D. 2012, *MNRAS*, **425**, 1264
- Webber, W. R. 1998, *ApJ*, **506**, 329
- Williams, J. P., & Cieza, L. A. 2011, *ARA&A*, **49**, 67
- Woitke, P., Kamp, I., & Thi, W.-F. 2009, *A&A*, **501**, 383
- Woitke, P., Riaz, B., Duchêne, G., et al. 2011, *A&A*, **534**, A44
- Woitke, P., Min, M., Pinte, C., et al. 2016, *A&A*, **586**, A103
- Wolk, S. J., Harnden, Jr., F. R., Flaccomio, E., et al. 2005, *ApJS*, **160**, 423
- Yen, H.-W., Liu, H. B., Gu, P.-G., et al. 2016, *ApJ*, **820**, L25

Ch. Rab et al.: Stellar energetic particle ionization

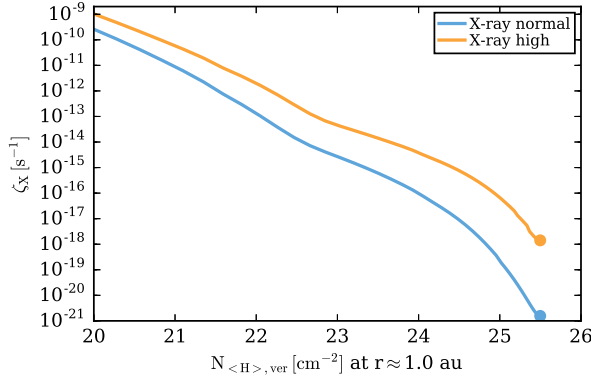


Fig. A.1. X-ray ionization rate ζ_X as a function of vertical hydrogen column density of the disk at a distance of 1 au from the star. Shown are the resulting ionization rates for the two different X-ray spectra (see Sect. 2.3.1). The dots mark the same location ($r = 1$ au, $z = 0$ au) in the disk as the dots in Fig. A.2.

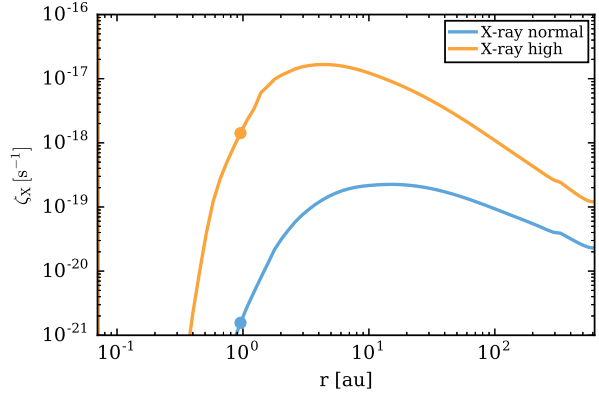


Fig. A.2. X-ray ionization rate ζ_X as a function of radius in the midplane of the disk ($z = 0$). Shown are the resulting ionization rates for the two different X-ray spectra (see Sect. 2.3.1). The dots mark the same location ($r = 1$ au, $z = 0$ au) in the disk as the dots in Fig. A.1.

Appendix A: X-ray radiative transfer

Here we have used the newly developed X-ray radiative transfer module of PRODiMO. The details of this module will be presented in a forthcoming paper Rab et al. (in prep.). Here we only briefly describe the implementation and present results concerning the X-ray ionization rate for comparison with other models.

The main difference between the new model and the existing implementation of Aresu et al. (2011), Meijerink et al. (2012) is the treatment of X-ray scattering. We used the absorption and scattering cross-section from the publicly available *xraylib* library¹ (Schoonjans et al. 2011). For the X-ray radiative transfer we use the same numerical approach (e.g. use of wavelength bands) as is used for the dust radiative transfer in PRODiMO (Woitke et al. 2009). We assumed isotropic scattering but applied a correction factor (anisotropic factor g) to account for anisotropic Compton scattering. According to Cleeves et al. (2016), neglecting anisotropic scattering has only a limited impact on the X-ray ionization rate of about a factor of two. We consider this possible deviation as not significant for the results presented here. We further disregarded the dust in the X-ray radiative transfer, since with the assumed gas to dust ratio of 100 and dust settling X-ray photons mainly interact with the gas (Bethell & Bergin 2011; Glassgold et al. 2012).

The X-ray chemistry in PRODiMO is presented in detail in Meijerink et al. (2012). The interaction of X-rays with the gas changes the species abundances and consequently also the X-ray opacities. We therefore iterated between the X-ray radiative transfer and the chemistry until convergence is reached.

In Figs. A.1 and A.2 we show the X-ray ionization rate ζ_X for our disk model (Sect. 2.4) and for both X-ray spectra (Sect. 2.3.1). Figure A.1 shows ζ_X as a function of vertical column density at 1 au whereas Fig. A.2 shows ζ_X in the midplane of the disk as a function of radius. These results are in good quantitative agreement with Ercolano & Glassgold (2013) and Cleeves et al. (2015) considering that different disk models and different implementations of X-ray radiative transfer (e.g. cross-sections) are applied.

¹ <https://github.com/tschoonj/xraylib>

Appendix B: Chemistry

For the chemical reaction network we use the UMIST 2012 database for gas phase chemistry (McElroy et al. 2013) for a selection of 235 species. Additionally the network includes X-ray chemistry (Aresu et al. 2011; Meijerink et al. 2012), PAH (polycyclic aromatic hydrocarbons) chemistry (Thi et al. 2014), adsorption and desorption (thermal, CR and photo desorption) for ice species and H₂ formation on grains (Woitke et al. 2009). In total the network includes 3143 chemical reactions. For the ice species we use the binding energies from the UMIST 2012 release but updated a couple of values for oxygen bearing species (see Sect. B.2). Further details on the network can be found in Kamp et al. (2017). The most relevant gas phase reactions for HCO⁺ and N₂H⁺ with their rate coefficients are listed in Table B.1.

To test the robustness of our chemical model with respect to HCO⁺ and N₂H⁺ we performed chemical tests with time-dependent chemistry, varying binding energies and the KIDA chemical network (Kinetic Database for Astrochemistry, Wakelam et al. 2012, 2015). The different test models are described in Table B.2 and discussed in the following sections. The results for the HCO⁺ and N₂H⁺ column densities are shown in Figs. B.1 and B.2.

B.1. N₂ shielding

Dust shielding of N₂ photodissociation is strongly reduced in protoplanetary disks due to dust evolution (e.g. dust growth) and shielding by H₂ becomes important (Li et al. 2013). To account for this we implemented the H, H₂ shielding and self-shielding functions for N₂ of Li et al. (2013) in our chemistry model. The data are taken from the Leiden photodissociation database².

We find that N₂ shielding is very important for the abundance structure of N₂H⁺. In models without N₂ shielding the vertical column density of N₂H⁺ is reduced by one order of magnitude throughout the disk. Further the warm N₂H⁺ layer above the vertical CO ice-line vanishes.

² <http://home.strw.leidenuniv.nl/~heays/photo/>

A&A 603, A96 (2017)

Table B.1. Rate coefficients for the main formation and destruction pathways of HCO^+ and N_2H^+ .

Reaction	α	β	γ	$^a k(25 \text{ K})$ ($\text{cm}^3 \text{ s}^{-1}$)	Type	Reference
$\text{H}_3^+ + \text{CO} \rightarrow \text{H}_2 + \text{HCO}^+$	1.35(-9)	-0.14	-3.4	2.2(-9)	Ion-neutral	1
$\text{HCO}^+ + \text{e}^- \rightarrow \text{H} + \text{CO}$	2.40(-7)	-0.69	0.0	1.3(-6)	Dissociative recombination	2
$\text{HCO}^+ + \text{H}_2\text{O} \rightarrow \text{CO} + \text{H}_3\text{O}^+$	2.50(-9)	-0.50	0.0	8.7(-9)	Ion-neutral	3
$\text{H}_3^+ + \text{N}_2 \rightarrow \text{H}_2 + \text{N}_2\text{H}^+$	1.80(-9)	0.0	0.0	1.8(-9)	Ion-neutral	4
$\text{N}_2\text{H}^+ + \text{e}^- \rightarrow \text{H} + \text{N}_2$	2.77(-7)	-0.87	0.0	2.4(-6)	Dissociative recombination	5
$\text{N}_2\text{H}^+ + \text{e}^- \rightarrow \text{NH} + \text{N}$	2.09(-8)	-0.74	0.0	1.3(-7)	Dissociative recombination	5
$\text{N}_2\text{H}^+ + \text{CO} \rightarrow \text{N}_2 + \text{HCO}^+$	8.8(-10)	0.0	0.0	8.8(-10)	Ion-neutral	6

Notes. The rate coefficient is given by the modified Arrhenius equation $k(T) = \alpha \times (T/300 \text{ K}) \times \exp(-\gamma/T)$.

References. UMIST 2012 database (McElroy et al. 2013); (1) Klippenstein et al. (2010); (2) Mitchell (1990); (3) Adams et al. (1978); (4) Rakshit (1982); (5) Lawson et al. (2011); (6) Payzant (1975), Herbst et al. (1975), Bohme et al. (1980).

Table B.2. Chemical test models.

Name	Description
EBUMIST	original binding energies from UMIST 2012
EBN2	N_2 to CO binding energy ratio of 0.9 according to experiments
N2SH	no N_2 shielding
KIDA2011	gas phase chemical network from the KIDA 2011 release
KIDA2014	gas phase chemical network from the KIDA 2014 release

Notes. All chemical test models are based on the reference model CL_XN.

B.2. Binding energies

B.2.1. Oxygen binding energy

Several laboratory experiments (e.g. Ward et al. 2012; He et al. 2014; Minissale et al. 2016a,b) reported binding energies for oxygen in the range of $E_B(\text{O}) = 1500\text{--}1800 \text{ K}$. This is significantly higher than the value of $E_B(\text{O}) = 800 \text{ K}$ listed in the UMIST 2012 database. We therefore updated the binding energies for oxygen and several other oxygen bearing species with the values listed in Minissale et al. (2016b). The new values with their references are given in Table B.3.

The higher binding energy for oxygen has a significant impact on N_2H^+ . Using the UMIST 2012 binding energy reduces the N_2H^+ column density by about a factor of three for $r \gtrsim 50 \text{ au}$ (see model EBUMIST in Fig. B.1). Similar to CO, oxygen also destroys N_2H^+ via the reaction $\text{O} + \text{N}_2\text{H}^+ \rightarrow \text{N}_2 + \text{OH}^+$. Due to this reaction the N_2H^+ abundance is strongly reduced in a thin layer below the vertical CO ice line and above the vertical oxygen ice line. With the higher binding energy for oxygen this thin layer vanishes as oxygen freezes-out at higher temperatures than CO.

For HCO^+ the dip in the column density profile at $r \approx 50 \text{ au}$ alone is significantly affected. In this region HCO^+ is efficiently destroyed by water. Removing oxygen and OH from the gas phase reduces also the water abundance near the vertical CO ice line, consequently the HCO^+ abundance increases.

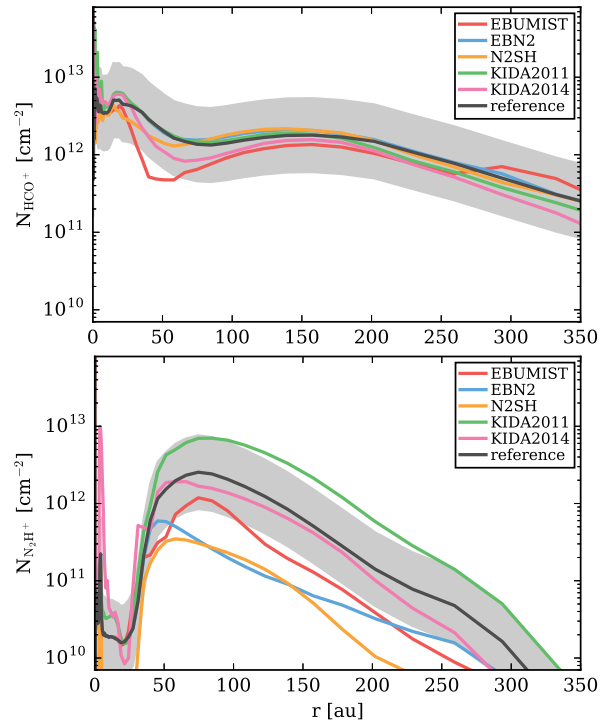


Fig. B.1. Comparison of column densities for HCO^+ and N_2H^+ for models with different chemical networks or binding energies (see Table B.2). The grey shaded area marks a difference of a factor of 3 in the column densities relative to the reference model (black line).

B.2.2. N_2 binding energy

In the UMIST 2012 database $E_B(\text{N}_2) = 0.67 \times E_B(\text{CO})$ (see Table B.3). This ratio is close to the value of 0.65 used to explain observations of prestellar cores showing that N_2 freezes out at lower temperatures than CO (e.g. Bergin & Langer 1997; Bergin et al. 2001; Ceccarelli & Dominik 2005). Also disk observations of N_2H^+ indicate that $E_B(\text{N}_2) < E_B(\text{CO})$ (Qi et al. 2003, 2013b). However, the ratio of 0.65 is in contradiction with laboratory experiments which show $E_B(\text{N}_2) \approx 0.9 \times E_B(\text{CO})$ (Öberg et al. 2005; Bisschop et al. 2006; Fayolle et al. 2016). One explanation for this discrepancy might be differential freeze-out but it

Ch. Rab et al.: Stellar energetic particle ionization

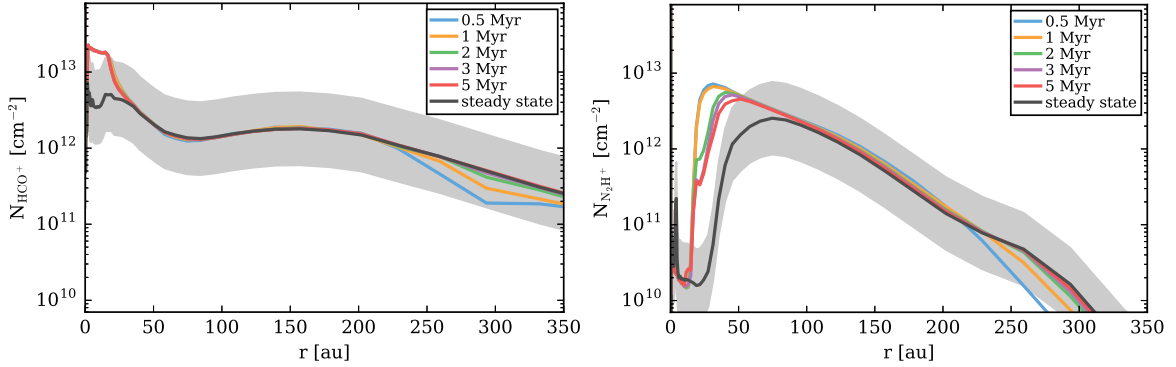


Fig. B.2. Comparison of time-dependent and steady-state chemistry models. Shown are the vertical column densities for HCO^+ and N_2H^+ at different chemical ages of the disk (colored lines) and the steady-state results (black line). The grey shaded area marks a difference of a factor 3 in the column densities relative to the steady-state model.

Table B.3. Important binding energies.

Species	E_B UMIST 2012 (K)	E_B (K)
CO	1150 ^a	
N_2	790 ^b	
O	800 ^c	1500 ^e
O_2	1000 ^d	1250 ^f
O_3	1800 ^d	2100 ^g
OH	2850 ^d	4600 ^h

Notes. The second column shows the values from the UMIST 2012 database (McElroy et al. 2013), the third column the updated values from Minissale et al. (2016b).

References. ^(a) Garrod & Herbst (2006), Collings et al. (2004); ^(b) Öberg et al. (2005); ^(c) Tielens & Allamandola (1987); ^(d) Garrod & Herbst (2006); ^(e) Bergeron et al. (2008); ^(f) Noble et al. (2012); ^(g) Borget et al. (2001), Minissale et al. (2014); ^(h) Dulieu et al. (2013).

is unclear if this is sufficient (Bisschop et al. 2006; Fayolle et al. 2016).

In our models the N_2H^+ column density drops by about one order of magnitude if we set $E_B(\text{N}_2) = 0.9 \times E_B(\text{CO})$ (model EBN2 in Fig. B.1). Contrary to our model Aikawa et al. (2015) find that in their disk model the N_2H^+ abundance structure is not strongly affected by setting $E_B(\text{N}_2) = E_B(\text{CO})$. They argue that due to the sink effect, CO is depleted anyway and therefore the N_2H^+ abundance is not strongly affected by setting $E_B(\text{N}_2) = E_B(\text{CO})$. We have not included dust surface chemistry in our model therefore the CO sink effect is less efficient. Aikawa et al. (2015) argue that the sink effect depends on various parameters (turbulence in the disk, efficiency of the conversion of CO to less volatile species) therefore they also studied a no-sink model. In this no-sink model the N_2H^+ abundance is sensitive to the binding energy of N_2 , very similar to our models.

The main difference between the sink and no-sink model is the location of the CO ice line and the N_2H^+ layer. In the sink model CO is also depleted at temperatures higher than its sublimation temperature, consequently the CO ice line moves to higher and warmer layers of the disk. In the no-sink model the CO ice line is given by the adsorption/desorption equilibrium for CO which depends on the chosen CO binding energy. However, with the exception of the exact location of the CO ice line and the N_2H^+ layer our models with $E_B(\text{N}_2) = 0.67 \times E_B(\text{CO})$ are

in good agreement with the full chemical network/sink model of Aikawa et al. (2015). We discuss the impact of the CO ice line location on our results in Sect. 4.2.1.

B.3. Comparison to the KIDA chemical network

The reaction rates for nitrogen chemistry are not as well known as for carbon/oxygen chemistry (e.g. Hily-Blant et al. 2010; Le Gal et al. 2014). Wakelam et al. (2013) reviewed a large number of important reactions for nitrogen chemistry. The new derived reactions rates are included in the latest KIDA gas phase chemistry database release (Wakelam et al. 2015).

We ran models using the KIDA gas phase chemistry database instead of the UMIST 2012 database (see Table B.2). We used the KIDA 2011 (Wakelam et al. 2012) and the KIDA 2014 (Wakelam et al. 2015) releases. The additional chemistry included in PRODiMO (e.g. X-ray chemistry) remains the same.

Figure B.1 shows the resulting HCO^+ and N_2H^+ column densities for the KIDA2011 and KIDA2014 model in comparison to the reference model (UMIST 2012). In the KIDA2011 model the N_2H^+ column density is about a factor of three higher compared to the reference and KIDA2014 models. The reason are updated rate coefficients for the dissociative recombination reactions of N_2H^+ with electrons. The reaction rates at 20 K for $\text{N}_2\text{H}^+ + e^- \rightarrow \text{N}_2 + \text{H}$ ($\text{N}_2\text{H}^+ + e^- \rightarrow \text{NH} + \text{N}$) are a about a factor of five (three) higher in the KIDA 2014/UMIST 2012 releases than in the KIDA 2011 release. This explains the higher N_2H^+ abundance in the KIDA 2011 model. However, we find a good agreement for the KIDA 2014 and the UMIST 2012 release for both molecules HCO^+ and N_2H^+ .

Appendix C: Steady-state versus time-dependent chemistry

For our models we have assumed that the chemistry reaches a steady-state within typical lifetimes of disks (couple of million years). To verify this assumption we run time-dependent chemistry models for the reference models CL_XN and CL_XN. We find that for the species considered in this work HCO^+ and N_2H^+ the chemistry reaches steady-state within ≈ 1 Myr in a large fraction of the disk. This is in agreement with the models of Aikawa et al. (2015) although they use a different, in particular larger chemical network.

In Fig. B.2 we compare the vertical column densities N_{HCO^+} and $N_{\text{N}_2\text{H}^+}$ of the steady-state model to the results of the

A&A 603, A96 (2017)

time-dependent models at different times. For $r \gtrsim 30$ au and $t \gtrsim 1$ Myr to column densities of the steady-state and the time-dependent model are nearly identical. However, the steady-state model underestimates N_{HCO^+} and $N_{\text{N}_2\text{H}^+}$ for $r \lesssim 30$ au. The differences are caused by the “sink effect” for CO and N_2 (see Sect. 3.3 and Aikawa et al. 2015). This erosion of CO and N_2 and other neutral molecules in the disk midplane by the reaction with He^+ is a slow chemical process (e.g. Furuya & Aikawa 2014; Bergin et al. 2014; Helling et al. 2014) and is therefore over-estimated in the steady-state models.

As N_2H^+ resides in deeper layers than HCO^+ the deviations in the column densities are more pronounced. As a consequence the N_2H^+ column density does not exactly trace the CO ice line in the midplane of the disk. The midplane CO ice line is located at $r \approx 12$ au in the time-dependent model, whereas in the steady-state model $N_{\text{N}_2\text{H}^+}$ indicates a CO ice line at $r \approx 30$ au. We note that in the low CR model CL_XN the sink effect is less efficient due to the lower midplane ionization rate, therefore the deviations in the steady-state models for N_{HCO^+} and $N_{\text{N}_2\text{H}^+}$ are smaller ($N_{\text{N}_2\text{H}^+}$ indicates a CO ice line at $r \approx 20$ au).

Our comparison shows that for the bulk of N_{HCO^+} and $N_{\text{N}_2\text{H}^+}$ the assumption of steady-state chemistry is well justified. In particular our conclusions concerning the impact of SP ionization are not affected by the artifacts in the steady-state models. A steady-state model requires about a factor of ten less computational time than the time-dependent models. The use of the steady-state models allows us to study other important aspects like the impact of CO depletion (Sect. 4.2.2) or the comparison of different chemical networks.

Appendix D: The Turner model

In Turner & Drake (2009) the SP ionization rate is calculated for a mean solar mass nebulae disk model. To calculate the SP ionization rate at the surface of the disk they scaled their CR ionization rate of $\zeta_{\text{CR}} = 5 \times 10^{-18} \text{ s}^{-1}$ by a factor of $10^4(r/\text{au})^{-2}$. To account for the attenuation of SPs as a function of hydrogen column density they applied the same equation as they use for Galactic cosmic rays (their Eq. (2)).

To compare our results with the approach of Turner & Drake (2009) we implemented their method in our model. We also used their X-ray input spectrum and applied our X-ray radiative transfer to calculate the X-ray ionization rate. In Fig. D.1 we show the resulting X-ray, SP and CR ionization rates as a function of radius at a vertical column density of $\approx 8 \text{ g cm}^{-2}$ ($\approx 3 \times 10^{24} \text{ cm}^{-2}$) for the Turner model (CI_T) and for our CI_XN_SP model. A comparison of Fig. D.1 with Fig. 1 of Turner & Drake (2009) shows that the CI_T model reproduces their SP ionization rates. We note that in our disk model (i.e. lower disk mass) only for $r < 10$ au a vertical column density of $> 3 \times 10^{24} \text{ cm}^{-2}$ is reached; therefore only the inner 10 au are shown.

Figure D.1 clearly shows the differences of the two approaches. In our models SPs can only penetrate the disk radially and therefore cannot reach the disk midplane (see Sect. 3.2). In the Turner model the particles can also penetrate the disk vertically down to the midplane as they use the same equation for SP attenuation as is used for Galactic CRs. We cannot reproduce their results if we allow only for radial transport of particles. The differences in the X-ray ionization rate are due to the different X-ray spectrum ($L_X = 2 \times 10^{30} \text{ erg s}^{-1}$, $T_X = 5.8 \times 10^7 \text{ K}$, see Table 2) used by Turner & Drake (2009).

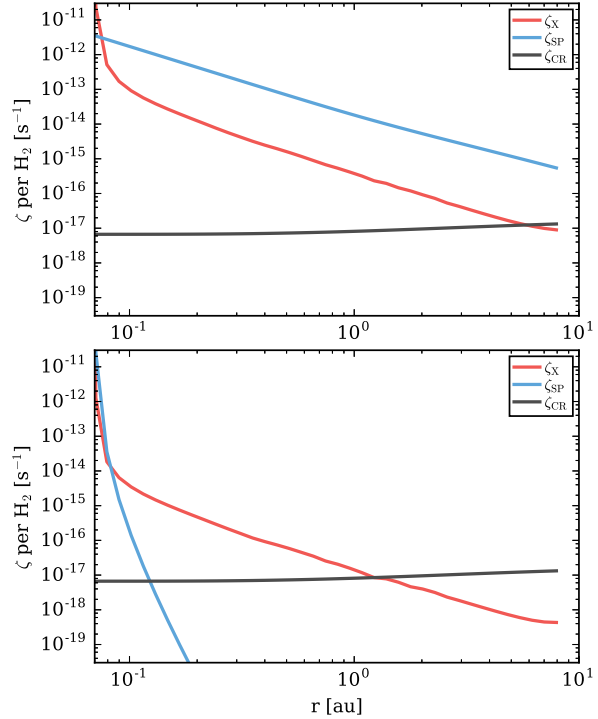


Fig. D.1. Ionization rates at a vertical column density of $N_{(\text{H}),\text{ver}} = 3.4 \times 10^{24} \text{ cm}^{-2}$ ($\approx 8 \text{ g cm}^{-2}$) as a function of distance to the star. The top panel shows the Turner model (CI_T), the bottom panel the CI_XN_SP model (see Table 5).

Appendix E: Comparison to observations

We compared the $\text{HCO}^+ J = 3-2$ and $\text{N}_2\text{H}^+ J = 3-2$ line fluxes from our reference model to the observations of Öberg et al. (2010, 2011a). From their sample we choose the targets where both lines were detected (the six targets shown in Fig. 6 of Öberg et al. 2011a). The observed integrated line fluxes are in the range of $3.1-17.8 \text{ Jy km s}^{-1}$ for $\text{HCO}^+ J = 3-2$ and in the range of $0.4-2.9 \text{ Jy km s}^{-1}$ for $\text{N}_2\text{H}^+ J = 3-2$ (all line fluxes are scaled to a distance of 140 pc). Excluding IM Lup, an extremely large and massive disk, from the sample gives a much narrower range of $3.1-5.4 \text{ Jy km s}^{-1}$ and $0.4-1.4 \text{ Jy km s}^{-1}$ for $\text{HCO}^+ J = 3-2$ and $\text{N}_2\text{H}^+ J = 3-2$, respectively.

To calculate the line fluxes for our model we use the line transfer module of PRODiMO (Woitke et al. 2011) and the molecular data from the Leiden Atomic and Molecular Database (Schöier et al. 2005; Botschwina et al. 1993; Flower 1999). For our reference model CI_XN we find fluxes of 2.4 Jy km s^{-1} and $0.78 \text{ Jy km s}^{-1}$ for $\text{HCO}^+ J = 3-2$ and $\text{N}_2\text{H}^+ J = 3-2$, respectively. As the sample of Öberg et al. (2011a) is probably biased towards large and massive disks we also calculated the fluxes for a disk four times more massive. We find fluxes of 4.3 Jy km s^{-1} and $1.18 \text{ Jy km s}^{-1}$ for $\text{HCO}^+ J = 3-2$ and $\text{N}_2\text{H}^+ J = 3-2$, respectively. These results are well within the range of the observations.

Chapter 4

The chemistry of episodic accretion in embedded objects

The main goal of this project was to investigate the impact of episodic accretion events on the chemistry of the circumstellar environment of young stars with a focus on observable tracers. This work was done in the context of the ongoing Swiss-Austrian SNF-FWF project *Episodic accretion in star formation* (PIs.: M. Audard, E. Vorobyov). We extended the PRODiMo disk code with a proper treatment for an envelope structure and modelled the time-evolution of the CO abundance after an FU Ori like luminosity burst for a structure typical of a Class I object. We produced synthetic ALMA observations to investigate the potential of CO as a tracer of post-burst targets. The new code developments are fully integrated into the PRODiMo code and are available on a collaborative basis. The new features will be used in the future for modelling of Herschel and ALMA data in the context of the SNF-FWF project. The results of this project were published in the paper *The chemistry of episodic accretion in embedded objects - 2D radiation thermochemical models of the post-burst phase*. In this thesis, the original published version is included.

Bibliography reference

Astronomy & Astrophysics, Volume 604, id.A15 (2017),
DOI: [10.1051/0004-6361/201730812](https://doi.org/10.1051/0004-6361/201730812).

Individual contributions to the paper

Own contribution: writing of the paper, code development for PRODiMo and model runs.
V. Elbakyan: provided the initial routines for constructing the envelope structure.
E. Vorobyov, M. Güdel, O. Dionatos, M. Audard, A. Postel: valuable scientific input on episodic accretion and embedded objects; members of the SNF-FWF project.
I. Kamp, W.-F. Thi, P. Woitke: main developers of PRODiMo; modelling support.
All authors read the manuscript before publication and provided valuable scientific input and very useful suggestions concerning the presentation and writing of the paper.

A&A 604, A15 (2017)
 DOI: 10.1051/0004-6361/201730812
 © ESO 2017

**Astronomy
&
Astrophysics**

The chemistry of episodic accretion in embedded objects

2D radiation thermo-chemical models of the post-burst phase

Ch. Rab¹, V. Elbakyan², E. Vorobyov^{3,2,1}, M. Güdel¹, O. Dionatos¹, M. Audard⁴, I. Kamp⁵, W.-F. Thi⁶,
 P. Woitke⁷, and A. Postel⁴

¹ University of Vienna, Dept. of Astrophysics, Türkenschanzstr. 17, 1180 Wien, Austria
 e-mail: christian.rab@univie.ac.at

² Research Institute of Physics, Southern Federal University, Stachki 194, Rostov-on-Don 344090, Russia

³ Institute of Fluid Mechanics and Heat Transfer, TU Wien, 1060 Vienna, Austria

⁴ Department of Astronomy, University of Geneva, Ch. d'Ecogia 16, 1290 Versoix, Switzerland

⁵ Kapteyn Astronomical Institute, University of Groningen, PO Box 800, 9700 AV Groningen, The Netherlands

⁶ Max-Planck-Institut für extraterrestrische Physik, Giessenbachstrasse 1, 85748 Garching, Germany

⁷ SUPA, School of Physics & Astronomy, University of St. Andrews, North Haugh, St. Andrews KY16 9SS, UK

Received 17 March 2017 / Accepted 9 May 2017

ABSTRACT

Context. Episodic accretion is an important process in the evolution of young stars and their environment. The observed strong luminosity bursts of young stellar objects likely have a long lasting (i.e. longer than the burst duration) impact on the chemical evolution of the disk and envelope of young stars.

Aims. We aim to investigate the observational signatures of the chemical evolution in the post-burst phase for embedded sources. With such signatures it is possible to identify targets that experienced a recent luminosity burst.

Methods. We present a new model for the chemistry of episodic accretion based on the two dimensional, radiation thermo-chemical disk code PRODiMO (PROtoplanetary DIsk MOdel). We have extended PRODiMO with a proper treatment for envelope structures. For a representative Class I model, we calculated the chemical abundances in the post-burst phase and produced synthetic observables such as intensity maps and radial intensity profiles.

Results. During a burst, many chemical species, such as CO, sublime from the dust surfaces. As the burst ends they freeze out again (post-burst phase). This freeze-out happens from inside-out due to the radial density gradient in the disk and envelope structure. This inside-out freeze-out produces clear observational signatures in spectral line emission, such as rings and distinct features in the slope of radial intensity profiles. We fitted synthetic C¹⁸O $J = 2-1$ observations with single and two component fits and find that post-burst images are much better matched by the latter. Comparing the quality of such fits therefore allows identification of post-burst targets in a model-independent way.

Conclusions. Our models confirm that it is possible to identify post-burst objects from spatially resolved CO observations. However, to derive proper statistics, such as the strength and frequencies of bursts, from observations it is important to consider the inclination and structure of the target and dust properties, as these have a significant impact on the freeze-out timescale.

Key words. stars: protostars – stars: low-mass – accretion, accretion disks – astrochemistry – methods: numerical

1. Introduction

Protostellar accretion is an important constituent part of the star formation process, affecting the evolution of young stars and their circumstellar disks. It provides mass, angular momentum, and entropy for the nascent protostar and it feeds gravitational energy of accreted matter back to the disk via accretion luminosity, which, in the early evolution, can dominate the photospheric luminosity of the protostar (Elbakyan et al. 2016). Notwithstanding its importance, the character of protostellar accretion is poorly known, mainly due to the difficulty with observing the deeply embedded sources, and several theoretical and empirical models have been proposed to explain how young stars accumulate their mass (e.g. Shu 1977; Hartmann & Kenyon 1985; Bonnell et al. 1997; McKee & Tan 2003).

Among these theories, the paradigm of variable accretion with episodic bursts (Hartmann & Kenyon 1985) has recently gained much attention thanks to ample indirect evidence

that protostellar accretion may have a highly variable character with prolonged episodes of low-rate (quiescent) accretion punctuated with short, but intense accretion bursts (see a review by Audard et al. 2014). Episodic accretion can have numerous and interesting implications not only for the disk dynamical and chemical evolution, but also for the evolution of pre-main-sequence stars. For instance, prolonged periods of low accretion luminosity between the bursts can promote disk gravitational fragmentation (Stamatellos et al. 2012). Episodic luminosity bursts can affect the disk and envelope chemical composition (Lee 2007; Visser & Bergin 2012; Vorobyov et al. 2013; Jørgensen et al. 2015) and increase the growth rate of dust particles facilitating giant planet formation (Hubbard 2017).

Finally, variable accretion with episodic bursts can help to resolve the “luminosity problem” of embedded protostars (Dunham & Vorobyov 2012), explain the existence of the very low luminosity objects (VELLOs) in the protostellar phase (Vorobyov et al. 2017a), and affect the positions of

pre-main-sequence stars on the HR diagram (Baraffe et al. 2012; Hosokawa et al. 2011; Vorobyov et al. 2017b). Until recently, episodic bursts were a feature exclusively attributed to low-mass star formation, but recent numerical models and observations demonstrated that massive stars can also have accretion bursts (Burns et al. 2016; Caratti o Garatti et al. 2016; Meyer et al. 2017).

Two of the most pressing questions concerning episodic accretion are: do all young stars experience accretion bursts and what is the frequency of these bursts? The number of directly detected objects showing strong optical bursts remains low (see e.g. Audard et al. 2014), as the typical timescale for the burst duration is about 100 yr. It is therefore difficult to derive conclusive statistics and make a firm statement about the universality of the accretion burst phenomenon.

One option to identify outburst sources is through chemistry. During a burst the surrounding environment of young stars is heated up and molecules, frozen out on dust grains, can sublimate. One observational consequence of this scenario is the outward shift of ice lines. The Atacama Large Millimeter Array (ALMA) observations of the FU Ori source V883 Ori indicate a location of the water ice line in the disk at 42 au (Cieza et al. 2016). This is significantly farther away than the expected location of the water ice line in disks of young low mass stars (typically one to five au).

After the burst the environment cools down quickly (less than one day, Johnstone et al. 2013) and the molecules can freeze out again (Lee 2007; Kim et al. 2011, 2012; Visser & Bergin 2012; Vorobyov et al. 2013; Visser et al. 2015). The freeze-out happens on a timescale of approximately 1000 to 10^4 yr, up to two order of magnitudes longer than a typical burst. Detections of objects currently in this post-burst phase, where the molecules are not yet frozen-out again, would significantly increase the statistical sample of known sources that experienced an episodic accretion event.

There are already observational indications for chemistry driven by accretion bursts. Kim et al. (2011, 2012) argue that the high CO₂ ice column densities measured in the envelopes of young stars can be explained by efficient conversion of CO to CO₂ during burst-phases. However, the chemical details of such a process are still unclear.

Jørgensen et al. (2013) found clear indications of a recent burst in IRAS 15398-3359. Their spatially resolved ALMA observations show a lack of HCO⁺ close to the centre of the source although significant amounts of CO are detected. This HCO⁺ hole is likely produced by the efficient destruction of HCO⁺ by water that sublimated during a burst and has not yet frozen out again.

A further indication is the detection of extended C¹⁸O $J = 2-1$ emission in eight out of a sample of 16 Class 0/I sources observed with the Submillimeter Array (SMA). By comparing the observations to 1D models of protostellar envelopes Jørgensen et al. (2015) find that about half of their targets show extended emission with respect to their current bolometric luminosity. Again this can be explained by a recent burst and the delayed freeze-out of CO in the post-burst phase where the objects show their quiescent bolometric luminosity again. As discussed by Jørgensen et al. (2015) only rough estimates concerning the burst frequency can be made from their sample as the sample size is still low and their results depend on the chosen binding energy of CO. A similar scenario is proposed by Kóspál et al. (2016) to explain the measured low degree of CO depletion in the disk of the EXOr prototype EX Lupi.

Visser et al. (2015) modelled line fluxes of a diverse sample of Class 0/I objects with a combined 1D dust radiative transfer and sophisticated chemical model. They identified several line ratios to measure the time passed since the last accretion burst. However, the values derived from different line ratios show a large scatter. They concluded that one reason for this scatter might be their too-simple 1D structure model.

In order to put the chemical diagnostic of bursts on a more sophisticated footing, we introduce here a new two dimensional model for the chemistry of episodic accretion. This model is based on the radiation thermo-chemical disk code PRODiMO (PROtoplanetary DIsk MOdel, Woitke et al. 2009; Kamp et al. 2010; Thi et al. 2011; Woitke et al. 2016). We apply PRODiMO to calculate the dust temperature, radiation field and the chemical abundances during the burst and in the post-burst phase. For a proper treatment of the remaining envelope of embedded sources we extended PRODiMO with a parametric prescription for the envelope density structure. As a first application of this new 2D model we study the chemical evolution of gas-phase CO and the resulting observational signatures in the post-burst phase by means of synthetic observations of C¹⁸O $J = 2-1$ for a representative Class I model. We also investigate the impact of the disk component and inclination of the target on observables. We argue that the radial intensity profiles for C¹⁸O $J = 2-1$ show distinct signatures that allow for the identification of targets in the post-burst phase in a model independent way, in particular independent of the CO binding energy.

In Sect. 2 we describe the physical structure of our model, the chemical network we use and how we simulate a burst. We discuss the chemical evolution of gas-phase CO and present synthetic observations for the C¹⁸O $J = 2-1$ spectral line emission for different structures (e.g. with or without a disk component) and inclinations in Sect. 3. In Sect. 4 we outline a new method to identify targets in the post-burst phase and compare our results to other models. Finally we present our conclusions in Sect. 5.

2. Method

We modelled a Class I burst scenario using the radiation thermo-chemical disk code PRODiMO (Woitke et al. 2009; Kamp et al. 2010; Thi et al. 2011; Woitke et al. 2016). We applied PRODiMO to solve the wavelength dependent continuum radiative transfer which provides the temperature structure and the local radiation field for a given fixed density structure. On top of this we solved for the chemical abundances using time-dependent chemistry to follow the chemical evolution during the burst and post-burst phase. With the line transfer module of PRODiMO (Woitke et al. 2011) we produced synthetic observables (spectral line cubes) and used the CASA ALMA simulator to produce realistic images and radial intensity profiles.

2.1. Physical model

2.1.1. Gas density structure

The physical and structure parameters of our representative Class I model are based on the model of Whitney et al. (2003). The Whitney et al. (2003) model includes a disk component and an envelope structure with an outflow cavity. For the envelope geometry they use the infall solution including rotation (e.g. Ulrich 1976; Terebey et al. 1984) and for the disk a flared density structure is assumed.

Similar to Whitney et al. (2003) we calculated the two density structures independently and put the disk structure on top of

Ch. Rab et al.: The chemistry of episodic accretion in embedded objects

the envelope structure wherever the disk density is higher than the envelope density. In the following we describe in detail the envelope and disk structure and the chosen parameter values.

For the envelope structure we used the infalling rotating envelope model of [Ulrich \(1976\)](#) where the density ρ in units of $[\text{g cm}^{-3}]$ is given by

$$\rho(r, \mu) = \frac{\dot{M}_{\text{if}}}{4\pi} (2GM_* r^3)^{-1/2} \left(\frac{1}{2} + \frac{\mu}{2\mu_0} \right)^{-1/2} \left(\frac{\mu}{\mu_0} + \frac{2\mu_0^2 R_c}{r} \right)^{-1}. \quad (1)$$

\dot{M}_{if} is the mass infall rate of the envelope, G the gravitational constant, M_* is the stellar mass, r is the radial distance to the star in the centre, R_c is the centrifugal radius, $\mu = \cos\theta$ is the cosine polar angle of a streamline of infalling particles and μ_0 is the value of μ far from the protostar ($r \rightarrow \infty$). The streamline angles are calculated via the equation

$$\mu_0^3 + \mu_0(r/R_c - 1) - \mu(r/R_c) = 0. \quad (2)$$

Class I objects show prominent bipolar cavities. To account for the cavity we again followed the approach of [Whitney et al. \(2003\)](#). We used a cavity with an opening angle of 20° and subsequently applied a simple power-law to account for a curved cavity shape ([Whitney et al. 2003](#)). We assumed that the cavity is empty. The parameters for the envelope density structure are listed in [Table 1](#). For those parameters the resulting mass of the envelope is $M_{\text{env}} \approx 0.2 M_\odot$.

For the disk component we used an axisymmetric flared gas density structure with a Gaussian vertical profile, and a power law with a tapered outer edge for the radial surface density profile (e.g. [Lynden-Bell & Pringle 1974](#); [Andrews et al. 2009](#)). The density structure for an azimuthally symmetric disk in hydrostatic equilibrium as a function of the spatial coordinates r (distance to the star) and z (height of the disk) is given by

$$\rho(r, z) = \frac{\Sigma(r)}{\sqrt{2\pi} \cdot h(r)} \exp\left(-\frac{z^2}{2h(r)^2}\right) [\text{g cm}^{-3}], \quad (3)$$

where $\Sigma(r)$ describes the radial surface density profile and $h(r)$ is the scale height of the disk. For the surface density $\Sigma(r)$ we assumed a simple power-law distribution with a tapered outer edge

$$\Sigma(r) = \Sigma_0 \left(\frac{r}{R_{\text{in}}} \right)^{-\epsilon} \exp\left(-\left(\frac{r}{R_{\text{tap}}}\right)^{2-\gamma}\right) [\text{g cm}^{-2}], \quad (4)$$

where R_{tap} is the characteristic radius and R_{in} the inner radius of the disk. The constant Σ_0 is determined via the relation $M_{\text{disk}} = 2\pi \int \Sigma(r) r dr$ and [Eq. \(4\)](#). For the disk parameters chosen here $\Sigma_0 = 270 [\text{g cm}^{-2}]$. The vertical scale height $h(r)$ is described by a power law with a flaring power index β :

$$h(r) = H(100 \text{ au}) \left(\frac{r}{100 \text{ au}} \right)^\beta \quad (5)$$

where $H(100 \text{ au})$ gives the disk scale height at $r = 100 \text{ au}$.

The two density structures for the envelope and the disk were calculated independently. To merge the two structures we took the higher value of the density from the two components at a certain point of the domain. To secure a rather smooth transition at the outer border of the disk we varied the power index γ for the tapered outer edge of the disk. This means that the disk structure in the outer regions no longer follows the viscous evolution (i.e. $\epsilon \neq \gamma$).

Table 1. Main parameters of the Class I model.

Quantity	Symbol	Value
stellar mass	M_*	$0.5 M_\odot$
stellar effective temp.	T_*	5000 K
stellar luminosity	L_*	$1.0 L_\odot$
disk gas mass	M_{disk}	$0.02 M_\odot$
disk inner radius	R_{in}	0.6 au
disk tapering-off radius	R_{tap}	100 au
column dens. pow. ind.	ϵ	1.0
tapering parameter	γ	-1.0
reference scale height	$H(100 \text{ au})$	10 au
flaring power index	β	1.1
centrifugal radius	R_c	100 au
mass infall rate	\dot{M}_{if}	$5 \times 10^{-6} M_\odot \text{ yr}^{-1}$
outer radius	R_{out}	5000 au
cavity opening angle	β_{cav}	20°
dust to gas mass ratio	δ	0.01
min. dust particle radius	a_{min}	$0.005 \mu\text{m}$
max. dust particle radius	a_{max}	$1 \mu\text{m}$
envelope		$1000 \mu\text{m}$
disk		3.5
dust size dist. power ind.	a_{pow}	3.5
dust composition ^a	Mg _{0.7} Fe _{0.3} SiO ₃	60%
(volume fractions)	amorph. carbon	20%
	vacuum	20%
cosmic ray H ₂ ion. rate	ζ_{CR}	$5 \times 10^{-17} \text{ s}^{-1}$
strength of interst. FUV	χ^{ISM}	1^b
distance	d	200 pc

Notes. ^(a) Optical constants are from [Dorschner et al. \(1995\)](#) and [Zubko et al. \(1996, BE-sample\)](#); resulting dust material density $\rho_{\text{dp}} \approx 2.2 \text{ g cm}^{-3}$. ^(b) χ^{ISM} is given in units of the Draine field ([Draine & Bertoldi 1996](#); [Woitke et al. 2009](#)).

For the inner radius of the structure we used $R_{\text{in}} = 0.6 \text{ au}$ which corresponds roughly to the dust condensation radius during the burst (assuming that the burst happens close to the star, [Sect. 2.3](#)). The total hydrogen number density $n_{(\text{H})} = n_{\text{H}} + 2n_{\text{H}_2}$ at the inner border is $n_{(\text{H})}(R_{\text{in}}) \approx 2 \times 10^{14} \text{ cm}^{-3}$. The structure extends out to $R_{\text{out}} = 5000 \text{ au}$ with $n_{(\text{H})}(R_{\text{out}}) \approx 6 \times 10^4 \text{ cm}^{-3}$.

All parameters of the model are listed in [Table 1](#). The resulting gas density structure of our representative Class I model is shown in the first column of [Fig. 1](#).

2.1.2. Dust properties

We assumed a canonical dust to gas mass ratio of 0.01 for the disk and envelope structure. Observations and models show clear evidence for dust growth in disks (e.g. [Birnstiel et al. 2010](#); [Williams & Cieza 2011](#); [Pinte et al. 2016](#)). We accounted for this by using two different dust populations for the disk and the envelope structure.

For both structures we used a simple power law for the dust size distribution function $f(a) \propto a^{-a_{\text{pow}}}$, where a is the grain radius. In the disk the minimum and maximum dust sizes are $a_{\text{min}} = 0.005 \mu\text{m}$ and $a_{\text{max}} = 1000 \mu\text{m}$, respectively. Scattered light images from dense cloud cores (“coreshine”) indicate that the maximum dust particle size is likely larger than in the diffuse interstellar medium ([Steinacker et al. 2015](#); [Ysard et al. 2016](#)).

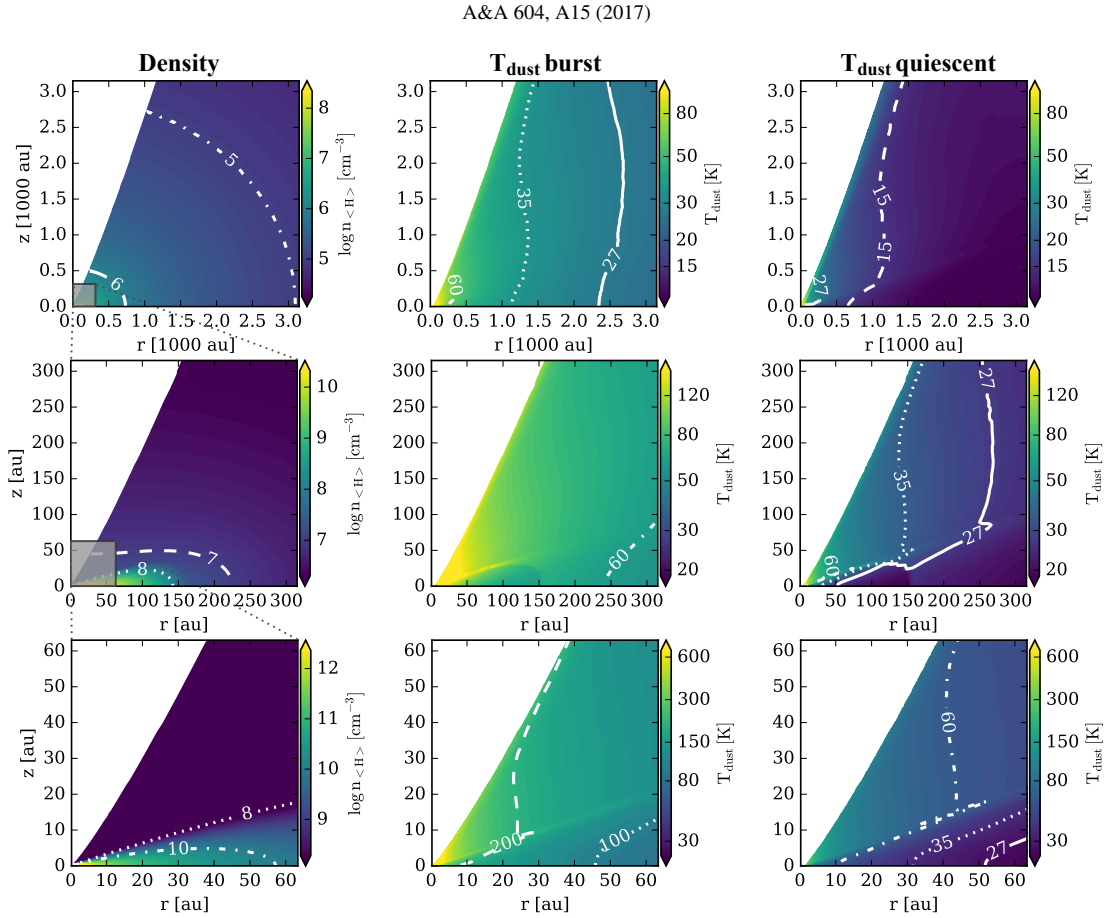


Fig. 1. Density and temperature structure for the representative Class I model. *From left to right:* total hydrogen number density $n_{\text{(H)}}$, T_{dust} during the burst, and T_{dust} in the quiescent (post-burst) phase. The *second* and *third* row show a zoom-in to the inner 300 and 60 au (marked by the grey squares in the density plots). The white solid contour in the temperature plots for $T = 27$ K roughly indicates the CO ice line. Some artefacts are visible in the temperature structure (e.g. *last two panels in the second row*). These are due to the sharp transition of the two dust populations used for the disk and envelope, but have no significant impact on the large scale temperature structure.

We therefore adopted a value of $a_{\text{max}} = 1 \mu\text{m}$ for the envelope. For both dust size distributions we used 300 logarithmically spaced size bins. For the slope we adopted the canonical value for interstellar grains of $a_{\text{pow}} = 3.5$ (Mathis et al. 1977).

For the dust composition we assumed a mixture of 60% (by volume) amorphous laboratory silicate, 20% amorphous carbon and 20% vacuum (porosity of grains). These values are similar to the proposed dust composition of Woitke et al. (2016) for modelling of T Tauri disks. To calculate the dust opacities we applied Mie theory (Mie 1908). The detailed dust properties are given in Table 1, the resulting dust opacities for both dust populations are shown in Fig. 2.

We did not include ice-coated grains in our opacity calculations. Such grains would show a distinct opacity feature at $\approx 3 \mu\text{m}$ (e.g. Ossenkopf & Henning 1994). We also ignored any change in the dust opacity which might be caused by the burst itself, such as the observed crystallization of dust particles in the disk surface layers of EX Lupi (Ábrahám et al. 2009). Although such opacity features are clearly observable in spectral energy distributions they do not have a significant impact on our results. This is because we are only interested in the overall change in the dust temperature structure during a burst and do not model spectral energy distributions in detail (see also Appendix A).

2.2. Chemical model

Our chemical network is based on the UMIST 2012 database for gas phase chemistry (McElroy et al. 2013). We used a reduced network and only selected chemical reactions from UMIST 2012 for a set of 76 gas phase species. We expanded the gas phase network by reactions for adsorption and desorption for all neutral species (excluding atomic and molecular hydrogen and noble gases). We also considered H_2 formation on dust grains (Cazaux & Tielens 2002; Woitke et al. 2009). For the adsorption and desorption reactions we used the binding energies from the UMIST 2012 release but updated a couple of values (see Table A.3) to be consistent with Visser et al. (2015). In total our network consists of 105 species and 1211 chemical reactions. For more details on the chemical network see also Kamp et al. (2017).

We used time-dependent chemistry to follow the evolution of the chemical abundances during and after the burst (see Sect. 2.3). As initial conditions for time-dependent chemistry we chose the same abundances as Visser et al. (2015), which are typical for prestellar core conditions (see Table A.2).

The most important chemical process for episodic accretion chemistry is the freeze-out and sublimation (adsorption and

Ch. Rab et al.: The chemistry of episodic accretion in embedded objects

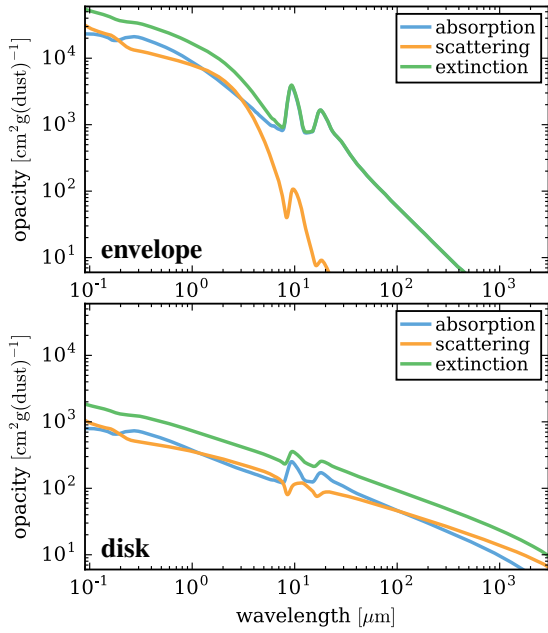


Fig. 2. Dust opacities for the envelope and the disk dust population.

Table 2. Dust properties of relevance for the chemistry in the disk, envelope and for a uniform distribution with $a = 0.1 \mu\text{m}$.

	Disk	Envelope	$0.1 \mu\text{m}$
Mean dust size $\langle a^2 \rangle^{1/2} [\mu\text{m}]$	0.0112	0.0108	0.1
Mean dust size $\langle a^3 \rangle^{1/3} [\mu\text{m}]$	0.0653	0.0202	0.1
Particle abundance $n_d/n_{\text{(H)}}$	9.0(-12) ^a	3.0(-10)	2.5(-12)
Surface $4\pi\langle a^2 \rangle n_d/n_{\text{(H)}} [\text{cm}^2]$	1.4(-22)	4.4(-21)	3.2(-21)

Notes. Here we assumed the same dust composition as given in Table 1 for the disk, envelope and the $0.1 \mu\text{m}$ cases. ^(a) $x(y)$ means $x \times 10^y$.

desorption) of neutral species (e.g. Visser et al. 2015). Besides thermal desorption we also include non-thermal desorption by cosmic rays and photons (Woitke et al. 2009; Kamp et al. 2017). However, the most relevant aspect of episodic accretion chemistry is the balance between adsorption and thermal desorption. Therefore we explain the modelling of these processes in PRODiMO in detail.

2.2.1. Adsorption

For the chemistry we did not use a fixed single dust size but derived averaged dust sizes from the same dust size distributions as were used for the dust opacity calculations (Woitke et al. 2009, 2016). The adsorption (freeze-out) rate per volume for a species i is given by

$$R_{i,\text{ads}} = n_i 4\pi \langle a^2 \rangle n_d \alpha v_{i,\text{th}} [\text{cm}^{-3} \text{s}^{-1}] \quad (6)$$

where $\langle a^2 \rangle = \int_{a_{\text{min}}}^{a_{\text{max}}} a^2 f(a) da$ is the second moment of the dust size distribution, n_d is the dust particle number density and $\alpha = 1$ the sticking efficiency. The thermal velocity for species i is given by $v_{i,\text{th}} = \sqrt{kT_{\text{gas}}/2\pi m_i}$, where T_{gas} is the gas temperature and m_i the mass of the species in [g]. In Table 2 several important dust size distribution quantities for the chemistry are listed. For comparison we also list the values assuming only a single dust size of

$0.1 \mu\text{m}$ (see also Woitke et al. 2016). The adsorption rate is the relevant quantity for the freeze-out timescale. We will discuss this in detail in Sect. 3.1.

2.2.2. Thermal desorption

The thermal desorption rate of a species i is given by

$$R_{i,\text{des}} = n_{i\#, \text{des}} v_{i,\text{osc}} \exp\left(-\frac{E_{i,\text{B}}}{kT_d}\right) [\text{cm}^{-3} \text{s}^{-1}]. \quad (7)$$

$n_{i\#, \text{des}}$ is the fraction of the number density of species i on the dust grains (# indicates the ice phase) prone to desorption (see below). $v_{i,\text{osc}} = \sqrt{(2n_{\text{surf}} k E_{i,\text{B}})/(\pi^2 m_i)}$ is the vibrational frequency where $n_{\text{surf}} = 1.5 \times 10^{15} \text{cm}^{-2}$ (Hasegawa et al. 1992) is the surface density of available adsorption sites and $E_{i,\text{B}}$ is the adsorption binding energy for species i . The vibrational frequency for CO is $v_{\text{osc}}(\text{CO}) = 1.1 \times 10^{12} \text{s}^{-1}$ for $E_{\text{B}}(\text{CO}) = 1307 \text{K}$.

We assumed that only a certain fraction of the total (thick) ice mantle on the dust grain is effectively desorbed (Aikawa et al. 1996, 2015). The total number density of active surface places (i.e. prone to desorption) in the ice mantle is given by

$$n_{\text{act}\#} = 4\pi \langle a^2 \rangle n_d n_{\text{surf}} N_{\text{lay}}, \quad (8)$$

where $\langle a^2 \rangle$ is the second moment of the dust size distribution (see Sect. 2.2.1), n_d the number density of dust particles and N_{lay} is the number of active layers. We adopted $N_{\text{lay}} = 2$ (i.e. only the outermost two layers can be desorbed, Aikawa et al. 1996). The number density $n_{i\#, \text{des}}$ of active ice units for a species i is given by (Woitke et al. 2009)

$$n_{i\#, \text{des}} = \begin{cases} n_{i\#}, & \text{if } n_{\text{tot}\#} < n_{\text{act}\#} \\ n_{\text{act}\#} \frac{n_{i\#}}{n_{\text{tot}\#}}, & \text{otherwise} \end{cases} \quad (9)$$

where $n_{i\#}$ is the number density of the ice species i and $n_{\text{tot}\#}$ the sum of the number density of all ice species. In the case of thick ice mantles ($n_{\text{tot}\#} \geq n_{\text{act}\#}$) the desorption rate Eq. (7) is of zeroth order, which means that $R_{i,\text{des}}$ does not (strongly) depend on the actual number density of the considered ice species (e.g. Collings et al. 2004, 2015). In case of thin ice mantles (i.e. not all available active adsorption sites are occupied), Eq. (7) transforms to a first-order desorption rate, which means that $R_{i,\text{des}}$ scales linearly with $n_{i\#}$.

According to the temperature-programmed desorption (TPD) laboratory experiments zero-order desorption should be the preferred method to estimate desorption rates (Collings et al. 2004, 2015). For our method to estimate the thermal desorption rate, actually in most areas of our model structure zero-order desorption applies (i.e. roughly speaking everywhere where water is frozen-out). The main effective difference between first-order and zero-order desorption is that in the case of zero-order desorption the number of ice molecules which can sublimate is limited. As a consequence the residual gas phase abundances in the freeze-out zone is lower for zero-order desorption compared to first-order desorption where all molecules in the ice mantle are prone to desorption.

In Appendix A we compare our chemical model to the model of Visser et al. (2015). We find a good agreement between the two models in particular concerning the main aspects of episodic accretion chemistry (e.g. delayed freeze-out, shift of ice-lines).

2.3. Burst scenario

To simulate a luminosity burst we followed the approach of Visser et al. (2015). For the burst they assume an instantaneous increase of the protostellar luminosity by a factor of 100, compared to the quiescent phase, and a burst duration of 100 yr. After the burst the luminosity drops instantaneously to the quiescent value. The envelope density structure is kept fixed at all times (i.e. any dynamical changes of the structure are neglected, see also Sect. 4.3.1).

Just increasing the stellar luminosity is a very simplified picture of an episodic accretion event. Most of the excess energy during the burst is actually produced in a small and hot accretion disk close to the protostar ($r < 1$ au; Zhu et al. 2007, 2008). However, for the chemistry mainly the resulting temperature change in the envelope and disk structure matters and the process producing the excess luminosity during the burst is not relevant. Furthermore, the inner region of the surrounding dust structure is optically thick and the photons emitted by the protostar and accretion disk are reprocessed to longer wavelengths. Consequently, the temperature in regions farther out is not sensitive to the details of the inner region as the outer regions mainly sees the reprocessed photons (Johnstone et al. 2013).

To model the emission of the central luminosity source we used PHOENIX stellar atmosphere models (Brott & Hauschildt 2005) for a given stellar mass $M_* = 0.5 M_\odot$, luminosity $L_* = 1.0 L_\odot$ and effective temperature $T_* = 5000$ K. For the burst we increased L_* by a factor of 100 but kept all other stellar parameters fixed. We note those parameters should not be interpreted as proper protostellar parameters but rather as a very simple approximation to simulate the energy output produced close to the protostar during a burst. We performed some tests varying the properties of the input stellar spectrum (e.g. T_*) and also used the burst spectrum of FU Orionis (Zhu et al. 2007) as input. We find that our results presented here are not strongly sensitive to the shape of the used stellar spectrum. The increase of the dust temperature during the burst is mostly proportional to the luminosity ($T_d \propto L_*^{0.25}$; see Johnstone et al. 2013, and Appendix A).

In the following we describe the main steps of our model to simulate the chemical evolution in the post-burst phase:

1. *Quiescent RT*: continuum radiative transfer using the quiescent protostellar luminosity to calculate the local radiation field and temperatures used for the chemical evolution in the pre-burst and post-burst phases.
2. *Init chemistry*: evolve the chemistry, starting with prestellar core abundances (see Table A.2), under quiescent conditions (i.e. temperature structure) for 10^5 yr to calculate the initial chemical abundances prior to the burst. We will discuss the impact of the initial chemical abundances on our results in Sect. 4.3.3.
3. *Burst RT*: continuum radiative transfer (RT) for the given burst luminosity to calculate the local radiation field and temperatures at every point of the structure.
4. *Burst chemistry*: evolve the chemistry for the duration of the burst starting from given initial abundances. During the chemistry step the radiation field and temperatures are kept fixed at the burst values.
5. *Post-burst chemistry*: follow the chemical evolution for 10^5 yr under quiescent conditions and produce synthetic observations at distinct time steps.

We have assumed here that the temperature change due to the burst and after the burst happens instantaneously. Johnstone et al. (2013) indeed find that the dust in a typical

protostellar envelope very quickly reaches its equilibrium temperature after a luminosity change (< 1 day). We applied their semi-analytic method to our structure, including the disk, and find that the heating times can increase by at most two orders of magnitude. We also neglected any possible differences between the gas and dust temperature (see Johnstone et al. 2013, for a discussion) and assume that the gas and dust temperatures are equal at all times. Considering the long timescales for the chemistry (see Sect. 3.1), it is a reasonable simplification to assume that the temperature reacts instantaneously to the luminosity change of the central heating source (see also Visser et al. 2015).

The temperature structure for the burst and quiescent phases are shown in Fig. 1. The main difference in the envelope temperature structure compared to 1D spherical models are the lower temperatures close to the midplane. The disk absorbs most of the stellar radiation and therefore casts a shadow onto the envelope, consequently the temperatures are lower within the disk shadow. This becomes also apparent by the temperature contours shown in Fig. 1 which are not circular.

2.4. Synthetic observations

To produce synthetic observations we use the built-in line radiative transfer module of PRODiMO (Woitke et al. 2011). For the line radiative transfer we assume a Keplerian velocity field for the disk component and free-fall velocity for the envelope structure (i.e. neglect rotation of the envelope for simplicity).

To produce realistic images and radial intensity profiles for spectral line emission we convolve the line cubes produced by PRODiMO with a given synthetic beam but also perform full ALMA/CASA simulations (see Appendix B). In this work we focus on the $C^{18}O J = 2-1$ line. Our chemical model does not include CO isotopologue chemistry (e.g. Visser et al. 2009a). Instead, we calculated the abundance of $C^{18}O$ by applying a fixed $^{16}O/^{18}O$ isotopologue ratio of 498.7 (e.g. Scott et al. 2006). For the excitation calculations we used the collision rate coefficients for $C^{18}O$ with H_2 from Yang et al. (2010) provided by the LAMDA database (Leiden Atomic and Molecular Database, Schöier et al. 2005).

3. Results

3.1. Adsorption timescale

The adsorption or freeze-out timescale is the most relevant quantity in episodic accretion chemistry. It defines the time range in which one can still see chemical signatures initially caused by an accretion burst.

At first we bring Eq. (6) (without n_i) in the same form as Charnley et al. (2001)

$$k_{i,\text{ads}} = 1.45 \times 10^4 \alpha \left(\frac{T_{\text{gas}}}{M_i} \right)^{1/2} \pi \langle a^2 \rangle n_d \text{ [s}^{-1}\text{]}, \quad (10)$$

where M_i is the molecular weight of species i . In PRODiMO the number density of dust particles n_d is given by

$$n_d = \frac{\rho_{\text{gas}} \delta}{\frac{4\pi}{3} \langle a^3 \rangle \rho_{\text{dp}}} \text{ [cm}^{-3}\text{]}, \quad (11)$$

where $\rho_{\text{gas}} = 2.28 \times 10^{-24} n_{(\text{H})}$ is the gas density in $[\text{g cm}^{-3}]$, δ is the dust to gas mass ratio, $\langle a^3 \rangle$ is the third moment of the dust size distribution and ρ_{dp} is the material density of a dust particle

Ch. Rab et al.: The chemistry of episodic accretion in embedded objects

in $[\text{g cm}^{-3}]$. The adsorption timescale $t_{i,\text{ads}} = k_{i,\text{ads}}^{-1}$ can then be written in the form

$$t_{i,\text{ads}} = 2.9 \times 10^{-12} M_i^{1/2} \alpha^{-1} \frac{\rho_{\text{dp}}}{\delta} T_{\text{gas}}^{-1/2} \frac{\langle a^3 \rangle}{\langle a^2 \rangle} \rho_{\text{gas}}^{-1} [\text{yr}]. \quad (12)$$

Equation (12) includes all the quantities and parameters of our model that have an impact on $t_{i,\text{ads}}$. However, for the results presented here we do not vary all parameters, in particular $\alpha = 1$ (sticking efficiency), $\rho_{\text{dp}} \approx 2.2 \text{ g cm}^{-3}$ and $\delta = 0.01$ are the same for all models and are constant in time and space.

Here, we want to focus on the impact of the dust grain size. The ratio $\langle a^3 \rangle / \langle a^2 \rangle$ represents a mean particle radius \bar{a} , where the averaging is surface weighted. This means \bar{a} is actually dominated by the small dust particle population. Using \bar{a} instead of a simple averaging over grain sizes is more appropriate to model the adsorption process, as the total available dust surface is most relevant here and the total surface is mainly provided by the large number of small grains (see also Vasyunin et al. 2011).

We use here two different dust populations for the disk and envelope, consequently also \bar{a} varies. For our chosen dust populations $\bar{a}_{\text{disk}} = 2.24 \mu\text{m}$ and $\bar{a}_{\text{env}} = 0.07 \mu\text{m}$. This means that t_{ads} increases by a factor of ≈ 32 in the disk, compared to the case with only small dust grains (neglecting any temperature change).

In PRODIMO the same dust properties are consistently used for the dust radiative transfer and the chemistry. In other chemical models usually a mean dust size and a dust abundance is assumed. Typical values are $\bar{a} = 0.1 \mu\text{m}$ and $n_d = 10^{-12} n_{\text{H}}$ which can directly be used in Eq. (10) to calculate $t_{i,\text{ads}}$ (e.g. Eq. (3) of Rodgers & Charnley 2003). For such values $t_{i,\text{ads}}$ is about a factor of three longer compared to our dust model for the envelope (for a given density and temperature). These examples show the importance of dust properties like the assumed material density and dust size for the adsorption timescale as already briefly discussed by Vorobyov et al. (2013; see also Sect. 4.2)

Our results concerning the $t_{i,\text{ads}}$ show for the first time the importance of dust properties and evolution for the chemistry of episodic accretion in a quantitative manner. This indicates that in particular for more evolved sources dust evolution processes like dust growth but also radial migration and dust settling which are important especially for the disk (see e.g. Vasyunin et al. 2011; Akimkin et al. 2013), should be taken into account for modelling the chemistry of episodic accretion.

3.2. CO gas phase abundance

In this section we present the CO gas phase abundance structure of our 2D model for the quiescent phase (i.e. no burst) and the detailed time evolution of the abundance in the post-burst phase. In the post-burst phase the envelope and disk have already cooled down to quiescent conditions (see Sect. 2.3) and CO sublimated during the burst can freeze out again.

In Fig. 3 we show the CO gas phase abundance $\epsilon(\text{CO}) = n_{\text{CO}}/n_{\text{H}}$ for the inner 3000 au of the 2D structure at five different times after the end of the burst. The bottom right panel in Fig. 3 shows the radial profiles of the vertically averaged CO abundance $\epsilon_{\text{avg}}(\text{CO})$. $\epsilon_{\text{avg}}(\text{CO})$, as a function of radius, is given by the ratio $\epsilon_{\text{avg}}(\text{CO}) = N_{\text{CO,ver}}/N_{\text{H,ver}}$, where $N_{\text{CO,ver}}$ is the vertical column density of gas-phase CO and $N_{\text{H,ver}}$ is the total hydrogen column density ($N_{\text{H,ver}} = N_{\text{H,ver}} + 2N_{\text{H}_2,\text{ver}}$). At first we discuss the CO abundance pattern for the quiescent phase and subsequently the detailed evolution of the CO gas phase abundance shortly after the burst (post-burst phase).

3.2.1. Quiescent phase

Due to our choice for the initial chemical abundances prior to the burst (Sect. 2.3) the pre-burst CO abundance structure is identical to what is shown in the $t = 10^5 \text{ yr}$ panel in Fig. 3, which we call the quiescent phase. We will discuss the consequences of the chosen initial abundances and the possible impact of recurrent bursts in Sect. 4.3.3. The main features of the averaged CO abundance profile in the quiescent phase are

- an inner region within the quiescent radial CO ice line ($r \approx 300 \text{ au}$) with an average CO abundance close to the canonical value of $\epsilon_{\text{avg}}(\text{CO}) \approx 2 \times 10^{-4}$ (the impact of the disk component is discussed in the following paragraphs);
- strong freeze-out of CO just outside the radial CO ice line with $\epsilon_{\text{avg}}(\text{CO}) \lesssim 10^{-6}$;
- a gradual increase of $\epsilon_{\text{avg}}(\text{CO})$ with radius until $\epsilon_{\text{avg}}(\text{CO})$ reaches again the canonical value at the outskirts of the structure.

Such a quiescent profile is consistent with observations of embedded sources (e.g. Jørgensen et al. 2005; Yıldız et al. 2010; Anderl et al. 2016), which in particular show the gradual increase of the CO abundance with radius, beyond the CO ice line. This implies that our simple model (i.e. assuming a steady-state structure) indeed captures the main characteristics of the CO abundance structure of embedded sources.

In our model the detailed appearance of the positive slope of $\epsilon_{\text{avg}}(\text{CO})$ for $r \gtrsim 750 \text{ au}$ has two reasons. Averaging the CO abundance vertically is not the ideal representation at large scales where the density structure is rather spherical. The second reason is of physical nature. Due to the lower densities the freeze-out becomes less efficient as collisions of molecules with dust particles become less likely. As a consequence non-thermal desorption processes such as cosmic-ray and photo desorption become, relatively speaking, more important. In addition the outer parts of the envelope ($r \gtrsim 1500 \text{ au}$) are also affected by the interstellar background radiation field included in our model, further increasing the impact of photo-desorption in the outskirts of the envelope.

3.2.2. Post-burst phase

During the burst all CO sublimates in the inner 2000–3000 au. Only there the temperature increases above the CO sublimation temperature of $T_{\text{sub}}(\text{CO}) \approx 27 \text{ K}$ (see Fig. 1). For $r \gtrsim 2000\text{--}3000 \text{ au}$ $\epsilon(\text{CO})$ is not affected by the burst and the pre-burst abundances are preserved. In the first panel of Fig. 3 ($t = 10 \text{ yr}$), the impact of the disk on the post-burst CO abundance in the outer regions is also apparent. Around the midplane of the structure ($z = 0 \text{ au}$) the disk absorbs most of the stellar radiation and casts a shadow into the envelope. As a consequence CO sublimates only up to $r = 2000 \text{ au}$ in the shadowed region.

Looking at the averaged abundance panel in Fig. 3, the evolution of $\epsilon_{\text{avg}}(\text{CO})$ in the post-burst phase shows three distinct features:

- the fast depletion of CO in the zone with the disk ($r \lesssim 150 \text{ au}$);
- the peak in $\epsilon_{\text{avg}}(\text{CO})$ at $150 \lesssim r \lesssim 300 \text{ au}$;
- the slow depletion of CO with time in the region $300 \lesssim r \lesssim 2500 \text{ au}$.

In the zone with the disk, $\epsilon_{\text{avg}}(\text{CO})$ is mainly determined by the high density in the disk. The temperatures close to the midplane of the disk are below $T_{\text{sub}}(\text{CO})$ and CO freezes out on a timescale

A&A 604, A15 (2017)

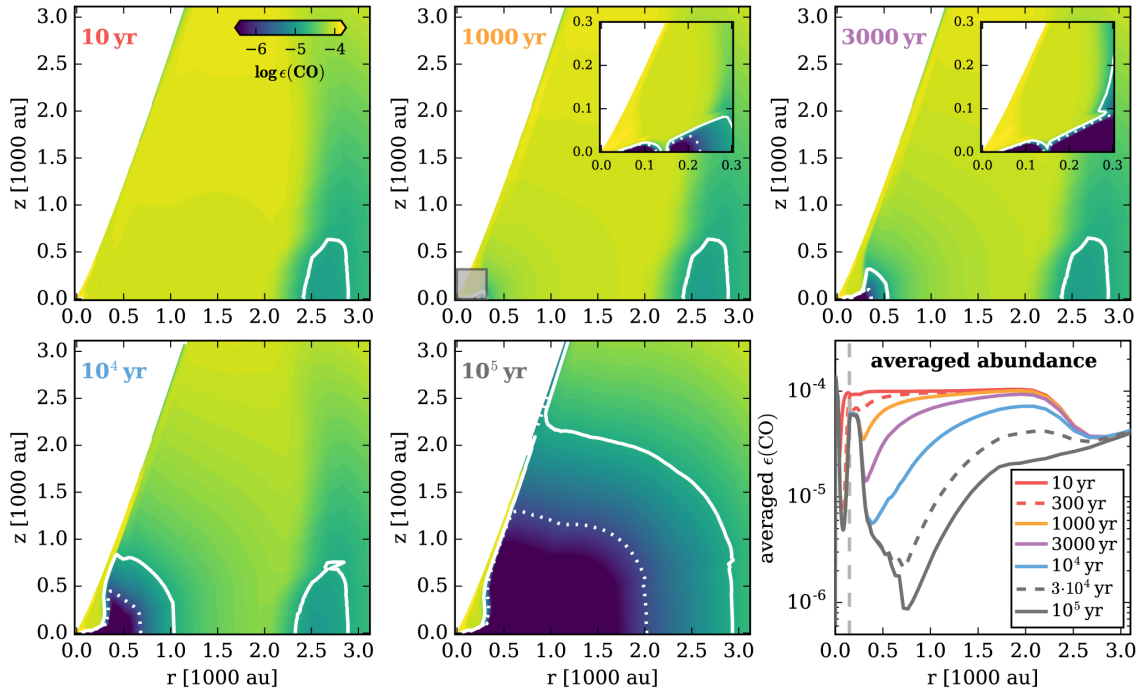


Fig. 3. Evolution of the CO gas phase abundance $\epsilon(\text{CO})$ in the post-burst phase. The 2D contour plots show $\epsilon(\text{CO})$ for five different times of $t = 10, 1000, 3000, 10^4$ and 10^5 yr after the end of the burst. The white solid and dashed contours indicate $\epsilon(\text{CO}) = 10^{-5}$ and $\epsilon(\text{CO}) = 10^{-6}$, respectively. The 1000 and 3000 yr panels include a zoom in for the inner 300 au (marked by the grey box). The bottom right panel shows the evolution of the vertically averaged CO abundance as a function of the midplane radius (the dashed lines are for $t = 300$ and $t = 3 \times 10^4$ yr). The vertical grey dashed line marks the radial disk to envelope transition at $r \approx 150$ au. The black solid line corresponds to the quiescent phase ($t = 10^5$ yr).

of $\lesssim 100$ yr. Only within the radial CO ice line (at $r \approx 50$ au in the disk midplane) CO remains in the gas phase at all times. Above the disk (see the inset in the plot for $t = 1000$ yr) the temperature is higher than $T_{\text{sub}}(\text{CO})$ and CO remains in the gas phase at all times.

In the zone with $150 \lesssim r \lesssim 300$ au CO is mostly in the gas phase but shows some depletion with $\epsilon_{\text{avg}}(\text{CO}) \approx 6 \times 10^{-5}$. The radius $r \approx 300$ au can be seen as the radial CO ice line in the envelope (i.e. similar to a structure without a disk). Due to the disk shadow the temperatures near the midplane of the structure are below $T_{\text{sub}}(\text{CO})$ and, similar to the disk component, CO freezes out quickly. However, the vertical density gradient in this region is much flatter compared to the disk and regions which are not in the shadow of the disk contribute equally to $\epsilon_{\text{avg}}(\text{CO})$. Nevertheless, the disk causes some depletion of CO within the radial CO ice line of the envelope. A 1D envelope model would not show such an additional depletion and the average CO abundance would reach the canonical value of $\epsilon_{\text{avg}}(\text{CO}) \approx 2 \times 10^{-4}$ within the envelope CO ice line.

Beyond $r \gtrsim 300$ au the dust temperature is below $T_{\text{sub}}(\text{CO})$ and CO can freeze out throughout the whole structure. Due to the lower densities in this zone (e.g. $n_{(\text{H})}(r = 300 \text{ au}) \approx 5 \times 10^6 \text{ cm}^{-3}$ and $n_{(\text{H})}(r = 2500 \text{ au}) \approx 10^5 \text{ cm}^{-3}$) the freeze-out timescale increases significantly. The delayed freeze-out is nicely seen in the averaged abundance profiles and in the 2D contour plots. Using Eq. (12) the freeze-out timescales at ≈ 300 au and ≈ 2500 au are ≈ 400 yr and $\approx 20\,000$ yr respectively. The difference in the timescale for these two points is mainly a result of the density gradient; the temperature varies only by a factor of two, the density by a factor of ≈ 50 . As a consequence we see an inside-out

freeze-out of CO similar to the 1D models of Visser et al. (2015; see also Appendix A).

As Fig. 3 shows, it is not trivial to provide a single number for a radial CO ice line in a complex 2D structure. The picture is further complicated by the slow evolution of the CO abundance in the post-burst phase. However, it will be beneficial for the rest of the paper to define two distinct locations for the radial CO ice lines. The first is the CO ice line in the quiescent phase which is at $R_{\text{Q}}(\text{CO}\#) \approx 300$ au (# stands for ice), the second is the location of the ice line during the burst at $R_{\text{B}}(\text{CO}\#) \approx 2500$ au. These two radial CO ice lines roughly correspond to the location of the $T_{\text{dust}} = 27$ K (the CO sublimation temperature) contours seen in Fig. 1 but are also clearly visible in Fig. 3. We do not consider the CO ice line in the disk for the further discussion, because the main action in the post-burst phase, concerning the CO abundance, is happening in regions $R_{\text{Q}}(\text{CO}\#) \lesssim r \lesssim R_{\text{B}}(\text{CO}\#)$.

Comparing our model to the spherical symmetric 1D model of Visser et al. (2015; see Appendix A) shows that the evolution of the CO abundance with time is qualitatively speaking similar in both models. Although adding a disk component has a significant impact on the temperature structure, the density gradient on large scales (the envelope) is not affected. As the freeze-out timescale is mainly determined by the density, the time-evolution of the CO gas phase abundance in the outer regions of the envelope is therefore not strongly affected by the presence of a disk (see also Sect. 3.4). However, as already discussed, the disk has an impact on the actual freeze-out timescale in the inner region of the structure and on the detailed location of the CO ice line(s) in the envelope structure which are relevant for the quantitative interpretation of observations.

Ch. Rab et al.: The chemistry of episodic accretion in embedded objects

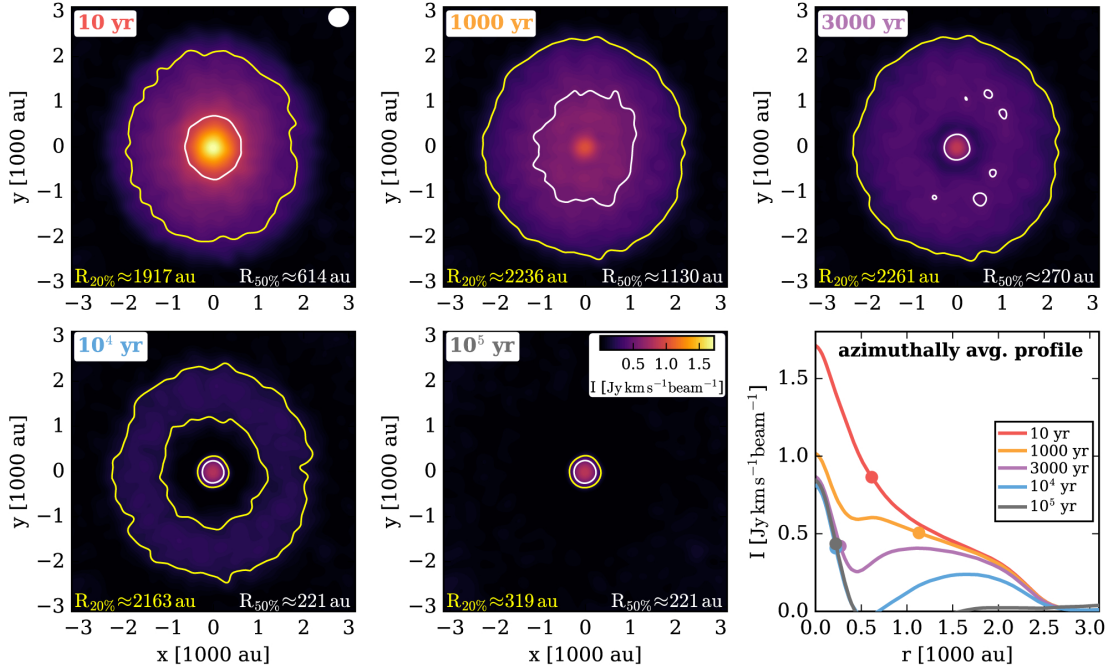


Fig. 4. $\text{C}^{18}\text{O } J = 2-1$ ALMA simulations for the representative Class I model. The first five panels from top left to the bottom right show integrated intensity maps for the post-burst phase at 10, 1000, 3000, 10^4 and 10^5 yr years after the end of the burst (see also Fig. 3). The target is seen face-on (looking down the outflow cavity, inclination $=0^\circ$). The white ellipse in the top left plot shows the synthetic beam ($1.81'' \times 1.65''$). The linear scale for the intensity is shown in the bottom centre plot. The white and yellow contour lines show 50% and 20% of the peak intensity level for each map. The plot at the bottom right shows the azimuthally averaged intensity profiles for the different times. The dots in this plot mark the full width half maximum of the profile ($R_{50\%}$).

3.3. ALMA simulations

To study the impact of the chemical evolution in the post-burst phase on observables we present synthetic observations for the $\text{C}^{18}\text{O } J = 2-1$ spectral line using proper line radiative transfer (Sect. 2.4) and CASA/ALMA simulations (see Appendix B for details). We use $\text{C}^{18}\text{O } J = 2-1$ for two main reasons. Firstly, CO has a low sublimation temperature, therefore CO sublimates also in the outer regions of the structure where the timescale for freeze-out is the longest. This increases the probability to detect extended CO emission long after the burst (Jørgensen et al. 2015). Secondly, choosing $\text{C}^{18}\text{O } J = 2-1$ allows for comparison of our results to the 1D models of Jørgensen et al. (2015) as they used the measured extent of the $\text{C}^{18}\text{O } J = 2-1$ emission to identify post-burst objects.

Figure 4 shows $\text{C}^{18}\text{O } J = 2-1$ intensity maps for the same times as shown in Fig. 3. The target is seen at an inclination of 0° (i.e. face-on); the observer looks down the outflow cavity along the z axis. The last panel in Fig. 4 shows the azimuthally averaged radial intensity profiles. To indicate the extent of the emission we show contours for 50% and 20% of the peak intensity. The radius for the 50% contour is also marked in the averaged intensity profiles. The radius of the 50% contour, $R_{50\%}$, can be seen as a measure for the extent of the CO emission. We follow this approach as in observational studies often the full width at half maximum (FWHM) of a Gaussian fitted to the observation, is used to measure the extent of emission (e.g. the radius is given by $\text{FWHM}/2$, see also Sect. 4.1). However, the $R_{50\%}$ radius shown in Fig. 4 is not necessarily equal to the $\text{FWHM}/2$ of a fitted Gaussian as we use here the full profile.

From the azimuthally averaged radial intensity profiles in Fig. 4 one can see that the observations nicely trace the evolution of the gas-phase CO as discussed in Sect. 3.2. Due to the faster freeze-out of CO in the inner regions a dark gap appears in the intensity maps. This gap is already visible at $t = 1000$ yr and grows with time until it disappears at $t \geq 10000$ yr, when all the CO released into the gas phase during the burst, is frozen-out again.

Another interesting aspect is the evolution of the peak intensity. As seen in the panel for the radial profiles, the peak intensity reaches its final or quiescent level already at $t \approx 1000$ yr. We note that for this particular simulation the disk is not resolved (the beam size corresponds to 300–350 au at a distance of 200 pc). Nevertheless, the peak intensity is mostly determined by emission from and close to the disk if the structure is seen face-on. Therefore the peak intensity evolves on a timescale of 100 to 1000 yr. As a consequence of the differential freeze-out also the apparent extent of the emission is affected. As nicely seen in the averaged profiles, the $R_{50\%}$ radius at $t = 1000$ yr is larger than at $t = 10$ yr. In Fig. 5 we show the same model as in Fig. 4 but the target is now seen at an inclination of 90° (edge-on, perpendicular to the outflow axis). The main difference to the face-on view is the absence of a gap and the X-shape of the emission in the post-burst phase, best seen in the panel for $t = 10^4$ yr. The reason for the absence of the gap is that for inclined targets one mainly sees the CO on large scales which dominates the emission along the line of sight. Therefore a detection of the gap is only likely for targets seen nearly face-on, where one can peek down the outflow cavity. In our models the gap is only visible for inclinations $\lesssim 23^\circ$ (see Fig. C.1).

A&A 604, A15 (2017)

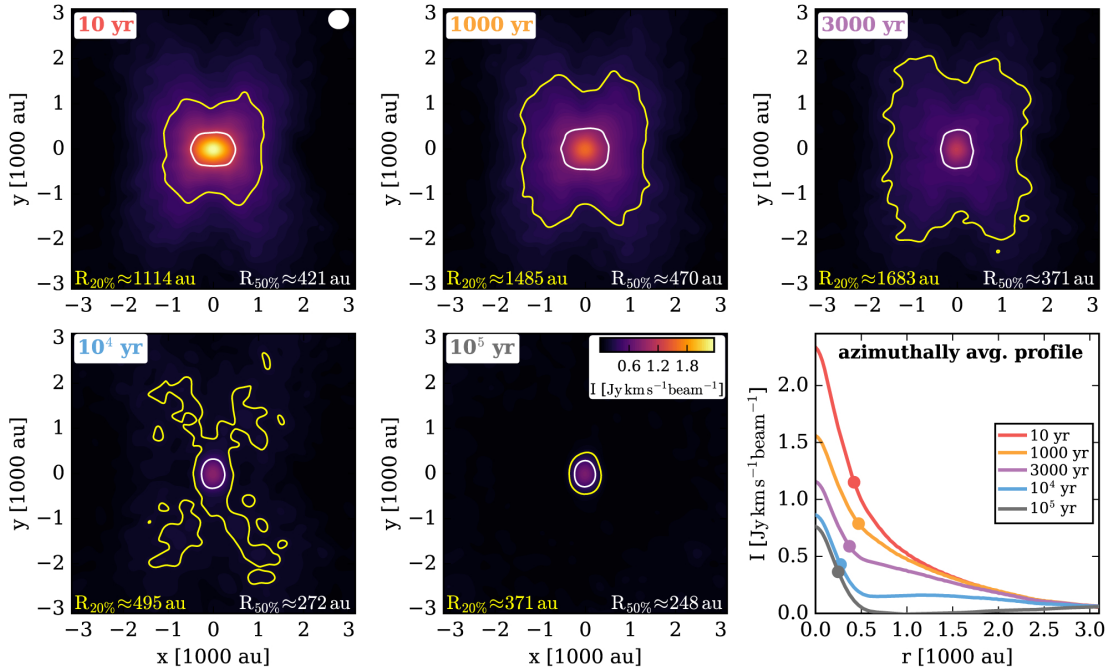


Fig. 5. The same as Fig. 4 but for an inclination of 90° (edge on, perpendicular to the outflow axis).

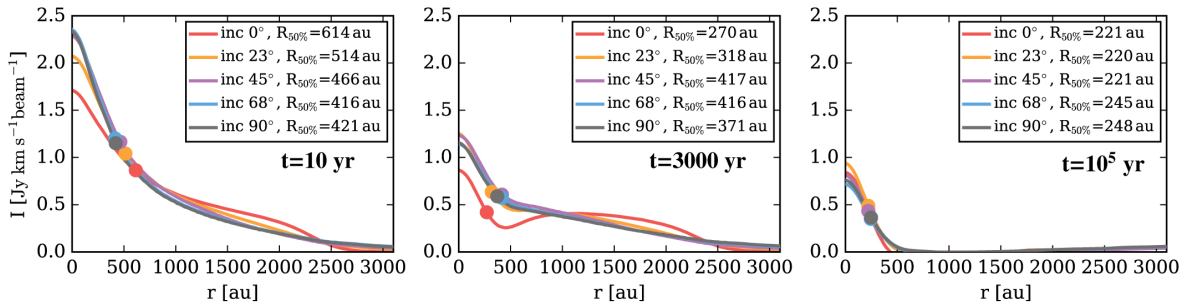


Fig. 6. Impact of inclination on the radial intensity profiles. Shown are azimuthally averaged radial $\text{C}^{18}\text{O } J = 2-1$ intensity profiles for models with different inclinations (coloured lines in each panel) at three different times after the burst (different panels). The large dot in each profile indicates the $R_{50\%}$ radius corresponding to the value given in the legend.

The X-shape of the emission is a consequence of the outflow cavity and again the different freeze-out timescales. In regions with the outflow cavity one sees simply less material (as the cavity is empty) and therefore also weaker emission. Perpendicular to the outflow cavity axis we see more material, but due to higher densities close to the midplane of the structure ($y = 0$ in Fig. 5) CO freezes out faster than close to the outflow walls. The higher densities close to the midplane are due to the rotationally flattened structure and the disk. Further in the disk shadow the temperature is cooler and the CO ice line close to the midplane is located at smaller radii compared to the regions close to the outflow walls (see Fig. 3). As a consequence of these effects the X-shape of the emission is most pronounced at high inclinations (see also Fig. C.1).

In Fig. 6 we show azimuthally averaged intensity profiles at three different times (including the quiescent state) after the burst, where in each panel models with different inclinations are shown. In the quiescent state ($t = 10^5$ yr) inclination has only a

marginal impact on the resulting intensity profiles and the $R_{50\%}$ radii vary only by about 10%. For times shortly after the burst ($t = 10$ yr and $t = 3000$ yr) the situation is more complex. For $t = 10$ yr the extent of the CO emission is larger for smaller inclinations whereas for $t = 3000$ yr the opposite is true. The reason for this is the freeze-out of CO in the inner regions which affects the peak intensity and therefore also the $R_{50\%}$ radius but also optical depth effects play a role here (see Sect. 4.3.2). However, even for inclined targets the peak intensity evolves on shorter timescales than the extended emission which is a consequence of the different freeze-out timescales. Similar to the face-on models the measured $R_{50\%}$ radius can be larger in the post-burst face than during or shortly after the burst.

The presented ALMA simulations clearly show that the inside-out freeze-out produces distinct observational signatures (such as the gap) in spatially resolved images of $\text{C}^{18}\text{O } J = 2-1$. The main requirement for real interferometric observations is that the different spatial scales are properly captured and

Ch. Rab et al.: The chemistry of episodic accretion in embedded objects

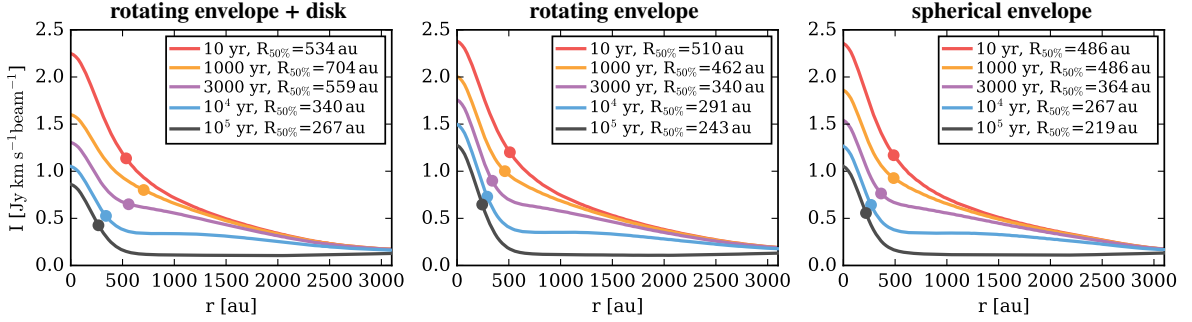


Fig. 7. Impact of structure on the radial intensity profiles. Shown are azimuthally averaged radial intensity profiles for $C^{18}O J = 2-1$ for models with an inclination of 45° at different times in the post-burst phase. Density structures from *left to right*: rotating envelope with a disk component, rotating envelope without a disk, a spherical symmetric envelope (all models include an outflow cavity). The large dot in each profile indicates the $R_{50\%}$ radius corresponding to the value given in the legend.

that the large scale emission is not filtered out. Although we presented here only ALMA simulations also other existing (sub)mm interferometers like the IRAM Plateau de Bure Interferometer/Northern Extended Millimeter Array (IRAM-PdBI/NOEMA) and Submillimeter Array (SMA) are capable of performing such observations (e.g. Jørgensen et al. 2015; Anderl et al. 2016).

3.4. Impact of structure

Additionally to our representative Class I model we performed the same burst simulations for “simpler” structures, namely a rotating-envelope model without a disk and a spherical symmetric model. The main parameters, like the stellar properties, the outflow cavity and the extension of the models are the same. The main difference lies in the radial density profiles. For the rotating-envelope model the slope of the density gradient flattens towards the centre; in the spherical model the radial density distribution is simply proportional to $r^{-1.5}$ (i.e. setting the centrifugal radius R_c in Eq. (1) to zero).

In Fig. 7 we show a comparison of the three different structure models. Shown are the averaged radial intensity profiles at several times after the burst. The inclination is 45° (see Fig. D.1 for the other inclinations). To produce those synthetic observations we did not perform full ALMA simulations but present simple beam-convolved simulations, with the same beam size as we used for the ALMA simulations. The beam-convolved simulations represent the radial intensity profiles from the ALMA simulations very well (see Appendix B) and are mainly used to save computational resources.

At first sight, the evolution of the radial intensity profiles look quite similar for all three structure models, but there are also distinct differences. In particular, the evolution of the peak intensity happens on different timescales. For the envelope+disk model the peak intensity drops quickly with time due to the fast freeze-out (≈ 100 yr) in the midplane of the disk. The two other structure models show a slower evolution of the peak intensity, where the rotating envelope model shows the slowest due to the flattening of the density profile towards the centre.

In Fig. 7 we also indicate the $R_{50\%}$ radius and give the actual value in the legend of each panel. In the envelope+disk model $R_{50\%}$ is larger at all times than in the two other structure models. The reason for this is actually the lower peak intensity and not the extension of the CO emission. Due to the higher density and lower temperatures in the disk midplane, CO freezes out quicker

and the averaged CO abundance is lower compared to the structure models without a disk.

The comparison of the three structure models shows that on large scales the evolution of the radial intensity profiles are similar. However, due to the different density structures in the inner regions ($r < 500$ au) the peak intensity evolves on different timescales. As a consequence, the actual measured extent of the emission is larger for structures with a steeper density gradient or a high density component, such as a disk, in the inner regions. Such effects are relevant for the quantitative interpretations of CO observations in the post-burst phase and can only be properly captured by 2D models like the one presented here.

4. Discussion

4.1. A model independent method to identify post-burst sources

To measure the radial extent of emission it is common to use the FWHM of a 1D/2D Gaussian fitted to the observational data. Such an approach is also used in Jørgensen et al. (2015) to estimate the extent of $C^{18}O J = 2-1$ for a sample of Class 0/I sources to identify targets that experienced a recent burst. Jørgensen et al. (2015) find extended $C^{18}O J = 2-1$ emission, with respect to the extent expected from the currently observed source luminosity, for half of their targets.

It is interesting to see what radial extent for CO would be measured from our models, using a similar fitting procedure. We fit either one or two Gaussians to the beam convolved images using the CASA task `imfit`. The fit also includes a zero level offset to account for the background $C^{18}O$ emission on large scales. To compare the fitting results to the synthetic observations we use again azimuthally averaged radial intensity profiles, produced in the same way as for the synthetic observations.

In Fig. 8 we show the derived radial intensity profiles at six different times after the burst. Each panel of Fig. 8 shows the synthetic profile and the profiles derived from the two different fitting methods (1GF and 2GF, respectively). Further the measured $R_{50\%}$ radii are given (correspond to $FWHM/2$ of the fitted Gaussians). In the case of the two-component fit (2GF) both measured radii for the individual Gaussians and the ratio of the two radii are denoted.

Comparing the $R_{50\%}$ radius in the quiescent phase to the measured radii in the post-burst phase shows that the single Gaussian (1GF) indeed is a reliable method to identify extended CO emission in the post-burst phase. However, it is interesting to see that

A&A 604, A15 (2017)

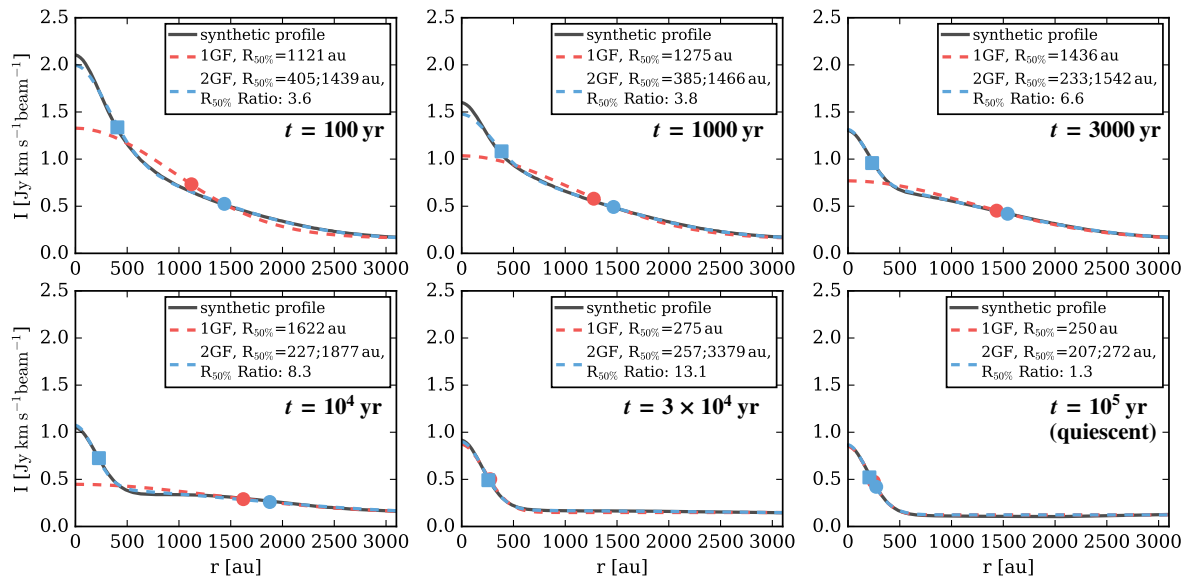


Fig. 8. $\text{C}^{18}\text{O } J = 2-1$ radial intensity profiles derived from fitting the synthetic observations. Shown are the results for an inclination of 45° at five different times (given in the panels) in the post-burst phase and in the quiescent phase (*last panel*). Each individual panel shows the “real” beam convolved simulations (black solid line), a fit using one Gaussian (1GF, red dashed line) and a fit using two Gaussians (2GF, blue dashed line). In the legend the $FWHM/2$ ($R_{50\%}$) value for the fitted Gaussian(s) is denoted (indicated by the big dots). For the 2GF both radii (for each Gaussian) and the ratio of the two radii are provided. For comparison, the actual CO ice lines in the quiescent phase and in the burst phase are located at $R_Q(\text{CO}\#) \approx 300$ au and $R_B(\text{CO}\#) \approx 2500$ au, respectively (see Sect. 3.2 and Fig. 3).

$R_{50\%}$ increases with time until all CO sublimated during the burst is frozen-out again ($t \approx 3 \times 10^4$ yr). The reason for this is that the fit is more sensitive to the extended emission (larger area) and that the peak of the profiles evolves on a shorter timescale than the most extended emission (see Sects. 3.3 and 3.4). It is also apparent that the emission at small radii is not well fitted with the 1GF in the post-burst phase, only in the quiescent phase the emission is reasonably well represented by a single Gaussian.

The two Gaussian fitting procedure (2GF) fits the synthetic profiles in the post-burst phase significantly better than the single Gaussian fits, now also the emission on small scales is fitted well. Typically the χ^2 value of the 2GF is a factor of approximately four lower than for the 1GF for $t < 3 \times 10^4$ yr. $R_{50\%}$ for the extended emission (the larger of the two radii indicated in Fig. 8) derived from the two-component fit is usually slightly larger compared to the 1GF, but considering uncertainties those radii are quite similar. In the case of very weak extended emission or in the quiescent phase, the 2GF either fails (see Appendix E) or the quality of the 2GF and 1GF is nearly identical.

It is not surprising that fitting two components provides better results than a single component fit, simply because the 2GF has more free parameters. Besides this mathematical argument there are also physical reasons why a two component fit is a good representation of the post-burst emission pattern. The CO emission in the post-burst phase can be separated into two components. One component corresponds to the emission coming from within the radial CO line corresponding to the current (quiescent) temperature structure ($R_Q(\text{CO}\#) \approx 300$ au, see Sect. 3.2). This component exists in all phases: burst, post-burst and quiescent phase. The second component corresponds to the extended emission coming from the region $R_Q(\text{CO}\#) \leq r \leq R_B(\text{CO}\#)$. In the post-burst phase CO freezes out between these two ice lines

where the longest freeze-out timescale is close to $R_B(\text{CO}\#)$. In the actual observation we see (depending on the viewing angle) a superposition of these two components, it is therefore advantageous to actually use also two components to fit such observations.

Besides the better quality of 2GF compared to the 1GF, the 2GF fitting procedure has several further advantages:

- with the 2GF procedure one obtains information about the CO ice line in the quiescent and burst-phase as two radii are measured. The measured smaller radius corresponds to the quiescent CO ice line and the larger radius to the burst CO ice line. Of course both quantities are only a rough estimate and especially the measured quiescent CO ice line should be seen as an upper limit (i.e. depending on the spatial resolution available);
- the ratio of the two radii provides some rough indication for the time since the last burst. The ratio usually increases with time as can be seen in Fig. 8. The ratio increases because of the different freeze-out timescales in the inner region and outer region. Emission close to $R_B(\text{CO}\#)$ is seen for longer than the emission close to $R_Q(\text{CO}\#)$;
- for the quiescent phase the 1GF is actually a better representation of the observations as only one component is seen. For the quiescent phase the 2GF either fails at all or performs equally well as the 1GF fit. Only for the post-burst profile the 2GF is superior (typically at least a factor four lower χ^2 values). By using the two methods to fit real observations it is therefore possible to identify post-burst targets in a model independent way. For the 1GF the measured extent needs to be compared to a model predicting the actual extent for the current measured source luminosity. The 1GF approach depends in particular on the binding energy of CO which defines the location of the CO ice line(s) (see Jørgensen et al. 2015, for a

Ch. Rab et al.: The chemistry of episodic accretion in embedded objects

discussion). This is not the case for the 2GF approach. In that case it is possible to identify post-burst sources by simply comparing the quality of the 2GF to the 1GF. A significantly better quality of the 2GF already indicates that the object is currently in the post-burst phase. Therefore the 2GF method does not require any detailed modelling to identify post-burst objects.

We also tested the 2GF method for the different structure models, different inclinations and different spatial resolutions (see Appendix E for further examples). Although the absolute numbers for the measured radii can vary, the main arguments in favour of the 2GF are also valid for those models. However, it still must be shown how well the procedure works with other models (in particular chemical models) and subsequently with real observational data. However, the main physical argument for the two Gaussian fitting procedure is actually the inside-out freeze-out of CO in the zone between the quiescent and burst CO ice lines. This is a very robust chemical result as it is mainly based on the adsorption timescales and is also seen in other models (e.g. Visser et al. 2015; Vorobyov et al. 2013). The 2GF method is therefore a robust and consistent way to identify post-burst targets and to derive statistically relevant information such as the strength and frequencies of bursts.

4.2. CO extent versus bolometric luminosity

As mentioned above, Jørgensen et al. (2015) identified post-burst candidates by relating the measured extent of $C^{18}O J = 2-1$ emission to the currently measured bolometric luminosity of the target. To compare our results to this approach we show in Fig. 9 a similar CO extent versus current bolometric luminosity plot as in Jørgensen et al. (2015) and populate this plot with the values derived from our models.

We want to emphasize that the models of Jørgensen et al. (2015) are very different to the models presented in this paper. They use 1D models with a spherical power-law density distribution $\rho \propto r^{-1.5}$ and calculate the temperature structure with a radiative transfer code for a range of luminosities. The CO abundance is modelled with a simple step function where the CO abundance is decreased by two orders of magnitude for $T < 30$ K. To measure the extent of CO in those models they convolved the synthetic images with a $\approx 2''$ beam and fitted a single 1D Gaussian in the visibility plane. The $FWHM/2$ of this fitted Gaussian gives the radius of the CO emission (the $R_{50\%}(C^{18}O 2-1)$ axis in Fig. 9). Because of all these differences we do not aim for a direct comparison of the models but rather to use the results of Jørgensen et al. (2015) as a reference frame.

To populate Fig. 9 we calculate the bolometric luminosity of the model by integrating the synthetic spectral energy distribution and measure the CO extent by fitting our synthetic $C^{18}O J = 2-1$ images as already described in Sect. 4.1. To be more consistent with Jørgensen et al. (2015) we use here the $R_{50\%}(C^{18}O 2-1)$ derived from the single Gaussian fitting procedure. We want to note that the measured bolometric luminosity actually depends on inclination and does not necessarily represent the true source luminosity. If a Class I object is seen face-on one sees the maximum protostellar flux and scattered emission where for the edge-on case the protostar is usually obscured (see Whitney et al. 2003, for a detailed discussion). For our models presented here the measured bolometric luminosity is typically about a factor of two to three higher for the face-on case and a factor of two lower for the edge-on case, compared to the true

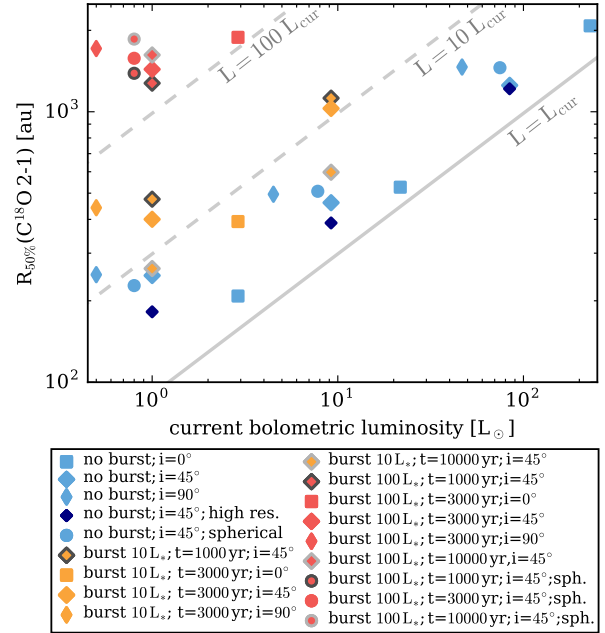


Fig. 9. Measured $C^{18}O J = 2-1$ extent versus current bolometric luminosity. The blue symbols show models in quiescent state (no burst) with protostellar luminosities L_* of 1, 10 and $100 L_\odot$. The red symbols are for strong burst models with burst luminosities of $L_{*,B} = 100 \times L_*$. The orange symbols show weak burst models with $L_{*,B} = 10 \times L_*$. For both groups of burst models the results in the post-burst phase are shown. The edges of the symbols indicate the time past since the end of the burst of 1000 yr (black edge), 3000 yr (no edge) and 10000 yr (grey edge). The different shapes of the symbols indicate different inclinations of 0° (square), 45° (diamond) and 90° (thin diamond). For all models a beam size of $1.81'' \times 1.65''$ was used, except for the models indicated by the dark blue symbols where a beam size of $0.5'' \times 0.5''$ (high res.) was used. The grey solid and dashed lines are the model results from Jørgensen et al. (2015) for a 1D spherical model of a Class 0 protostellar envelope with varying protostellar luminosities.

source luminosity. These values are in good agreement with the results of Whitney et al. (2003).

In Fig. 9 we show various different models. The first group of models are models without a burst (quiescent). We show models with a protostellar luminosity L_* of 1, 10 and $100 L_\odot$. For each of those models we plot the measured CO extent versus the actual bolometric luminosity (calculated from the synthetic SEDs) for three different inclinations. Further we show no-burst models using only a spherical structure (no disk component) and models where the CO extent was derived from synthetic observations with a higher spatial resolution (beam with $0.5'' \times 0.5''$; corresponds to ≈ 100 au resolution at a distance of 200 pc).

The second group of models corresponds to strong burst models with a burst luminosity 100 times the quiescent luminosity ($L_{*,B} = 100 \times L_*$). These models are the same as discussed in Sect. 3. For those models we show the measured CO extent in the post-burst phase at three different times, for different inclinations and also for the spherical structure model. We note that for the post-burst models the current measured bolometric luminosity is equal to the quiescent phase as the burst is over and the temperature structure already reached its quiescent state. The third group of models represents weak bursts, where

the quiescent stellar luminosity is increased only by a factor of ten during the burst ($L_{*,B} = 10 \times L_*$).

A close inspection of Fig. 9 unveils several interesting aspects of our 2D radiation thermo-chemical model:

- *Inclination*: a glance at the models without a burst shows that the impact of inclination is twofold. The different inclinations produce a scatter along the luminosity axis although the physical structure and properties of the models are otherwise the same (see discussion above). The different inclinations cause also some scatter for the measured CO extent, but compared to the bolometric luminosity this is rather limited. We note that those effects are a natural outcome of our 2D model and cannot be properly captured with 1D models. However, due to our simplistic model for the outflow cavity (i.e. it is empty and we consider only one opening angle for the cavity) our here presented models can only provide a rough estimate for the impact of inclination.
- *Structure*: comparing the spherical models to the disk+envelope models shows again that the details of the structure are not particularly significant on large scales (see also Sect. 3.4).
- *Spatial resolution*: high spatial resolution observations ($0.5'' \times 0.5''$ beam) provide obviously more accurate results for objects with a small CO extent, whereas for objects with large CO extent the measured radii are nearly identical to the radii of the low resolution models ($1.81'' \times 1.65''$ beam).
- *Strong bursts* ($100 \times L_*$): as already discussed in previous sections, the extent of the CO emission appears larger at later times after the burst. Figure 9 clearly shows that strong recent bursts are easily detectable for $\approx 10\,000$ yr after the end of the burst. Although the measured radii for the CO extent vary slightly with time the radii are at least a factor of approximately four larger compared to the CO extent expected from the current bolometric luminosity. We want to emphasize that for such strong bursts it is important to not filter out large scale structures in interferometric observations, otherwise such post-burst targets would not be detected (see also Jørgensen et al. 2015).
- *Weak bursts* ($10 \times L_*$): for the weak burst models with a quiescent stellar luminosity of $L_* = 10 L_\odot$ and a burst luminosity of $L_{*,B} = 100 L_\odot$ the measured CO extent is slightly smaller than for the strong burst models which also have $L_{*,B} = 100 L_\odot$. The reason for this is that the contrast between the quiescent component in the inner region, which is more extended for $L_* = 10 L_\odot$, and the extended post-burst component of the CO emission is weaker compared to strong burst models. In particular the peak luminosity is higher resulting in a slightly narrower width of the fitted Gaussian. In contrast to the strong burst models the weak burst models do not indicate extended CO emission at $t = 10\,000$ yr after the burst (i.e. $R_{50\%}$ is similar to the quiescent state). One reason for this is, again, the weaker contrast between the quiescent and extended emission components the other is the freeze-out timescale. In the weak burst model with $L_* = 1 L_\odot$ and $L_{*,B} = 10 L_\odot$ the CO ice line during the burst is at smaller radii ($R_B(\text{CO}\#) \approx 800$ au) where the freeze-out timescale is about a factor of three shorter than in the corresponding strong burst models ($R_B(\text{CO}\#) \approx 2500$ au). Generally speaking, weak bursts are harder to detect in the post-burst phase and therefore the detection probability for weak bursts decreases significantly. Such limitations need to be considered for deriving statistical quantities such as burst frequencies from post-burst observations.

After having discussed the details of Fig. 9, a more global view of Fig. 9 shows that our model results are qualitatively in good agreement with the results of Jørgensen et al. (2015). Although there are quantitative differences in the models, which are not surprising as we use a different structure and chemical model, the general agreement is certainly a strong argument in favour of the CO extent method. The main advantage of using CO as a post-burst tracer is the expected long-freeze out timescale which allows us to detect bursts up to 10 000 s of years after the actual end of the burst (Visser et al. 2015; Jørgensen et al. 2015).

4.3. Further considerations

4.3.1. Dynamical evolution and outflows

We assume here a steady-state structure and consequently ignore any dynamical evolution of the system. The issue here is that the CO abundance is out of equilibrium with the temperature structure.

For our representative Class I model the free-fall timescale at $r = 2500$ au is $t_{\text{ff}} \approx 20\,000$ yr, which is actually comparable to the freeze-out timescale of $t_{\text{ads}} \approx 23\,000$ yr at this distance. Close to the quiescent CO ice line at $r = 300$ au the timescales are $t_{\text{ff}} \approx 800$ yr and $t_{\text{ads}} \approx 400$ yr (now $t_{\text{ads}} < t_{\text{ff}}$). Considering those timescales, CO initially in the gas phase at $r = 2500$ au will have been frozen-out when it reaches $r = 300$ au where it will sublimate again (see also Visser et al. 2009b).

Nevertheless, as $t_{\text{ff}} \approx t_{\text{ads}}$, the dynamical evolution likely has an impact on our results. A parcel of gas located at $r = 2500$ au moving with the free-fall velocity would move inwards by ≈ 130 au in ≈ 1000 yr. In the post-burst scenario this means that the burst CO ice line moves inward even if there would be no freeze-out at all (we assume here that CO outside of the burst CO ice line is mostly in the ice phase). This simple example should be seen as a worst case scenario, as we have ignored any rotational motion. Rotation will slow down the inward motion and the impact of dynamical infall on the CO ice line location would be less severe. However, our results for the expected measured CO extent in the post-burst phase should be seen as upper limits. On smaller scales the impact of dynamical evolution is less severe as there usually $t_{\text{ads}} < t_{\text{ff}}$ (see above). Although the dynamical evolution might reduce the timescale on which post-burst targets can be detected it does not affect our main conclusions.

This is also indicated by the hydrodynamic models of Vorobyov et al. (2013). They use the thin-disk approximation (averaged vertical quantities) to model the evolution of a protostellar system starting from the collapse up to the T Tauri phase (see also Vorobyov & Basu 2010). They model the dynamical evolution of CO, including adsorption and desorption processes, during and after accretion bursts. From their Fig. 3 one can see that their model shows similar features as presented here. In particular the radial gradient in the gas-phase CO abundance, resulting in a ring-like structure in our synthetic observations, can also be seen in their models. This provides further confidence that our results are not significantly affected by the dynamical evolution.

Nevertheless, the dynamical timescale can vary from object to object (e.g. different central masses, rotation of the envelope) and further investigations concerning the impact on observables in the post-burst phase are desirable (e.g. by producing synthetic observations from models like presented in Vorobyov et al. 2013).

Although our model includes an outflow cavity, the outflow itself is not modelled at all. This is not necessarily an issue as long as C^{18}O emission from the envelope and disk is not polluted

by emission from the outflow. Indeed observations indicate that $C^{18}O$ traces mainly the envelope of embedded sources, in contrast to the more optically thick isotopologues ^{12}CO and ^{13}CO , which commonly show high velocity wings in their spectral line profiles (e.g. Frank et al. 2014; Dionatos et al. 2010). Recent observations indicate that this is also the case for burst sources (e.g. Kóspál et al. 2017; Ruíz-Rodríguez et al. 2017; Zurlo et al. 2017).

In case outflows contribute to $C^{18}O$ emission it should be possible to disentangle the outflow and envelope emission components, as outflow velocities are higher than typical infall and rotation velocities of envelopes. Of course this is only possible for spectrally and spatially resolved observations and if the $C^{18}O$ emission (in particular from the outflow) is mostly optically thin.

Outflows most likely also have an impact on the shape of the surrounding envelope structure, in particular in burst sources where strong outflows might be common (Ruíz-Rodríguez et al. 2017; Zurlo et al. 2017). Our here presented structure represents therefore a rather idealistic case as dynamical processes likely produce inhomogeneities in the density distribution. We want to emphasize here that our model primarily shows the impact of chemistry on the observables and that real observations will be to some extent also affected by dynamical processes.

4.3.2. Optical depth effects

It is commonly assumed that the $C^{18}O J = 2-1$ line emission is on average optically thin in embedded sources (e.g. Jørgensen et al. 2015; Anderl et al. 2016). This is also the case for most regions in our model, at least in the quiescent phase. However, even in the quiescent phase in parts of the region around the disk $C^{18}O J = 2-1$ becomes optically thick (at least in the line centre). This means that the innermost region, in particular the disk midplane, are to some extent obscured in the synthetic observations.

During the burst and shortly after the burst the optically thick region is much larger (up to $r \approx 1000$ au depending on the viewing angle) due to the additional gas-phase CO in the outer regions of the structure. However, with time CO freezes out again and one can see deeper into the structure. This is also apparent from the synthetic images shown in Figs. 4 and 5. In the face-on images, the gap (close to the quiescent CO ice line) is seen as CO freezes out faster than at larger radii, consequently also the emission sooner becomes optically thin than at larger radii. If the object is inclined one sees more gas-phase CO along the line of sight from the outer region and therefore the inner regions are not seen as clearly. Although in parts of the structure the $C^{18}O J = 2-1$ line emission is optically thick during and shortly after the burst the evolution of the CO freeze-out is still visible as the emission becomes optically thin with time. A comparison of the synthetic images and radial intensity profiles to the CO gas phase evolution shown in Fig. 3 also reveals that the observations nicely trace the actual evolution of the gas-phase CO in the model.

In our model there is also some CO in the gas phase outside of the region affected by the burst ($r \gtrsim 3000$ au, see Fig. 3). In this region the freeze-out of CO is not efficient due to the low densities ($n_{(H)} < 10^5 \text{ cm}^{-3}$) and photo-desorption. However, as the densities are low this region is optically thin in our model and does not affect the $C^{18}O J = 2-1$ line emission from the central region. However, for some targets such a region might be more extended than in our model where the outer radius is $r = 5000$ au. For such a case even the $C^{18}O J = 2-1$ might show some self-absorption and the view towards the central region

might be obscured. For such deeply embedded objects a more optically thin tracer like $C^{17}O$ would be required.

4.3.3. Recurrent bursts and initial chemical abundances

For the pre-burst initial chemical abundances we used values derived from a quiescent chemical evolution for 10^5 yr (Sect. 2.3). However, depending on the burst frequency, periodic bursts can alter the initial abundances. The burst-frequencies, in particular for strong and rather long lasting bursts (≈ 100 yr) like modelled here, are not well known (Audard et al. 2014). However, models and observations indicate that accretion bursts are periodic with time spans between bursts of roughly 5000–50 000 yr (e.g. Vorobyov & Basu 2015; Scholz et al. 2013; Audard et al. 2014; Jørgensen et al. 2015).

For the case of quiescent periods longer than $t \approx 3 \times 10^4$ yr between bursts our results would not be affected at all. For such long quiescent periods the chemical abundances (at least CO) have already reached their quiescent (steady-state) levels again (see Sect. 3.2). In case of higher burst frequencies the chemistry still will be out of equilibrium between two subsequent bursts and the pre-burst initial abundances would be different to what we have used here.

Taking our model presented here as an example, but assuming that another burst happened about 5000 yr ago, the pre-burst initial CO abundances for the second burst would be similar to what is shown in the $t = 3000$ yr panel of Fig. 3. However, if the second burst is at least as strong as the first one (here $L_{*,B} = 100 L_{\odot}$), CO would again sublimate out to similar radii as for the first burst and the abundance at the beginning of the post-burst phase would look the same (at least very similar) to what is shown in the model presented here. A more complicated scenario arises in the case of a weaker second burst. For such a case the second burst will sublimate CO only up to smaller radii than the first stronger burst and the initial post-burst abundance structure will have signatures of both bursts. As a consequence radial intensity profiles will likely show more complex shapes than what is shown here. Nevertheless, such profiles still show extended emission and can be used to identify post-burst targets.

For the future we plan to model such a repetitive burst scenario using as input the burst properties (e.g. burst frequencies and luminosities) derived from theoretical models like presented in Vorobyov et al. (2013) and Vorobyov & Basu (2015). A detailed study of such models will allow identification of possible observational signatures of repetitive bursts with short quiescent periods.

5. Summary and conclusions

We have presented a new two dimensional model for the chemistry of episodic accretion in embedded objects. The model is based on the radiation thermo-chemical disk code PRODiMO. We extended PRODiMO with a parametric prescription for a rotating envelope structure to model a representative Class I source consisting of a disk and envelope component. Our model features different dust size distributions for the disk (evolved dust) and envelope (ISM like dust).

For this density structure we simulated a single burst scenario by simply increasing the quiescent luminosity by a certain factor and calculated the temperature structure and local radiation field for the quiescent and burst phase. Applying a medium sized chemical network, we followed the time evolution of the CO gas phase abundance $\epsilon(CO)$ during the burst and

A&A 604, A15 (2017)

post-burst phase. Further we presented synthetic observations (ALMA simulations) as a function of time (after the burst) for the $C^{18}O$ $J = 2-1$ spectral line to investigate observational signatures of the chemical evolution in the post-burst phase. Our main findings are:

- We used surface weighted averaged dust sizes derived from realistic dust size distributions for the disk and envelope to calculate the adsorption rate. For the disk we use grain sizes up to $1000\mu\text{m}$, for the envelope up to $1\mu\text{m}$. Compared to the commonly used single dust size of $0.1\mu\text{m}$ the freeze-out timescale decreases by a factor of three in the envelope and a factor of 90 in the disk for such dust size distributions. However, as the freeze-out timescale is also a function of gas density the freeze-out timescale in the disk is typically shorter than in the envelope. As the density decreases as a function of distance from the protostar, the freeze-out of e.g. CO happens from inside (high densities) out (low densities).
- Including a disk component has a significant impact on the temperature structure of the envelope. Due to the disk shadow the temperatures close to the midplane of the envelope are cooler compared to structures without a disk. In contrast to a model without a disk, the average CO abundance within the radial CO ice line of the envelope is therefore depleted (by a factor of three in our model). Such effects can not be properly modelled by 1D models. However, on large scales the freeze-out chemistry is mainly driven by the density gradient in the envelope, which is not affected by the disk. Therefore the CO gas phase evolution in the post-burst phase is similar to structures without a disk component.
- The synthetic $C^{18}O$ $J = 2-1$ ALMA observations show that the inside-out freeze-out produces distinct observational signatures. The most striking feature is a clearly visible gap in the intensity images which is caused by the differences in the freeze-out timescales between the zone close to the quiescent CO ice line and the zone close to the burst CO ice line. Such a gap is likely only visible if the target is seen nearly face-on, when one can peek down the outflow cavity. For inclined targets such a gap is not visible. However, the inside-out freeze-out still has an impact on the intensity maps (X-shaped emission pattern) and radial intensity profiles. The peak intensity of the radial profiles drops on shorter timescales than the extended emission.
- Based on our models we propose a new method to identify post-burst targets via spatially resolved $C^{18}O$ observations of embedded objects. The $C^{18}O$ emission in the post-burst phase consists of two components, one corresponds to the centrally peaked emission, which also exists during the quiescent phase, the second component corresponds to the extended emission which only exists for a limited time (up to $10\,000\text{yr}$) after the burst. The post-burst emission pattern is much better fitted by a two Gaussian fit where the quiescent emission pattern is better matched with a single Gaussian. A successful two Gaussian fit is therefore already an indication for a recent burst. This method is model independent and in particular does not depend on the CO binding energy.
- Our model results confirm that measuring the extent of CO emission in embedded sources (Vorobyov et al. 2013; Jørgensen et al. 2015) is an efficient method to identify post-burst objects up to $\approx 10\,000\text{yr}$ after the a burst. However, to derive reliable statistical properties such as burst frequencies from an observational sample, the possible different structures and inclinations of the individual targets should be taken into account.

Acknowledgements. We would like to thank Ruud Visser for providing a detailed and clear referee's report that helped to improve the paper. We also want to thank Zhaohuan Zhu for providing the burst spectrum of FU Orionis. CH.R. and E.V. acknowledge funding by the Austrian Science Fund (FWF): project number I2549-N27. CH.R. and M.G. acknowledge funding by the Austrian Science Fund (FWF): project number P24790. M.A. and A.P. acknowledge funding by the Swiss National Science Foundation (SNSF): project number: 200021L_163172. The research leading to these results has received funding from the European Union Seventh Framework Programme FP7-2011 under grant agreement No. 284405. This publication was partly supported from the FFG ASAP 12 project *JetPro** (FFG-854025). This publication was supported by the Austrian Science Fund (FWF). The computational results presented have been achieved using the Vienna Scientific Cluster (VSC). This research has made use of NASA's Astrophysics Data System. All figures were made with the free Python module Matplotlib (Hunter 2007). This research made use of Astropy, a community-developed core Python package for Astronomy (Astropy Collaboration et al. 2013).

References

- Ábrahám, P., Juhász, A., Dullemond, C. P., et al. 2009, *Nature*, **459**, 224
- Aikawa, Y., Miyama, S. M., Nakano, T., & Umebayashi, T. 1996, *ApJ*, **467**, 684
- Aikawa, Y., Furuya, K., Nomura, H., & Qi, C. 2015, *ApJ*, **807**, 120
- Akimkin, V., Zhukovska, S., Wiebe, D., et al. 2013, *ApJ*, **766**, 8
- Anderl, S., Maret, S., Cabrit, S., et al. 2016, *A&A*, **591**, A3
- Andrews, S. M., Wilner, D. J., Hughes, A. M., Qi, C., & Dullemond, C. P. 2009, *ApJ*, **700**, 1502
- Astropy Collaboration, Robitaille, T. P., Tollerud, E. J., et al. 2013, *A&A*, **558**, A33
- Audard, M., Ábrahám, P., Dunham, M. M., et al. 2014, *Protostars and Planets VI*, **387**
- Baraffe, I., Vorobyov, E., & Chabrier, G. 2012, *ApJ*, **756**, 118
- Birmstiel, T., Ricci, L., Trotta, F., et al. 2010, *A&A*, **516**, L14
- Bonnell, I. A., Bate, M. R., Clarke, C. J., & Pringle, J. E. 1997, *MNRAS*, **285**, 201
- Brott, I., & Hauschildt, P. H. 2005, in *The Three-Dimensional Universe with Gaia*, eds. C. Turon, K. S. O'Flaherty, & M. A. C. Perryman, *ESA SP*, **576**, 565
- Brown, W. A., & Bolina, A. S. 2007, *MNRAS*, **374**, 1006
- Burns, R. A., Handa, T., Nagayama, T., Sunada, K., & Omodaka, T. 2016, *MNRAS*, **460**, 283
- Caratti o Garatti, A., Stecklum, B., Weigelt, G., et al. 2016, *A&A*, **589**, L4
- Cazaux, S., & Tielens, A. G. G. M. 2002, *ApJ*, **575**, L29
- Charnley, S. B., Rodgers, S. D., & Ehrenfreund, P. 2001, *A&A*, **378**, 1024
- Cieza, L. A., Casassus, S., Tobin, J., et al. 2016, *Nature*, **535**, 258
- Collings, M. P., Anderson, M. A., Chen, R., et al. 2004, *MNRAS*, **354**, 1133
- Collings, M. P., Frankland, V. L., Lasne, J., et al. 2015, *MNRAS*, **449**, 1826
- Dionatos, O., Nisini, B., Codella, C., & Giannini, T. 2010, *A&A*, **523**, A29
- Dorschner, J., Begemann, B., Henning, T., Jaeger, C., & Mutschke, H. 1995, *A&A*, **300**, 503
- Draine, B. T., & Bertoldi, F. 1996, *ApJ*, **468**, 269
- Dunham, M. M., & Vorobyov, E. I. 2012, *ApJ*, **747**, 52
- Elbakyan, V. G., Vorobyov, E. I., & Glebova, G. M. 2016, *Astron. Rep.*, **60**, 879
- Fayolle, E. C., Balfe, J., Loomis, R., et al. 2016, *ApJ*, **816**, L28
- Frank, A., Ray, T. P., Cabrit, S., et al. 2014, *Protostars and Planets VI*, 451
- Fraser, H. J., Collings, M. P., McCoustra, M. R. S., & Williams, D. A. 2001, *MNRAS*, **327**, 1165
- Hartmann, L., & Kenyon, S. J. 1985, *ApJ*, **299**, 462
- Hasegawa, T. I., Herbst, E., & Leung, C. M. 1992, *ApJS*, **82**, 167
- Hosokawa, T., Offner, S. S. R., & Krumholz, M. R. 2011, *ApJ*, **738**, 140
- Hubbard, A. 2017, *MNRAS*, **465**, 1910
- Hunter, J. D. 2007, *Computing In Science & Engineering*, **9**, 90
- Ivezic, Z., Groenewegen, M. A. T., Men'shchikov, A., & Szczerba, R. 1997, *MNRAS*, **291**, 121
- Johnstone, D., Hendricks, B., Herczeg, G. J., & Bruderer, S. 2013, *ApJ*, **765**, 133
- Jørgensen, J. K., Schöier, F. L., & van Dishoeck, E. F. 2002, *A&A*, **389**, 908
- Jørgensen, J. K., Schöier, F. L., & van Dishoeck, E. F. 2005, *A&A*, **435**, 177
- Jørgensen, J. K., Visser, R., Sakai, N., et al. 2013, *ApJ*, **779**, L22
- Jørgensen, J. K., Visser, R., Williams, J. P., & Bergin, E. A. 2015, *A&A*, **579**, A23
- Kamp, I., Tilling, I., Woitke, P., Thi, W.-F., & Hogerheijde, M. 2010, *A&A*, **510**, A18
- Kamp, I., Thi, W.-F., Woitke P., et al. 2017, *A&A*, submitted
- Kim, H. J., Evans, II, N. J., Dunham, M. M., et al. 2011, *ApJ*, **729**, 84
- Kim, H. J., Evans, II, N. J., Dunham, M. M., Lee, J.-E., & Pontoppidan, K. M. 2012, *ApJ*, **758**, 38

Ch. Rab et al.: The chemistry of episodic accretion in embedded objects

- Kóspál, Á., Ábrahám, P., Csengeri, T., et al. 2016, *ApJ*, **821**, L4
Kóspál, Á., Ábrahám, P., Csengeri, T., et al. 2017, *ApJ*, **836**, 226
Kristensen, L. E., van Dishoeck, E. F., Bergin, E. A., et al. 2012, *A&A*, **542**, A8
Lee, J.-E. 2007, *Journal of Korean Astronomical Society*, **40**, 83
Lynden-Bell, D., & Pringle, J. E. 1974, *MNRAS*, **168**, 603
Mathis, J. S., Rumpl, W., & Nordsieck, K. H. 1977, *ApJ*, **217**, 425
McElroy, D., Walsh, C., Markwick, A. J., et al. 2013, *A&A*, **550**, A36
McKee, C. F., & Tan, J. C. 2003, *ApJ*, **585**, 850
McMullin, J. P., Waters, B., Schiebel, D., Young, W., & Golap, K. 2007, in *Astronomical Data Analysis Software and Systems XVI*, eds. R. A. Shaw, F. Hill, & D. J. Bell, *ASP Conf. Ser.*, **376**, 127
Meyer, D. M.-A., Vorobyov, E. I., Kuiper, R., & Kley, W. 2017, *MNRAS*, **464**, L90
Mie, G. 1908, *Annalen der Physik*, **330**, 377
Minissale, M., Loison, J.-C., Baouche, S., et al. 2015, *A&A*, **577**, A2
Minissale, M., Dulieu, F., Cazaux, S., & Hocuk, S. 2016, *A&A*, **585**, A24
Noble, J. A., Congiu, E., Dulieu, F., & Fraser, H. J. 2012, *MNRAS*, **421**, 768
Ossenkopf, V., & Henning, T. 1994, *A&A*, **291**, 943
Pinte, C., Dent, W. R. F., Ménard, F., et al. 2016, *ApJ*, **816**, 25
Rodgers, S. D., & Charnley, S. B. 2003, *ApJ*, **585**, 355
Ruíz-Rodríguez, D., Cieza, L. A., Williams, J. P., et al. 2017, *MNRAS*, **466**, 3519
Schöier, F. L., van der Tak, F. F. S., van Dishoeck, E. F., & Black, J. H. 2005, *A&A*, **432**, 369
Scholz, A., Froebrich, D., & Wood, K. 2013, *MNRAS*, **430**, 2910
Scott, P. C., Asplund, M., Grevesse, N., & Sauval, A. J. 2006, *A&A*, **456**, 675
Shu, F. H. 1977, *ApJ*, **214**, 488
Stamatellos, D., Whitworth, A. P., & Hubber, D. A. 2012, *MNRAS*, **427**, 1182
Steinacker, J., Andersen, M., Thi, W.-F., et al. 2015, *A&A*, **582**, A70
Terebey, S., Shu, F. H., & Cassen, P. 1984, *ApJ*, **286**, 529
Thi, W.-F., Woitke, P., & Kamp, I. 2011, *MNRAS*, **412**, 711
Ulrich, R. K. 1976, *ApJ*, **210**, 377
Vasyunin, A. I., Wiebe, D. S., Birnstiel, T., et al. 2011, *ApJ*, **727**, 76
Visser, R., & Bergin, E. A. 2012, *ApJ*, **754**, L18
Visser, R., van Dishoeck, E. F., & Black, J. H. 2009a, *A&A*, **503**, 323
Visser, R., van Dishoeck, E. F., Doty, S. D., & Dullemond, C. P. 2009b, *A&A*, **495**, 881
Visser, R., Bergin, E. A., & Jørgensen, J. K. 2015, *A&A*, **577**, A102
Vorobyov, E. I., & Basu, S. 2010, *ApJ*, **719**, 1896
Vorobyov, E. I., & Basu, S. 2015, *ApJ*, **805**, 115
Vorobyov, E. I., Baraffe, I., Harries, T., & Chabrier, G. 2013, *A&A*, **557**, A35
Vorobyov, E. I., Elbakyan, V., Dunham, M. M., & Guedel, M. 2017a, *A&A*, **600**, A36
Vorobyov, E. I., Elbakyan, V. G., & Hosokawa, T. 2017b, *A&A*, in press
DOI: 10.1051/0004-6361/201630356
Whitney, B. A., Wood, K., Bjorkman, J. E., & Wolff, M. J. 2003, *ApJ*, **591**, 1049
Williams, J. P., & Cieza, L. A. 2011, *ARA&A*, **49**, 67
Woitke, P., Kamp, I., & Thi, W.-F. 2009, *A&A*, **501**, 383
Woitke, P., Riaz, B., Duchêne, G., et al. 2011, *A&A*, **534**, A44
Woitke, P., Min, M., Pinte, C., et al. 2016, *A&A*, **586**, A103
Yang, B., Stancil, P. C., Balakrishnan, N., & Forrey, R. C. 2010, *ApJ*, **718**, 1062
Yıldız, U. A., van Dishoeck, E. F., Kristensen, L. E., et al. 2010, *A&A*, **521**, L40
Ysard, N., Köhler, M., Jones, A., et al. 2016, *A&A*, **588**, A44
Zhu, Z., Hartmann, L., Calvet, N., et al. 2007, *ApJ*, **669**, 483
Zhu, Z., Hartmann, L., Calvet, N., et al. 2008, *ApJ*, **684**, 1281
Zubko, V. G., Mennella, V., Colangeli, L., & Bussoletti, E. 1996, *MNRAS*, **282**, 1321
Zurlo, A., Cieza, L. A., Williams, J. P., et al. 2017, *MNRAS*, **465**, 834

A&A 604, A15 (2017)

Table A.1. Model parameters for the comparison with Visser et al. (2015).

Quantity	Symbol	Value
stellar mass	M_*	$0.5 M_\odot$
stellar effective temp.	T_*	5000 K
stellar luminosity	L_*	$1.6 L_\odot$
strength of interst. FUV	χ^{ISM}	1^a
cosmic ray H_2 ion. rate	ζ_{CR}	$5 \times 10^{-17} \text{ s}^{-1}$
centrifugal radius	R_c	0 au ^b
mass infall rate	\dot{M}_{if}	$2 \times 10^{-5} M_\odot \text{ yr}^{-1}$
inner radius	$R_{\text{E,in}}$	6.2 au
outer radius	$R_{\text{E,out}}$	6200 au
cavity opening angle	β_{cav}	20°
dust/gas mass ratio	d/g	0.01
min. dust particle radius	a_{min}	$0.005 \mu\text{m}$
max. dust particle radius	a_{max}	$0.25 \mu\text{m}$
dust size dist. power index	a_{pow}	3.5^c

Notes. ^(a) χ^{ISM} is given in units of the Draine field (Draine & Bertoldi 1996; Woitke et al. 2009). ^(b) Using $R_c = 0$ results in a spherical symmetric density distribution. ^(c) For the dust composition see Table 1

Table A.2. Initial abundances for the time-dependent chemistry.

Species	$\epsilon(X)$
H	5.0(-5)
H_2	0.5
He	0.09
CO	5.17(-5)
CO#	4.89(-5)
$\text{CO}_2\#$	3.91(-5)
N	4.12(-5)
N_2	1.57(-5)
$\text{NH}_3\#$	2.25(-6)
$\text{H}_2\text{O}\#$	1.41(-4)
S	8.00(-8)
Si	8.00(-9)
Na	2.00(-9)
Mg	7.00(-9)
Fe	3.00(-9)

Notes. These are the same abundances as in Visser et al. (2015).

Appendix A: Comparison to Visser et al. (2015)

In this Section we present a comparison of our model and the 1D model of Visser et al. (2015). The main goal of this comparison is to verify our chemical model, as we use in contrast to Visser et al. (2015) a rather small chemical network. For the comparison we chose their model for the low-mass protostar IRAS 15398. For that model Visser et al. (2015) presented detailed density, temperature and molecular abundance profiles.

Visser et al. (2015) uses the 1D spherical density and temperature profiles from the *DUSTY* (Ivezic et al. 1997) radiative transfer models of Kristensen et al. (2012) and Jørgensen et al. (2002). The outburst is modelled by increasing the quiescent stellar luminosity of $L_* = 1.6 L_\odot$ by a factor of 100. Their chemical network is based on the 2012 release of the UMIST Database for Astrochemistry (McElroy et al. 2013). In addition they include adsorption and desorption for all neutral molecules,

Table A.3. Adsorption Energies of key molecules.

Species	E_B [K]
O	$1420^{1,2}$
CO	1307^3
CO_2	2300^3
H_2O	5773^4
N_2	1200^5
NH_3	2790^6

Notes. ⁽¹⁾ Minissale et al. (2015), ⁽²⁾ Minissale et al. (2016), ⁽³⁾ Noble et al. 2012, ⁽⁴⁾ Fraser et al. (2001), ⁽⁵⁾ Visser et al. (2015), Fayolle et al. (2016), ⁽⁶⁾ Brown & Bolina (2007). The adsorption energies for all other species are taken from the UMIST 2012 release (McElroy et al. 2013), http://udfa.ajmarkwick.net/downloads/RATE12_binding_energies.dist.txt.

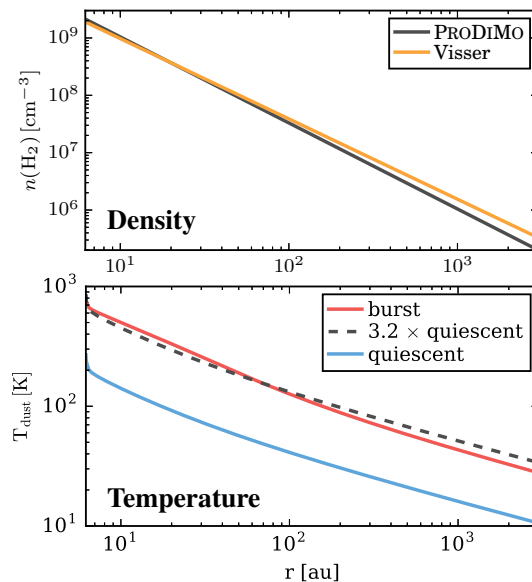


Fig. A.1. Radial midplane density and temperature profiles of the model used for the comparison to the 1D model of Visser et al. (2015). In the molecular hydrogen density plot (top panel) also the density profile of Kristensen et al. (2012) and Visser et al. (2015) is shown. In the temperature plot (bottom panel) the red solid line represents the burst phase and the blue solid line the quiescent period. The dashed grey line shows the quiescent temperature profile multiplied by a factor of 3.2.

formation of H_2 on dust grains and hydrogenation of C, N and O on dust grain surfaces.

For the density structure we use the same 2D description for the envelope structure as discussed in Sect. 2.1.1. To achieve a similar density distribution as used by Visser et al. (2015), a power-law with $\rho(r) \propto r^{-1.4}$, we set the centrifugal radius R_c in Eq. (1) to zero and do not include a disk component. This provides a spherical symmetric density distribution following a radial power-law with $\rho(r) \propto r^{-1.5}$ (i.e. slightly steeper than the profile used by Visser et al. 2015). The model still includes an outflow cavity with an opening angle of 20° .

For the stellar properties and the burst we used the same parameters as Visser et al. (2015). The effective temperature T_* of the star is not given in Visser et al. (2015). However, as their dust continuum model is based on Kristensen et al. (2012) and

Ch. Rab et al.: The chemistry of episodic accretion in embedded objects

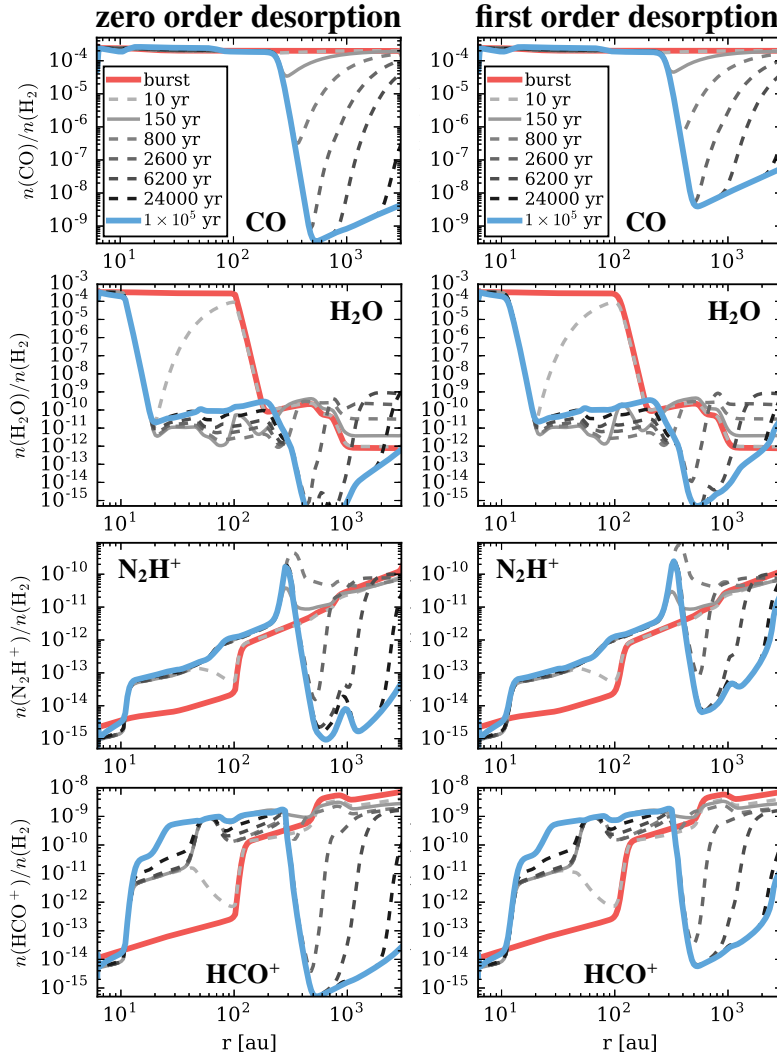


Fig. A.2. Radial midplane abundance profiles for the model used for the comparison to Visser et al. (2015). In contrast to the rest of the paper the abundances are given relative to molecular hydrogen like in Visser et al. (2015). Shown are, from top to bottom, CO, H₂O, N₂H⁺ and HCO⁺ during the burst (red solid line) and at different times in the post-burst phase (grey and blue solid lines). The *left column* shows a model with zeroth order desorption (PRODIMO standard) the *right column* a model using first order desorption. This figure can be compared to Fig. 1 of Visser et al. (2015).

Jørgensen et al. (2002) we assumed $T_* = 5000$ K as given in Jørgensen et al. (2002). We have not used the same dust opacities as Kristensen et al. (2012), who use the opacities from Ossenkopf & Henning (1994). We applied the same dust composition as in the main paper (see Sect. 2.1.2) and only adapt the dust size distribution. All relevant physical parameters for the comparison model are summarized in Table A.1.

As we used a 2D model we only compare the midplane (i.e. the plane perpendicular to the outflow axis) quantities of our model to the 1D model of Visser et al. (2015). In the midplane the differences caused by the different structures used (e.g. outflow cavity) should be minimal. In Fig. A.1 we show the radial density and temperature profiles in the midplane. In the plot for the density also the power-law density profile used by Visser et al. (2015) is shown for comparison. As we used a two-dimensional structure, a slightly different density profile, and different dust opacities, it is not surprising that there are some deviations in the dust temperatures compared the model of Visser et al. (2015). In the quiescent state our model gives a dust temperature at the inner radius of $T_d(R_{E,in}) = 269$ K and a radius

where the dust temperature reaches 10 K of $r(T_d = 10 \text{ K}) \approx 3400$ au, compared to $T_d(R_{E,in}) = 250$ K and $r(T_d = 10 \text{ K}) \approx 2700$ au of Visser et al. (2015).

Consistent with Visser et al. (2015) the temperature increases throughout the envelope during the outburst. According to Johnstone et al. (2013) this increase follows roughly $T_d \propto L_*^{0.25}$. For an increase of the luminosity by a factor of 100 this corresponds to an increase of T_d by a factor of ≈ 3.2 . This is also the case in our model as seen in Fig. A.1.

To compare the results of our chemical model with Visser et al. (2015) we adapted their initial chemical abundances (Table A.2) and their adsorption energies for key molecules (Table A.3). All other chemical model parameters (e.g. sticking coefficient) are left unchanged (see Sect. 2.2 for details). In Fig. A.2 we show radial midplane abundance profiles for the molecules CO, H₂O, N₂H⁺ and HCO⁺ during the burst and at several times after the burst (post-burst phase). The Figure shows the results for a model using zeroth order desorption and a model where we used first order desorption. Figure A.2 can be directly compared to Fig. 1 in Visser et al. (2015).

A&A 604, A15 (2017)

In general our chemical model results are in good agreement with Visser et al. (2015). Our model nicely reproduces the main aspects of episodic accretion chemistry, namely the delayed freeze-out of neutral gas phase molecules and the outward shift of ice lines (here shown for CO and H₂O). Also the profiles for ions (N₂H⁺ and HCO⁺) are in good agreement with Visser et al. (2015). The chemistry of the ions is strongly sensitive to the gas phase abundances of the neutrals as the ions are efficiently destroyed by reactions with H₂O and/or CO. As a consequence HCO⁺ and N₂H⁺ trace the ice lines of H₂O and CO (see Visser & Bergin 2012; Visser et al. 2015, for details).

However, we also find differences in particular for the quiescent abundance profiles ($t = 10^5$ yr in Fig. A.2). The minimum abundances in the quiescent state for all shown molecules are about an order of magnitude lower (even more for water) than in the model of Visser et al. (2015). Further, at radii ≥ 1000 au the ion abundances are more than a factor of 100 below the values found by Visser et al. (2015). To some extent this deviation can be explained by the differences in the structure and radiative transfer model. However, we find that the abundances profiles are not very sensitive to changes in, for example, the density profile, and the quiescent abundances change at most by a factor of a few.

Most likely the differences are caused by the details of the model for the adsorption and desorption processes. Many different parameters like the sticking coefficient, desorption yields and the average dust sizes (see Sect. 2.2) are relevant. However, we find that actually the treatment of the thermal desorption process is most relevant. Comparing the results for the zeroth order desorption and first order desorption in Fig. A.2, clearly shows an increase of the minimum abundances by an order of magnitude if first order desorption is used (see Sect. 2.2).

The above discussed results show that for a spherical symmetric structure, our model is in good agreement with the model of Visser et al. (2015) for both the dust radiative transfer and the chemistry. In particular the two models agree very well concerning the main aspect of episodic accretion chemistry which is the delayed freeze-out of neutral species in the post-burst phase.

Appendix B: ALMA/CASA simulations

To produce as realistic as possible synthetic observations we use the Common Astronomy Software Applications (CASA) package (McMullin et al. 2007). We use CASA to either convolve the spectral line cubes with an artificial beam or to run full ALMA simulations. For the azimuthally averaged radial intensity profiles we use the task `casairing` provided by the Nordic ALMA regional centre.

In the following we describe in detail the main steps for the ALMA simulations used to produce C¹⁸O $J = 2-1$ (ALMA Band 6) line images and radial profiles.

1. We performed spectral line transfer with PRODiMO to produce line cubes with 101 velocity channels (spectral resolution of 0.1 km s⁻¹).
2. We used the most compact 12m Array configuration (full operations) in combination with the ACA (Atacama Compact Array) to cover all spatial scales. The observation time for the full array is 2h and for the ACA 10h (a factor of five longer than for the 12m Array, as recommend in the ALMA proposal guide for Cycle 4). The maximum recoverable scale for the full Array and ACA are 12.6'' and 29.0'' (2520 au and 5800 au at a distance of 200 pc), respectively.

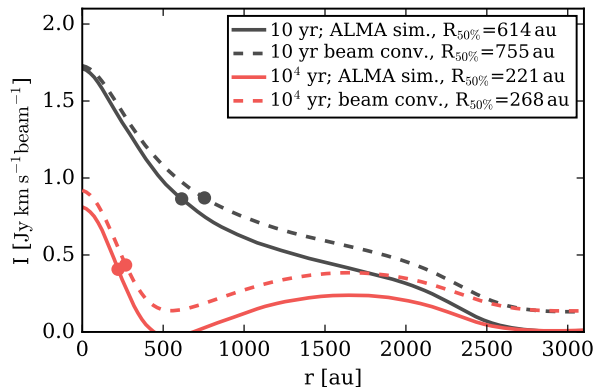


Fig. B.1. Comparison of full ALMA simulations to beam convolved models (same beam size). Shown are azimuthally averaged C¹⁸O $J = 2-1$ radial intensity profiles at 10 and 10⁴ yr after the burst. The solid lines are for full ALMA simulations, the dashed lines are for the beam convolved models.

The observations are simulated with the task `simobserve` (including noise).

3. With the tasks `concat` and `split` we combined the observations and rebinned the line cube by a factor of five, resulting in 20 channels with a spectral resolution of ≈ 0.5 km s⁻¹.
4. We performed continuum subtraction in the visibility plane using the task `uvcontsub`.
5. We reconstructed the images with `simanalyze` applying a threshold of 1 mJy and `briggs` weighting. The resulting synthetic beam size is approximately 1.81'' \times 1.65'' (362 au \times 330 au at a distance of 200 pc) and the root mean square noise of the images is $\text{rms} \lesssim 0.04$ Jy beam⁻¹.
6. We generated moment zero maps (intensity maps) with the task `immoments`.
7. We generated azimuthally averaged radial intensity profiles with `casairing` (Nordic ALMA regional centre).

We also performed simulations where the line cubes of PRODiMO are simply convolved with an elliptical beam of the same size as is used for the ALMA simulations. A comparison of the simple beam convolved simulations to the full ALMA simulations shows that we lose about 30% of the total flux in the ALMA simulations. This is also seen in Fig. B.1 where we show a comparison of radial intensity profiles for the full ALMA simulations and the beam convolved simulations. However, Fig. B.1 also shows that the full ALMA simulations recover the main spatial features of the profile very well but miss some flux in particular at larger scales. The cause of this might be an insufficient coverage of spatial scales and/or a imperfect image reconstruction (cleaning).

Appendix C: ALMA simulations for inclined models

In Fig. C.1 we show the same C¹⁸O $J = 2-1$ ALMA simulation as shown in Figs. 4 and 5 but for inclinations of 23°, 45° and 68°. Fig. C.1 shows that the gap in the C¹⁸O $J = 2-1$ emission is only visible for weakly inclined targets and that the X-shape of the emission is most pronounced for strongly inclined targets (see Sect. 3.3 for details).

Ch. Rab et al.: The chemistry of episodic accretion in embedded objects

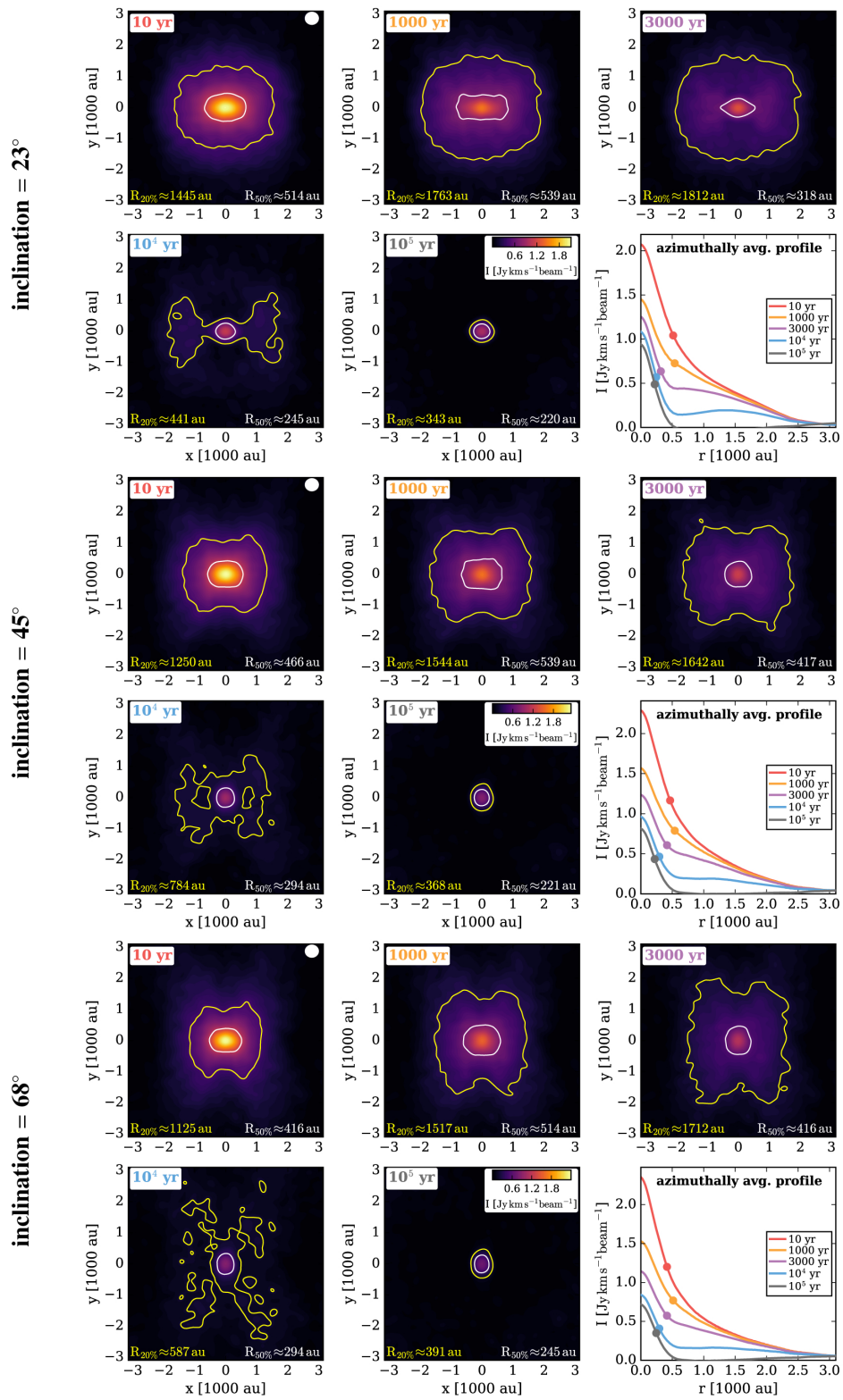


Fig. C.1. Same as Figs. 4 and 5 but for inclinations of 23° , 45° and 68° (from top to bottom).

A&A 604, A15 (2017)

Appendix D: Radial intensity profiles for the structure models

In Fig. D.1 we show radial $\text{C}^{18}\text{O } J=2-1$ intensity profiles for our structure models (see Fig. 7) but for all five inclinations considered for the synthetic observations.

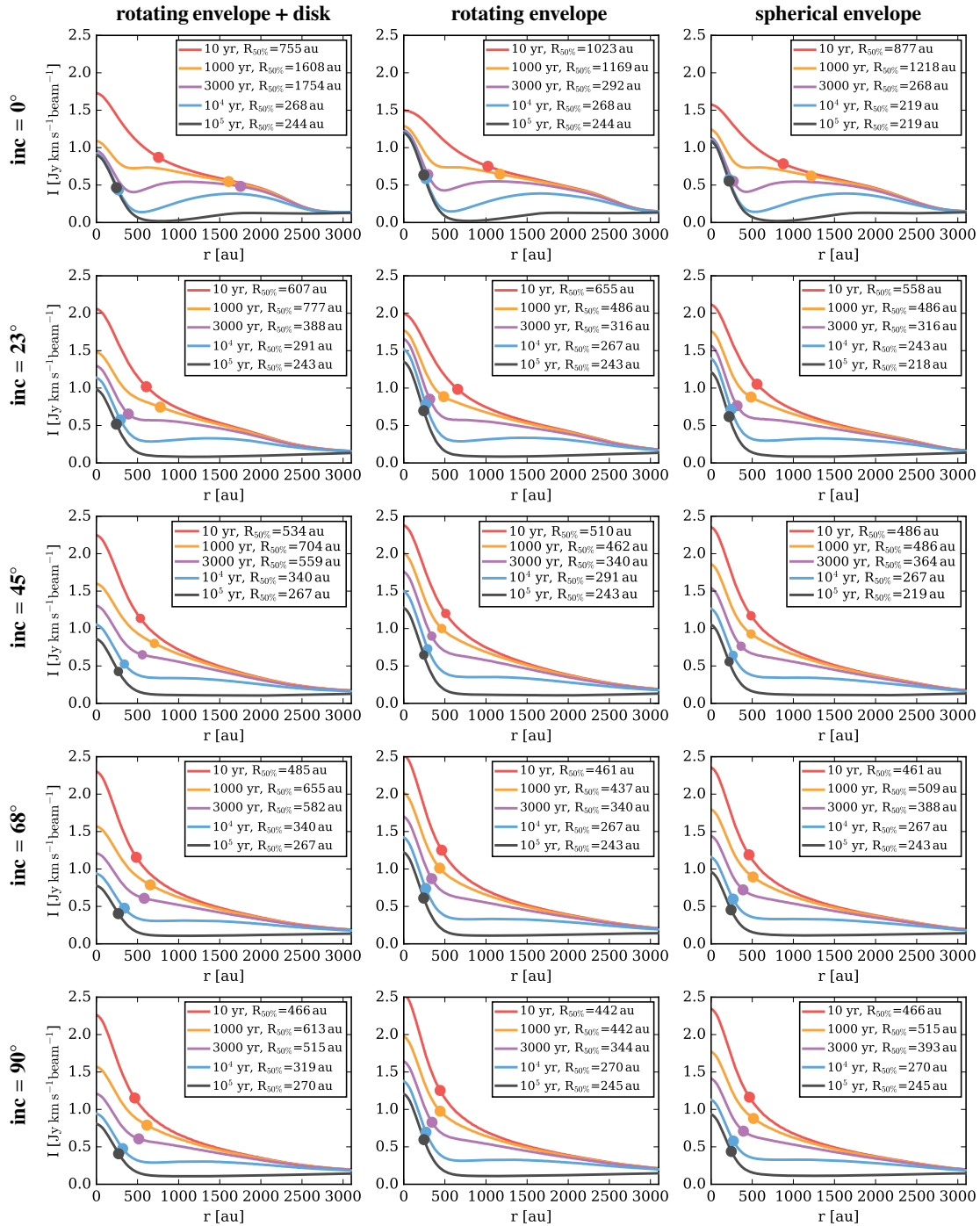


Fig. D.1. Time evolution of the azimuthally averaged $\text{C}^{18}\text{O } J=2-1$ radial intensity profiles for the three different structure models (columns) viewed at five different inclinations (rows). See also Fig. 7 for details.

Ch. Rab et al.: The chemistry of episodic accretion in embedded objects

Appendix E: Further fitting examples

To test the robustness of our fitting procedure discussed in Sect. 4.1 we applied the procedure to models with an inclination of 0° (Fig. E.1), a CO binding energy of 960 K (Fig. E.2), a spherical structure without a disk (Fig. E.3), a higher spatial resolution (Fig. E.4), a weaker burst (Fig. E.5) and a model using

the full ALMA simulations (Fig. E.6). These figures show that the method for identifying post-burst targets outlined in Sect. 4.1 is not strongly sensitive to model properties such as inclination, structure, spatial resolution of the observations, and the actual CO binding energy.

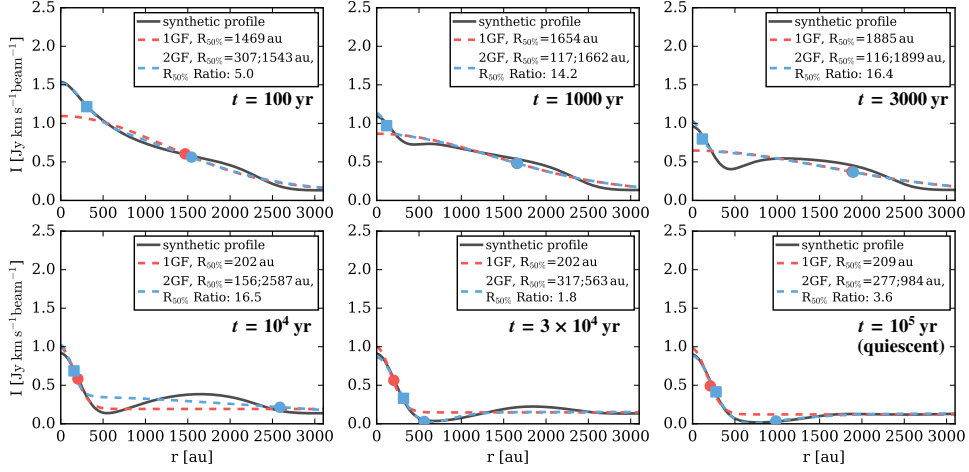


Fig. E.1. Same as Fig. 8 but for a model with an inclination of 0° (face-on).

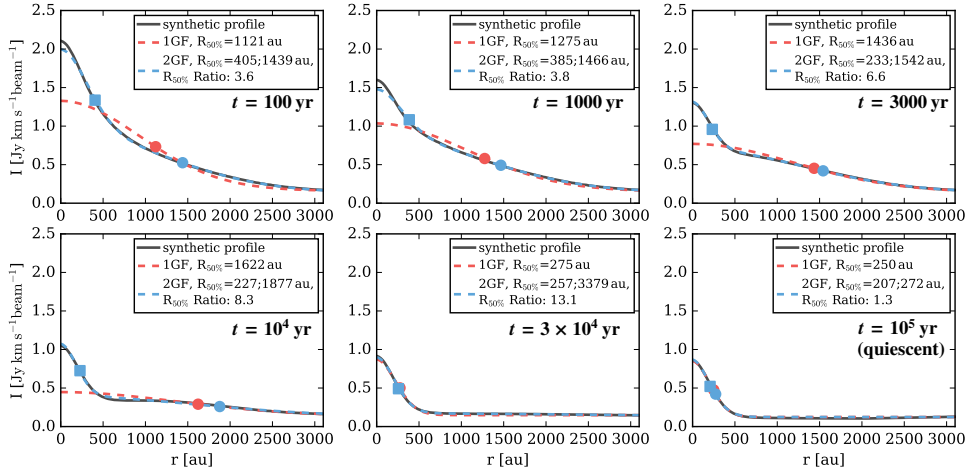


Fig. E.2. Same as Fig. 8 but for a model with a CO binding energy of 960 K (CO sublimation temperature of ≈ 20 K). We note the two Gaussian fit (2GF) for $t = 3 \times 10^4$ yr did not converge for this particular model.

A&A 604, A15 (2017)

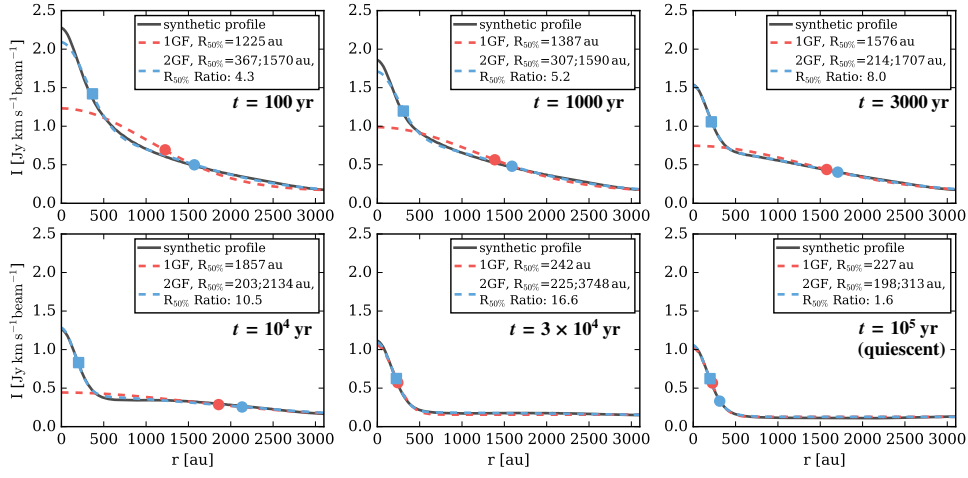
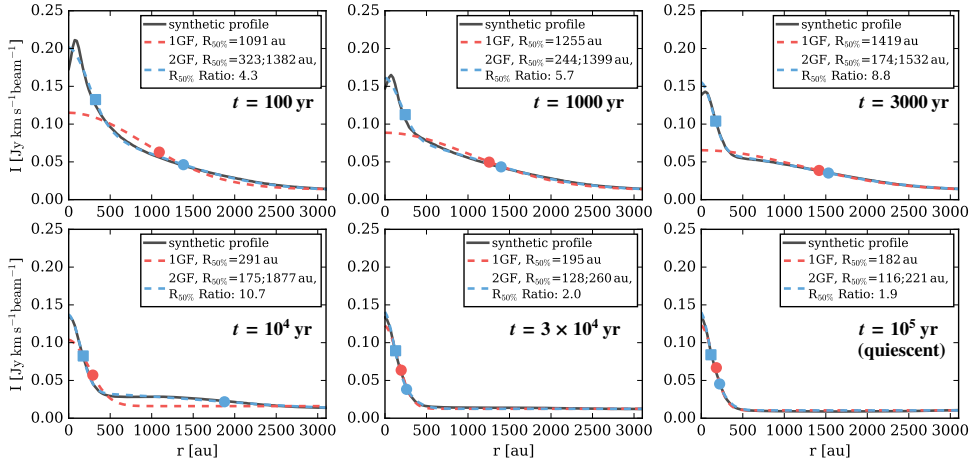
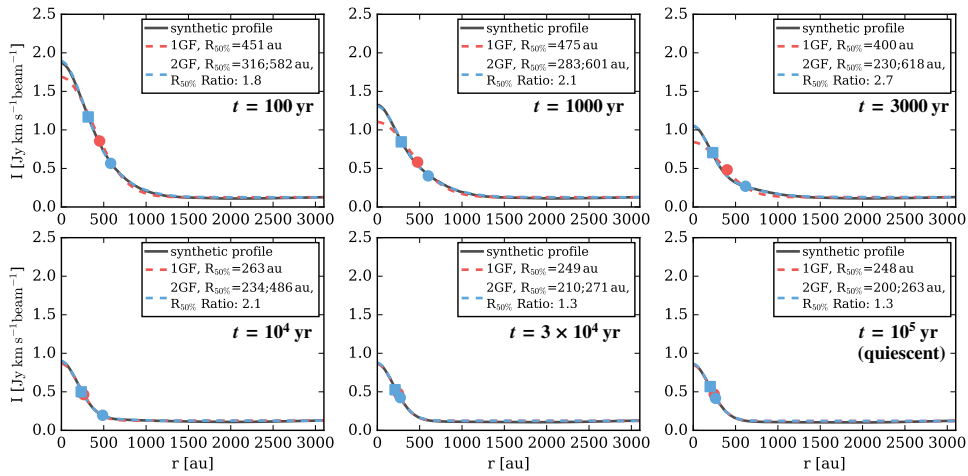


Fig. E.3. Same as Fig. 8 but for a model with a spherical density distribution (see Sect. 3.4).

Fig. E.4. Same as Fig. 8 but for a model with a synthetic beam of $0.5'' \times 0.5''$.Fig. E.5. Same as Fig. 8 but for a model with a weak burst of $10 \times L_*$.

Ch. Rab et al.: The chemistry of episodic accretion in embedded objects

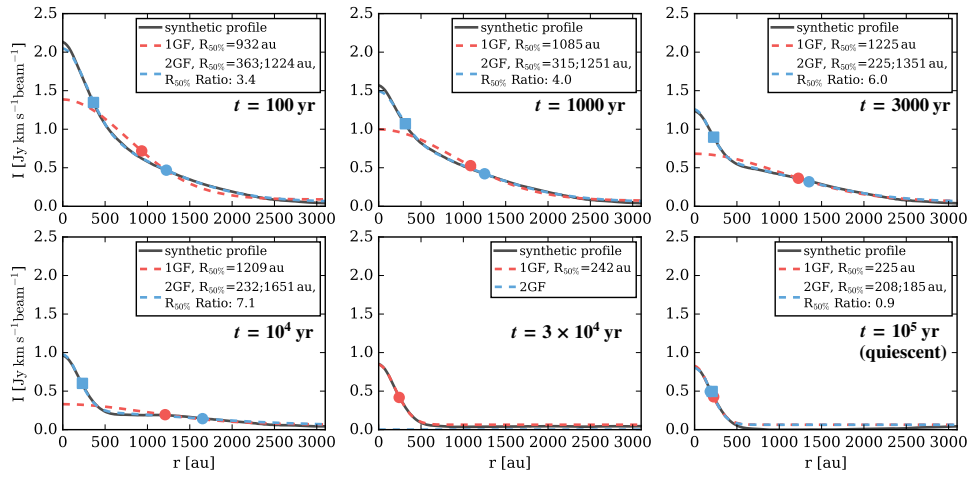


Fig. E.6. Same as Fig. 8 but for the full ALMA simulations with an inclination of 45° . For the corresponding images see Fig. C.1.

Chapter 5

Summary & Outlook

We investigated the impact of high-energy processes, such as X-rays, stellar energetic particles and accretion bursts on the circumstellar environment of young solar-like stars. We used the radiation thermo-chemical disk model PRODiMO, which considers disk radiative transfer, chemistry and heating/cooling processes. To achieve our scientific goals several new features were implemented in PRODiMO, including

- an X-ray radiative transfer module including scattering, dust as an X-ray opacity source and X-ray background fields,
- stellar energetic particles as a new high-energy ionization agent,
- and a parameterized prescription for an envelope structure to model Class I objects.

Those features are fully integrated into the main PRODiMO code and can be(are) already used by existing PRODiMO users and are also available for new PRODiMO users on a collaborative basis, following the existing PRODiMO usage policy.

The new features were applied and presented in three published/submitted papers. In the first paper (Chapter 2) we investigate the relevance of dust as an X-ray opacity source and the importance of X-ray background fields for disk chemistry. To show the impact on disk chemistry we compared the column densities of the common disk ionization tracers HCO^+ and N_2H^+ for models with varying dust properties and X-ray background fields.

We applied a similar approach to investigate the importance of stellar energetic particle (SP) ionization for disk chemistry (Chapter 3). We used detailed stellar particle transport calculations to estimate the SP ionization rate throughout the disk and compared it to competing high-energy ionization sources such as X-rays and cosmic rays. Further, we discussed possible ways to constrain the stellar particle flux of T Tauri stars via molecular ion observations of disks.

In the last paper (Chapter 4) we present a new 2D model to simulate the impact of an FU Ori like luminosity burst on the thermal and chemical structure of the circumstellar environment (disk plus envelope) of Class I objects. We modelled the temperature structure and the chemical structure of the circumstellar environment, using detailed radiative transfer and time-dependent chemistry. We investigated the impact of structure

(e.g. with disk or without) and dust properties on chemical timescales (i.e. the freeze-out timescale). Further, we produced synthetic observables for the post-burst period as a function of time, to identify observable signatures of a recent burst. In the following, we summarize our main findings separately for each paper.

X-ray radiative transfer in protoplanetary disks

- For typical Class II protoplanetary disks with evolved dust properties (e.g. grain growth), dust does not play a significant role as an X-ray opacity source. For ISM (interstellar medium) like dust populations (i.e. small grains) dust becomes a significant X-ray opacity source and should therefore be considered in X-ray radiative transfer models for less evolved disks, still embedded in an envelope (see Sections 2.2.3 and 2.3.2).
- X-ray background fields can dominate the X-ray radiation field in the outer regions of protoplanetary disks ($r \gtrsim 20$ au). However, the total H_2 ionization rate would still be dominated by cosmic rays, if they reach the disk (see Sect. 2.3.1).
- X-ray background fields can have an observable impact on the outer disk chemistry, if cosmic rays are efficiently attenuated before they reach the disk or if the X-ray background field is about a factor of ten stronger than what is expected for a typical low-mass star formation region (see Sect. 2.3.2). This indicates that for a typical disk in a star formation region like Taurus, the X-ray background field has only little impact on the disk chemistry and evolution (see Sect. 2.4.1).

Stellar energetic particle ionization

- Stellar energetic particles (SP) are unable to penetrate hydrogen column densities larger than $N_{(\text{H})} \gtrsim 10^{25} \text{ cm}^{-2}$, assuming that they have similar energies as solar energetic particles. Furthermore, their high energies ($E \gtrsim 10 \text{ MeV}$) makes scattering inefficient. Radial column densities (measured from the star outwards) in the midplane of protoplanetary disks are typically much larger than 10^{25} cm^{-2} , as a consequence stellar energetic particles are not an important disk midplane ionization source (see Sect. 3.3.1).
- SPs can become the dominant H_2 ionization source in the warm molecular layer in the inner 100 – 200 au of protoplanetary disks. SP ionization can increase the column densities of the disk ionization tracers HCO^+ and N_2H^+ by factors of three to ten, assuming typical X-ray and cosmic-ray ionization rates (see Sections 3.3.2 and 3.3.3).
- Our models show that the expected high SP flux of T Tauri stars produces observable signatures in molecular ion emission of protoplanetary disks. To observationally constrain the SP flux of T Tauri stars, simultaneous modelling of spatially resolved molecular ion emission tracing different vertical layers of the disk is required. This is necessary to disentangle the contribution of SPs from the competing high energy ionization sources such as X-rays and cosmic rays. (see Sect. 3.4.1).

The chemistry of episodic accretion in embedded objects

- After the end of a luminosity burst, when the circumstellar environment has cooled down again, the molecules sublimated during the burst freeze out again. Due to the radial density gradient in the disk/envelope structure, this happens from inside-out (from higher densities to lower densities). The presence of the disk has two consequences, the envelope becomes cooler due to the disk shadow and the molecules freeze out quicker in the disk due to the high densities (see Sect. 4.3.2). For a realistic disk dust population (e.g. large grains) the freeze-out timescale in the disk can increase by two orders of magnitude, compared to ISM like small grains (see Sect. 4.3.1). However, for typical disk and envelope density structures, the radial density gradient remains the dominant factor for the freeze-out timescale and the overall chemical evolution in the post-burst phase.
- The inside-out freeze-out produces distinct observable signatures, such as rings and X-shaped patterns, in spectral line images. The observability of those features depends on the viewing angle and on the structure properties, in particular, the size of the outflow cavity. It is possible to observe those features with modern (sub)mm interferometers, however, it is required that both, small (i.e. disk) and large (outer envelope) spatial scales are properly captured by the observations (see Sect. 4.3.3).
- Based on our models, we developed a model-independent procedure to identify post-burst sources directly from spatially resolved observations. A fit consisting of two-components (i.e. two Gaussians) matches the emission patterns of post-burst sources significantly better than a single component fit, whereas a single-component fit is a better match for sources showing no signatures of a recent burst (i.e. quiescent phase). With this method, it is possible to identify post-burst targets directly from observations without detailed modelling. However, to derive quantities such as the time passed since the last burst or burst frequencies, detailed modelling is necessary (see Sect. 4.4.1).

With our extension to ProDiMo concerning high-energy ionization in disks it is now possible to thoroughly model and interpret spatially resolved observations of molecular ions. With modern (sub)mm telescopes like ALMA (Atacama Large Millimeter Array), NOEMA (NOthern Extended Millimeter Array) and SMA (Submillimeter Array) such observations are becoming more and more common and will allow for further detailed investigations on the question of the dominant high-energy disk ionization source and on disk ionization in general.

We plan to extend such studies also to Herbig Ae/Be stars (intermediate mass stars with $M_* \gtrsim 2 - 3 M_\odot$). Compared to T Tauri stars, Herbig Ae/Be stars show lower X-ray luminosities but have stronger UV-fields. Those differences in their stellar properties should have an impact on the disk ionization structure. Observations indicate that compared to T Tauri disks, molecular ion lines of Herbig Ae/Be disks might be weaker (e.g. Dutrey et al. 2007; Öberg et al. 2011). However, more molecular ion observations of Herbig Ae/Be stars and detailed models are required to exclude other possible causes. Comparing disk ionization models and observations from T Tauri stars and Herbig Ae/Be stars would certainly be beneficial for a deeper understanding of high-energy disk ionization processes. For detailed modelling of disk observational data, a good knowledge

of the stellar properties and the disk structure is required. To achieve this, fitting of multi-wavelength observations is necessary. An approach which was successfully applied within the EU-FP7 project DIANA (see Sect. 1.6).

We also plan to further improve our models for high-energy ionization in disks. One very interesting subject is non-stellar ionization sources such as shocks in jets. Shocks can produce X-rays and potentially also energetic particles far away (up to ≈ 1000 au) from the central star (Güdel et al. 2007b; Padovani et al. 2016). Such ionization sources would irradiate the disk from above and penetrate the disk nearly vertically. However, it is yet unclear if those sources have a significant impact on disk ionization. Another possible improvement for our models is a proper treatment of magnetic fields in the stellar particle transport calculations. With the modelling approach presented here, it would then be possible to derive constraints for the disk magnetic field structure from molecular ion observations (see Sect. 3.4.3).

Little is known yet about the relevance of high-energy ionization for the early phases of low-mass star formation (Class 0/I). X-rays are detected in Class I objects but not yet in Class 0 protostars and their impact on the disk and envelope chemistry in those early stages is unclear. *Herschel* observations of HCO^+ and N_2H^+ in Class 0 protostars indicate an H_2 ionization rate orders of magnitude higher than the interstellar cosmic-ray ionization rate (Ceccarelli et al. 2014; Favre et al. 2017). The authors interpreted those observations as a strong indication for the presence of a high stellar energetic particle flux, although their origin remains unclear (Padovani et al. 2015). With our extensions for ProDiMo presented here, namely the X-ray radiative transfer, stellar energetic particle ionization and the disk+envelope structure model, it is now possible to model those high-energy processes also for embedded sources. Such models will provide new insights into the ionization processes in embedded objects.

Our studies on the chemistry of episodic accretion will be continued within the ongoing SNF-FWF project “Episodic accretion in star formation”. The main goals of this project are the interpretation of continuum and gas observation of FU Ori like stars, where the focus is on the modelling of *Herschel* and ALMA data. For this, we will use ProDiMo and the star/disk formation hydrodynamics code of E. Vorobyov (Co-PI of the project). We plan to develop an interface between the hydro code and ProDiMo to model observational data but also to make predictions for future observations.

The main scientific goals of the episodic accretion project are a better understanding of the triggering mechanism of episodic accretion events and to study the impact of luminosity bursts on the chemical evolution of the circumstellar material. In particular, we want to identify possible permanent chemical signatures caused by episodic accretion. Further, we want to apply the ProDiMo model for episodic accretion chemistry that we have presented in this thesis to EXors. EXors, named after their prototype EX Lupi, show repetitive, short-lived outbursts with luminosities of the order of $10 L_\odot$. The EXor phenomenon is more common in Class II sources and the short duration of the EXOr bursts ($\approx 1 - 10$ yrs) makes it possible to observe the target in the burst and quiescent phases. ProDiMo is the ideal tool to model such observations and to gain deeper knowledge about the episodic accretion phenomenon and its triggering mechanism.

References

- Adams, F. C. (2010). The Birth Environment of the Solar System. *Annual Reviews Astronomy and Astrophysics*, 48:47–85.
- Adams, F. C., Fatuzzo, M., and Holden, L. (2012). Background X-ray Radiation Fields Produced by Young Embedded Star Clusters. *PASP*, 124:913–921.
- Alexander, R., Pascucci, I., Andrews, S., Armitage, P., and Cieza, L. (2014). The Dispersal of Protoplanetary Disks. *Protostars and Planets VI*, pages 475–496.
- Alexander, R. D., Clarke, C. J., and Pringle, J. E. (2004). On the origin of ionizing photons emitted by T Tauri stars. *Monthly Notices of the Royal Astronomical Society*, 348:879–884.
- Alexander, R. D., Clarke, C. J., and Pringle, J. E. (2005). Constraints on the ionizing flux emitted by T Tauri stars. *Monthly Notices of the Royal Astronomical Society*, 358:283–290.
- ALMA Partnership, Brogan, C. L., Pérez, L. M., Hunter, T. R., Dent, W. R. F., Hales, A. S., Hills, R. E., Corder, S., Fomalont, E. B., Vlahakis, C., Asaki, Y., Barkats, D., Hirota, A., Hodge, J. A., Impellizzeri, C. M. V., Kneissl, R., Liuzzo, E., Lucas, R., Marcelino, N., Matsushita, S., Nakanishi, K., Phillips, N., Richards, A. M. S., Toledo, I., Aladro, R., Brogiere, D., Cortes, J. R., Cortes, P. C., Espada, D., Galarza, F., Garcia-Appadoo, D., Guzman-Ramirez, L., Humphreys, E. M., Jung, T., Kamenno, S., Laing, R. A., Leon, S., Marconi, G., Mignano, A., Nikolic, B., Nyman, L.-A., Radiszcz, M., Remijan, A., Rodón, J. A., Sawada, T., Takahashi, S., Tilanus, R. P. J., Vila Vilaro, B., Watson, L. C., Wiklind, T., Akiyama, E., Chapillon, E., de Gregorio-Monsalvo, I., Di Francesco, J., Gueth, F., Kawamura, A., Lee, C.-F., Nguyen Luong, Q., Mangum, J., Pietu, V., Sanhueza, P., Saigo, K., Takakuwa, S., Ubach, C., van Kempen, T., Wootten, A., Castro-Carrizo, A., Francke, H., Gallardo, J., Garcia, J., Gonzalez, S., Hill, T., Kaminski, T., Kurono, Y., Liu, H.-Y., Lopez, C., Morales, F., Plarre, K., Schieven, G., Testi, L., Videla, L., Villard, E., Andreani, P., Hibbard, J. E., and Tatematsu, K. (2015). The 2014 ALMA Long Baseline Campaign: First Results from High Angular Resolution Observations toward the HL Tau Region. *The Astrophysical Journal Letters*, 808:L3.
- Andre, P., Ward-Thompson, D., and Barsony, M. (1993). Submillimeter continuum observations of Rho Ophiuchi A - The candidate protostar VLA 1623 and prestellar clumps. *The Astrophysical Journal*, 406:122–141.
- Andrews, S. M., Rosenfeld, K. A., Kraus, A. L., and Wilner, D. J. (2013). The Mass Dependence between Protoplanetary Disks and their Stellar Hosts. *The Astrophysical Journal*, 771:129.
- Andrews, S. M., Wilner, D. J., Zhu, Z., Birnstiel, T., Carpenter, J. M., Pérez, L. M., Bai, X.-N., Öberg, K. I., Hughes, A. M., Isella, A., and Ricci, L. (2016). Ringed Substructure and a Gap at 1 au in the Nearest Protoplanetary Disk. *The Astrophysical Journal Letters*, 820:L40.
- Ansdell, M., Williams, J. P., van der Marel, N., Carpenter, J. M., Guidi, G., Hogerheijde, M., Mathews, G. S., Manara, C. F., Miotello, A., Natta, A., Oliveira, I., Tazzari, M., Testi, L., van Dishoeck, E. F., and van Terwisga, S. E. (2016). ALMA Survey of Lupus Protoplanetary Disks. I. Dust and Gas Masses. *The Astrophysical Journal*, 828:46.
- Antonoz, F., Ménard, F., Pinte, C., Le Bouquin, J.-B., Benisty, M., Thi, W.-F., Absil, O., Duchêne, G., Augereau, J.-C., Berger, J.-P., Casassus, S., Duvert, G., Lazareff, B., Malbet, F., Millan-Gabet, R., Schreiber, M. R., Traub, W., and Zins, G. (2015). The VLTI/PIONIER near-infrared interferometric survey of southern T Tauri stars. I. First results. *Astronomy & Astrophysics*, 574:A41.

- Appenzeller, I. and Mundt, R. (1989). T Tauri stars. *A&A Rev.*, 1:291–334.
- Aresu, G. (2012). *High energy irradiated protoplanetary disks : the X-rays and FUV role in thermo-chemical modeling*. PhD thesis, Groningen University.
- Aresu, G., Kamp, I., Meijerink, R., Spaans, M., Vicente, S., Podio, L., Woitke, P., Menard, F., Thi, W.-F., Güdel, M., and Liebhart, A. (2014). [O I] disk emission in the Taurus star-forming region. *Astronomy & Astrophysics* , 566:A14.
- Aresu, G., Kamp, I., Meijerink, R., Woitke, P., Thi, W.-F., and Spaans, M. (2011). X-ray impact on the protoplanetary disks around T Tauri stars. *Astronomy & Astrophysics* , 526:A163.
- Arnaud, K. A. (1996). XSPEC: The First Ten Years. In Jacoby, G. H. and Barnes, J., editors, *Astronomical Data Analysis Software and Systems V*, volume 101 of *Astronomical Society of the Pacific Conference Series*, page 17.
- Audard, M., Ábrahám, P., Dunham, M. M., Green, J. D., Grosso, N., Hamaguchi, K., Kastner, J. H., Kóspál, Á., Lodato, G., Romanova, M. M., Skinner, S. L., Vorobyov, E. I., and Zhu, Z. (2014). Episodic Accretion in Young Stars. *Protostars and Planets VI*, pages 387–410.
- Avrett, E. H. and Hummer, D. G. (1965). Non-coherent scattering, II: Line formation with a frequency independent source function. *Monthly Notices of the Royal Astronomical Society* , 130:295.
- Bai, X.-N. and Stone, J. M. (2013). Wind-driven Accretion in Protoplanetary Disks. I. Suppression of the Magnetorotational Instability and Launching of the Magnetocentrifugal Wind. *The Astrophysical Journal* , 769:76.
- Balbus, S. A. and Hawley, J. F. (1991). A powerful local shear instability in weakly magnetized disks. I - Linear analysis. II - Nonlinear evolution. *The Astrophysical Journal* , 376:214–233.
- Bergin, E. A., Cleeves, L. I., Gorti, U., Zhang, K., Blake, G. A., Green, J. D., Andrews, S. M., Evans, II, N. J., Henning, T., Öberg, K., Pontoppidan, K., Qi, C., Salyk, C., and van Dishoeck, E. F. (2013). An old disk still capable of forming a planetary system. *Nature*, 493:644–646.
- Bertout, C. (1989). T Tauri stars - Wild as dust. *Annual Reviews Astronomy and Astrophysics*, 27:351–395.
- Birnstiel, T., Fang, M., and Johansen, A. (2016). Dust Evolution and the Formation of Planetesimals. *Space Science Reviews*, 205:41–75.
- Blake, G. A. and Boogert, A. C. A. (2004). High-Resolution 4.7 Micron Keck/NIRSPEC Spectroscopy of the CO Emission from the Disks Surrounding Herbig Ae Stars. *The Astrophysical Journal Letters* , 606:L73–L76.
- Brott, I. and Hauschildt, P. H. (2005). A PHOENIX Model Atmosphere Grid for Gaia. In Turon, C., O’Flaherty, K. S., and Perryman, M. A. C., editors, *The Three-Dimensional Universe with Gaia*, volume 576 of *ESA Special Publication*, page 565.
- Bruderer, S. (2013). Survival of molecular gas in cavities of transition disks. I. CO. *Astronomy & Astrophysics* , 559:A46.
- Calvet, N. and Gullbring, E. (1998). The Structure and Emission of the Accretion Shock in T Tauri Stars. *The Astrophysical Journal* , 509:802–818.
- Cazaux, S. and Tielens, A. G. G. M. (2002). Molecular Hydrogen Formation in the Interstellar Medium. *The Astrophysical Journal Letters* , 575:L29–L32.
- Cazaux, S. and Tielens, A. G. G. M. (2004). H₂ Formation on Grain Surfaces. *The Astrophysical Journal* , 604:222–237.
- Ceccarelli, C., Dominik, C., López-Sepulcre, A., Kama, M., Padovani, M., Caux, E., and Caselli, P. (2014). Herschel Finds Evidence for Stellar Wind Particles in a Protostellar Envelope: Is This What Happened to the Young Sun? *The Astrophysical Journal Letters* , 790:L1.
- Chapillon, E., Guilloteau, S., Dutrey, A., Piétu, V., and Guélin, M. (2012). Chemistry in disks. VI. CN and HCN in protoplanetary disks. *Astronomy & Astrophysics* , 537:A60.
- Chiang, E. I. and Goldreich, P. (1997). Spectral Energy Distributions of T Tauri Stars with Passive Circumstellar Disks. *The Astrophysical Journal* , 490:368.

- Cleeves, L. I. (2016). Multiple Carbon Monoxide Snow Lines in Disks Sculpted by Radial Drift. *The Astrophysical Journal Letters* , 816:L21.
- Cleeves, L. I., Adams, F. C., and Bergin, E. A. (2013). Exclusion of Cosmic Rays in Protoplanetary Disks: Stellar and Magnetic Effects. *The Astrophysical Journal* , 772:5.
- Cleeves, L. I., Bergin, E. A., and Adams, F. C. (2014). Exclusion of Cosmic Rays in Protoplanetary Disks. II. Chemical Gradients and Observational Signatures. *The Astrophysical Journal* , 794:123.
- Cleeves, L. I., Bergin, E. A., Qi, C., Adams, F. C., and Öberg, K. I. (2015). Constraining the X-Ray and Cosmic-Ray Ionization Chemistry of the TW Hya Protoplanetary Disk: Evidence for a Sub-interstellar Cosmic-Ray Rate. *The Astrophysical Journal* , 799:204.
- Cleeves, L. I., Öberg, K. I., Wilner, D. J., Huang, J., Loomis, R. A., Andrews, S. M., and Czekala, I. (2016). The Coupled Physical Structure of Gas and Dust in the IM Lup Protoplanetary Disk. *The Astrophysical Journal* , 832:110.
- D'Alessio, P., Canto, J., Calvet, N., and Lizano, S. (1998). Accretion Disks around Young Objects. I. The Detailed Vertical Structure. *The Astrophysical Journal* , 500:411.
- Dauphas, N. and Chaussidon, M. (2011). A Perspective from Extinct Radionuclides on a Young Stellar Object: The Sun and Its Accretion Disk. *Annual Review of Earth and Planetary Sciences*, 39:351–386.
- de Gregorio-Monsalvo, I., Ménard, F., Dent, W., Pinte, C., López, C., Klaassen, P., Hales, A., Cortés, P., Rawlings, M. G., Tachihara, K., Testi, L., Takahashi, S., Chapillon, E., Mathews, G., Juhasz, A., Akiyama, E., Higuchi, A. E., Saito, M., Nyman, L.-Å., Phillips, N., Rodón, J., Corder, S., and Van Kempen, T. (2013). Unveiling the gas-and-dust disk structure in HD 163296 using ALMA observations. *Astronomy & Astrophysics* , 557:A133.
- Dent, W. R. F., Greaves, J. S., and Coulson, I. M. (2005). CO emission from discs around isolated HAeBe and Vega-excess stars. *Monthly Notices of the Royal Astronomical Society* , 359:663–676.
- Dere, K. P., Landi, E., Mason, H. E., Monsignori Fossi, B. C., and Young, P. R. (1997). CHIANTI - an atomic database for emission lines. *A&AS*, 125.
- Desch, S. J., Connolly, Jr., H. C., and Srinivasan, G. (2004). An Interstellar Origin for the Beryllium 10 in Calcium-rich, Aluminum-rich Inclusions. *The Astrophysical Journal* , 602:528–542.
- Draine, B. T. (2003). Scattering by Interstellar Dust Grains. II. X-Rays. *The Astrophysical Journal* , 598:1026–1037.
- Draine, B. T. and Bertoldi, F. (1996). Structure of Stationary Photodissociation Fronts. *The Astrophysical Journal* , 468:269.
- Dubrulle, B., Morfill, G., and Sterzik, M. (1995). The dust subdisk in the protoplanetary nebula. *Icarus*, 114:237–246.
- Dullemond, C. P., Hollenbach, D., Kamp, I., and D'Alessio, P. (2007). Models of the Structure and Evolution of Protoplanetary Disks. *Protostars and Planets V*, pages 555–572.
- Dullemond, C. P. and Monnier, J. D. (2010). The Inner Regions of Protoplanetary Disks. *Annual Reviews Astronomy and Astrophysics*, 48:205–239.
- Dullemond, C. P., van Zadelhoff, G. J., and Natta, A. (2002). Vertical structure models of T Tauri and Herbig Ae/Be disks. *Astronomy & Astrophysics* , 389:464–474.
- Dunham, M. M. and Vorobyov, E. I. (2012). Resolving the Luminosity Problem in Low-mass Star Formation. *The Astrophysical Journal* , 747:52.
- Dutrey, A., Guilloteau, S., Piétu, V., Chapillon, E., Wakelam, V., Di Folco, E., Stoecklin, T., Denis-Alpizar, O., Gorti, U., Teague, R., Henning, T., Semenov, D., and Grosso, N. (2017). The Flying Saucer: Tomography of the thermal and density gas structure of an edge-on protoplanetary disk. *ArXiv e-prints*.
- Dutrey, A., Henning, T., Guilloteau, S., Semenov, D., Piétu, V., Schreyer, K., Bacmann, A., Launhardt, R., Pety, J., and Gueth, F. (2007). Chemistry in disks. I. Deep search for N₂H⁺ in the protoplanetary disks around LkCa 15, MWC 480, and DM Tauri. *Astronomy & Astrophysics* , 464:615–623.

- Dutrey, A., Semenov, D., Chapillon, E., Gorti, U., Guilloteau, S., Hersant, F., Hogerheijde, M., Hughes, M., Meeus, G., Nomura, H., Piétu, V., Qi, C., and Wakelam, V. (2014). Physical and chemical structure of planet-forming disks probed by millimeter observations and modeling. In Beuther, H., Klessen, R., Dullemond, C., and Henning, T., editors, *Protostars and Planets VI*, pages 317–338. University of Arizona Press.
- Ercolano, B., Clarke, C. J., and Drake, J. J. (2009). X-Ray Irradiated Protoplanetary Disk Atmospheres. II. Predictions from Models in Hydrostatic Equilibrium. *The Astrophysical Journal* , 699:1639–1649.
- Ercolano, B. and Pascucci, I. (2017). The dispersal of planet-forming discs: theory confronts observations. *Royal Society Open Science*, 4:170114.
- Espaillet, C., Muzerolle, J., Najita, J., Andrews, S., Zhu, Z., Calvet, N., Kraus, S., Hashimoto, J., Kraus, A., and D’Alessio, P. (2014). An Observational Perspective of Transitional Disks. *Protostars and Planets VI*, pages 497–520.
- Facchini, S., Birnstiel, T., Bruderer, S., and van Dishoeck, E. F. (2017). Different dust and gas radial extents in protoplanetary disks: consistent models of grain growth and CO emission. *Astronomy & Astrophysics* , 605:A16.
- Favre, C., Lopez-Sepulcre, A., Ceccarelli, C., Dominik, C., Caselli, P., Caux, E., Fuente, A., Kama, M., Le Boulot, J., Lefloch, B., Lis, D., Montmerle, T., Padovani, M., and Vastel, C. (2017). The onset of energetic particle irradiation in Class 0 protostars. *ArXiv e-prints*.
- Feigelson, E. D. (2010). X-ray insights into star and planet formation. *Proceedings of the National Academy of Science*, 107:7153–7157.
- Feigelson, E. D., Garmire, G. P., and Pravdo, S. H. (2002). Magnetic Flaring in the Pre-Main-Sequence Sun and Implications for the Early Solar System. *The Astrophysical Journal* , 572:335–349.
- Feigelson, E. D. and Montmerle, T. (1999). High-Energy Processes in Young Stellar Objects. *Annual Reviews Astronomy and Astrophysics*, 37:363–408.
- Flaccomio, E., Micela, G., and Sciortino, S. (2012). X-ray variability of pre-main-sequence stars. Toward an explanation of the different X-ray properties of classical and weak-line T Tauri stars. *Astronomy & Astrophysics* , 548:A85.
- Flaccomio, E., Micela, G., Sciortino, S., Feigelson, E. D., Herbst, W., Favata, F., Harnden, Jr., F. R., and Vrtilik, S. D. (2005). Rotational Modulation of X-Ray Emission in Orion Nebula Young Stars. *ApJS*, 160:450–468.
- Flaherty, K. M., Hughes, A. M., Rose, S. C., Simon, J. B., Qi, C., Andrews, S. M., Kóspál, Á., Wilner, D. J., Chiang, E., Armitage, P. J., and Bai, X.-n. (2017). A Three-dimensional View of Turbulence: Constraints on Turbulent Motions in the HD 163296 Protoplanetary Disk Using DCO⁺. *The Astrophysical Journal* , 843:150.
- France, K., Schindhelm, E., Bergin, E. A., Roueff, E., and Abgrall, H. (2014). High-resolution Ultraviolet Radiation Fields of Classical T Tauri Stars. *The Astrophysical Journal* , 784:127.
- Furuya, K. and Aikawa, Y. (2014). Reprocessing of Ices in Turbulent Protoplanetary Disks: Carbon and Nitrogen Chemistry. *The Astrophysical Journal* , 790:97.
- Getman, K. V., Flaccomio, E., Broos, P. S., Grosso, N., Tsujimoto, M., Townsley, L., Garmire, G. P., Kastner, J., Li, J., Harnden, Jr., F. R., Wolk, S., Murray, S. S., Lada, C. J., Muench, A. A., McCaughrean, M. J., Meeus, G., Damiani, F., Micela, G., Sciortino, S., Bally, J., Hillenbrand, L. A., Herbst, W., Preibisch, T., and Feigelson, E. D. (2005). Chandra Orion Ultradeep Project: Observations and Source Lists. *ApJS*, 160:319–352.
- Giardino, G., Favata, F., Micela, G., Sciortino, S., and Winston, E. (2007). The onset of X-ray emission in young stellar objects. A Chandra observation of the Serpens star-forming region. *Astronomy & Astrophysics* , 463:275–288.
- Glassgold, A. E., Najita, J., and Igea, J. (1997). X-Ray Ionization of Protoplanetary Disks. *The Astrophysical Journal* , 480:344.
- Gorti, U. and Hollenbach, D. (2009). Photoevaporation of Circumstellar Disks By Far-Ultraviolet, Extreme-Ultraviolet and X-Ray Radiation from the Central Star. *The Astrophysical Journal* , 690:1539–1552.

- Gorti, U., Liseau, R., Sándor, Z., and Clarke, C. (2016). Disk Dispersal: Theoretical Understanding and Observational Constraints. *Space Science Reviews*, 205:125–152.
- Gounelle, M., Chaussidon, M., and Rollion-Bard, C. (2013). Variable and Extreme Irradiation Conditions in the Early Solar System Inferred from the Initial Abundance of ^{10}Be in Isheyevo CAIs. *The Astrophysical Journal Letters*, 763:L33.
- Grady, C. A., Hamaguchi, K., Schneider, G., Stecklum, B., Woodgate, B. E., McCleary, J. E., Williger, G. M., Sitko, M. L., Ménard, F., Henning, T., Brittain, S., Troutmann, M., Donehew, B., Hines, D., Wisniewski, J. P., Lynch, D. K., Russell, R. W., Rudy, R. J., Day, A. N., Shenoy, A., Wilner, D., Silverstone, M., Bouret, J.-C., Meusinger, H., Clampin, M., Kim, S., Petre, R., Sahu, M., Endres, M., and Collins, K. A. (2010). Locating the Accretion Footprint on a Herbig Ae Star: MWC 480. *The Astrophysical Journal*, 719:1565–1581.
- Gregory, S. G., Jardine, M., Collier Cameron, A., and Donati, J.-F. (2006). Rotationally modulated X-ray emission from T Tauri stars. *Monthly Notices of the Royal Astronomical Society*, 373:827–835.
- Güdel, M. (2007). The sun in time: Activity and environment. *Living Reviews in Solar Physics*, 4(1):3.
- Güdel, M. (2015). Ionization and heating by X-rays and cosmic rays. In *European Physical Journal Web of Conferences*, volume 102 of *European Physical Journal Web of Conferences*, page 00015.
- Güdel, M., Briggs, K. R., Arzner, K., Audard, M., Bouvier, J., Feigelson, E. D., Franciosini, E., Glauser, A., Grosso, N., Micela, G., Monin, J.-L., Montmerle, T., Padgett, D. L., Palla, F., Pillitteri, I., Rebull, L., Scelsi, L., Silva, B., Skinner, S. L., Stelzer, B., and Telleschi, A. (2007a). The XMM-Newton extended survey of the Taurus molecular cloud (XEST). *Astronomy & Astrophysics*, 468:353–377.
- Güdel, M., Skinner, S. L., Briggs, K. R., Audard, M., Arzner, K., and Telleschi, A. (2005). Evidence for an X-Ray Jet in DG Tauri A? *The Astrophysical Journal Letters*, 626:L53–L56.
- Güdel, M. and Telleschi, A. (2007). The X-ray soft excess in classical T Tauri stars. *Astronomy & Astrophysics*, 474:L25–L28.
- Güdel, M., Telleschi, A., Audard, M., Skinner, S. L., Briggs, K. R., Palla, F., and Dougados, C. (2007b). X-rays from jet-driving protostars and T Tauri stars. *Astronomy & Astrophysics*, 468:515–528.
- Guilloteau, S., Dutrey, A., Piétu, V., and Boehler, Y. (2011). A dual-frequency sub-arcsecond study of proto-planetary disks at mm wavelengths: first evidence for radial variations of the dust properties. *Astronomy & Astrophysics*, 529:A105.
- Gullbring, E., Calvet, N., Muzerolle, J., and Hartmann, L. (2000). The Structure and Emission of the Accretion Shock in T Tauri Stars. II. The Ultraviolet-Continuum Emission. *The Astrophysical Journal*, 544:927–932.
- Guzmán, V. V., Öberg, K. I., Loomis, R., and Qi, C. (2015). Cyanide Photochemistry and Nitrogen Fractionation in the MWC 480 Disk. *The Astrophysical Journal*, 814:53.
- Hamidouche, M., Looney, L. W., and Mundy, L. G. (2006). Resolving and Probing the Circumstellar Disk of the Herbig Ae Star MWC 480 at $\lambda = 1.4$ mm: Evolved Dust? *The Astrophysical Journal*, 651:321–327.
- Hartmann, L., Calvet, N., Gullbring, E., and D’Alessio, P. (1998). Accretion and the Evolution of T Tauri Disks. *The Astrophysical Journal*, 495:385–400.
- Hartmann, L., Herczeg, G., and Calvet, N. (2016). Accretion onto Pre-Main-Sequence Stars. *Annual Reviews Astronomy and Astrophysics*, 54:135–180.
- Haworth, T. J., Facchini, S., Clarke, C. J., and Cleaves, L. I. (2017). First evidence of external disc photoevaporation in a low mass star forming region: the case of IM Lup. *Monthly Notices of the Royal Astronomical Society*, 468:L108–L112.
- Helling, C., Woitke, P., Rimmer, P. B., Kamp, I., Thi, W.-F., and Meijerink, R. (2014). Disk Evolution, Element Abundances and Cloud Properties of Young Gas Giant Planets. *Life*, volume 4, issue 2, pages 142–173, 4:142–173.

- Henning, T. and Semenov, D. (2013). Chemistry in Protoplanetary Disks. *Chemical Reviews*, 113:9016–9042.
- Herbig, G. H. (1966). On the interpretation of FU orionis. *Vistas in Astronomy*, 8:109–125.
- Herbig, G. H. (1977). Eruptive phenomena in early stellar evolution. *The Astrophysical Journal*, 217:693–715.
- Herczeg, G. J., Wood, B. E., Linsky, J. L., Valenti, J. A., and Johns-Krull, C. M. (2004). The Far-Ultraviolet Spectra of TW Hydrae. II. Models of H₂ Fluorescence in a Disk. *The Astrophysical Journal*, 607:369–383.
- Honda, M., Maaskant, K., Okamoto, Y. K., Kataza, H., Yamashita, T., Miyata, T., Sako, S., Fujiyoshi, T., Sakon, I., Fujiwara, H., Kamizuka, T., Mulders, G. D., Lopez-Rodriguez, E., Packham, C., and Onaka, T. (2015). High-resolution 25 μm Imaging of the Disks around Herbig Ae/Be Stars. *The Astrophysical Journal*, 804:143.
- Igea, J. and Glassgold, A. E. (1999). X-Ray Ionization of the Disks of Young Stellar Objects. *The Astrophysical Journal*, 518:848–858.
- Imanishi, K., Koyama, K., and Tsuboi, Y. (2001). Chandra Observation of the ρ Ophiuchi Cloud. *The Astrophysical Journal*, 557:747–760.
- Jørgensen, J. K., Visser, R., Williams, J. P., and Bergin, E. A. (2015). Molecule sublimation as a tracer of protostellar accretion. Evidence for accretion bursts from high angular resolution C¹⁸O images. *Astronomy & Astrophysics*, 579:A23.
- Joy, A. H. (1945). T Tauri Variable Stars. *The Astrophysical Journal*, 102:168.
- Kamp, I., Thi, W.-F., Woitke, P., Rab, C., Bouma, S., and Menard, F. (2017). Consistent dust and gas models for protoplanetary disks: II. Chemical networks and rates. *Astronomy & Astrophysics*, in press.
- Kamp, I., Tilling, I., Woitke, P., Thi, W.-F., and Hogerheijde, M. (2010). Radiation thermochemical models of protoplanetary disks. II. Line diagnostics. *Astronomy & Astrophysics*, 510:A18.
- Kamp, I., Woitke, P., Pinte, C., Tilling, I., Thi, W.-F., Menard, F., Duchene, G., and Augereau, J.-C. (2011). Continuum and line modelling of discs around young stars. II. Line diagnostics for GASPS from the DENT grid. *Astronomy & Astrophysics*, 532:A85.
- Kenyon, S. J. and Hartmann, L. (1987). Spectral energy distributions of T Tauri stars - Disk flaring and limits on accretion. *The Astrophysical Journal*, 323:714–733.
- Kenyon, S. J. and Hartmann, L. (1995). Pre-Main-Sequence Evolution in the Taurus-Auriga Molecular Cloud. *ApJS*, 101:117.
- Kenyon, S. J., Hartmann, L. W., Strom, K. M., and Strom, S. E. (1990). An IRAS survey of the Taurus-Auriga molecular cloud. *The Astronomical Journal*, 99:869–887.
- Kusakabe, N., Grady, C. A., Sitko, M. L., Hashimoto, J., Kudo, T., Fukagawa, M., Muto, T., Wisniewski, J. P., Min, M., Mayama, S., Werren, C., Day, A. N., Beerman, L. C., Lynch, D. K., Russell, R. W., Brafford, S. M., Kuzuhara, M., Brandt, T. D., Abe, L., Brandner, W., Carson, J., Egner, S., Feldt, M., Goto, M., Guyon, O., Hayano, Y., Hayashi, M., Hayashi, S. S., Henning, T., Hodapp, K. W., Ishii, M., Iye, M., Janson, M., Kandori, R., Knapp, G. R., Matsuo, T., McElwain, M. W., Miyama, S., Morino, J.-I., Moro-Martin, A., Nishimura, T., Pyo, T.-S., Suto, H., Suzuki, R., Takami, M., Takato, N., Terada, H., Thalmann, C., Tomono, D., Turner, E. L., Watanabe, M., Yamada, T., Takami, H., Usuda, T., and Tamura, M. (2012). High-contrast Near-infrared Polarization Imaging of MWC480. *The Astrophysical Journal*, 753:153.
- Lada, C. J. (1987). Star formation - From OB associations to protostars. In Peimbert, M. and Jugaku, J., editors, *Star Forming Regions*, volume 115 of *IAU Symposium*, pages 1–17.
- Li, Z.-Y., Banerjee, R., Pudritz, R. E., Jørgensen, J. K., Shang, H., Krasnopolsky, R., and Maury, A. (2014). The Earliest Stages of Star and Planet Formation: Core Collapse, and the Formation of Disks and Outflows. *Protostars and Planets VI*, pages 173–194.
- Lynden-Bell, D. and Pringle, J. E. (1974). The evolution of viscous discs and the origin of the nebular variables. *Monthly Notices of the Royal Astronomical Society*, 168:603–637.

- Mannings, V. and Sargent, A. I. (1997). A High-Resolution Study of Gas and Dust around Young Intermediate-Mass Stars: Evidence for Circumstellar Disks in Herbig Ae Systems. *The Astrophysical Journal* , 490:792–802.
- Mathis, J. S., Mezger, P. G., and Panagia, N. (1983). Interstellar radiation field and dust temperatures in the diffuse interstellar matter and in giant molecular clouds. *Astronomy & Astrophysics* , 128:212–229.
- Matthews, B. C., Krivov, A. V., Wyatt, M. C., Bryden, G., and Eiroa, C. (2014). Observations, Modeling, and Theory of Debris Disks. *Protostars and Planets VI*, pages 521–544.
- McClure, M. K., Bergin, E. A., Cleeves, L. I., van Dishoeck, E. F., Blake, G. A., Evans, II, N. J., Green, J. D., Henning, T., Öberg, K. I., Pontoppidan, K. M., and Salyk, C. (2016). Mass Measurements in Protoplanetary Disks from Hydrogen Deuteride. *The Astrophysical Journal* , 831:167.
- McElroy, D., Walsh, C., Markwick, A. J., Cordiner, M. A., Smith, K., and Millar, T. J. (2013). The UMIST database for astrochemistry 2012. *Astronomy & Astrophysics* , 550:A36.
- Meeus, G., Montesinos, B., Mendigutía, I., Kamp, I., Thi, W. F., Eiroa, C., Grady, C. A., Mathews, G., Sandell, G., Martin-Zaïdi, C., Brittain, S., Dent, W. R. F., Howard, C., Ménard, F., Pinte, C., Roberge, A., Vandenbussche, B., and Williams, J. P. (2012). Observations of Herbig Ae/Be stars with Herschel/PACS. The atomic and molecular contents of their protoplanetary discs. *Astronomy & Astrophysics* , 544:A78.
- Meijerink, R., Aresu, G., Kamp, I., Spaans, M., Thi, W.-F., and Woitke, P. (2012). Far-ultraviolet and X-ray irradiated protoplanetary disks: a grid of models. I. The disk structure. *Astronomy & Astrophysics* , 547:A68.
- Meyer, B. S. and Clayton, D. D. (2000). Short-Lived Radioactivities and the Birth of the sun. *Space Science Reviews*, 92:133–152.
- Mihalas, D. (1978). *Stellar atmospheres /2nd edition/*.
- Min, M., Dullemond, C. P., Dominik, C., de Koter, A., and Hovenier, J. W. (2009). Radiative transfer in very optically thick circumstellar disks. *Astronomy & Astrophysics* , 497:155–166.
- Min, M., Hovenier, J. W., and de Koter, A. (2005). Modeling optical properties of cosmic dust grains using a distribution of hollow spheres. *Astronomy & Astrophysics* , 432:909–920.
- Min, M., Rab, C., Woitke, P., Dominik, C., and Ménard, F. (2016). Multiwavelength optical properties of compact dust aggregates in protoplanetary disks. *Astronomy & Astrophysics* , 585:A13.
- Miotello, A., Bruderer, S., and van Dishoeck, E. F. (2014). Protoplanetary disk masses from CO isotopologue line emission. *Astronomy & Astrophysics* , 572:A96.
- Miotello, A., van Dishoeck, E. F., Williams, J. P., Ansdell, M., Guidi, G., Hogerheijde, M., Manara, C. F., Tazzari, M., Testi, L., van der Marel, N., and van Terwisga, S. (2017). Lupus disks with faint CO isotopologues: low gas/dust or high carbon depletion? *Astronomy & Astrophysics* , 599:A113.
- Mulders, G. D., Min, M., Dominik, C., Debes, J. H., and Schneider, G. (2013). Why circumstellar disks are so faint in scattered light: the case of HD 100546. *Astronomy & Astrophysics* , 549:A112.
- Mumma, M. J. and Charnley, S. B. (2011). The Chemical Composition of Comets - Emerging Taxonomies and Natal Heritage. *Annual Reviews Astronomy and Astrophysics*, 49:471–524.
- Murillo, N. M., Lai, S.-P., Bruderer, S., Harsono, D., and van Dishoeck, E. F. (2013). A Keplerian disk around a Class 0 source: ALMA observations of VLA1623A. *Astronomy & Astrophysics* , 560:A103.
- Myers, P. C. (2014). Protostar Mass Functions in Young Clusters. *The Astrophysical Journal* , 781:33.
- Nomura, H., Tsukagoshi, T., Kawabe, R., Ishimoto, D., Okuzumi, S., Muto, T., Kanagawa, K. D., Ida, S., Walsh, C., Millar, T. J., and Bai, X.-N. (2016). ALMA Observations of a Gap and a Ring in the Protoplanetary Disk around TW Hya. *The Astrophysical Journal Letters* , 819:L7.

- Öberg, K. I., Guzmán, V. V., Furuya, K., Qi, C., Aikawa, Y., Andrews, S. M., Loomis, R., and Wilner, D. J. (2015). The comet-like composition of a protoplanetary disk as revealed by complex cyanides. *Nature*, 520:198–201.
- Öberg, K. I., Qi, C., Fogel, J. K. J., Bergin, E. A., Andrews, S. M., Espaillat, C., van Kempen, T. A., Wilner, D. J., and Pascucci, I. (2010). The Disk Imaging Survey of Chemistry with SMA. I. Taurus Protoplanetary Disk Data. *The Astrophysical Journal*, 720:480–493.
- Öberg, K. I., Qi, C., Fogel, J. K. J., Bergin, E. A., Andrews, S. M., Espaillat, C., Wilner, D. J., Pascucci, I., and Kastner, J. H. (2011). Disk Imaging Survey of Chemistry with SMA. II. Southern Sky Protoplanetary Disk Data and Full Sample Statistics. *The Astrophysical Journal*, 734:98.
- Owen, J. E. and Kollmeier, J. A. (2017). Dust traps as planetary birthsites: basics and vortex formation. *Monthly Notices of the Royal Astronomical Society*, 467:3379–3392.
- Padovani, M., Hennebelle, P., Marcowith, A., and Ferrière, K. (2015). Cosmic-ray acceleration in young protostars. *Astronomy & Astrophysics*, 582:L13.
- Padovani, M., Marcowith, A., Hennebelle, P., and Ferrière, K. (2016). Protostars: Forges of cosmic rays? *Astronomy & Astrophysics*, 590:A8.
- Pascucci, I., Ricci, L., Gorti, U., Hollenbach, D., Hendl, N. P., Brooks, K. J., and Contreras, Y. (2014). Low Extreme-ultraviolet Luminosities Impinging on Protoplanetary Disks. *The Astrophysical Journal*, 795:1.
- Piétu, V., Dutrey, A., and Guilloteau, S. (2007). Probing the structure of protoplanetary disks: a comparative study of DM Tau, LkCa 15, and MWC 480. *Astronomy & Astrophysics*, 467:163–178.
- Pinte, C., Dent, W. R. F., Ménard, F., Hales, A., Hill, T., Cortes, P., and de Gregorio-Monsalvo, I. (2016). Dust and Gas in the Disk of HL Tauri: Surface Density, Dust Settling, and Dust-to-gas Ratio. *The Astrophysical Journal*, 816:25.
- Pinte, C., Harries, T. J., Min, M., Watson, A. M., Dullemond, C. P., Woitke, P., Ménard, F., and Durán-Rojas, M. C. (2009). Benchmark problems for continuum radiative transfer. High optical depths, anisotropic scattering, and polarisation. *Astronomy & Astrophysics*, 498:967–980.
- Pinte, C., Ménard, F., Duchêne, G., and Bastien, P. (2006). Monte Carlo radiative transfer in protoplanetary disks. *Astronomy & Astrophysics*, 459:797–804.
- Pinte, C., Ménard, F., Duchêne, G., Hill, T., Dent, W.R.F., Woitke, P., Maret, S., van der Plas, G., Hales, A., Kamp, I., Thi, W.-F., de Gregorio-Monsalvo, I., Rab, C., Quanz, S., Avenhaus, H., Carmona, A., and Casassus, S. (2017). Altitude, velocity and temperature of the CO layers. Imaging the vertical CO snow line in the disc surrounding IM Lupi. *Astronomy & Astrophysics*. in press.
- Pinte, C., Padgett, D. L., Ménard, F., Stapelfeldt, K. R., Schneider, G., Olofsson, J., Panić, O., Augereau, J. C., Duchêne, G., Krist, J., Pontoppidan, K., Perrin, M. D., Grady, C. A., Kessler-Silacci, J., van Dishoeck, E. F., Lommen, D., Silverstone, M., Hines, D. C., Wolf, S., Blake, G. A., Henning, T., and Stecklum, B. (2008). Probing dust grain evolution in IM Lupi’s circumstellar disc. Multi-wavelength observations and modelling of the dust disc. *Astronomy & Astrophysics*, 489:633–650.
- Preibisch, T., Kim, Y.-C., Favata, F., Feigelson, E. D., Flaccomio, E., Getman, K., Micela, G., Sciortino, S., Stassun, K., Stelzer, B., and Zinnecker, H. (2005). The Origin of T Tauri X-Ray Emission: New Insights from the Chandra Orion Ultradeep Project. *ApJS*, 160:401–422.
- Rab, C., Baldovin-Saavedra, C., Dionatos, O., Vorobyov, E., and Güdel, M. (2016). The Gas Disk: Evolution and Chemistry. *Space Science Reviews*, 205:3–40.
- Reames, D. V. (2015). What Are the Sources of Solar Energetic Particles? Element Abundances and Source Plasma Temperatures. *Space Science Reviews*, 194:303–327.
- Rothman, L. S., Gordon, I. E., Babikov, Y., Barbe, A., Chris Benner, D., Bernath, P. F., Birk, M., Bizzocchi, L., Boudon, V., Brown, L. R., Campargue, A., Chance, K., Cohen, E. A., Coudert, L. H., Devi, V. M., Drouin, B. J., Fayt, A., Flaud, J.-M., Gamache, R. R.,

- Harrison, J. J., Hartmann, J.-M., Hill, C., Hodges, J. T., Jacquemart, D., Jolly, A., Lamouroux, J., Le Roy, R. J., Li, G., Long, D. A., Lyulin, O. M., Mackie, C. J., Massie, S. T., Mikhailenko, S., Müller, H. S. P., Naumenko, O. V., Nikitin, A. V., Orphal, J., Perevalov, V., Perrin, A., Polovtseva, E. R., Richard, C., Smith, M. A. H., Starikova, E., Sung, K., Tashkun, S., Tennyson, J., Toon, G. C., Tyuterev, V. G., and Wagner, G. (2013). The HITRAN2012 molecular spectroscopic database. *Journal of Quantitative Spectroscopy and Radiative Transfer*, 130:4–50.
- Sallum, S., Follette, K. B., Eisner, J. A., Close, L. M., Hinz, P., Kratter, K., Males, J., Skemer, A., Macintosh, B., Tuthill, P., Bailey, V., Defrère, D., Morzinski, K., Rodigas, T., Spalding, E., Vaz, A., and Weinberger, A. J. (2015). Accreting protoplanets in the LkCa 15 transition disk. *Nature*, 527:342–344.
- Schindhelm, E., France, K., Herczeg, G. J., Bergin, E., Yang, H., Brown, A., Brown, J. M., Linsky, J. L., and Valenti, J. (2012). Ly α Dominance of the Classical T Tauri Far-ultraviolet Radiation Field. *The Astrophysical Journal Letters*, 756:L23.
- Schöier, F. L., van der Tak, F. F. S., van Dishoeck, E. F., and Black, J. H. (2005). An atomic and molecular database for analysis of submillimetre line observations. *Astronomy & Astrophysics*, 432:369–379.
- Semenov, D. and Wiebe, D. (2011). Chemical Evolution of Turbulent Protoplanetary Disks and the Solar Nebula. *ApJS*, 196:25.
- Shu, F. H., Shang, H., Glassgold, A. E., and Lee, T. (1997). X-rays and fluctuating X-winds from protostars. *Science*, 277:1475–1479.
- Simon, M., Dutrey, A., and Guilloteau, S. (2000). Dynamical Masses of T Tauri Stars and Calibration of Pre-Main-Sequence Evolution. *The Astrophysical Journal*, 545:1034–1043.
- Sitko, M. L., Carpenter, W. J., Kimes, R. L., Wilde, J. L., Lynch, D. K., Russell, R. W., Rudy, R. J., Mazuk, S. M., Venturini, C. C., Puetter, R. C., Grady, C. A., Polomski, E. F., Wisniewski, J. P., Brafford, S. M., Hammel, H. B., and Perry, R. B. (2008). Variability of Disk Emission in Pre-Main-Sequence and Related Stars. I. HD 31648 and HD 163296: Isolated Herbig Ae Stars Driving Herbig-Haro Flows. *The Astrophysical Journal*, 678:1070–1087.
- Teague, R., Guilloteau, S., Semenov, D., Henning, T., Dutrey, A., Piétu, V., Birnstiel, T., Chapillon, E., Hollenbach, D., and Gorti, U. (2016). Measuring turbulence in TW Hydrae with ALMA: methods and limitations. *Astronomy & Astrophysics*, 592:A49.
- Teague, R., Semenov, D., Gorti, U., Guilloteau, S., Henning, T., Birnstiel, T., Dutrey, A., van Boekel, R., and Chapillon, E. (2017). A Surface Density Perturbation in the TW Hydrae Disk at 95 au Traced by Molecular Emission. *The Astrophysical Journal*, 835:228.
- Teague, R., Semenov, D., Guilloteau, S., Henning, T., Dutrey, A., Wakelam, V., Chapillon, E., and Pietu, V. (2015). Chemistry in disks. IX. Observations and modelling of HCO⁺ and DCO⁺ in DM Tauri. *Astronomy & Astrophysics*, 574:A137.
- Thi, W.-F., Hocuk, S., Kamp, I., Woitke, P., Rab, C., Cazaux, S., and Caselli, P. (2017a). Warm dust surface chemistry in protoplanetary disks - formation of phyllosilicates. *Astronomy & Astrophysics*. submitted.
- Thi, W.-F., Hocuk, S., Kamp, I., Woitke, P., Rab, C., Cazaux, S., and Caselli, P. (2017b). Warm dust surface chemistry in protoplanetary disks - H₂ and HD formation. *Astronomy & Astrophysics*. submitted.
- Thi, W.-F., Pinte, C., Pantin, E., Augereau, J. C., Meeus, G., Ménard, F., Martin-Zaïdi, C., Woitke, P., Riviere-Marichalar, P., Kamp, I., Carmona, A., Sandell, G., Eiroa, C., Dent, W., Montesinos, B., Aresu, G., Meijerink, R., Spaans, M., White, G., Ardila, D., Lobreton, J., Mendigutía, I., and Brittain, S. (2014). Gas lines from the 5-Myr old optically thin disk around HD 141569A . Herschel observations and modeling. *Astronomy & Astrophysics*, 561:A50.
- Thi, W.-F., van Zadelhoff, G.-J., and van Dishoeck, E. F. (2004). Organic molecules in protoplanetary disks around T Tauri and Herbig Ae stars. *Astronomy & Astrophysics*, 425:955–972.

- Thi, W.-F., Woitke, P., and Kamp, I. (2011). Radiation thermo-chemical models of protoplanetary discs - III. Impact of inner rims on spectral energy distributions. *Monthly Notices of the Royal Astronomical Society*, 412:711–726.
- Tilling, I., Woitke, P., Meeus, G., Mora, A., Montesinos, B., Riviere-Marichalar, P., Eiroa, C., Thi, W.-F., Isella, A., Roberge, A., Martin-Zaidi, C., Kamp, I., Pinte, C., Sandell, G., Vacca, W. D., Ménard, F., Mendigutía, I., Duchêne, G., Dent, W. R. F., Aresu, G., Meijerink, R., and Spaans, M. (2012). Gas modelling in the disc of HD 163296. *Astronomy & Astrophysics*, 538:A20.
- Tobin, J. J., Looney, L. W., Wilner, D. J., Kwon, W., Chandler, C. J., Bourke, T. L., Loinard, L., Chiang, H.-F., Schnee, S., and Chen, X. (2015). A Sub-arcsecond Survey Toward Class 0 Protostars in Perseus: Searching for Signatures of Protostellar Disks. *The Astrophysical Journal*, 805:125.
- Trapman, L., Miotello, A., Kama, M., van Dishoeck, E. F., and Bruderer, S. (2017). Far-infrared HD emission as a measure of protoplanetary disk mass. *Astronomy & Astrophysics*, 605:A69.
- Turner, N. J., Fromang, S., Gammie, C., Klahr, H., Lesur, G., Wardle, M., and Bai, X.-N. (2014). Transport and Accretion in Planet-Forming Disks. *Protostars and Planets VI*, pages 411–432.
- Umebayashi, T. and Nakano, T. (2009). Effects of Radionuclides on the Ionization State of Protoplanetary Disks and Dense Cloud Cores. *The Astrophysical Journal*, 690:69–81.
- van Boekel, R., Henning, T., Menu, J., de Boer, J., Langlois, M., Müller, A., Avenhaus, H., Boccaletti, A., Schmid, H. M., Thalmann, C., Benisty, M., Dominik, C., Ginski, C., Girard, J. H., Gisler, D., Lobo Gomes, A., Menard, F., Min, M., Pavlov, A., Pohl, A., Quanz, S. P., Rabou, P., Roelfsema, R., Sauvage, J.-F., Teague, R., Wildi, F., and Zurlo, A. (2017). Three Radial Gaps in the Disk of TW Hydrae Imaged with SPHERE. *The Astrophysical Journal*, 837:132.
- van der Marel, N., van Dishoeck, E. F., Bruderer, S., Birnstiel, T., Pinilla, P., Dullemond, C. P., van Kempen, T. A., Schmalzl, M., Brown, J. M., Herczeg, G. J., Mathews, G. S., and Geers, V. (2013). A Major Asymmetric Dust Trap in a Transition Disk. *Science*, 340:1199–1202.
- van der Plas, G., Casassus, S., Ménard, F., Perez, S., Thi, W. F., Pinte, C., and Christiaens, V. (2014). Spatially Resolved HCN $J = 4-3$ and CS $J = 7-6$ Emission from the Disk around HD 142527. *The Astrophysical Journal Letters*, 792:L25.
- Vorobyov, E. I. and Basu, S. (2010). The Burst Mode of Accretion and Disk Fragmentation in the Early Embedded Stages of Star Formation. *The Astrophysical Journal*, 719:1896–1911.
- Wakelam, V., Herbst, E., Loison, J.-C., Smith, I. W. M., Chandrasekaran, V., Pavone, B., Adams, N. G., Bacchus-Montabonel, M.-C., Bergeat, A., Béroff, K., Bierbaum, V. M., Chabot, M., Dalgarno, A., van Dishoeck, E. F., Faure, A., Geppert, W. D., Gerlich, D., Galli, D., Hébrard, E., Hersant, F., Hickson, K. M., Honvault, P., Klippenstein, S. J., Le Picard, S., Nyman, G., Pernot, P., Schlemmer, S., Selsis, F., Sims, I. R., Talbi, D., Tennyson, J., Troe, J., Wester, R., and Wiesenfeld, L. (2012). A Kinetic Database for Astrochemistry (KIDA). *ApJS*, 199:21.
- Wakelam, V., Loison, J.-C., Herbst, E., Pavone, B., Bergeat, A., Béroff, K., Chabot, M., Faure, A., Galli, D., Geppert, W. D., Gerlich, D., Gratier, P., Harada, N., Hickson, K. M., Honvault, P., Klippenstein, S. J., Le Picard, S. D., Nyman, G., Ruaud, M., Schlemmer, S., Sims, I. R., Talbi, D., Tennyson, J., and Wester, R. (2015). The 2014 KIDA Network for Interstellar Chemistry. *ApJS*, 217:20.
- Walsh, C., Millar, T. J., and Nomura, H. (2013). Molecular Line Emission from a Protoplanetary Disk Irradiated Externally by a Nearby Massive Star. *The Astrophysical Journal Letters*, 766:L23.
- Walsh, C., Nomura, H., Millar, T. J., and Aikawa, Y. (2012). Chemical Processes in Protoplanetary Disks. II. On the Importance of Photochemistry and X-Ray Ionization. *The Astrophysical Journal*, 747:114.

- Williams, J. P. and Best, W. M. J. (2014). A Parametric Modeling Approach to Measuring the Gas Masses of Circumstellar Disks. *The Astrophysical Journal* , 788:59.
- Williams, J. P. and Cieza, L. A. (2011). Protoplanetary Disks and Their Evolution. *Annual Reviews Astronomy and Astrophysics*, 49:67–117.
- Woitke, P., Kamp, I., and Thi, W.-F. (2009). Radiation thermo-chemical models of protoplanetary disks. I. Hydrostatic disk structure and inner rim. *Astronomy & Astrophysics* , 501:383–406.
- Woitke, P., Min, M., Pinte, C., Thi, W.-F., Kamp, I., Rab, C., Anthonioz, F., Antonellini, S., Baldovin-Saavedra, C., Carmona, A., Dominik, C., Dionatos, O., Greaves, J., Güdel, M., Ilee, J. D., Liebhart, A., Ménard, F., Rigon, L., Waters, L. B. F. M., Aresu, G., Meijerink, R., and Spaans, M. (2016). Consistent dust and gas models for protoplanetary disks. I. Disk shape, dust settling, opacities, and PAHs. *Astronomy & Astrophysics* , 586:A103.
- Woitke, P., Min, M., Thi, W.-F., Roberts, C., Carmona, A., Kamp, I., and Ménard, F. (2017). Modelling infrared molecular emission lines from T Tauri stars. *Astronomy & Astrophysics* . submitted.
- Woitke, P., Riaz, B., Duchêne, G., Pascucci, I., Lyo, A.-R., Dent, W. R. F., Phillips, N., Thi, W.-F., Ménard, F., Herczeg, G. J., Bergin, E., Brown, A., Mora, A., Kamp, I., Aresu, G., Brittain, S., de Gregorio-Monsalvo, I., and Sandell, G. (2011). The unusual protoplanetary disk around the T Tauri star ET Chamaeleontis. *Astronomy & Astrophysics* , 534:A44.
- Wolk, S. J., Harnden, Jr., F. R., Flaccomio, E., Micela, G., Favata, F., Shang, H., and Feigelson, E. D. (2005). Stellar Activity on the Young Suns of Orion: COUP Observations of K5-7 Pre-Main-Sequence Stars. *ApJS*, 160:423–449.
- Woodall, J., Agúndez, M., Markwick-Kemper, A. J., and Millar, T. J. (2007). The UMIST database for astrochemistry 2006. *Astronomy & Astrophysics* , 466:1197–1204.
- Yang, H., Herczeg, G. J., Linsky, J. L., Brown, A., Johns-Krull, C. M., Ingleby, L., Calvet, N., Bergin, E., and Valenti, J. A. (2012). A Far-ultraviolet Atlas of Low-resolution Hubble Space Telescope Spectra of T Tauri Stars. *The Astrophysical Journal* , 744:121.
- Yen, H.-W., Liu, H. B., Gu, P.-G., Hirano, N., Lee, C.-F., Puspitaningrum, E., and Takakuwa, S. (2016). Gas Gaps in the Protoplanetary Disk around the Young Protostar HL Tau. *The Astrophysical Journal Letters* , 820:L25.
- Yu, M., Evans, II, N. J., Dodson-Robinson, S. E., Willacy, K., and Turner, N. J. (2017). Disk Masses around Solar-mass Stars are Underestimated by CO Observations. *The Astrophysical Journal* , 841:39.
- Yurkin, M. A. and Hoekstra, A. G. (2011). The discrete-dipole-approximation code ADDA: Capabilities and known limitations. *Journal of Quantitative Spectroscopy and Radiative Transfer* , 112:2234–2247.
- Zhu, Z. and Stone, J. M. (2014). Dust Trapping by Vortices in Transitional Disks: Evidence for Non-ideal Magnetohydrodynamic Effects in Protoplanetary Disks. *The Astrophysical Journal* , 795:53.
- Zhu, Z., Stone, J. M., Rafikov, R. R., and Bai, X.-n. (2014). Particle Concentration at Planet-induced Gap Edges and Vortices. I. Inviscid Three-dimensional Hydro Disks. *The Astrophysical Journal* , 785:122.

Appendix A

List of Figures

1.1	Sketch of the main stages of low-mass star formation.	3
1.2	Synthetic spectral energy distribution.	7
1.3	X-ray spectrum of DM Tau.	10
1.4	Schematic view of a protoplanetary disk.	13
1.5	General code structure of PRODiMO	18
1.6	Output of a PRODiMO model.	19
1.7	Disk heating and cooling processes.	26
1.8	Spectral energy distribution fit for MWC 480	29
1.9	Fitted line fluxes for MWC 480	30
1.10	Fitted line profiles for MWC 480	30
2.1	Gas disk structure	37
2.2	Large grains and small grains disk model	38
2.3	Optical constants for Astronomical Silicates in the X-ray regime	39
2.4	Gas and dust X-ray cross-sections for three different dust size distributions . . .	40
2.5	X-ray background field spectra	41
2.6	X-ray ionization rate for the 2D disk structure	41
2.7	X-ray ionization rate versus vertical column density	42
2.8	X-ray ionization rates for three different dust models	43
2.9	X-ray ionization rate including a X-ray background field	43
2.10	X-ray ionization rate in the midplane and at a vertical cut at $r = 150$ au	44
2.11	HCO^+ and N_2H^+ column densities for models with different dust size distributions	45
2.12	Column density profiles for HCO^+ and N_2H^+ including X-ray background fields	47
2.13	Comparison of X-ray photoelectric cross-sections	50
2.14	Comparison of X-ray ionization rates of PRODiMO to MOCASSIN	50
2.15	Comparison of X-ray ion. rates of PRODiMO to MOCASSIN for a flared spectrum	51
3.1	Solar energetic particle spectra	56
3.2	Stellar energetic particle and cosmic-ray input spectra	57
3.3	Stellar X-ray input spectra	58
3.4	Two dimensional structure of the reference disk model	59
3.5	Ionization rates as a function of hydrogen column density	60
3.6	Disk ionization rates as a function of vertical hydrogen column density	61

3.7	Dominant disk ionization source throughout the disk	61
3.8	2D molecular abundances for CO, HCO ⁺ and N ₂ H ⁺	62
3.9	Vertical column density profiles for HCO ⁺ and N ₂ H ⁺	63
3.10	Ionization rate weighted column densities for HCO ⁺ and N ₂ H ⁺	64
3.11	HCO ⁺ and N ₂ H ⁺ column densities for varying SP flux and X-ray emission	66
3.12	X-ray ionization rate as a function of vertical column density	71
3.13	X-ray ionization rate in the midplane of the disk	71
3.14	HCO ⁺ and N ₂ H ⁺ column densities for the chemical test models	72
3.15	Comparison of time-dependent and stead-state chemical models	73
3.16	Ionization rates at a fixed vertical column density	74
4.1	Density and temperature structure for the representative Class I model	80
4.2	Dust opacities for the envelope and the disk dust population	81
4.3	Evolution of the CO gas phase abundance in the post-burst phase	84
4.4	C ¹⁸ O $J=2-1$ ALMA simulations for the representative Class I model	85
4.5	C ¹⁸ O $J=2-1$ ALMA simulations for an edge-on model	86
4.6	Impact of inclination on the radial intensity profiles	86
4.7	Impact of structure on the radial intensity profiles	87
4.8	C ¹⁸ O $J=2-1$ radial intensity profiles derived from fitting synthetic observations	88
4.9	Measured C ¹⁸ O $J=2-1$ extent versus current bolometric luminosity	89
4.10	Midplane density and temperature profiles for the comparison to the 1D model	94
4.11	Midplane abundance profiles for the comparison to the 1D model	95
4.12	Comparison of full ALMA simulations to beam convolved models	96
4.13	C ¹⁸ O $J=2-1$ ALMA simulation for models with different inclinations	97
4.14	Time evolution of C ¹⁸ O $J=2-1$ intensity profiles for different structure models	98
4.15	Fitting example for a face-on model	99
4.16	Fitting example for a model with $E_B(\text{CO}) = 960 \text{ K}$	99
4.17	Fitting example for a model with a spherical density distribution	100
4.18	Fitting example for a model with a beam size of $0.5'' \times 0.5''$	100
4.19	Fitting example for a model with a weak burst	100
4.20	Fitting example for the full ALMA simulation	101

List of Tables

1.1	Star and disk properties of the MWC 480 model	31
2.1	Main parameters for the reference disk model	37
2.2	Dust models	38
3.1	Fitting parameters for the stellar particle ionization rate	57
3.2	Parameters for the stellar X-ray input spectra	58
3.3	Fitting parameters for the cosmic-ray ionization rate	58
3.4	Main fixed parameters of the disk model	59
3.5	Model series	60
3.6	Rate coefficients for the main formation/destruction reactions of HCO^+ and N_2H^+	72
3.7	Chemical test models	72
3.8	Important binding energies	73
4.1	Main parameters of the Class I model	79
4.2	Dust properties of relevance for the chemistry in the disk and envelope	81
4.3	Model parameters for the comparison with Visser et al. (2015)	94
4.4	Initial abundances for the time-dependent chemistry	94
4.5	Adsorption energies of key molecules	94

Zusammenfassung

Wie entstand unsere Sonne und unser Sonnensystem? Diese Frage ist von großem Interesse nicht nur für Astronomen. Wichtige Erkenntnisse bezüglich dieser Frage erlangen wir mittels Beobachtungen und theoretischen Untersuchungen von sonnenähnlichen, aber sehr jungen Sternen. Diese circa eine Million Jahre jungen Sterne sind eingebettet in einer Wolke aus Staub und Gas, aus der sich eine rotierende Scheibe formt. Diese protoplanetaren Scheiben sind die Geburtsstätten von Planeten.

Im Vergleich zur Sonne befinden sich junge Sterne in einer sehr aktiven und wilden Entwicklungsphase. Sie emittieren 10 000 mal mehr Röntgenstrahlen als unsere Sonne und produzieren wahrscheinlich auch signifikant mehr stellare energiereiche Teilchen (stark beschleunigte Protonen). Sowohl Röntgenstrahlen als auch die Teilchen haben genug Energie, um molekularen Wasserstoff, das am häufigsten vorhandene Molekül in der Umgebung des Sterns, zu ionisieren und spielen daher eine wichtige Rolle in der Entwicklung der zirkumstellaren Materie. Diese jungen Sterne befinden sich noch in ihrer Wachstumsphase, da sie immer noch Materie aus ihre Umgebung einsammeln. Diese Akkretion von Materie erfolgt nicht kontinuierlich, sondern ist gekennzeichnet durch kurze, ca. 100 Jahre dauernden Phasen von stark erhöhter Materieakkretion. In diesen Phasen erhöht sich die Helligkeit des jungen Objektes abrupt um mehr als das hundertfache. Solche Akkretionsausbrüche haben eine signifikante Auswirkung auf die Entwicklung des Sterns und seiner zirkumstellaren Wolke. In dieser Arbeit untersuchen wir die Auswirkung solcher energiereichen Prozesse auf die chemische Entwicklung der zirkumstellaren Wolke. Darüber hinaus, versuchen wir, beobachtbare Signaturen zu finden, um die Eigenschaften junger Sterne, wie zum Beispiel deren vermeintlich erhöhte Teilchenproduktion oder Akkretionsgeschichte, besser zu bestimmen und zu verstehen.

Für unsere Studien verwendeten wir den Scheibenmodellierungs-Code PRODiMO (PROtoplanetary DIsk MOdel). PRODiMO simuliert Strahlungstransport, thermische und chemische Prozesse für eine statische Scheibenstruktur unter Berücksichtigung der stellaren Emission. Für diese Arbeit haben wir eine neues Röntgenstrahlungstransport-Modul entwickelt, das Streuung, Staubopazitäten und Hintergrundbestrahlung von Scheiben berücksichtigt. Mit Hilfe von bestehenden Teilchentransportmodellen implementierten wir den Prozess von Ionisation durch energiereiche Teilchen. Für unsere Untersuchungen bezüglich Akkretionsausbrüchen erweiterten wir PRODiMO mit einer parametrisierten Beschreibung der Dichtestruktur einer den Stern und die Scheibe umgebenden Wolke.

Wir simulierten die chemischen Auswirkungen von Röntgenstrahlung und stellaren energiereichen Teilchen für eine repräsentative protoplanetare Scheibe. Unsere Modelle zeigen, dass in typischen Sternentstehungsregionen das Röntgen-Hintergrundstrahlungsfeld nur wenig Einfluss auf die Chemie der Scheibe hat. Nur unter bestimmten Umständen (z.B. niedrige kosmische Strahlung, sehr starke Hintergrundstrahlung) hat das Hintergrundstrahlungsfeld beobachtbare Auswirkungen auf die Chemie der äußeren Scheibe. Unter Annahme von theoretisch vorhergesagten erhöhten Teilchenflüssen und dass die Teilchen die Scheibe auch erreichen, zeigen unsere Modelle einen signifikanten Einfluss der Teilchen auf die Chemie der Scheibe. Um den Teilchenfluss junger Sterne zu bestimmen sind allerdings räumlich hochaufgelöste Beobachtungen von Spektrallinien ionisierter Moleküle und detaillierte Modelle notwendig. Unsere Simulationen des Einflusses von Akkretionsausbrüchen auf die chemische Entwicklung der zirkumstellaren Wolke zeigen ausgeprägte

und beobachtbare Ring- und X-förmige Strukturen in der Linienemission von Molekülen. Ursache dieser Strukturen ist das zeitlich verzögerte Ausfrieren der Moleküle nach dem Ende des Helligkeitsausbruches. Basierend auf unseren Modellen entwickelten wir eine Methode zur direkten Identifizierung von Objekten, die einen bereits vergangenen Helligkeitsausbruch durchlebt haben. Diese Methode kann direkt, ohne detaillierte Modellierung, auf Beobachtungsdaten angewendet werden.

Mit unseren Modellen ist nun eine detaillierte Interpretation von räumlich hochaufgelösten Beobachtungen der Emission von ionisierten Molekülen möglich. Solche Beobachtungen sind derzeit noch rar, aber mit derzeitigen modernen (sub)mm Teleskopen möglich. Zudem planen wir, unsere Ionisations-Modelle auch auf frühere Phasen der Sternentstehung, in denen der Stern noch tief in der Gaswolke eingebettet ist, anzuwenden. Im Rahmen eines noch laufenden Projektes werden unsere Modelle für die Chemie der Akkretionsausbrüche zur Interpretation bestehender Beobachtungen verwendet und um permanente chemische Signaturen, verursacht durch die Helligkeitsausbrüche, zu identifizieren.

Astronomy and Astrophysics

Editor in Chief: T. Forveille

T. Forveille

Astronomy & Astrophysics
Observatoire de Paris
61, avenue de l'Observatoire
75014 Paris, France

Tel.: 33 0(1) 43 29 05 41
Fax: 33 0(1) 43 29 05 57
e-mail: aanda.paris@obspm.fr
Web: <http://www.aanda.org>

merging
Annales d'Astrophysique
Arkiv for Astronomi
Bulletin of the Astronomical Institutes
of the Netherlands
Bulletin Astronomique
Journal des Observateurs
Zeitschrift für Astrophysik
Bulletin of the Astronomical Institutes
of Czechoslovakia

Paris, September 22, 2017

Reprint Permission**Material:**

Article by Rab, C. et al. 2017 A&A 603, A96
Article by Rab, C. et al. 2017 A&A 604, A15

To be used in:

PhD thesis entitled "Modelling of energetic processes in the circumstellar environment of young solar like stars", University of Vienna

Permission granted to:

Christian Rab <christian.rab@univie.ac.at>

I hold copyright on the material referred to above, and hereby grant permission for its use as requested herewith.

The article should be reproduced in the same format as that published in A&A (for example, in an appendix). In particular, the present permission rules do not allow copy-and-pasting parts of the article into the main text of the thesis.

Credit should be given as follows:

Credit: Author, A&A, vol, page, year, reproduced with permission © ESO.



Thierry Forveille
A&A Editor-in-Chief

Acknowledgements

Some time ago I decided to quit my job as a software developer in an insurance company and started to study Astronomy and Astrophysics at the University of Vienna. I started my studies solely because of my interest in Astronomy and Astrophysics and would never have thought to actually go the whole way and write a PhD thesis. But here it is! It was a long and sometimes burdensome way but I really enjoyed it and never regretted my decision. But for sure, all this would not have been possible with the help and support of others.

My special gratitude goes to my supervisor Prof. Manuel Güdel. Manuel's lecture about Star and Planet formation was the reason why I got interested in this topic in the first place. He already provided me with an interesting topic for my Master thesis on radiative transfer in protoplanetary disks and subsequently offered me a PhD position. Without him, this work would not have been possible. THANK YOU VERY MUCH, Manuel, for all your support and patience during the process of writing the papers and this thesis. I hope we can continue to work together on those interesting topics (or other interesting ones) in the future.

Luckily I was not working in isolation during my time in Vienna as I was embedded in the star and planet formation group of Manuel. It was a pleasure for me to work in this group. My group colleagues always had an open ear for my smaller and bigger problems. A big "Thank You!" therefore goes to Odysseas, Carla, Colin, Eduard, Bibiana, Theresa, Armin and Ines. I also want to thank "my" Master student Robert, for always keeping his very positive attitude during our collaboration.

As it is with science, this PhD project experienced quite some adaptations with respect to the initial plan. One change concerns the collaboration with Prof. Peter Hauschildt and the use of his PHOENIX/3D code, which I used for my Master thesis. It was planned for this PhD to continue my work on PHOENIX/3D/DISK, which at some point was not possible anymore. Although this project did not go as planned I learned a lot by working with and extending PHOENIX/3D towards a protoplanetary disk code. I also enjoyed my visits to Hamburg and I want to thank Peter for his generous support. I certainly will profit from the PHOENIX/3D project for my future work on developing disk modelling codes and maybe there will be a possibility once to continue the PHOENIX/3D/DISK project.

My gratitude also goes to the main developers of ProDiMo Inga, Peter and Wing-Fai. They were always eager to answer me questions concerning ProDiMo and the science of protoplanetary disks. In particular, I want to thank Inga for her patience and for allowing me to finish my PhD at my new workplace at the University of Groningen. I also want to thank the whole DIANA team. The many team meetings were always very interesting and great fun. Although being part of a big EU funded project is not always a pleasure (I just say: deliverables, reports and reviews), it was overall a great and very important experience for me. I am looking forward to the ongoing and future collaborations with the DIANA team members.

I want to thank Marco for his invaluable contribution to the stellar particle paper. Without Marco's expertise in particle transport, this project would not have been a success. I hope we will continue to work on this topic in the near future. I also hope to once listen

to one of your music concerts!

During my PhD, I also joined a new project which led to the episodic accretion paper. I was part of the episodic accretion project already before there was funding. It was a very valuable experience for me being involved in the proposal writing and to see how hard it can be to get funding. I want to thank Marc, Eduard and Manuel for providing me with funding for my final period of the PhD. Special thanks go to Vardan who provided a very important piece for the episodic accretion paper. I am sure we will enjoy our further work on this subject.

My research would not have been possible without special computer equipment and software. I want to thank in particular all the various software developers and open source communities which develop and maintain important tools like LAPACK, BLAS, xraylib, matplotlib, astropy, numpy (just to mention a few) but also the Linux open source community in general. Nearly all of the models presented here were calculated on the Vienna Scientific Cluster and I want to thank the VSC team for keeping the VSC in a formidable shape.

During my studies, I met many new, interesting and funny people and I would say we had a lot of fun together. It is impossible for me to mention you all, so I hope it is okay if I just say: Thank you, it was a great pleasure. I also want to thank my “old” friends, in particular, Kritzi, Martin, Pfaffi und Schmidl for always trying to stay in touch with me, which I guess isn’t always easy.

Besonderer Dank für ihre Unterstützung auf meinem Lebensweg gilt meiner Mutter, Theresia, meinem Vater, Anton und meinen Geschwistern Anton, Franz, Kurt, Maria, Gerhard, Theresia, Martin, Andreas, Barbara und Manuela. Vielen Dank für all die kleinen und grossen Dinge, die ihr für mich gemacht habt!

Im besonderen möchte ich meiner Freundin Katrin und meinen Töchtern Anika und Franka danken. Vielen Dank für eure Geduld und Nachsichtigkeit, vor allem wenn ich in nicht “besonders guter” Stimmung war. Es ist eines der schönsten Dinge im Leben, nach einem anstrengenden und vielleicht nicht so erfolgreichen Arbeitstag, von zwei Kindern in Empfang genommen zu werden, die sich einfach nur freuen, weil man nach Hause kommt. Katrin ist nun schon seit fast 20 Jahren Teil meines Lebens. Sie unterstützte mich bei der schwierigen Entscheidung, meinen Job zu kündigen und ein Studium zu beginnen. Sie war bereit, für mich ihren Job aufzugeben und mit mir in die Niederlande zu übersiedeln. Katrin, ohne dich wäre das alles nicht möglich gewesen und ohne dich hätte ich dieses Abenteuer wohl auch nie gewagt. Ich liebe Dich!

Appendix B

Publication List

Peer-Reviewed

- Pinte, C., Ménard, F., Duchêne, G., Hill, T., Dent, W.R.F., Woitke, P., Maret, S., van der Plas, G., Hales, A., Kamp, I., Thi, W.-F., de Gregorio-Monsalvo, I., **Rab, Ch.**, Quanz, S., Avenhaus, H., Carmona, A., and Casassus, S. (2017). Altitude, velocity and temperature of the CO layers. Imaging the vertical CO snow line in the disc surrounding IM Lupi. *Astronomy & Astrophysics*. in press.
- Kamp, I., Thi, W.-F., Woitke, P., **Rab, Ch.**, Bouma, S., and Menard, F. (2017). Consistent dust and gas models for protoplanetary disks: II. Chemical networks and rates. *Astronomy & Astrophysics*, in press, DOI: [10.1051/0004-6361/201730388](https://doi.org/10.1051/0004-6361/201730388).
- Rab, Ch.**, Elbakyan, V., Vorobyov, E., Güdel, M., Dionatos, O., Audard, M., Kamp, I., Thi, W.-F., Woitke, P., and Postel, A. (2017a). The chemistry of episodic accretion in embedded objects. 2D radiation thermo-chemical models of the post-burst phase. *Astronomy & Astrophysics*, 604:A15, A15, DOI: [10.1051/0004-6361/201730812](https://doi.org/10.1051/0004-6361/201730812).
- Rab, Ch.**, Güdel, M., Padovani, M., Kamp, I., Thi, W.-F., Woitke, P., and Aresu, G. (2017b). Stellar energetic particle ionization in protoplanetary disks around T Tauri stars. *Astronomy & Astrophysics*, 603:A96, A96, DOI: [10.1051/0004-6361/201630241](https://doi.org/10.1051/0004-6361/201630241).
- Greenwood, A. J., Kamp, I., Waters, L. B. F. M., Woitke, P., Thi, W.-F., **Rab, Ch.**, Aresu, G., and Spaans, M. (2017). Thermochemical modelling of brown dwarf discs. *Astronomy & Astrophysics*, 601:A44, A44, DOI: [10.1051/0004-6361/201629389](https://doi.org/10.1051/0004-6361/201629389).
- Paunzen, E., Handler, G., Lendl, M., Baumann, B., **Rab, Ch.**, Meingast, S., Rode-Paunzen, M., Netopil, M., Antoci, V., Zhu, L., Zejda, M., and Božić, H. (2017). Search for variables in six Galactic open clusters. *New Astronomy*, 52:133–139, DOI: [10.1016/j.newast.2016.10.012](https://doi.org/10.1016/j.newast.2016.10.012).
- Rab, Ch.**, Baldovin-Saavedra, C., Dionatos, O., Vorobyov, E., and Güdel, M. (2016). The Gas Disk: Evolution and Chemistry. *Space Science Reviews*, 205:3–40, ISSN: 0038-6308, DOI: [10.1007/s11214-016-0325-5](https://doi.org/10.1007/s11214-016-0325-5).
- Woitke, P., Min, M., Pinte, C., Thi, W.-F., Kamp, I., **Rab, Ch.**, Anthonioz, F., Antonellini, S., Baldovin-Saavedra, C., Carmona, A., Dominik, C., Dionatos, O., Greaves, J., Güdel, M., Ilee, J. D., Liebhart, A., Ménard, F., Rigon, L., Waters, L. B. F. M., Aresu, G., Meijerink, R., and Spaans, M. (2016). Consistent dust and gas models for protoplanetary disks. I. Disk shape, dust settling, opacities, and PAHs. *Astronomy & Astrophysics*, 586:A103, A103, DOI: [10.1051/0004-6361/201526538](https://doi.org/10.1051/0004-6361/201526538).
- Min, M., **Rab, Ch.**, Woitke, P., Dominik, C., and Ménard, F. (2016). Multiwavelength optical properties of compact dust aggregates in protoplanetary disks. *Astronomy & Astrophysics*, 585:A13, A13, DOI: [10.1051/0004-6361/201526048](https://doi.org/10.1051/0004-6361/201526048).

Non Peer-Reviewed

Faraday Discuss. (2014). General discussion. *Faraday Discussions*, 168:423–448, DOI: [10.1039/C4FD90004A](https://doi.org/10.1039/C4FD90004A). Conference proceedings.

Min, M., **Rab, Ch.**, Dominik, C., and Woitke, P. (2013). The appearance of large aggregates in protoplanetary disks. In *Protostars and Planets VI, Heidelberg, July 15-20, 2013. Poster #2S044*. <http://www.mpia.de/homes/ppvi/posters/2S044.pdf>.

Rab, Ch., Woitke, P., Güdel, M., Min, M., and Diana Team (2013). X-ray Radiative Transfer in Protoplanetary Disks with ProDiMo. In *Protostars and Planets VI, Heidelberg, July 15-20, 2013. Poster #2B038*, page 38. <http://www.mpia.de/homes/ppvi/posters/2B038.pdf>.

Successful observing proposals

Eccentric wide hot-subdwarf binaries: Testing the circumbinary disk hypothesis

ALMA 2017.1.00614.S (3.1h)

J. Vos (PI), M. Vuckovic, S. Randall, **Ch. Rab**, A. Aller

Searching for the flow-base of the disk wind of TW Hya

ALMA 2016.1.01375.S (2.3h)

Ch. Rab (PI), O. Dionatos, W-F. Thi, M. Güdel, P. Woitke

Blowin' in the Wind: The Outflows of DG Tau

ALMA 2016.1.01120.S (2.4h)

M. Güdel (PI), O. Dionatos, S. Kraus, E. Vorobyov, S. Skinner, J. Forbrich, C. Schneider, M. Audard, **Ch. Rab**

Disk winds in the low accretion regime: a study of [NeII] emission in protoplanetary disks

ESO-P97A VLT-VISIR (26h)

C. Baldovin-Saavedra (PI), M. Güdel, M. Audard, **Ch. Rab**

Witnessing the Dissipation of Transition Disks

ESO-P97A VLT-UVES (9h)

C. Baldovin-Saavedra (PI), A. Carmona, M. Güdel, M. Audard, **Ch. Rab**

Curriculum Vitae

Christian Rab



Personal Information

Date of birth: April 4, 1978
Place of birth: Amstetten, Austria
Marital status: domestic partnership, two daughters (8 and 3 years)
Citizenship: Austria

Education

Oct. 2012 – PhD studies of Astronomy at the University of Vienna.
Supervisor: Manuel Güdel

Oct. 2009 – May 2012 Master studies of Astronomy at the University of Vienna.
Thesis: "Dust RT in Protoplanetary Disks with PHOENIX/3D"
Supervisor: Manuel Güdel. Passed with distinction.

Mar. 2006 – Aug. 2009 Bachelor studies of Astronomy at the University of Vienna.
Thesis: "Direct Evidence for Dark Matter in Clusters of Galaxies"
Supervisor: Christian Theis. Passed with distinction.

Sept. 1992 – Jun. 1997 HTL (higher technical school), St. Pölten, Austria
Department: EDP and Organisation/Computer Science.
Passed with merit.

Sept. 1987 – Jun. 1992 Secondary general school (Hauptschule), Blindenmarkt, Austria

Sept. 1984 – Jun. 1987 Primary school, Ferschnitz, Austria

Professional Experience

May 2017 – Postdoc - Kapteyn Institute, University of Groningen

Feb. 1999 – Jan. 2006 Software engineer - Dr. E. Hackhofer GesmbH, Vienna

Feb. 1998 – Jan. 1999 Alternative civilian service at a nursing home for the elderly

Oct. 1997 – Jan. 1998 Software engineer - Dr. E. Hackhofer GesmbH, Vienna